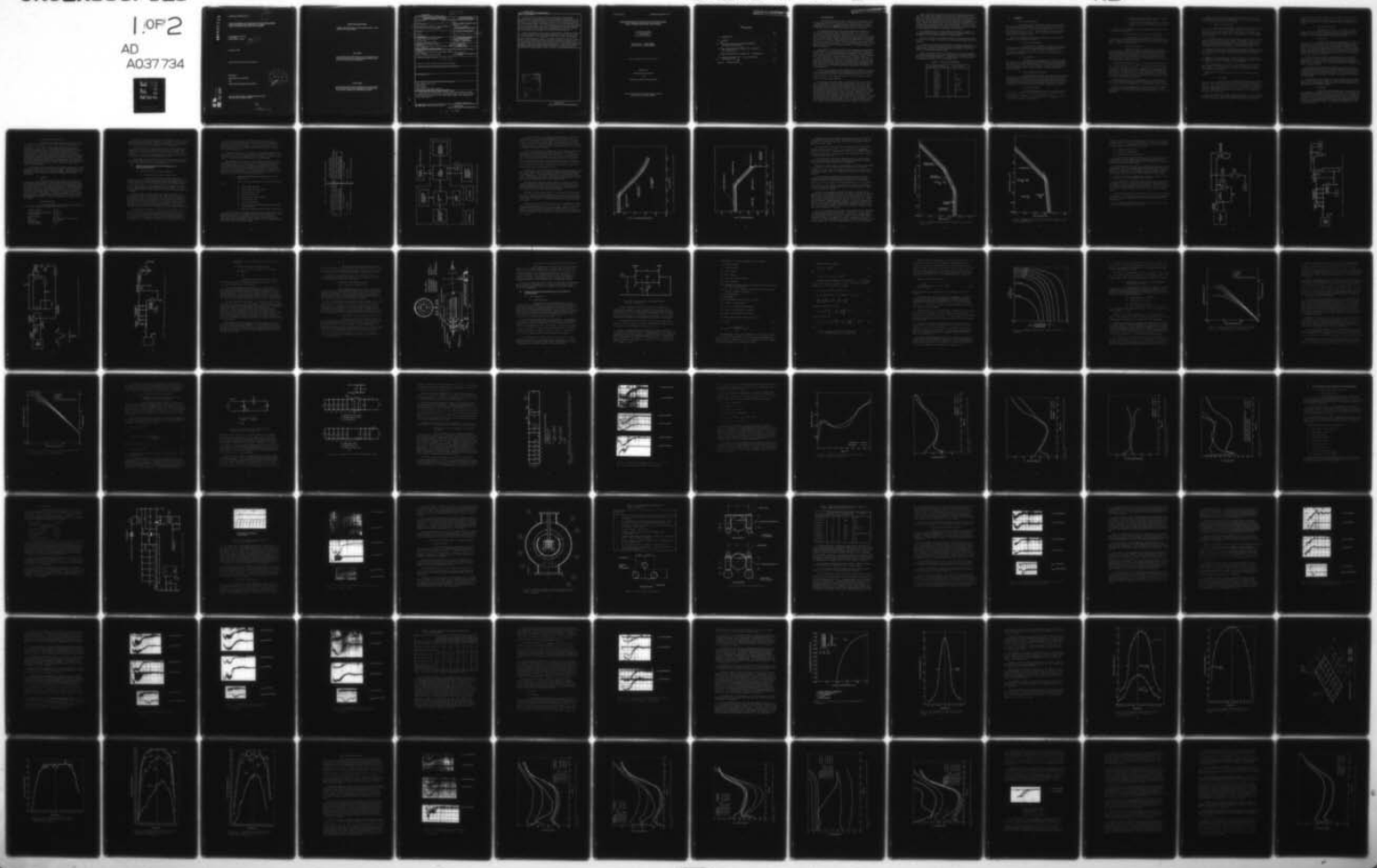
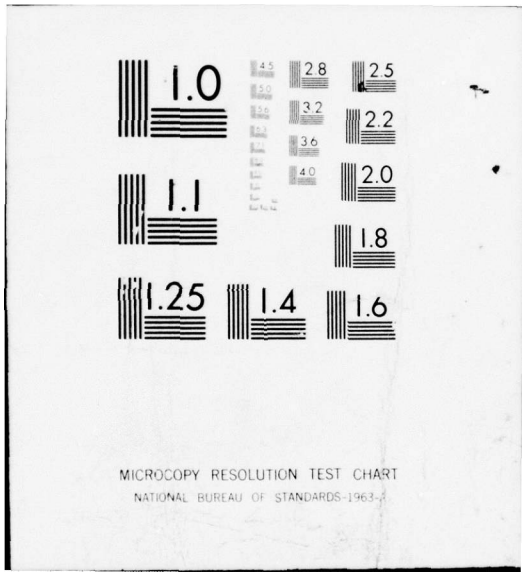
AD-A037 734 SYSTEMS SCIENCE AND SOFTWARE HAYWARD CALIF F/G 9/1
INVESTIGATION OF COUPLING OF FIELD EMISSION COLD CATHODE GUNS F--ETC(U)
FEB 77 G LODA, D A MESKAN DAAH01-74-C-0624
UNCLASSIFIED DRDMI-H-77-1 NL

1 OF 2
AD
A037734




1.0
1.1
1.25
1.4
1.6
1.8
2.0
2.2
2.5
2.8
3.2
3.6
4.0
4.5
5.0
5.6
MICROCOPY RESOLUTION TEST CHART
NATIONAL BUREAU OF STANDARDS-1963-A

ADA037734

TECHNICAL REPORT H-77-1

(9)

INVESTIGATION OF COUPLING OF FIELD EMISSION COLD CATHODE GUNS FOR GAS LASERS

Systems Science and Software
P.O. Box 4803
Hayward, California 94540

391271

4 February 1977

Approved for public release; distribution unlimited.

DDC
RECEIVED
APR 4 1977
A

Prepared for

High Energy Laser Laboratory

and

High Energy Laser Systems Project Office

AD No. ____
DDC FILE COPY

US Army Missile Research and Development Command
Redstone Arsenal, Alabama 35809

S/L
391271

DISPOSITION INSTRUCTIONS

DESTROY THIS REPORT WHEN IT IS NO LONGER NEEDED. DO NOT RETURN IT TO THE ORIGINATOR.

DISCLAIMER

THE FINDINGS IN THIS REPORT ARE NOT TO BE CONSTRUED AS AN OFFICIAL DEPARTMENT OF THE ARMY POSITION UNLESS SO DESIGNATED BY OTHER AUTHORIZED DOCUMENTS.

TRADE NAMES

USE OF TRADE NAMES OR MANUFACTURERS IN THIS REPORT DOES NOT CONSTITUTE AN OFFICIAL INDORSEMENT OR APPROVAL OF THE USE OF SUCH COMMERCIAL HARDWARE OR SOFTWARE.

(18) DRDMI-H (19) 77-1

UNCLASSIFIED

SECURITY CLASSIFICATION OF THIS PAGE (When Data Entered)

REPORT DOCUMENTATION PAGE

READ INSTRUCTIONS BEFORE COMPLETING FORM

1. REPORT NUMBER: H-77-1	2. GOVT ACCESSION NO.
3. RECIPIENT'S CATALOG NUMBER	
4. TITLE (and Subtitle): INVESTIGATION OF COUPLING OF FIELD EMISSION COLD CATHODE GUNS FOR GAS LASERS.	5. TYPE OF REPORT & PERIOD COVERED: Final Technical Report.
	6. PERFORMING ORG. REPORT NUMBER
7. AUTHOR(s): G. Loda, D. A. Meskan	8. CONTRACT OR GRANT NUMBER(s): DAAHD1-74-C-0624
9. PERFORMING ORGANIZATION NAME AND ADDRESS: Systems Science and Software, P.O. Box 4803, Hayward, California 94540	10. PROGRAM ELEMENT, PROJECT, TASK AREA & WORK UNIT NUMBERS: (DA) 1X363314D093, AMCMSC 633314.0930012
11. CONTROLLING OFFICE NAME AND ADDRESS: Commander, US Army Missile Research and Develppment Command, Attn: DRDMI-TI, Redstone Arsenal, Alabama 35809	12. REPORT DATE: 4 February 1977
	13. NUMBER OF PAGES
14. MONITORING AGENCY NAME & ADDRESS (if different from Controlling Office): Commander, US Army Missile Research and Development Command, Attn: DRDMI-H, Redstone Arsenal, Alabama 35809	15. SECURITY CLASS. (of this report): Unclassified
	15a. DECLASSIFICATION/DOWNGRADING SCHEDULE

16. DISTRIBUTION STATEMENT (of this Report) (12) 183p.

Approved for public release; distribution unlimited.

17. DISTRIBUTION STATEMENT (of the abstract entered in Block 20, if different from Report)

18. SUPPLEMENTARY NOTES

19. KEY WORDS (Continue on reverse side if necessary and identify by block number)

High energy lasers; cold
Cold cathode
Electron guns
High energy pulsed power systems
Electron beam controlled high energy lasers

20. ABSTRACT (Continue on reverse side if necessary and identify by block number)

Results of the first phase of the work under this contract have been reported previously in SSS-75-264, Repetitively Pulsed Cold Cathode Studies, Interim Technical Report for the period ending 30 March 1975 (Appendix of the present report).

ABSTRACT (Continued)

DD FORM 1 JAN 73 1473 EDITION OF 1 NOV 65 IS OBSOLETE

UNCLASSIFIED

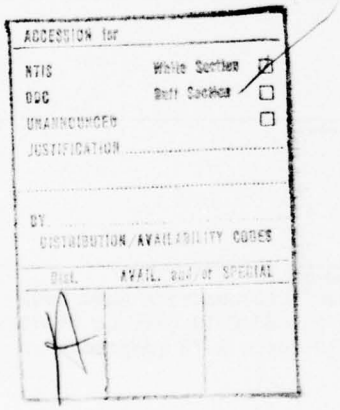
SECURITY CLASSIFICATION OF THIS PAGE (When Data Entered)

391 271

Block 20 (Concluded)

The objective of the first phase was to determine the operational characteristics of high repetition rate cold cathode electron guns and to use the data in the conceptual design of an example system. Measurements were performed on a cold cathode gun operated in a diode configuration, with and without focussing electrodes. Pulse lengths from 2 to 10 μsec and repetiton rates from 1 to 50 were studied. Much of the information from the first phase applies to triode as well as diode cold cathode guns; examples are the data regarding the relationship between vacuum system requirements and beam power, and the cathode voltage pulse requirements for effective cathode ignition.

Phase 2, the subject of this report, emphasized cold cathode gun operation in a triode configuration, using a self-biased control grid, with and without focussing electrodes. Also emphasized is operation at longer pulse lengths, 12 μsec, and pulse rates of 50 sec^{-1}, although pulse rates to 125 sec^{-1} were measured. This document provides the basis for extending the present data base to the design of new systems. Based upon data derived from this program, a conceptual design for a repetitively pulsed gun with a 7.5-kW beam is presented. A summary of the program and principle conclusions are given, and a review of possible applications for cold cathode technology is presented along with a discussion of the relationship of this technology to other electron beam sources.



4 February 1977 TECHNICAL REPORT H-77-1

INVESTIGATION OF COUPLING OF FIELD EMISSION COLD CATHODE GUNS FOR GAS LASERS

G. Loda and D. A. Meskan
Systems Science and Software
P.O. Box 4809
Hayward, California 94540

DA Project No. 1X363314D093
AMCMS Code No. 633314.0930012

Approved for public release; distribution unlimited.

Prepared for

High Energy Laser Laboratory

and

High Energy Laser Systems Project Office

US Army Missile Research and Development Command
Redstone Arsenal, Alabama 35809

PRECEDING PAGE BLANK-NOT FILMED

CONTENTS:

		Page
I.	INTRODUCTION	5
II.	SUMMARY	7
III.	REPETITIVE PULSE COLD CATHODE TECHNOLOGY IN SYSTEM APPLICATIONS	12
IV.	GRID CONTROLLED COLD CATHODE GUNS: ANALYSIS AND CALCULATIONS	30
V.	GRID CONTROLLED COLD CATHODE GUN: MEASUREMENTS	52
VI.	CONCEPTUAL DESIGN FOR A 7.5-kW BEAM POWER COLD CATHODE GUN	99
Appendix.	INTERIM REPORT	117

PRECEDING PAGE BLANK-NOT FILMED

I. INTRODUCTION

This final technical report documents results obtained during the contract period from 8 April 1974 to (contract completion date to be determined) for US Army Missile Research and Developmett Command (MIRADCOM) contract No. DAAH01-74-C-0624, Results of the first phase of the work under this contract have previously been reported.*

The experimental work of both program phases was performed on the S-Cubed Rapid Pulse Facility which was built for the study of repetitively pulsed cold cathode electron guns. The use of this facility enabled performance of a far more ambitious program than usual for the funding level. Because of the close relationship of the earlier and present work, and to avoid duplication of material such as descriptions of the test facility and diagnostic equipment, the Interim Report has been included as an Appendix. This Introduction and the next section, Summary, cover the entire program and identify the tasks performed in each program phase.

The objective of the first phase was to determine the operational characteristics of high repetition rate cold cathode electron guns and use the data in the conceptual design of an example system. Measurements were performed on a cold cathode gun operated in a diode configuration, with and without focussing electrodes. Pulse lengths from 2 to 10 μsec and repetition rates from 1 to 50 were studied. Most data were taken for 3-μsec pulses. Much of the information from the first phase applies to triode as well as diode cold cathode guns; examples are the data regarding the relationship between vacuum system requirements and beam power, and the cathode voltage pulse requirements for effective cathode ignition.

The work of the present phase emphasizes cold cathode gun operation in a triode configuration, using a self-biased control grid, with and without focussing electrodes. Also emphasized is operation at longer pulse lengths, 12 μsec, and pulse rates of 50 sec^{-1}, although pulse rates to 125 sec^{-1} were measured.

The motivation for development of grid-controlled cold cathode guns is the need for compact and efficient electron guns which produce low current density beams for laser applications. Until now, laser cold cathode guns have been diode types and have been used in applications where current densities in excess of several hundred milliamps per square centimeter are required, or used very inefficiently in lower current density applications. Because the cold cathode gun operates space-charge current limited, the only methods for obtaining lower current density from diode guns at a fixed cathode voltage are to increase the anode-cathode spacing and thereby make the gun very large (in some case the size becomes impractical), or to use a beam window structure which absorbs most of the beam and makes the system very inefficient.

Laser requirements generate an inverse relationship between electron beam current density and the square of the pulse length; therefore, the longer pulse lengths now of interest require low beam current densities. Because the objective of this phase was to use measured data to devise engineering data and charts required for designing repetitively pulsed cold cathode guns, there was more analytical and computational work performed than for the previous phase. This work, which is described and discussed in Section IV, provides the basis for extending the present data base to the design of new systems.

The experimental work of this phase is presented in Section V. An attempt has been made to minimize redundancy between Section V and the work of the first phase described in the Appendix.

Section VI contains a conceptual design for a repetitively pulsed gun with a 7.5-kW beam. The design is based on data derived from this program.

A summary of the program and principle conclusions are given in Section II. Section III provides a review of possible applications for cold cathode technology and discusses the relationship of this technology to other electron beam sources.

Table 1 provides a key to the sections of the report containing information specifically requested in Amendment 1 to Technical Requirement No. 1912 for this program. A similar table at the beginning of the Appendix provides a key to the earlier work.

TABLE 1. INDEX TO PROGRAM TASKS

Requirement Paragraph	Report Section
3.1	
3.1.1	
3.1.1.1	V
3.1.1.2	V B
3.1.1.3	V
3.1.1.4	V B, IV
3.1.1.5	V B, V C
3.1.2	
3.1.2.1	V B, IV
3.1.2.2	V B, IV
3.1.2.3	V B
3.1.2.3	V C, VI
3.1.3	IV, V, VI
3.1.4	VI
3.1.5	V
3.1.16	VI

II. SUMMARY

A. Phase I Program Summary

The S-Cubed Rapid Pulse Facility (RPF) has been used to study repetitive pulse operation of cold cathode electron beam guns with accelerating voltages to 300 kV, pulse lengths from 2 to 10 μsec and repetition rates to 50 sec^{-1}. Data obtained from this study were used to design conceptually a 15 × 200 cm repetitively pulsed cold cathode electron beam gun system.

Some of the highlights of the data obtained in this program are contained in the following paragraphs.

1. Emitter Foil Lifetime

Correlation of the number of emission sites and the mass removed per emission site indicates that cathode foil lifetimes in excess of 50,000 shots are easily achieved. Lifetimes up to 10^7 shots are probable, provided that a fast rising voltage pulse is applied to the cathode.

2. Gun Impedance

Measurement of gun impedance at 50 sec^{-1} for pulse widths from 3 to 9 μsec shows that both repetitively and single pulsed guns operate in a space-charge limited mode. It follows that existing data from single pulse guns can be used in the design of multiple pulse guns by using the voltage and area scaling rules for space-charge limited operation.

3. Beam Focussing and Efficiency

Demonstrations have shown that self-biasing focussing electrodes can shape the beam profile in both transverse and longitudinal dimensions. Measurements of the beam current density outside the foil window (using a collector array and cellophane dosimeters) revealed that the beam edge profile can be dramatically altered with focussing electrodes; this will increase gun efficiency substantially above 50%.

4. Vacuum Requirements

The measured gassing rate under high-average power conditions is consistent with thermal desorption of gas from the gun chamber walls. Operation of the gun at pressures of 10^{-4} torr causes rapid reabsorption and precludes gun clean up. This suggests two approaches to gun/vacuum system design:

a) Moderate vacuum technology should be used and operated with large vacuum pumps.

b) Very high vacuum technology should be developed for the large guns and smaller pumps should be used.

In either of the preceding cases, the extreme importance of a leak free system is emphasized.

5. Thermal Loading of the Electron Beam Window

Thermal loading of the window by 75 $\mu A/cm^2$ as required for a full scale system does not limit the life of the window foils. (Failure mechanisms such as gun arcs or repeated extreme flexing of the foil must be avoided.)

6. Beam Energy Spectrum

Measurements made by placing current collectors behind absorbers of various thicknesses correlated with calculations of electron energy spectra made with the Eltran Monte Carlo code. Input spectra based on the voltage and current waveforms were used. This demonstrated that anomalous low energy electrons, if present, are insignificant. Window loading can be calculated when the gun voltage and current waveform are known.

The design study focussed on a 15- × 200-cm electron beam gun system. The gun can operate at 50 sec^{-1} for 10-sec bursts and provide 0.5 A cm^2 at voltages up to 300 kV. The laboratory gun was purposely designed with full scale transverse dimensions, thereby simplifying the design of the full-scale gun. The electron beam window designed and built for the laboratory gun was also suitable for the full scale gun, although alternative methods for reducing foil flexing under multiple pulse conditions were suggested.

A vacuum system based on a conventional 10-in. oil diffusion pump and 24-cfm mechanical roughing pump best serves the present needs. Very clean, highly baked guns should be considered for future systems.

Assuming that the ECOM-MAPS-70 thyratron is available, a Blumlein-transformer with thyratron switching is the optimum choice for the power supply. The entire power supply should fit inside a 4- × 6- × 5-ft enclosure.

Summaries of the conceptual design parameters and drawings of the gun and system are provided. Alternatives to the chosen power supply, vacuum system and window are also provided.

B. Phase II Program Summary

During the second phase, the S-Cubed Rapid Pulse Facility's high voltage line pulser was modified to supply 12-μsec pulses at repetition rates from 50 to 125 sec^{-1}. The facility's electron gun's electrode structure was changed from a diode geometry to a self-biased triode geometry.

The modified facility was then used to study control of the electron beam by the grid and by focus electrodes. Measurements obtained in the study included temporal waveforms of various voltages currents of the gun and line pulser, and beam current. Time integrated foil dosimeter measurements were used to determine the post-foil beam shape.

An analytic model of the triode gun was developed; performance charts were derived from this model. A calculational model of the line pulser and triode gun was developed for use with the ECAP ciruuit analysis computer code.

Adequacy of the calculational model was verified by comparison of calculated and measured waveforms. Calculations were performed to study the response of the gun to changes in gun parameters.

Data obtained from both phases of the program were used to generate a conceptual design for a cold cathode triode electron gun and power supply. The computer model was used to generate waveforms for the conceptual design system.

Highlights of the second phase are given in the following paragraphs.

1. Line Pulser

The line pulser operated satisfactorily with ignitron switching and reverse pulse clipping at line pulse charge voltages up to 27 kV. Pulse repeatability was very good; the extremes of pulse jitter were ±2.5 μsec. The pulse jitter was due to the relatively primitive ignitron triggering system employed; it can undoubtedly be significantly reduced by installing an improved trigger system or by replacing the ignitrons with thyratrons.

The 1:17.5 high voltage pulse transformer, although not specifically designed for the load conditions, performed adequately. Better matching of line, transformer, and load impedance would improve pulse shape.

A self firing SF_6 pressurized spark gap was needed between the transformer output and the gun input to make the voltage pulse applied to steepen the cathode so that plasma formation would be uniformly initiated.

2. Pulse Repetition Rate

Rates from 50 to 125 sec^{-1} confirmed the observations of Phase I that the individual pulses in a pulse train do not interact. The only effect related to repetition rate are duty-cycle effects such as gun gassing and average power dissipation.

3. Pulse Length

Post-foil beam current pulse lengths of 12 μsec were obtained from the triode gun. The physical mechanism which limits pulse length in cold cathode diode guns, impedance collapse, is also operative in triode guns but does not necessarily terminate the beam pulse. Grid control is maintained while the circuit in the grid-cathode region is space-charge limited; after grid-cathode impedance collapse, the gun can operate as a space-charge limited diode in the grid-anode region, but without grid control.

At the time of grid-cathode impedance collapse, the grid and cathode attain the same voltage; if this voltage is large enough to accelerate the electrons to the kinetic energy needed to penetrate the window foil, the beam will continue after collapse of the impedance, but with a changed amplitude.

High frequency oscillations ($f \simeq 125$ MHz) were observed on the cathode and grid waveforms after impedance collapse and are thought to be dependent on stray capacitances and inductances in the gun and the connections between the gun and line pulser. The electrode spacing-time relationship for impedance collapse is approximately 1 cm/μsec in the usual range.

The magnitude of the changes in the voltage and current waveforms at the time of grid-cathode impedance collapse depends upon the impedances of the cathode, grid, and line pulser circuits immediately prior and subsequent to impedance collapse.

4. Beam Shape

Spreading of the beam between the grid and the foil was measured in directions parallel and transverse to the cathode using blue cellophane dosimeters. The ratio of beam width at the outside of the foil to width at the grid was approximately 1.8 for the parallel case and 3.5 to 4 for the transverse case. The reason for more spreading in the transverse direction is the geometrical divergence of the cylindrical grid-anode geometry; the geometrical spreading ratio for this gun is ≈1:2.8.

5. Pulse Shapes and Beam Current

Waveforms for cathode and grid voltage and current and collected post-foil beam current were obtained for repetition rates from 50 to 125 sec^{-1}, 12-μsec pulse lengths, and bursts of (typically) 7 or 14 pulses. By comparing these waveshapes with the calculated waveshapes based on a space-charge limited model, it was shown that the triode operates space-charge limited in the grid-cathode space. It was also found that in this particular geometry, a space-charge limited leakage current path existed between the cathode and ground. Because of the construction details of the gun, (radial electrode supports and feedthroughs) a configuration which eliminated the leakage current could not be achieved; therefore, calculated extrapolations of the data were used to study the gun's behavior over a broader parameter range.

It was found that the beam current is far more sensitive to changes in grid resistance than in the amount of leakage current, although gun efficiency is lower with higher leakage current. Those results are in agreement with the analysis of the triode presented in Section IV of this report.

6. Analysis

The gun's output current density was studied as a function of cathode voltage, grid opacity and resistance, beam area, and cathode to grid spacing. Data resulting from this analysis were plotted as families of curves and are useful in the design and analysis of triode guns. Two of the important conclusions of the analysis are that over a wide range of grid resistance the output current density responds in an inverse fashion with respect to grid resistance, and that the output current density is relatively insensitive to the grid-cathode spacing. A computer model which includes the leakage current was generated and provides a tool for extrapolation of data to other gun designs.

7. Conceptual Design

A conceptual design for a gun and power supply with the following parameters is presented in Section VI.

Cathode Voltage	250 kV
Current Density (post-foil)	25 mA/cm^2
Pulse Duration	10 μsec
Repetiton Rate	100 sec^{-1}
Duty	One 10-sec burst every 10 min
Beam Area	15 $\times$ 200 cm
Overall Length	118 in.
Outside Diameter	24 in.

The gun is a cold cathode triode in a cylindrical geometry. All electrodes are supported and connected at the ends of the gun, thus permitting the grid structure to enclose the cathode fully and alleviate the leakage current problem encountered in the test device.

The power supply is a pulse forming network (PFN) operating at a maximum of 35 to 38 kV; it is switched into the high voltage pulse transformer by hydrogen thyratrons. The beam current density is controlled by the value of the grid resistance. For 25 mA/cm^2 post-foil, the resistor has a value of approximately 4300 ohms.

Gun waveforms were calculated for the conceptual design gun using the computer model developed in this program. Transverse and longitudinal cross sections of the gun are presented.

III. REPETITIVE PULSE COLD CATHODE TECHNOLOGY IN SYSTEM APPLICATIONS

A. Cold Cathode Guns as System Components

1. Relationship to Complete Laser System

The work reported here has been performed with the specific objective of developing repetitively pulsed cold cathode electron guns with operating parameters defined by MIRADCOM requirements for CO_2 laser systems. The same technology has other applications; in this section some of these applications are discussed. The advantages or disadvantages of cold cathode technology relative to other technologies which may also be suitable for these other applications are considered.

Table 2 categorizes pulsed electrical lasers according to the method that is used to pump the laser gas. Electrical pumping can be accomplished by direct excitation with an electron beam or with an electrical discharge. All high energy, high average power pulsed electric discharge laser systems (EDL) are of the electron beam sustained discharge type. Intense ultraviolet (UV) radiation is used as the ionizing source in some low energy systems; electron beam sustained discharges are superior for high average power, high energy applications.

In e-beam sustained lasers, the electron beam produces a very low level of ionization in the laser gas, (typically one ion per 10^7 molecules) but this is sufficient to increase the electrical conductivity of the gas to the extent that a stable uniform electrical discharge can be produced by a separate power supply. The discharge provides essentially all of the energy for pumping the laser levels of the gas.

As Table 2 shows, there are similar methods for electrically initiating a chemical HF/DF laser. The e-beam sustained discharge appears to be the most advantageous in these laser systems also. In these lasers the electrical energy is used to generate the chemical species required for the chemical reaction which supplies the energy to pump the laser levels.

A complete laser system is composed of subsystems in addition to the electron gun, and in fact the gun is a rather small (although essential) portion of the total system in terms of weight, volume, and cost. Figure 1 is a generalized representation of an EDL system.

The components shown in Figure 1 are found in all electron beam sustained discharge laser systems. Specific requirements for each component depend upon the type of system; e.g., coud cathode electron guns require different types of modulators than do hot cathode guns. The system components which are affected most strongly by the choice of electron gun type are shown within the dashed line. They include the electron gun and power supply, the vacuum and cooling systems, the laser discharge chamber, and the discharge power supply.

2. Performance Advantages and Constraints of Cold Cathode Guns

Electron guns are specified by the following parameters:

a) Accelerating voltage.

b) Pulse length and pulse shape.

c) Pulse repetition rate.

d) Pulse burst length.

e) Electron beam current density.

f) Electron beam area.

g) Component lifetime.

h) Vacuum system requirements (operating pressure and throughput).

i) Electron beam window foil cooling requirements.

The three types used for laser systems are hot cathode, cold cathode, and plasma diode guns. Hot cathode guns were developed first for these applications and are the principal type now in use in large EDLs. Cold cathode guns were developed later and are now being introduced into large system applications. Plasma diodes are still being developed and are not used in any large systems.

TABLE 2. TYPES OF PULSED ELECTRIC DISCHARGE LASERS

Electrically Pumped (CO_2, CO, KrF)	Electrically Initiated, Chemically Pumped (HF/DF)
1. Externally Sustained Discharge	1. Externally Sustained Distharge
(A) E-Beam Sustained	(A) E-Beam Sustained
(B) UV Sustained	(B) UV Sustained
2. E-Beam Only	2. E-Beam Only
3. Self-Sustained Discharge	3. Self-Sustained Discharge

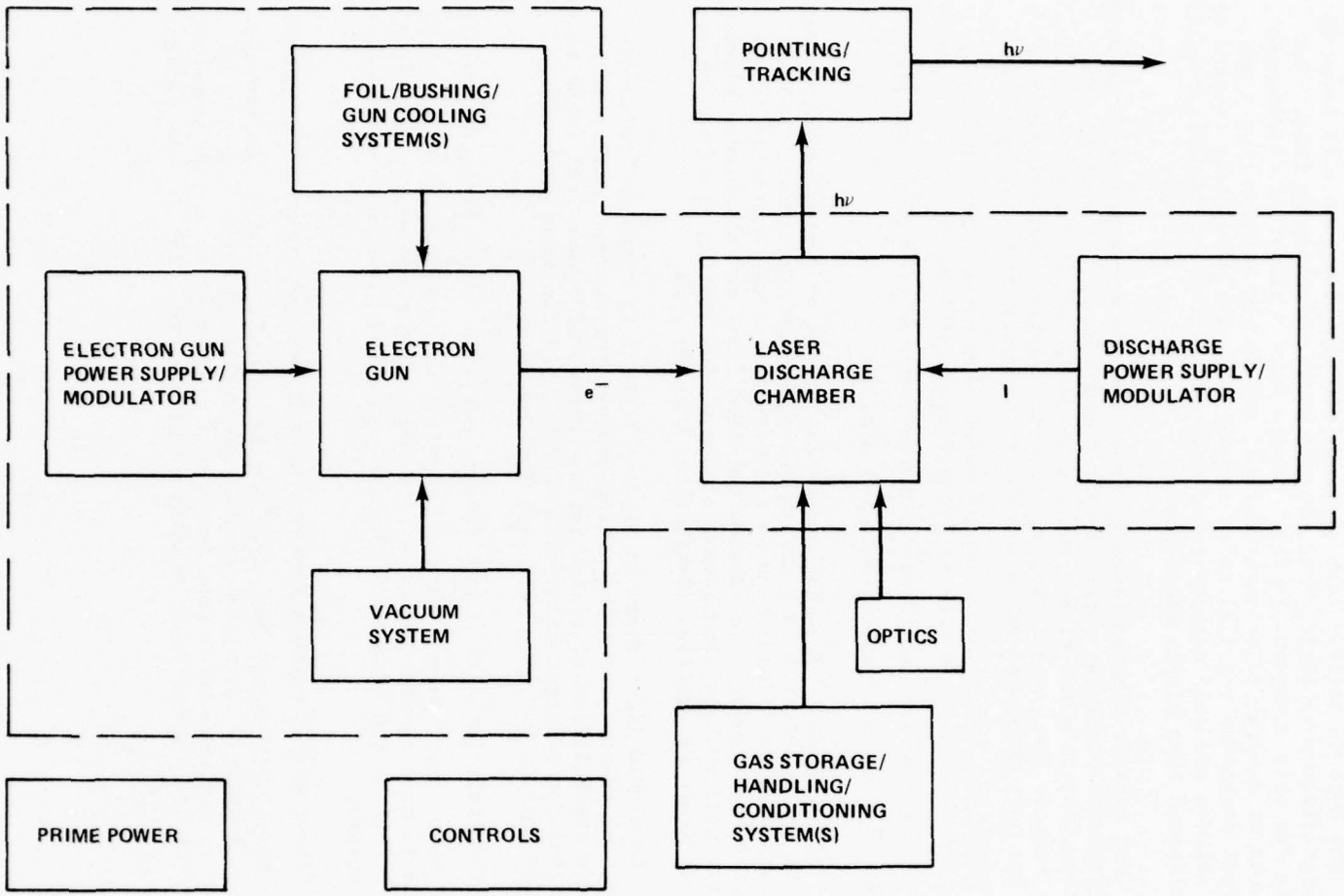


Figure 1. Pulsed high energy/power EDL system.

The authors believe that plasma diode electron guns will never be of significance to large, high average power, high energy EDLs. The basis for this viewpoint is that despite very substantial development efforts at several major laboratories, the accelerating voltages and current densities are limited to ranges which are adequately covered by hot cathode and cold cathode guns; both types are more reliable and less complicated than plasma diode guns.

Hot cathode electron guns operate over a wide parameter range which overlaps the operating range of cold cathode guns. In general, for applications in which either gun can be used, use of the cold cathode type reduces the overall complexity of the system. Hot cathode guns are the only developed means for obtaining continuous or long pulse ($\Delta t \gtrsim 20$ μsec) beams and very high repetition rates (prr $\gtrsim 10^3$ pps). They are generally operated to produce beams with pulse current density in the range of tens of mA/cm^2; however they can produce pulses with current densities of approximately 1 A/cm^2.

Figures 2 and 3 show the approximate range of current density, pulse length, and repetition rate for single pulse and repetitively pulsed hot cathode guns. These figures indicate two of the operating limits of hot cathode guns: the cathode emission limit and the window heating limit. Cold cathode guns have the same window heating limit but do not have the cathode emission limit of hot cathode guns.

The window limit shown in Figures 2 and 3 is based on "rules-of-thumb" for present technology which express the current density transmission capabilities of window foils. These rules have been found to be useful for electron beams with electron kinetic energies between 150 keV and 300 keV, for the usual foil materials.

The limit for peak charge density per short pulse is approximately 20 μC/cm^2. Short pulses are considered to be those for which the pulse length is much shorter than the time required for the energy deposited in the foil by the beam to be thermally conducted away from the deposition volume.

Time-averaged current density in continuous or repetitively pulsed beams should not exceed 200 μA/cm^2 to 300 μA/cm^2. Because the average current density $\bar{J}$ is related to the peak current density J, pulse length τ, and repetition rate (prr) by $\bar{J} = J\tau(\text{prr})$; it can be seen that if a foil is operated under conditions of maximum $\bar{J}$ and $J\tau$, the maximum prr $\simeq 10$ sec^{-1}.

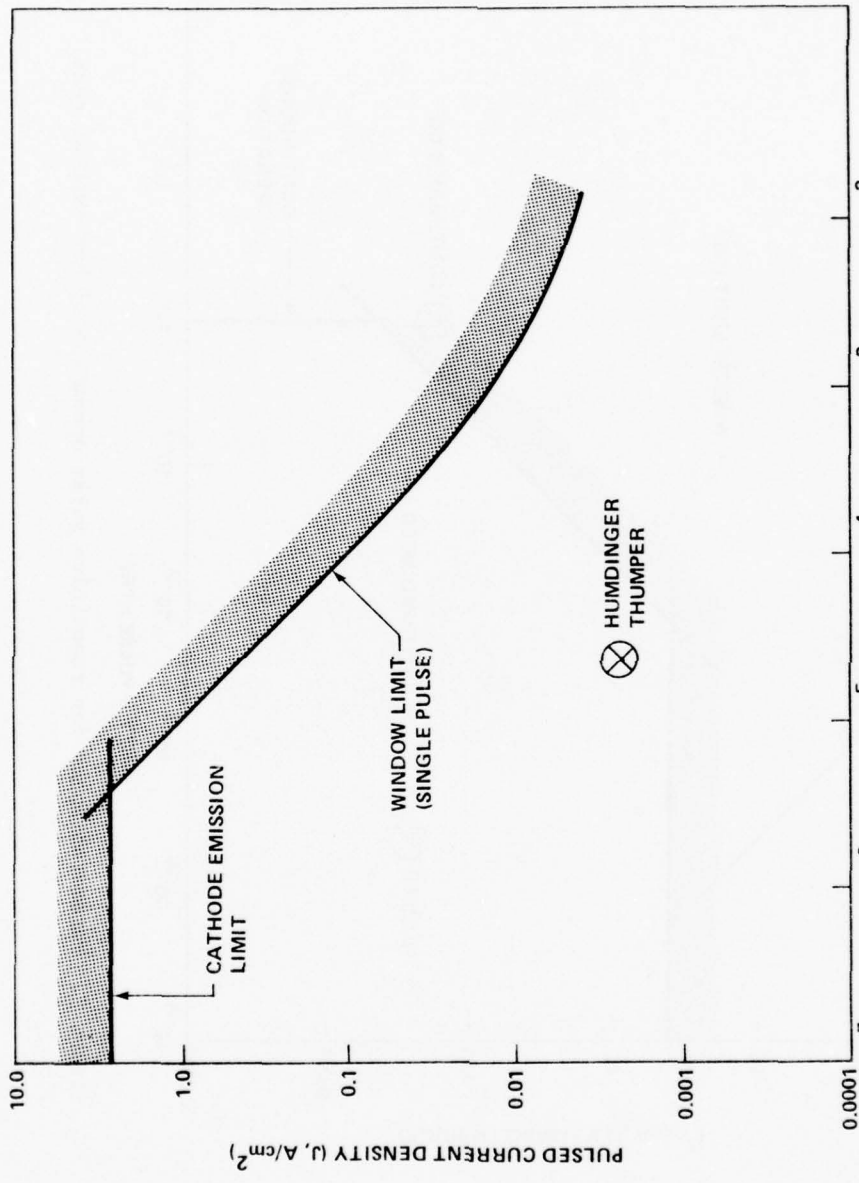


Figure 2. Parameter space for pulsed operation of hot cathode guns.

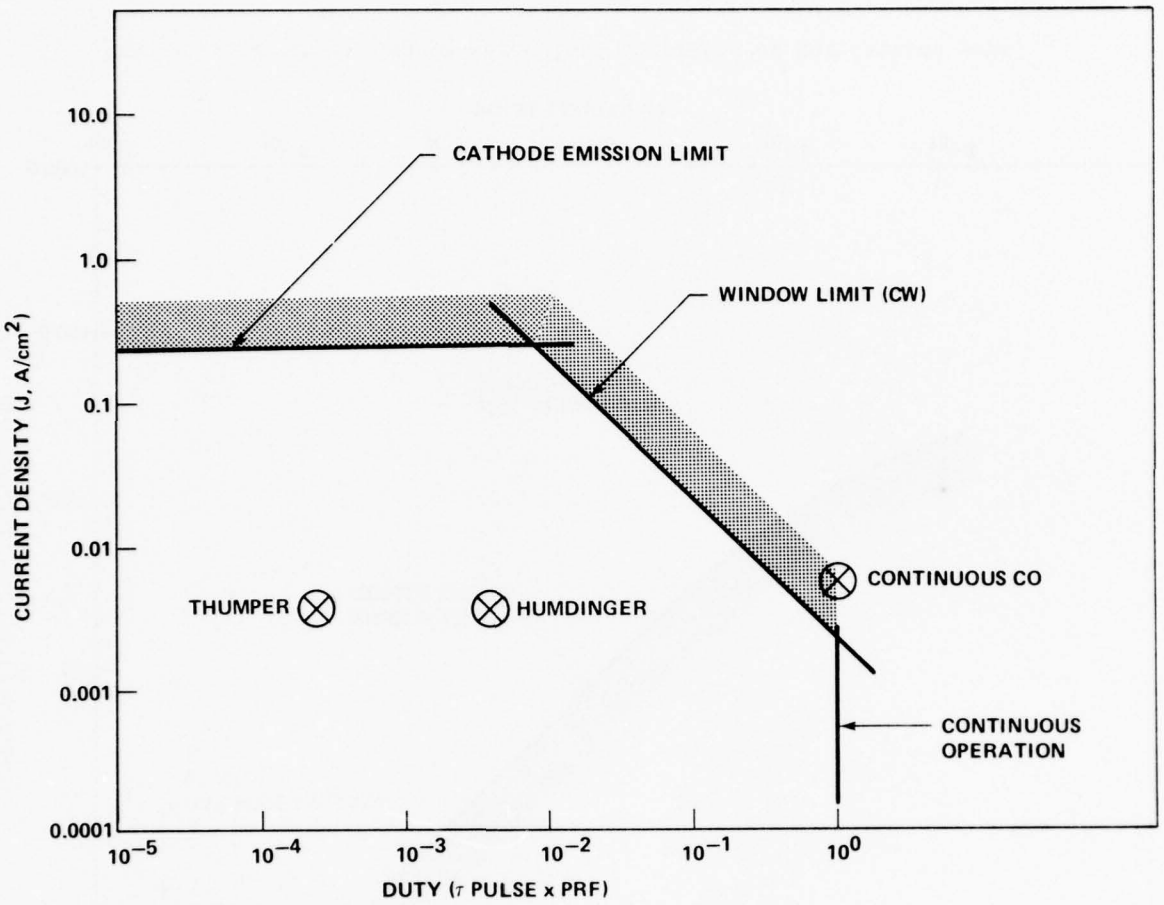


Figure 3. Parameter space for repetitive pulse operation of hot cathode guns.

Operation at average current densities greater than 300 $\mu A/cm^2$ may become feasible in the near future. Relaxation of this limit will benefit both hot and cold cathode guns, but will not give either type an advantage over the other.

The approximate operating points for several CO_2 and CO laser systems are shown in Figures 2 and 3. It can be seen that atmospheric pressure CO_2 EDLs are not significatnly limited by hot cathode emission or foil heating limits. Carbon monoxide EDLs definitely require advances in window cooling technology.

Cold cathode guns have several advantages over hot cathode guns; higher current density capability, lesser vacuum requirements, simpler construction and simpler power supply requirements.

The first of these, higher current density, is of limited importance in CO_2 EDLs, but is very important for CO, HF/DF, KrF, and others. As shown in Figures 4 and 5, the peak and average current density from cold cathode guns is limited by window foil technology, not by cathode emission.

Vacuum system requirements are significantly reduced for cold cathode systems, as discussed elsewhere in this report and appendix. Whereas cold cathode systems operate satisfactorily at pressures as high as the 10^{-4}-torr range, hot cathode systems should not be operated above 10^{-5} torr, and require a much lower base pressure, particularly if thoriated tungsten or other material which can be poisoned by impurities is used for the cathode.

Cold cathode guns are more rugged than even the simplest of hot cathode guns. The mechanical parts of cold cathode guns are structurally strong parts, few in number and operate at moderate temperatures compared to hot cathode guns. Hot cathode guns with filament type cathodes are relatively fragile, particularly when the cathodes are hot. Means must be provided for maintaining the geometry of the hot filaments; the usual method is a spring tensioning system to accommodate thermal expansion of the filaments. Larger, mechanically stronger cathodes can be used, but the power required to heat the more massive filaments reduces the overall efficiency of the gun.

It is in the matter of power supply requirements that the advantages of cold cathode guns are most striking. They obviously do not require the filament power supply as do the hot cathode guns. Filament power must be supplied to the hot cathode by means of a high voltage isolation transformer capable of standing off the full accelerating potential. This is a large and heavy piece of equipment. Continuous beam hot cathode diodes require only the high voltage power supply for the accelerating

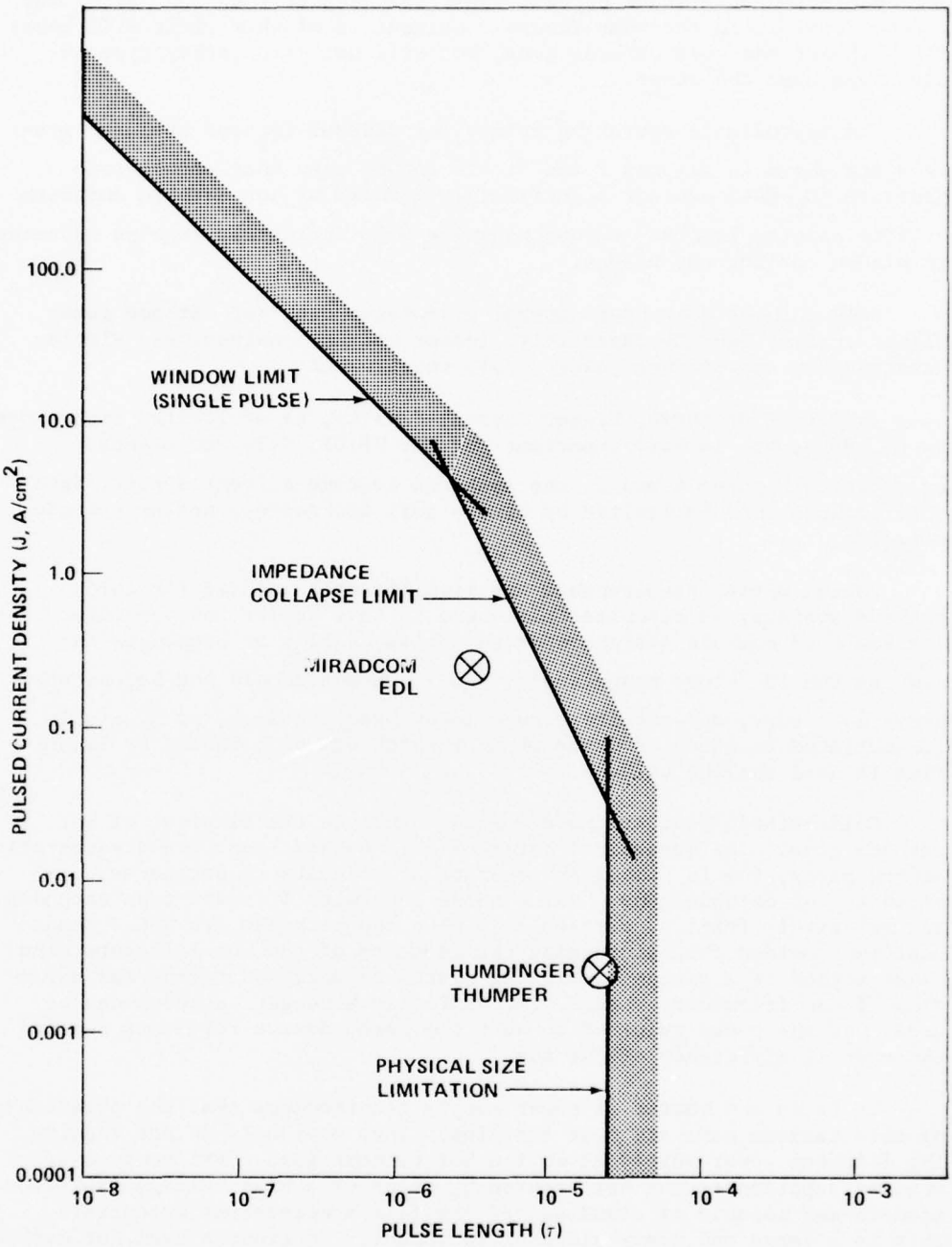


Figure 4. Parameter space for pulsed operation of cold cathode electron gun.

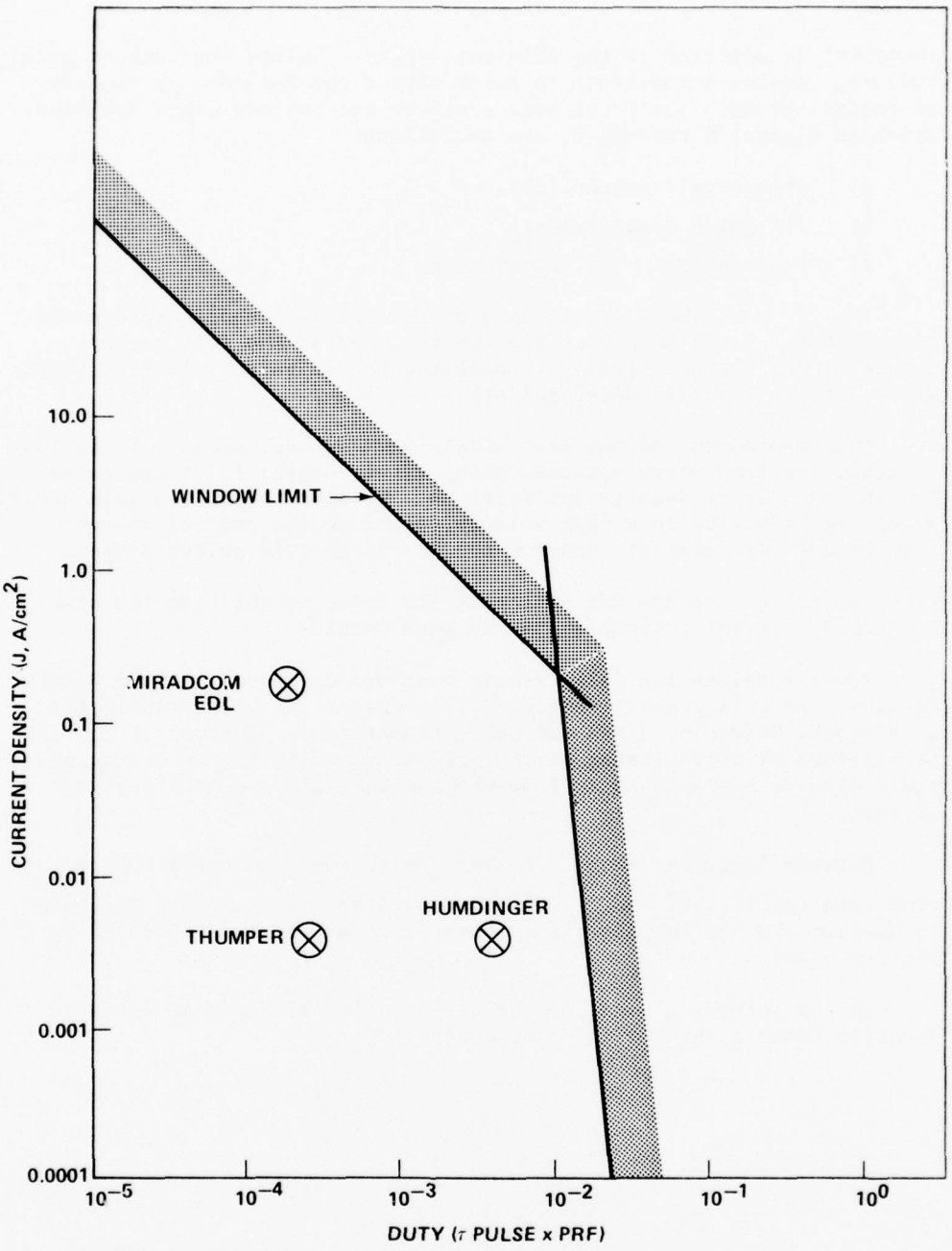


Figure 5. Parameter space for repetitive pulse operation of cold cathode electron gun.

potential in addition to the filament supply. Pulsed hot cathode guns, however, require a modulator to pulse either the cathode (in diodes) or control grids. The three main types of hot cathode power supplies, shown in Figures 6 through 8, are as follows:

a) Charge-grid pulser (dc).

b) PFN-pulse transformer.

c) Resonant air core transformer.

The first of these types has been the standard configuration for pulsed EDLs. The grid pulser must be isolated at the full cathode potential and control signals transmitted to the pulser via fiber-optic light links ("floating deck" pulser).

The second type has not been widely used, perhaps because it is less flexible for laboratory systems, being mainly useful for fixed pulse length and current density applications. It also requires a grid supply which can be pulsed to a high voltage, although the control system requirements are simpler than for the dc charge-grid pulser system.

The third type has the potential for lower weight than the other two types, but the control system is more complex.

Power supplies for cold cathode guns are discussed in some detail elsewhere in this report. Figure 9 illustrates the basic simplicity of a supply driven by a PFN and pulse transformer. Control of the gun is obtained by self-biasing of the grid as shown in Figure 9; the gun could also be operated as a diode without the grid and grid resistor circuit.

Present limitations on the pulse length ($\Delta\tau \lesssim 20$ μsec) and repetition rate (prr $\lesssim 1000$ sec^{-1}) unique to cold cathode guns are discussed in Section V B and the Appendix. These limits are also indicated in Figures 4 and 5.

In the following section, the use of cold cathode guns for some specific laser systems will be discussed.

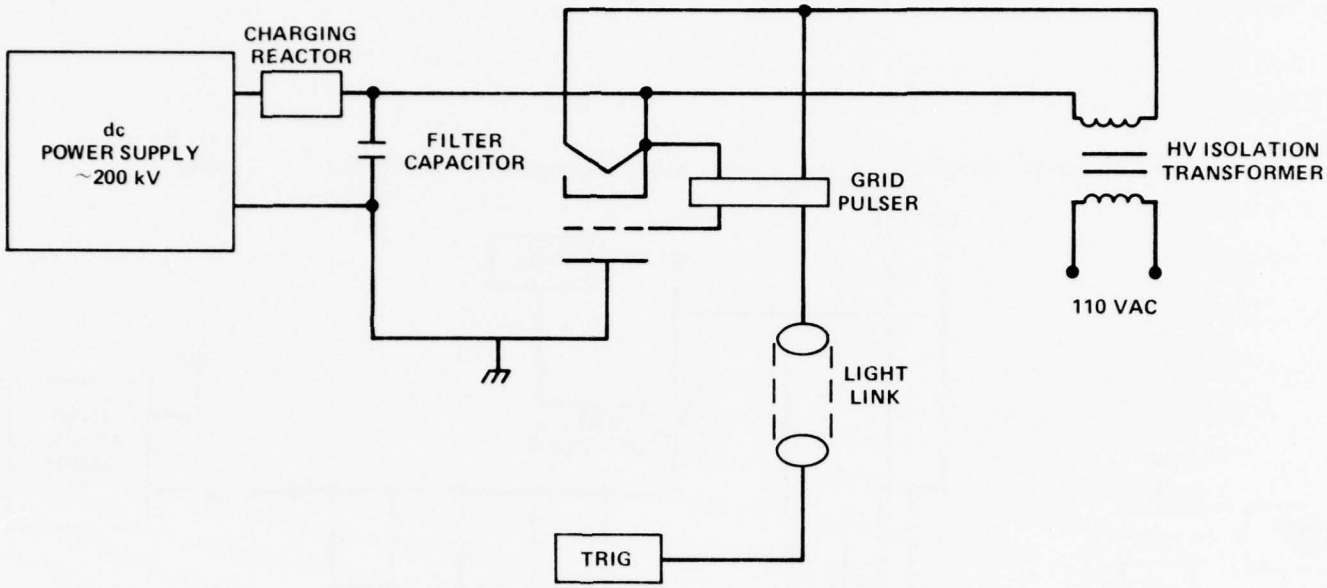


Figure 6. Charge/grid pulser power supply (dc) for hot cathode electron gun.

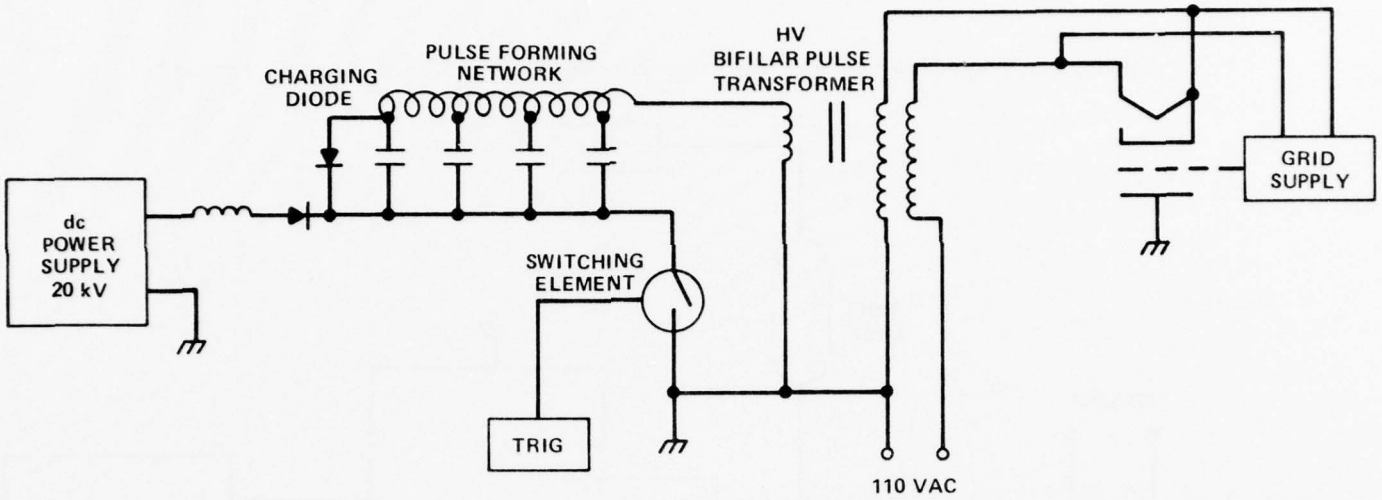


Figure 7. PFN/pulse transformer power supply for hot cathode electron gun.

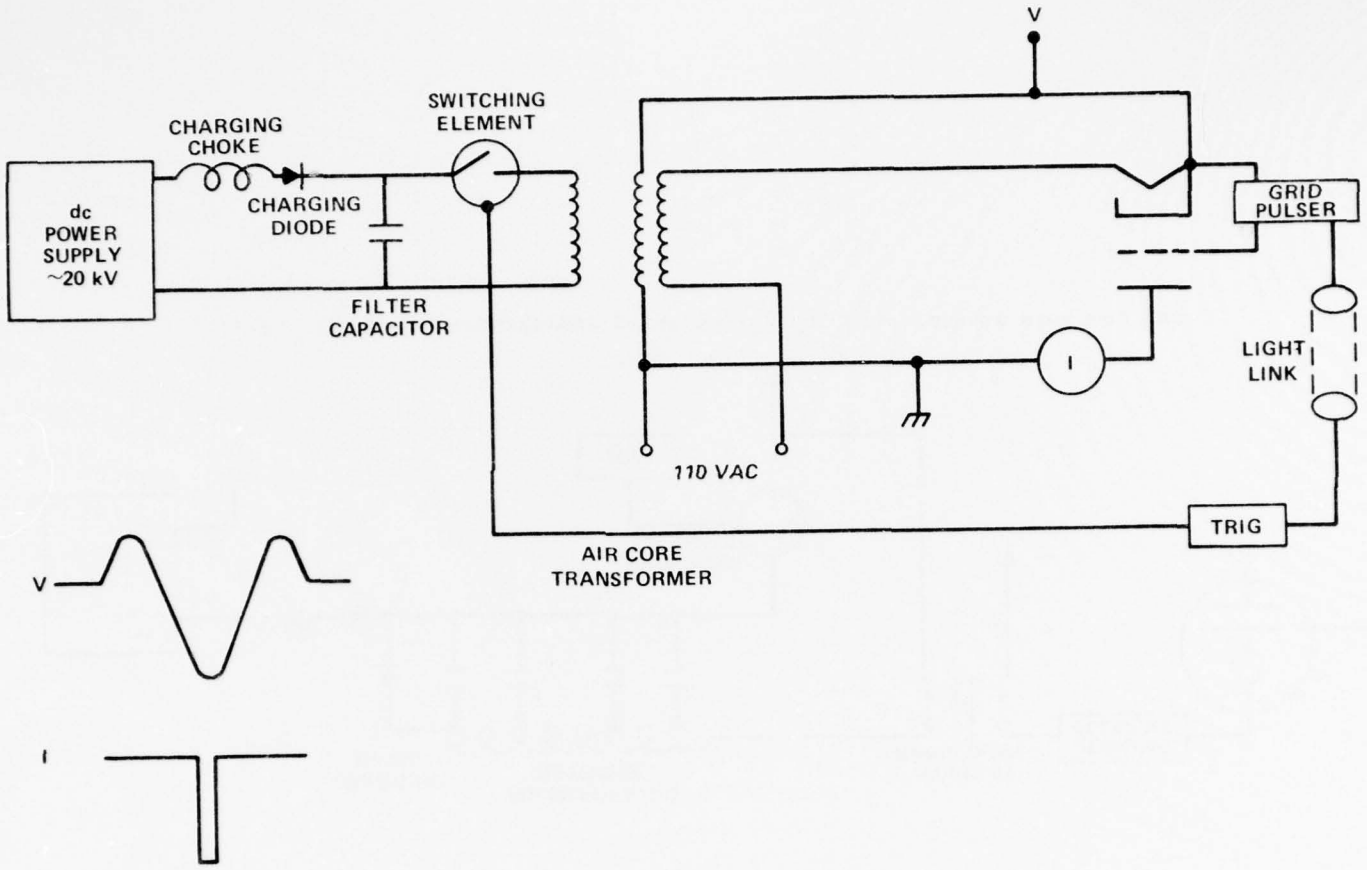


Figure 8. Resonance charging power supply for hot cathode electron gun.

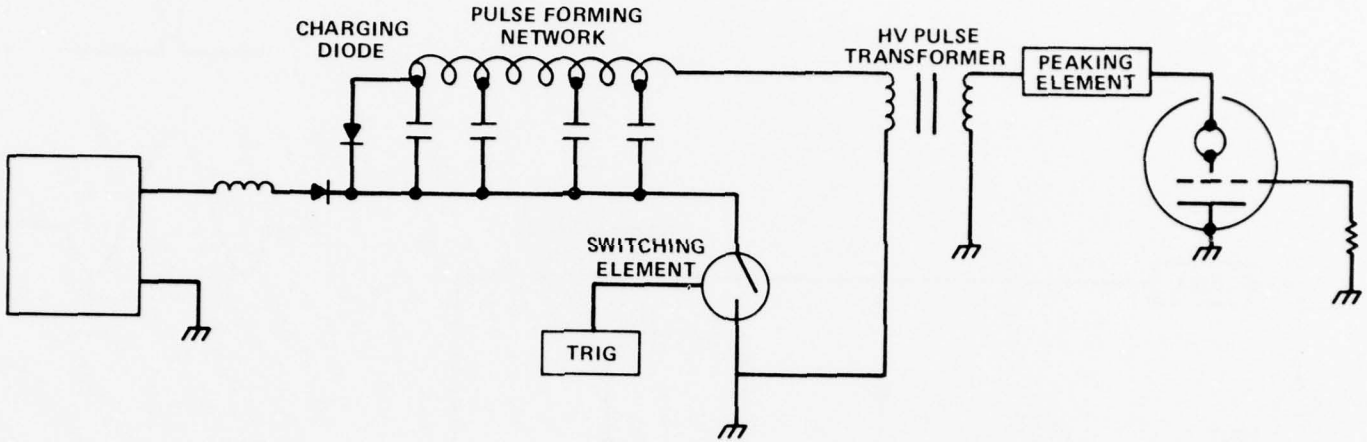


Figure 9. PFN/pulse transformer power supply for cold cathode electron gun.

B. Applicability of Cold Cathode Guns for Specific Types of Lasers

1. Moderate Pulse Length Repetitive Pulse [$1 \lesssim \Delta\tau \lesssim 20$ μsec, prr $\lesssim 1000$ sec^{-1}] CO_2 and CO Systems

a. CO_2

Typical CO_2 systems in this pulse and rate range require guns with an accelerating voltage of from 125 to 250 kV and current dentisy from 10 to 500 mA/cm^2.

Cold cathode guns are extremely well-suited to these systems. The first large high average power system using a cold cathod gun is the cold cathode electron beam laser (CCEBL) system at MIRADCOM. The gun, which produces a 200- × 15-cm beam, is presently driven by a high voltage PFN switched by thyratrons. Other drivers such as a low volatge PFN driving a pulse pulse transformer may also be tested. When operated at 50 pps, the CCEBL system will produce 100 kW of 10.6-μ optical power.

This same technology is applicable to the large CO_2 laser systems necessary for the study of controlled fusion. These are presently single pulse systems; large repetitive systems would presumably not be developed before the concept of this fusion approach is demonstrated. A two-sided, 200- × 35-cm cold cathode gun is being used an Los Alamos Scientific Laboratory (LASL) and a prototype cold cathode gun for a 1000-kJ, 0.5-nsec pulse system is being built for LASL by S-Cubed. This latter device, which could also be a prototype for large military systems, is a cylindrical gun with the electron beam emitted radially outward. (The geometrical concept is similar to the concept for the "Thumper" hot cathode gun).

Figure 10 shows a layout drawing of the cold cathode triode gun and gives the relevant operating parameters. In the LASL system, the gun will drive a laser amplifier producing ≈ 17 kJ in an optical pulse lasting less than 1 nsec. If the same gun and discharge volume were used to produce a longer pulse, 10 μsec for example, approximately 100 kJ would be generated per pulse.

b. CO

The current density requirements are greater for CO than for CO_2. Cold cathode guns can produce the required current densities in this pulse length and repetition rate range, but the maximum current that can be obtained is defined by window heating limits.

Assuming that the window problems can be overcome, the cold cathode gun will certainly prove superior to hot cathode guns because of the high current density that is required.

2. Short Pulse Length Repetitive Pulse

[$\Delta\tau \lesssim 1$ μsec, prf $\lesssim 1000$ sec^{-1}] KrF

Krypton fluoride lasers require high current densities because of the electronegative character of the gas, which rapidly attaches free electrons. Much of the previous work on KrF lasers has used direct excitation by very high current density electron beams. Recently however, electron beam sustained discharges in KrF have shown much promise and research is being vigorously pursued.

The KrF systems require higher pulsed current densities ($J > 1$ A/Cm^2) than CO_2 or CO; therefore, cold cathode guns are the obvious choice. Window heating is a problem, but the shorter pulse lengths alleviate the problem to the extent that higher peak current densities can be obtained without exceeding the ≈ 20 μC/pulse limit. Average current density constraints remain the same as previously discussed; hence, window cooling improvements could also greatly benefit these laser systems.

b. Electrically Initiated Chemical Lasers, HF/DF

Electrically initiated HF chemical lasers are being studied using cold cathode electron guns to sustain an electrical discharge which dissociates the pumping gas mixture and produces the species required for the lasing reaction. In these experiments, the electron beam parameters have typically been 400 keV, 2 A/cm^2 and 50 nsec. This range is very accessible to cold cathode technology, because with these short pulse lengths, current densities on the order of 1000 A/cm^2 can be obtained without destroying the foil. It is expected that if these lasers prove successful, cold cathode guns will be used for the electron beam.

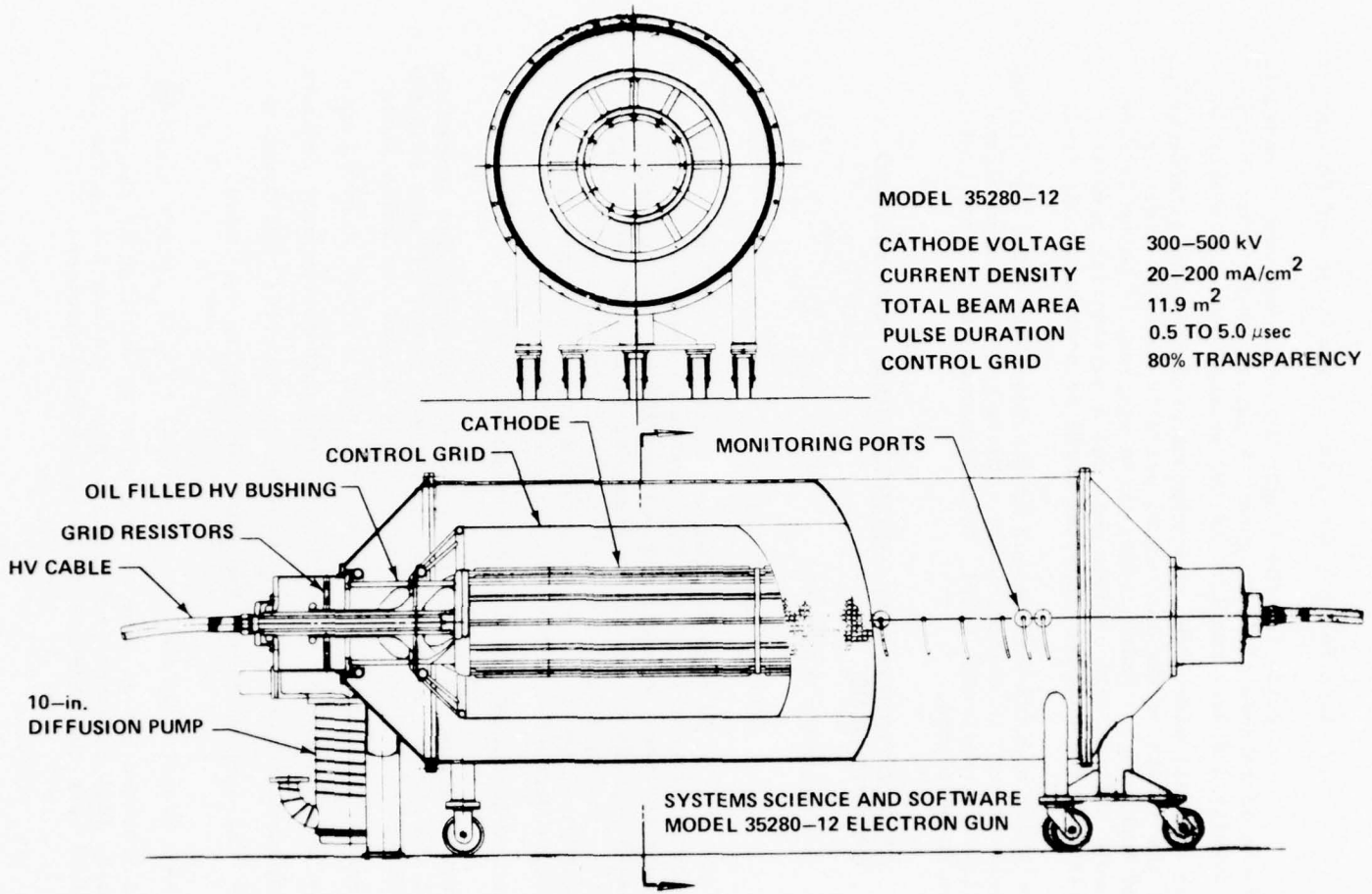


Figure 10. Systems Science and Software Model 35280-12 electron gun.

3. Long Pulse Length, Repetitive Pulse and Continuous

Pulse lengths longer than ≈20 μsec are an undeveloped regime for cold cathode electron guns. Figures 4 and 5 show that the current density and duty required in CO_2 systems such as Thumper and Humdinger are well within the operating range of the cold cathode gun, but that the length of the individual pulse is near the limit of developed technology. Nonetheless, these systems, if being designed today, could utilize cold cathode guns and a substantial benefit in simplification of the power supplies could be reasonably expected.

Continuous systems such as the Mobile Test Unit (MTU) and PEACEMAKER are at present best sustained by hot cathode guns (although plasma diodes might be applicable here), as continuous cold cathode guns have yet to be demonstrated.

IV. GRID CONTROLLED COLD CATHODE GUNS: ANALYSIS AND CALCULATIONS

A. Circuit Equations

1. General Equations

In this section, an idealized model of a cold cathode triode is considered for the purpose of deriving the relationship between the input current and voltage and the output current. This relationship depends on physical parameters of the gun and the grid resistance. The equations are derived for a planar geometry; the results for a cylindrical geometry can be obtained from the planar results by taking proper account of the geometric expansion of the beam; that is, the reduction in current density proportional to r^{-1}.

Figure 11 shows the model used for this analysis. The approximation that the current emitted from the cathode can be divided into two components has been used. The first, I_1, is the current which flows between the cathode and the grid. At the grid, a fraction of I_1 equal to kI_1 is intercepted by the grid and flows through the grid resistor to ground, producing a voltage $V_G = kI_1R_G$ on the grid. The fraction $I_1(1 - k) = TI_1$ passes through the grid and flows to the anode.

It is a fraction of the latter current, $I_2 = TI_1$, which would be extracted from the gun as beam current after attenuation by the gun's window foil, foil supports, and anode screen. Attenuation by the foil is dependent upon the kinetic energy of the beam electrons.

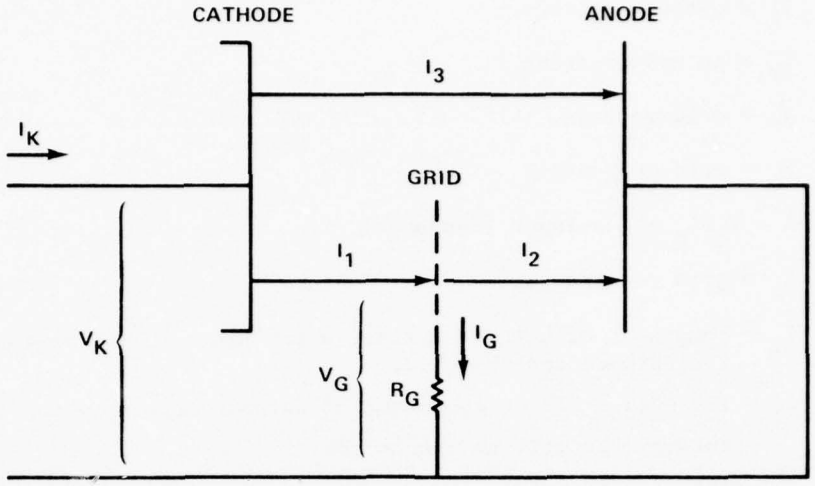


Figure 11. Circuit model of self-biased triode gun used in analysis.

The second component of the cathode current is denoted I_3 in Figure 11 and represents current that flows from the cathode and/or cathode support structure without passing through the grid. In a well-designed gun $I_3 = 0$; it is included in this analysis so that the effect of this loss mechanism on gun impendance and efficiency can be studied. This will allow analysis of the experimental results of this program.

It is assumed that the currents I_3 and I_1 are both space-charge limited; the former limited by the full cathode-anode voltage, V_K, and the latter by the cathode-grid voltage, $V_{KG} = V_K - V_G$.

Change of impendance during the pulse due to motion of cathode plasma is not included in the model. This phenomenon is quite pronounced in diode-type cold cathode guns but has limited effect in the resistively biased triode due to the stabilizing effect of the grid. Grid stabilization is discussed more completely in Section IV A2. The space-charge limited impedances are assumed to vary only as $V^{-1/2}$, or equivalently, $I^{-1/3}$ during the pulse.

Definitions of the model's parameters are as follows:

V_K = cathode voltage.

I_K = cathode current.

V_G = grid voltage.

I_G = grid current.

$Z = V_K/I_K$ = gun input impedance.

R_G = grid resistance.

I_1 = component of cathode current which flows in the region between the cathode and the grid.

$I_2 = TI_1 = (1 - k)I_1$ = component of cathode current which flows through the grid to the andode.

T = grid transparency.

k = grid opacity.

A_1 = cross-sectional area of beam I_1 at grid.

X_1 = cathode to grid distance.

$V_{KG} = V_K - V_G$ = cathode to grid voltage.

$J_1 = I_1/A_1$ = current density of beam I_1.

$J_2 = I_2/A_1$ = current density of beam I_2.

The space-charge limited currents are given by

$$I_3 = K_3 B_K^{3/2} \tag{1}$$

$$I_1 = K_1 V_{KG}^{3/2} = \frac{A_1 2.33 \cdot 10^{-6}}{X_1^2} V_{KG}^{3/2} \quad . \tag{2}$$

The parameters K_1 and K_3 are constants for a particular geometry. K_1 can be calculated reasonably well from known physical shapes and sizes; however, K_3 generally cannot be calculated, but can be estimated from measured values of gun voltage and current.

Equation (2) can be written

$$I_1 = K_1(V_K - I_G R_G)^{3/2} \quad (3)$$

and

$$I_2 = TI_1 = (1 - k)K_1(V_K - I_G R_G)^{3/2} \quad . \quad (4)$$

Two cases are now considered. For the first, $I_3 = 0$; therfore, $I_K = I_1$ and $Z = V_K/I_1$. The ratio $b = R_G/Z = 1/k(V_G/V_K)$ is defined (since $I_G R_G/V_K = bK$); Equation (4) becomes

$$I_2 = J_2 A_2 = K_1 V_K^{3/2}(1 - bk)^{3/2}(1 - k) \quad . \quad (5)$$

For the second case, $I_3 \neq 0$, and $Z(I_1 + I_3) = V_K$, or

$$\frac{I_1 R_G}{V_K} = \frac{R_G}{V_K}\left(\frac{V_K}{Z} - I_3\right) = b\left(1 - \frac{Z}{Z_3}\right) \quad ; \quad (6)$$

therefore, Equation (4) becomes

$$I_2 = K_1 V_K^{3/2}\left[1 - bk\left(1 - \frac{Z}{Z_3}\right)\right]^{3/2}(1 - k) \quad . \quad (7)$$

Also, it is noted that

$$I_K = I_1 + I_3 = K_1 V_K^{3/2}\left[1 - bk\left(1 - \frac{Z}{Z_3}\right)\right]^{3/2} + K_3 V_K^{3/2} \quad (8)$$

and

$$Z = \frac{V_K}{I_K} = \frac{1}{V_K^{1/2}\left(K_3 + K_1[1 - bk(1 - Z/Z_3)]^{3/2}\right)} \quad . \quad (9)$$

Equation (5) shows that when $I_3 = 0$, the beam current is $I_2 = 0$ for two cases. The first, $k = 1$, corresponds to an opaque grid. The second, $b = \frac{1}{k}$, gives the condition when the grid voltage equals the cathode voltage, When the grid resistor is chosen so that $b = R_G/Z = \frac{1}{k}$, the beam current goes to zero. This condition puts a limit on the range of grid resistors which can be used. Grids have typical values of k in the range from 0.4 to 0.1; corresponding values for b_{max} are 2.5 to 10.

Equation (5) has been rewritten

$$\frac{J_2 X_1^2}{2.33 \cdot 10^{-6} V_K^{3/2}} = (1 - k)\,(1 - bk)^{3/2} \qquad (10)$$

and plotted using b as a variable and k as a parameter, as shown in Figure 12.

The curves of Figure 12 are useful when considering the design of a cold cathode triode. The usual specified parameters are cathode voltage and post-foil beam current density. To use the curves, the required beam current density inside the gun, J_2, is first calculated from $BJ_2 = J_B$. The factor B accounts for beam attenuation by the foil, foil support, and anode screen.

Minimum values of X_1 are estimated next, consistent with the requirements discussed in Section V B for the smallest cathode-grid spacing suitable for the required pulse length. The term $(J_A X_1^2)/(2.33 \cdot 10^{-6} V_K^{3/2})$ can then be calculated and various feasible values of b and k estimated from the curves.

The total gun current is estimated by working backward from the anode current to the cathode current, since $(1 - k)I_K = J_2 A$. The gun impedance and R_G can then be estimated. Gun impedance is usually an important consideration, particularly in high average power systems, where it is necessary to provide good impedance matching between the power source and the gun.

In some systems there is a requirement to be able to vary the beam current density while maintaining constant gun voltage and impedance. Control of beam current density by variation of the grid resistance can be estimated from Figure 12. For fixed V_K, Z and X_1, Figure 12 shows how the current density will change with R_G, since $R_G = bZ$.

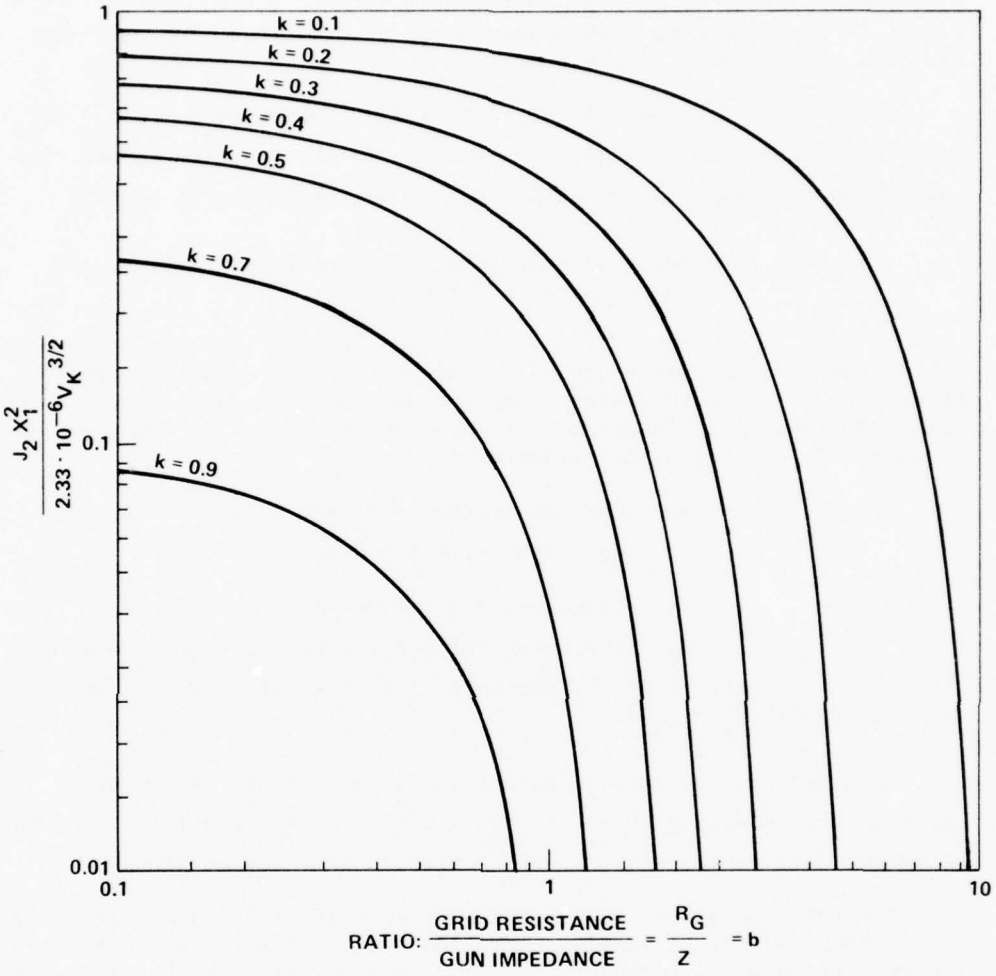


Figure 12. Normalized current density versus b, with k as a parameter.

The same curves can be used for the case $I_3 \neq 0$, by making the substitution $b' = b(1 - Z/Z_3)$ in Equation (7). The ratio Z/Z_3 is most likely to be determined from measurements or estimated, for purposes of first order design of the gun.

From the circuit definition, $Z \leq Z_3 \leq \infty$, therefore $0 \leq b(1 - Z/Z_3) \leq b$. One effect of the shunt impedance Z_3 is therefore to reduce the maximum usable value of the grid resistor by the factor $(1 - Z/Z_3)^{-1}$.

2. Anode Current as a Function of Grid Resistance and Cathode-Grid Spacing

In this section, a specific gun geometry is used as an example to discuss the dependence of gun current density on the resistance of the grid resistor and the spacing between the cathode and grid. An idealized planar geometry gun (no losses, or $I_3 = 0$) is considered with the following parameters:

a) Cathode voltage = V_k = 250 kV.

b) Grid opacity = k = 0.2.

c) Beam area = A = 1000 cm^2.

d) The total cathode current is then $I_1 = J_1 A$;

the total beam current at the anode is $I_2 = (1 - k)I_1 = 0.8I_1$; and the current density $J_2 = I_2/A$.

Equation (4) was used to calculate J_2 for various values of R_G and X_1. The resulting curves for J_2 are plotted in Figure 13. The gun impedance also varies with R_G; it is plotted on the same graph.

Several conclusions become apparent upon examination of Figure 13. The current density is easily controlled over a wide range by varying the grid resistance. However, in practical applications the allowable range of gun impedance must be considered. Assuming that the cathode voltage is to be held constant (as it is for the curves in Figure 13), the allowed change in beam current, and thus R_G, can only have values within limits determined by the acceptable gun impedance range.

For example, the X_1 = 10 cm curve in Figure 13 is considered. If the power supply design required that the gun impedance be between 800 and 1600 ohms, the current density range would be 125 to 250 mA/cm^2 and the corresponding grid resistance range would be 2600 to 7000 ohms.

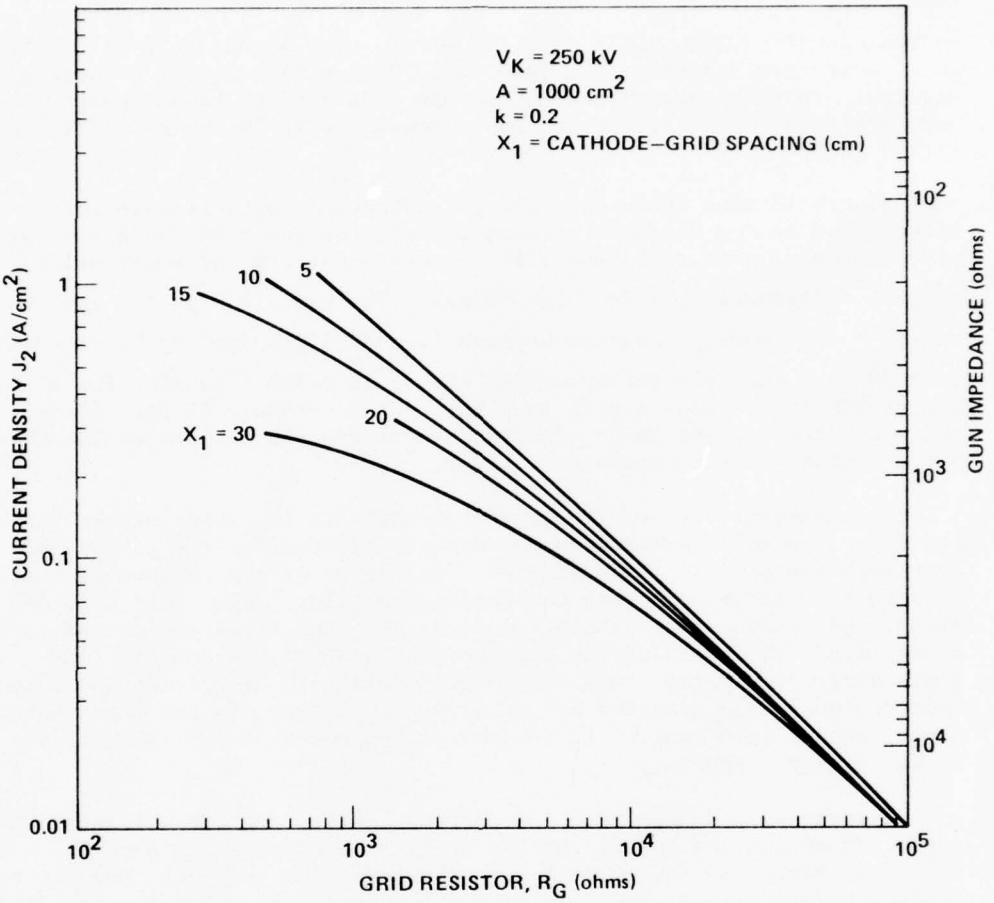


Figure 13. Anode current density (J_2) and gun impedance versus grid resistance (R_G) for a 1000-cm^2 beam.

The same current density in a gun with a larger beam area will obviously require higher total current and therefore result in lower impedance. Figure 14 shows curves for a 3000-cm^2 beam. The same current density range, 0.125 to 0.250 A/cm^2, corresponds to a grid resistance range from approximately 1050 to 2350 ohms for a 10-cm cathode grid spacing. In this case, however, because of the three times greater beam area and total current, the gun input impedance is in the range of 520 to 270 ohms.

Figure 13 also shows that the gun current density is relatively insensitive to the distance between the cathode and grid for a reasonably wide choice of grid resistance; it is more sensitive for small values of grid resistance than for high values. For example, for A = 1000 cm^2 and R_G = 3000 ohms, J_2 varies between 310 and 140 mA/cm^2 as X_1 is varied from 30 to 5 cm, or a factor of two change in current density for a factor of six in cathode to grid spacing. A space-charge limited diode for which the cathode-anode spacing changed from 30 to 5 cm would exhibit a factor of 36 increase in current.

The insensitivity of the current density to the grid-cathode spacing is a favorable factor when the dynamic behavior of the gun's electron emission process is considered. Expansion of the cathode plasma reduces the cathode-grid spacing during the pulse. In a cold cathode diode, reduction of the cathode-anode spacing and resultant change in diode impedance increases the beam current and reduces the gun impedance during the pulse. The self-biased cold cathode triodes discussed here are much less affected by the plasma expansion; as the curves show, one effect of grid control is to provide compensation for the change in cathode-grid spacing.

Therefore, gun impedance and current density are not the main factors influencing the choice for the grid-cathode spacing. A more important factor is the pulse length required from the gun. For every grid-cathode distance, there is a maximum achievable pulse length. The usual goal of designing a compact gun with a small grid-cathode space conflicts with requirements for longer pulse lengths.

For a fixed cathode voltage (250 kV in these examples), the sensitivity of the dependence of anode current density on grid-cathode spacing is independent of the beam area. This can be seen by comparing the curves of Figure 14 (A = 3000 cm^2) with those of Figure 13 (A = 1000 cm^2).

As Figures 13 and 14 also show, the maximum anode current density that can be achieved as the grid resistance is reduced is also a function of the grid-cathode spacing, varying as X_1^{-2} in the limit as $R_G \rightarrow 0$.

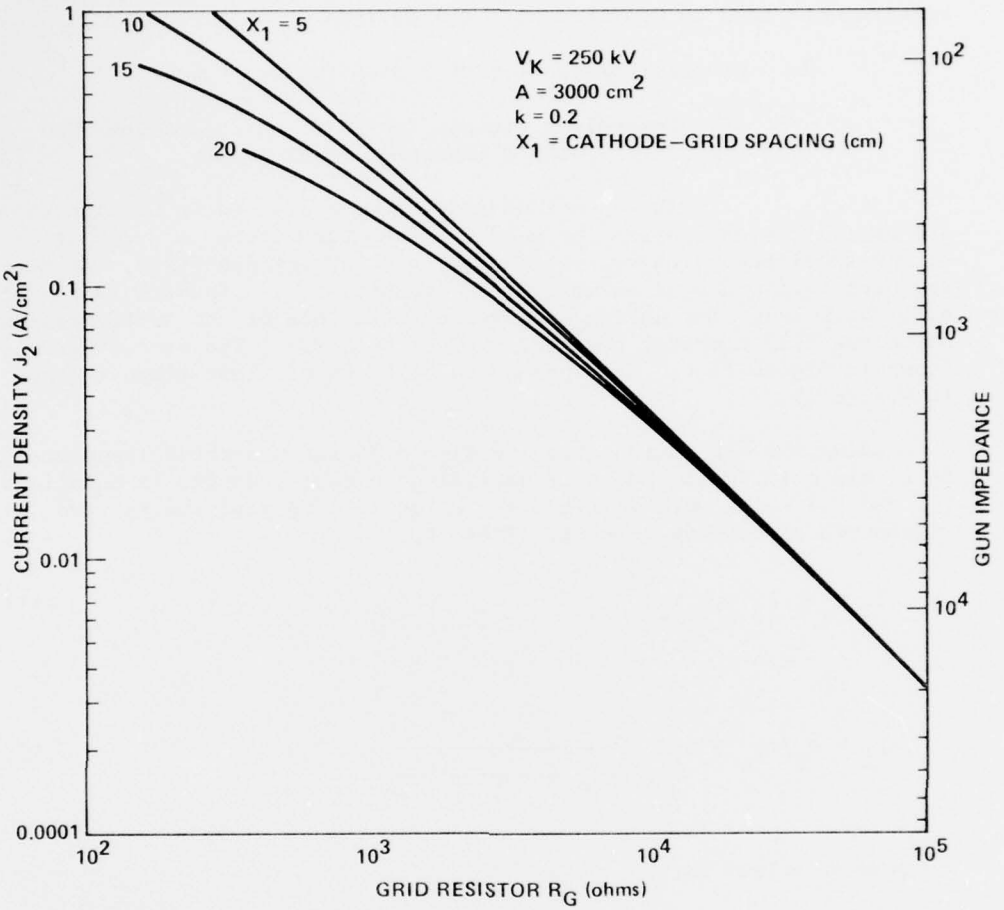


Figure 14. Anode current density (J_2) and gun impednace versus grid resistance (R_G) for a 3000-cm^2 beam.

In general, to achieve high (or moderate) gun input impedances for larger beam area guns it is necessary to keep the grid opacity, k, as small as possible, and the grid-cathode spacing, grid resistance, and gun voltage as large as possible. Unfortunately, these general requirements tend to conflict with gun designs which are compact.

B. Computer Simulation of System Performance

1. Equivalent Circuit for Grid Controlled Gun with a PFN/Pulse Transformer Power Supply

The equations and curves presented in Section IV A. are useful for estimating the needed system parameters in order to obtain specified voltages, impedances, and current densities. Another approach is the use of an equivalent circuit. This approach is especially convenient for making computer calculations of the system response, using the ECAP computer code for circuit analysis. The circuit model shown in Figure 11 can be represented by the equivalent circuit shown in Figure 15.

Using the expression given in Figure 15 for the three impedances, it is directly shown that this equivalent circuit results in Equations (1) and (3) which were derived in Section IV A to describe the two components of cathode current. That is,

$$I_3 = V_K/Z_3 = K_3 V_k^{3/2} \tag{11}$$

and

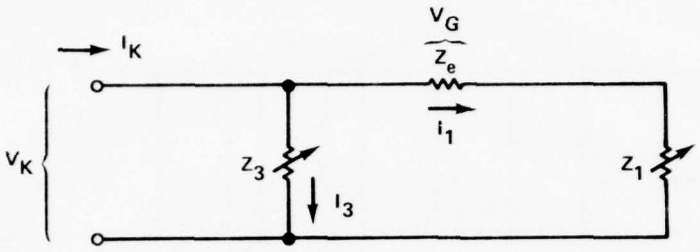
$$I_1 = V_K/(Z_e + Z_1) = \frac{V_K}{kR_G + \frac{1}{K_1^{2/3} I_1^{1/3}}} \quad , \tag{12}$$

which when solved for I_1 gives

$$I_1 = K_1(V_K - I_G R_G)^{3/2} \quad . \tag{13}$$

Equation (11) is identical to Equation (1); Equation (13) is identical to Equation (3).

The repetitively pulsed power supply consists of a PFN which is connected to the gun through a 17.5:1 pulse transformer and a voltage-peaking spark gap. This system is described more fully in Section V A. Figure 16 shows a simplified circuit diagram for the supply; Figure 16 (b) shows an equivalent circuit with the PFN impedances referred to the secondary of the pulse transformer. The impedance transformation is



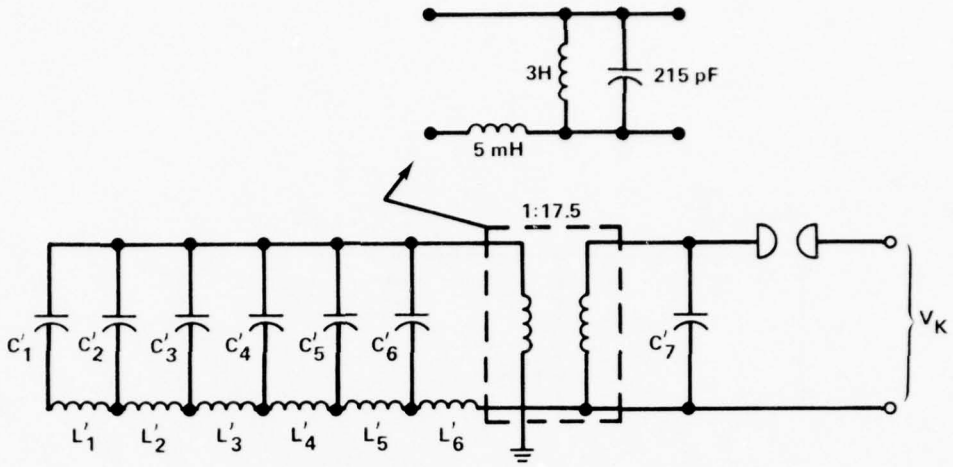
$$Z_3 = \frac{1}{K_3 V_K^{1/2}}; \quad Z_1 = \frac{1}{K_1 V_K^{1/2}}$$

$$Z_e = kR_G$$

Figure 15. Equivalent circuit model for triode electron gun with self-biased grid.

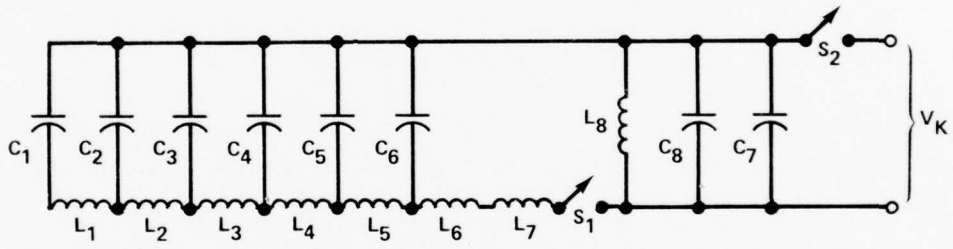
calculated in the usual way; i.e., circuit elements in the primary are transformed by multiplying their impedance value by n^2, where n = 17.5, the transformer's turns ratio. Figure 16 (a) also shows the equivalent circuit used for the pulse transformer, with circuit element values referenced to the secondary. Capacitor C_7', shown on the transformer output was usually connected during measurements. Its purpose was to provide additional energy storage prior to the firing of the peaking switch. In later measurements it was realized that the capacitance of the transformer windings (C_8 = 215 pF) was sufficient for the purpose, and C_7 was unnecessary.

Figure 17 shows the entire euuivalent circuit used for the ECAP computer calculation. Voltage V represents the pulse-charge voltage of the PFN (referred to the transformer secondary by multiplication by n). This voltage is applied to the pulse transformer at t = 0 when switch S_1 closes. The voltage V_S increases, but I_K = 0, until V_S reaches the value which fires the voltage peaking spark gap switch (S_2



C'_1 THROUGH C'_6; 0.22 μF EACH
L'_1 THROUGH L'_6; 4.57 μH EACH
C'_7 = 316 pF (TYPICAL)

(a)



C_1 THROUGH C_6; 718 pF
L_1 THROUGH L_6; 1.4 mH
L_7 = 5 mH; L_8 = 3 H; C_8 = 215 pF

(b)

Figure 16. Equivalent circuit for PFN pulsed power supply.

closes). Typically, switch S_2 closes when $V_S \simeq 250$ kV. The nonlinear impedances Z_1 and Z_3 are calculated in an approximate (step-wise) way by a built-in feature of the ECAP code.

Input to the code, in addition to the circuit values shown in Figure 17 are values for constants K_1, K_3, and k, which are estimated or calculated from the gun geometry or experimental results, the value of the grid resistor R_G, and the voltage for closing S_2.

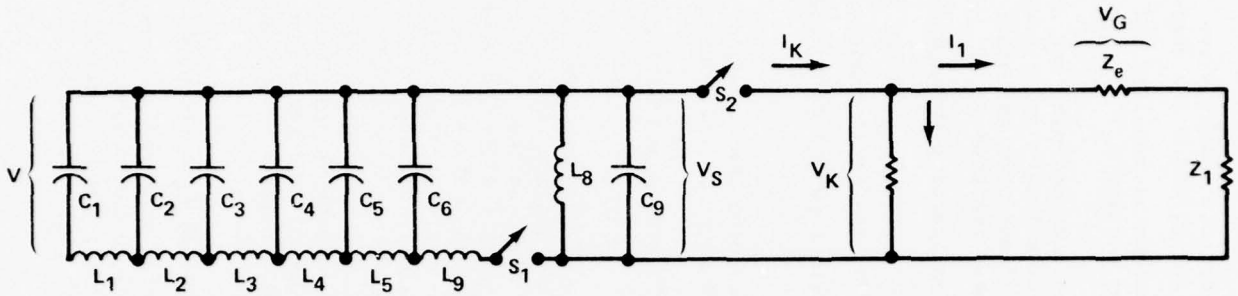
The ECAP code has provisions for calculating and plotting any of the branch currents or node voltages. Several voltages and currents which could be directly compared to measured waveforms and other useful parameters, were routinely plotted. These included V_K, I_K, V_G, the gun input impedance $Z = V_K/I_K$, and the current passing through the grid (internal beam current) $I_2 = I_K - V_G/R_G$. The current I_2 is the internal anode current of the gun. If I_2 is divided by the total transmission factor for the anode screen, foil support structure and foil, the quotient is the transmitted beam current.

Details of the procedure used for determining the values of the input constants and calculated waveforms are given in the next section.

2. Determination of Input Constants and Calculated Waveforms

For this example the set of measured waveforms shown in Figure 18 will be used. The specific cathode, grid structure, and focus electrodes for these measurements are described in Section V B. The parameters needed to derive the input parameters for the computer calculations are obtained from using the measured values of the voltage and current, in this case at t = 6 μsec. Generally, values calculated at t = 5 or 6 μsec were used; these times usually correspond to the peak value of cathode voltage and are approximately one-half of the pulse length. It is assumed that the code input constants could be evaluated at any time during the pulse. By choosing a point near the middle of the pulse, it is assumed that inclusion of effects due to gun turn-on transients or impedance collapse effects could be avoided which might be seen at times near the end of the pulse.

The initial voltage of capacitors C_1 through C_6 corresponds to the pulse-charge voltage of the PFN. The total measured ring-up factor for pulse charging the line is 29.40 referred to the secondary (Section V A 2). Because the dc charge voltage is 10 kV, the initial voltage for the capacitors is 294 kV. The peaking switch (S_2) was set to fire at



C_1 THROUGH C_6, 718 pF; C_9 = 531 pF (TYPICAL)

L_1 THROUGH L_5, 1.4 mH

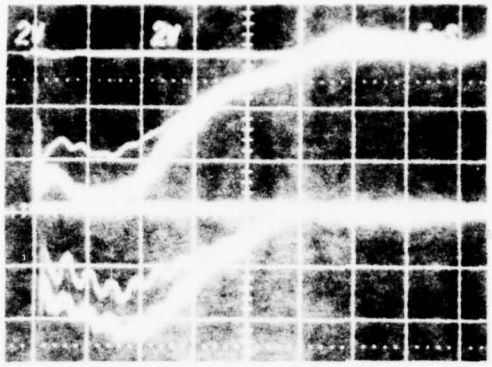
L_9 = 6.4 mH; L_8 = 3 H

$$Z_1 = \frac{1}{K_1 V_K^{1/2}} = \frac{1}{K_1^{2/3} I_1^{1/3}}$$

$$Z_3 = \frac{1}{K_3 V_K^{1/2}} = \frac{1}{K_3^{2/3} I_1^{1/3}}$$

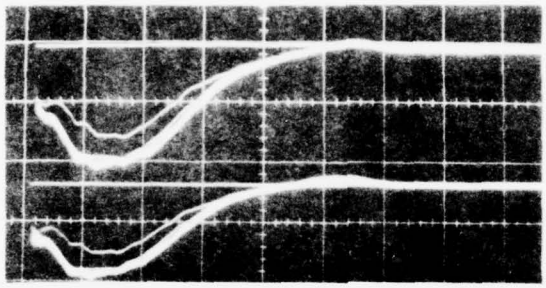
$$Z_e = kR_G$$

Figure 17. Complete equivalent circuit for pulsed power supply and triode electron gun used for ECAP calculations (all impedances referred to secondary of 1:17.5 pulse transformer).



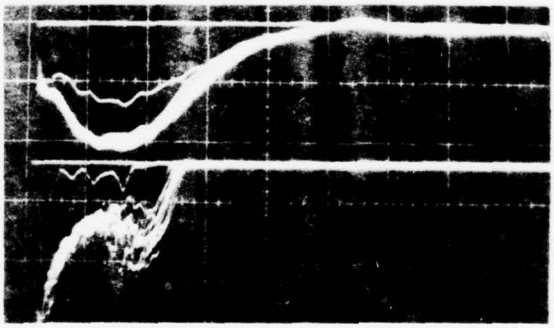
V_K: 54 kV/DIVISION

I_K: 40 A/DIVISION



V_G: 60 kV/DIVISION

I_G: 40 A/DIVISION



V_G: 60 kV/DIVISION

I_{coll}: 2.4 A/DIVISION

Figure 18. Gun waveforms, configuration 10-2-3.8, V_{dc} = 10 kV, R_G = 1940 ohms, 50 pps, 14 pulses, 5 μsec/division.

250 kV. If the peaking switch did not fire, the voltage V_S would rise to approximately twice the PFN voltage of 294 kV, because the line would be driving a high impedance load.

From the waveform of Figure 18 at t = 6 μsec, it is noted that V_K = 147 kV, I_K = 88 A, V_G = 120 kV, I_G = 60 A, and the total current collected 1-cm outside of the gun window is I_{coll} = 2.4 A. From these data, the following values are calculated for circuit constants:

$$R_G = V_G/I_G = 2000 \text{ ohms.}$$

$$I_2 = I_{coll}/T = 6 \text{ A.}$$

$$I_3 = I_K - (I_G + I_2) = 22 \text{ A.}$$

$$Z_e = V_G/(I_G + I_2) = 1818 \text{ ohms.}$$

$$K_1 = (I_K - I_3)^{2/3}/(V_K - V_G) = 6.28 \cdot 10^{-4}.$$

$$K_3 = I_3/V_k^{3/2} = 3.94 \cdot 10^{-7}.$$

Using these input values, the waveforms shown in Figures 19 through 23 were calculated. The measured waveforms are plotted in Figure 19 for comparison. Agreement between the calculated and measured waveform is reasonalby good, particularly with respect to pulse length (FWHM) and amplitude. The largest differences appear at the beginning and end of the pulse, probably due to initial transients and impedance changes which are discussed in Section V. The almost constant value of the gun input impedance during the pulse is interesting and of considerable importance for the design of these systems.

The greatest difference appears when the measured collected current waveform (corrected for window transmission and collector reflection) is compared to the calculated waveform. The major reason for the difference in waveshape is thought to be due to transient turn-on phenomena of the gun. Measurement error is another possible reason, as described further in Section V.

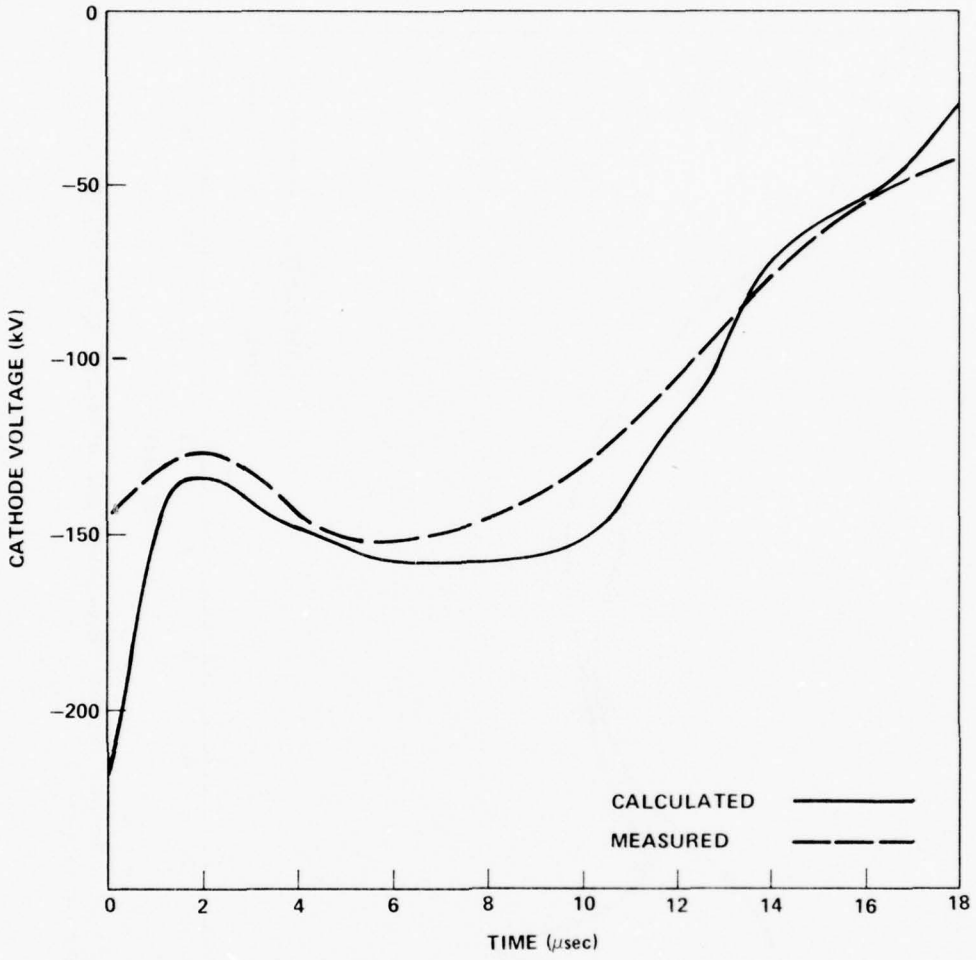


Figure 19. Comparison of calculated and measured cathode voltage from data of Figure 18.

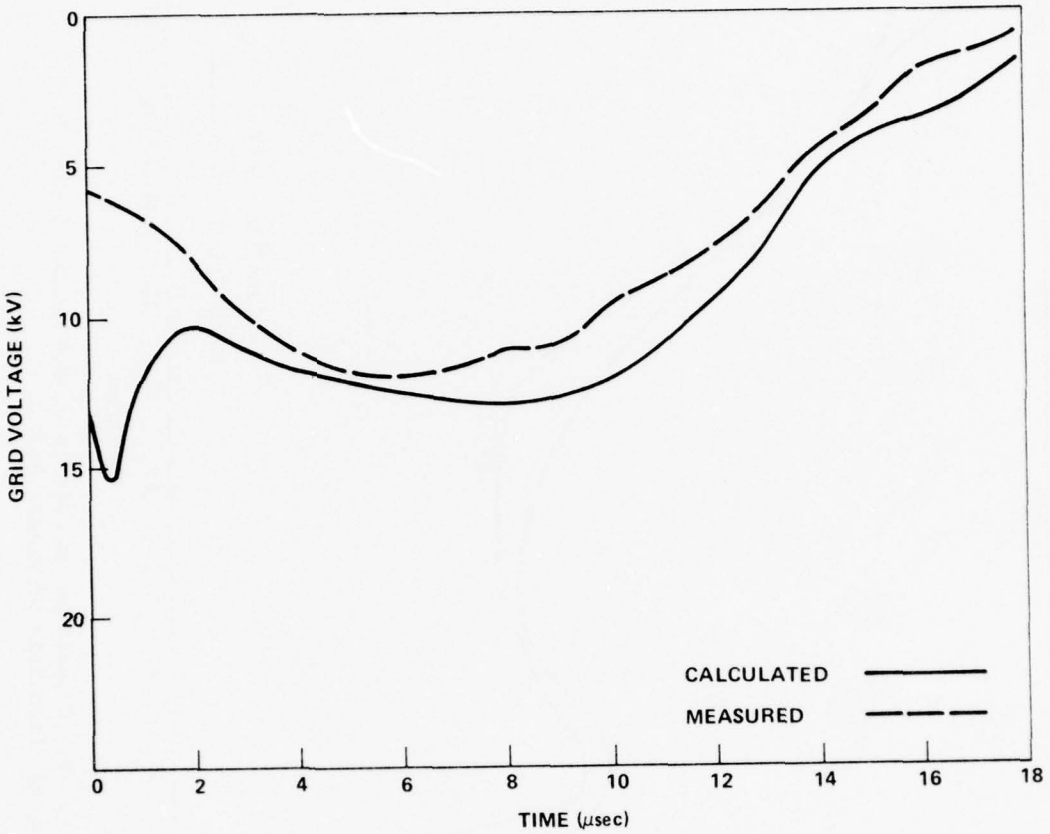


Figure 20. Comparison of calculated and measured grid voltage from data of Figure 18.

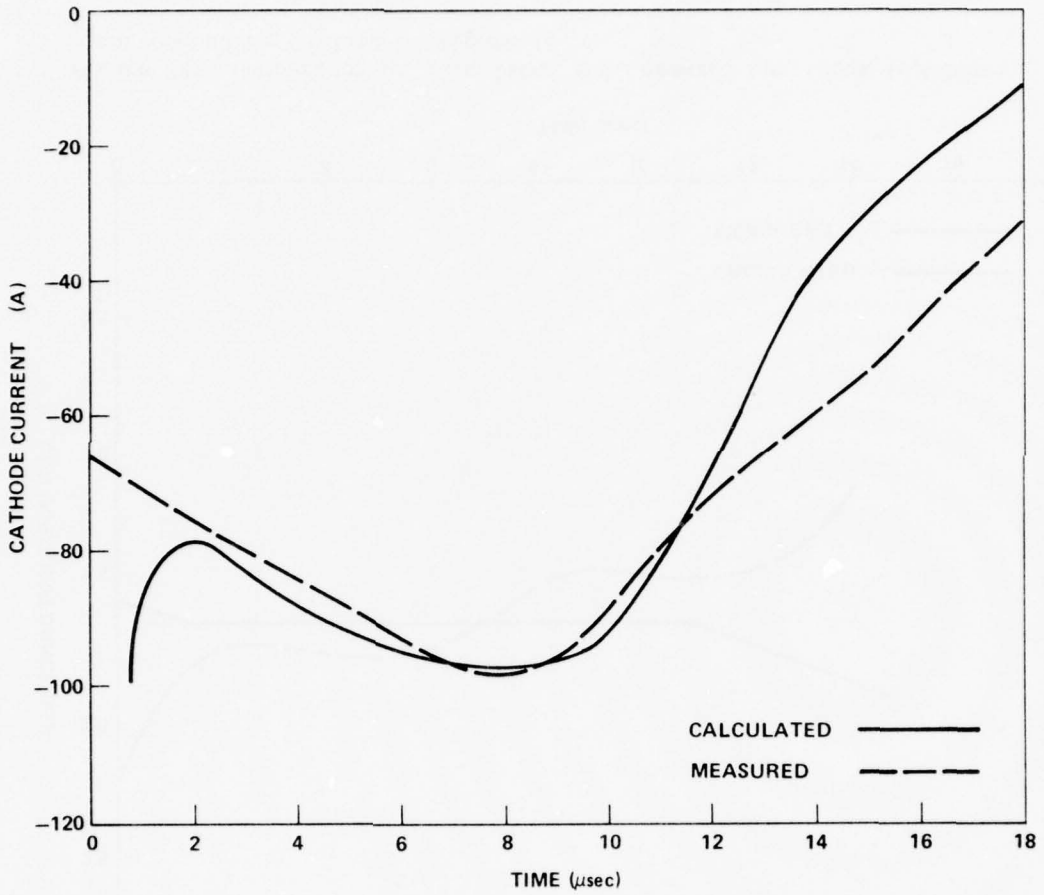


Figure 21. Comparison of calculated and measured cathode current for data of Figure 18.

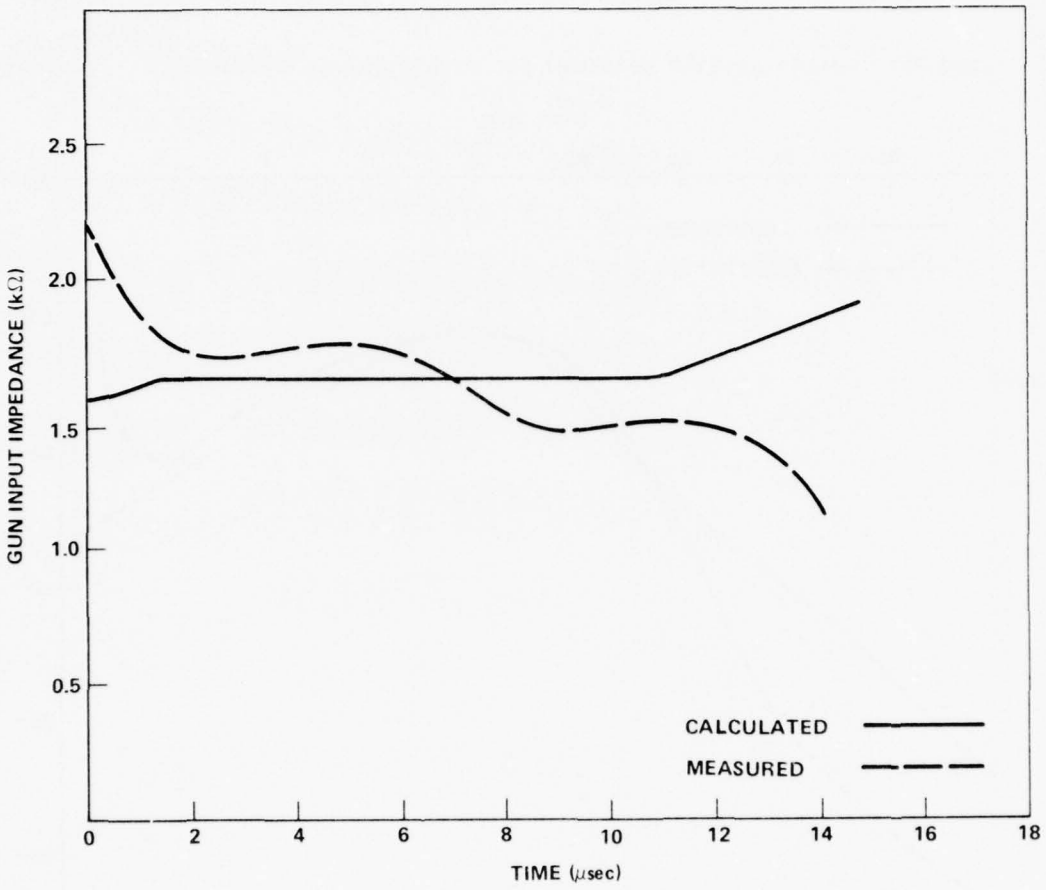


Figure 22. Comparison of calculated and measured gun input impedance corresponding to data of Figure 18.

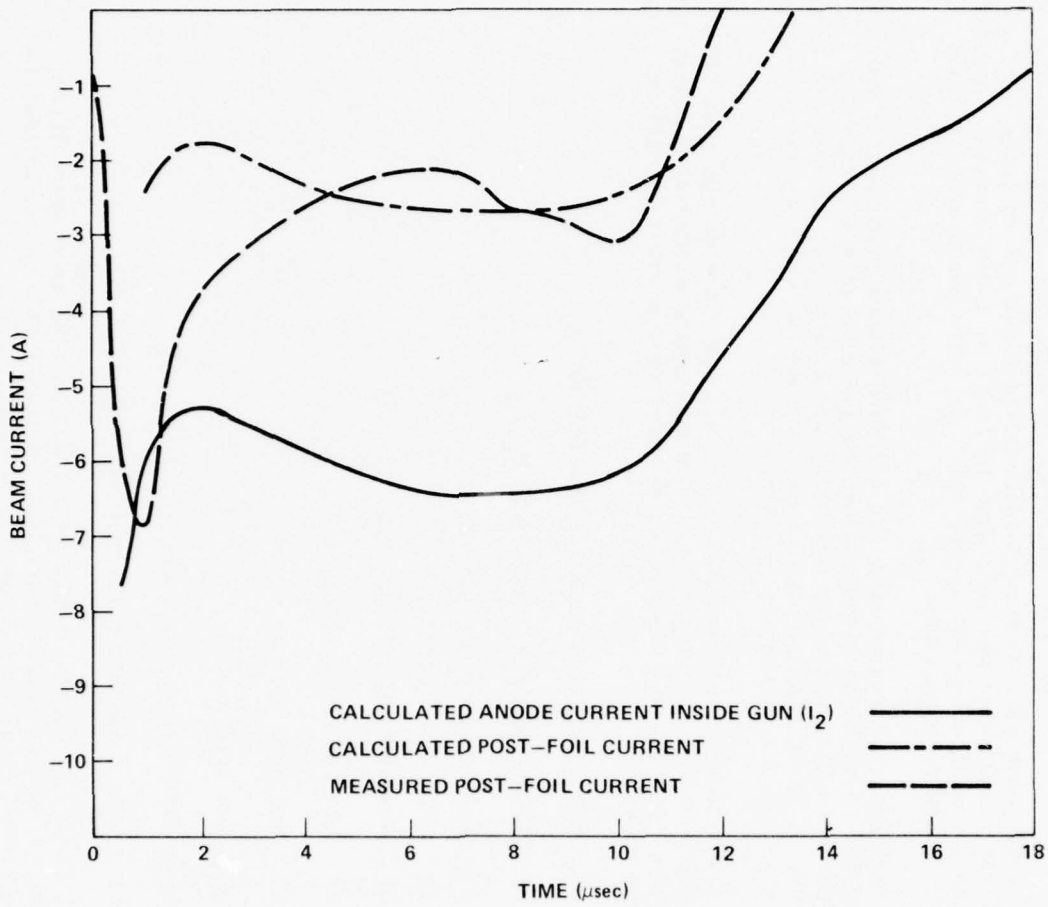


Figure 23. Comparison of calculated and measured beam current from data of Figure 18.

V. GRID CONTROLLED COLD CATHODE GUN: MEASUREMENTS

A. Test Facility and Diagnostic Methods

1. General Description

The test facility and diagnostic methods used in the second phase program were substantially identical to those of the first phase which are described in Sections 2 and 3 of the Appendix. Changes and additions made specifically for this phase are described in the following paragraphs.

The test facility consists of a lumped-element line pulser which is coupled to the cold cathode electron gun through a 17.5:1 pulse transformer. Direct current power for the line pulser is obtained from a 20 kV, 32 kW dc supply. Ignitrons are used as switching and pulse clipping elements in the line pulser.

A stainless steel vacuum chamber contains the electron gun. The electron beam is extracted through a water-cooled window of 0.001-in. aluminum. A 6-in. oil diffusion pumping system without a baffle or trap is used.

Measured quantities included the following:

a) Power supply voltage (dc), V_{dc}.

b) Power supply current (dc).

c) PFN pulse current.

d) Gun cathode voltage, V_K.

e) Gun cathode current, I_K.

f) Gun grid voltage, V_G.

g) Gun grid current, I_G.

h) Post foil beam current, I_{coll}.

i) Post foil beam current density.

Voltage and current monitors and probes used to measure these parameters, and other test equipment including cellophane dosimeters are described in Section 3A of the Appendix.

2. Line Pulser

The line pulser shown schematically in Figure A-2 of the Appendix was reconnected as shown in Figure 24. Each 0.22-μF capacitance in the PFN consists of five 0.044-μF capacitors connected in parallel. The pulse impedance of the PFN $Z = (L/C)^{1/2} = 4.56$ ohms. In this configuration, the nominal specifications of the line pulser, including the pulse transformer, are as follows:

Line impedance	4.56 ohms
Output voltage (maximum into matched load)	290 kV
Pulse duration (FWHM)	12 μsec
Pulse rate (maximum)	125 sec^{-1}
Duty (maximum)	0.36
Average power (maximum)	32 kW

Figure 25 shows the PFN voltage with the line operating at approximately 50 sec^{-1} and with the high voltage (HV) dc supply set at 5 kV. It can be seen that the total voltage swing during charging, produced by the series L-C circuit consisting of the 8 H charging inductor and the L and C of the PFN, is 8250 V. The charging time is approximately 8 msec, which permits full charging of the line for pulse rates to approximately 125 pps. From this measurement, the resonant charging ring-up factor was calculated to be $8250/5000 \simeq 1.7$.

This gives a total ring-up factor referred to the secondary of the 1:17.5 pulse transformer of approximately $1.7 \times 17.5 = 29.4$; hence, for example, a 10-kV dc voltage results in 147 kV at the output of the pulse transformer coupling the PFN to the gun, when the gun impedance is matched to the line impedance.

The PFN voltage is switched into the transformer by a single NL2458 mercury ignitron; a single tube of the same type is used to clip reverse voltages due to PFN line reflections. The turn-on ignitron is triggered by a pulse from the thyratron pulse chassis described in the Appendix. This pulse is stepped-up by the 1:10 pulse transformer at the ignitor of the ignitron.

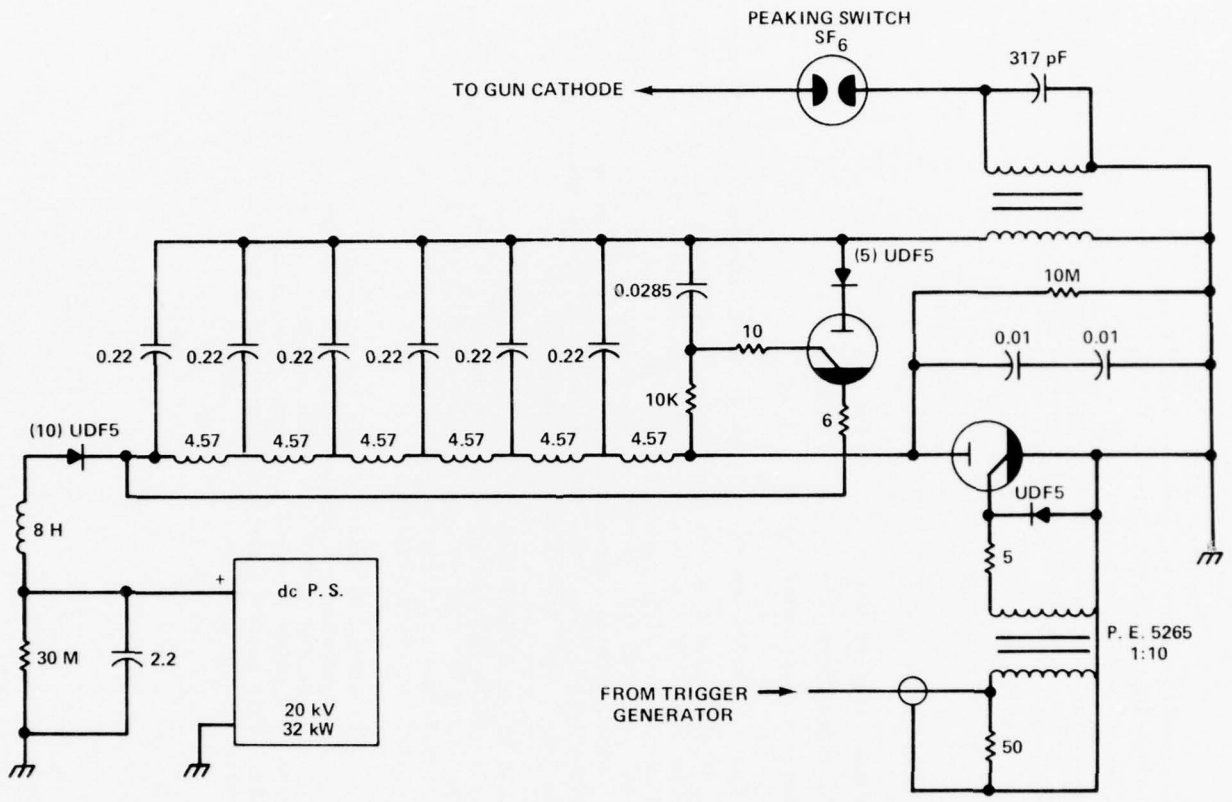
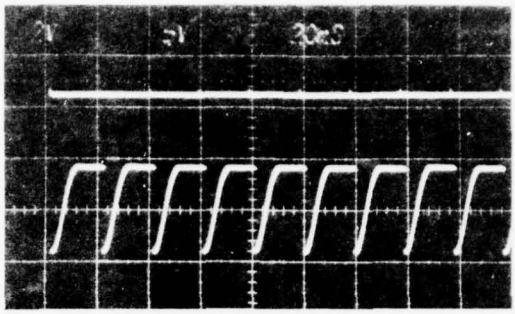


Figure 24. Line pulser schematic diagram.



PFN VOLTAGE: 5 kV/DIVISION
20 msec/DIVISION

Figure 25. PFN charging waveform, 50 pps
HV dc supply set for 5 kV.

The plate branch of the clipper ignitron has 5 UDF5 diodes in series. These diodes are extremely important for the correct operation of the circuit. If they are not in the circuit, the HV dc prevents the clipper tube from turning off. As can be seen in Figure 24, after the clipper turns on, there is a dc current path from the HV dc supply through the charging inductor to the cathode of the ignitron, then through the ignitron and pulse transformer primary winding to ground. Before the diodes were installed, the clipper ignitron would "latch-up," and the circuit breaker in the HV dc supply would open because of the excess power being consumed. There have been no problems of this type or any failures of the UDF5 diodes since their installation.

Figure 26 shows a set of waveforms including the current flowing through the clipper ignitron. These waveforms correspond to a particular gun configuration which produced gun oscillations and which will be discussed further in Section V B. At this point, only the last waveform, the clipper current, and the fact that it begins at approximately 14 μsec in this case are noted. The Figure 26 shows that at 14 μsec the principal gun pulse has ended.

3. Electrode Configurations

Figure A-5 of the Appendix is a photograph of the inside of the electron gun. It shows the cathode support electrode, focussing electrodes, and focus electrode support rings used during the first phase. This structure was converted to a triode geometry by removing the focus electrodes shown and using the supporting rings to support the grid assembly. New focus electrodes were then supported directly from the cathode support.

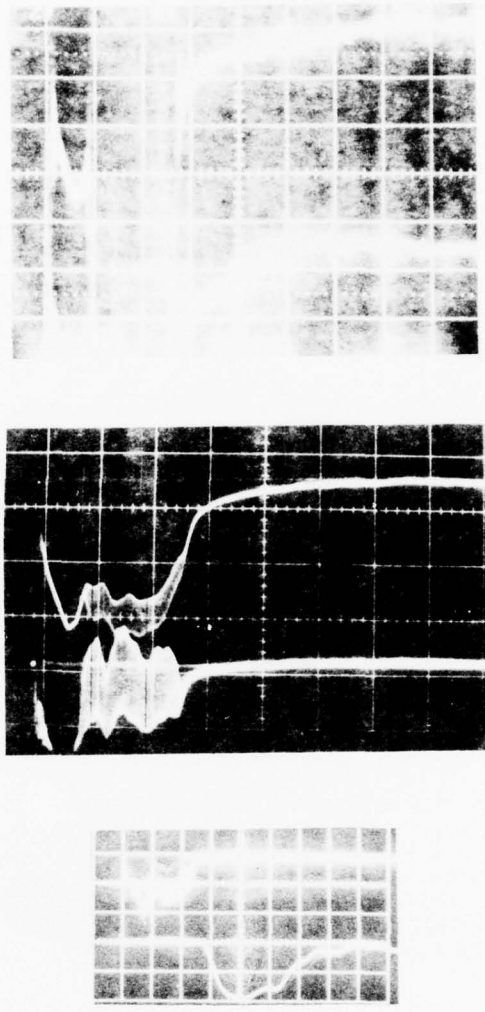


Figure 26. Gun waveforms, configuration 5-1-11.4, V_{dc} = 14 kV, R_G = 23 kΩ, 50 pps, 7 pulses.

The triode geometry is shown in Figure 27; the numbered components are identified in Table 3. The new focus electrode geometries are shown in Figure 28; Table 4 gives the dimensions which define the electrode geometries. Cathode-grid spacings were changed by raising or lowering the cathode support. The grid was always concentric with the vacuum chamber.

For some measurements, aluminum sheets were installed directly on the grid on order to form an aperture to define the electron beam area at the grid. The position of these plates is indicated in the diagram of Figure 27. The width of the open area of the aperture is denoted by dimension "A." In all cases except one, the aperture slit was aligned parallel to the cathode. The exception was Configuration 5-N-2A, for which azimuthal slit was positioned at the gun's midplane.

The focus electrodes were supported by ceramic insulators fastened to metal straps which fit over the cathode support. Corona balls and rings were used at the ends of the electrodes and insulators in order to control emission from the otherwise sharp edges at these points.

B. Repetition Rate, Pulse Length and Impedance Collapse

1. Repetition Rate

All of the measurements during the second phase program were consistent with the conclusions regarding repetition rate which were stated in the Appendix. Repetitive pulsing in the range of 50 to 125 sec^{-1}, and probably to rates above 1000 sec^{-1}, is adequately described as a repeated number of single pulses; no new physical phenomena are introduced.

The important factors related to repetitive pulsing are the cathode deterioration caused by the accumulated effects of a large number of shots, and average power related effects such as vacuum gassing and power supply component lifetime.

In the Appendix, tantalum cathode lifetime was estimated to be 10^6 to 10^7 shots; thus, as expected, no changes in gun performance which could be attributed to cathode wear were observed during the second phase.

In order to avoid the effects of vacuum gassing, the system was usually operated in a burst mode with each burst containing typically 7 or 14 pulses. The bursts were frequently repeated every few seconds. For example, when making the beam uniformity measurements with the cellophane dosimeter, typically between 20 and 60 seven-pulse bursts were fired with not more than 5 sec between bursts.

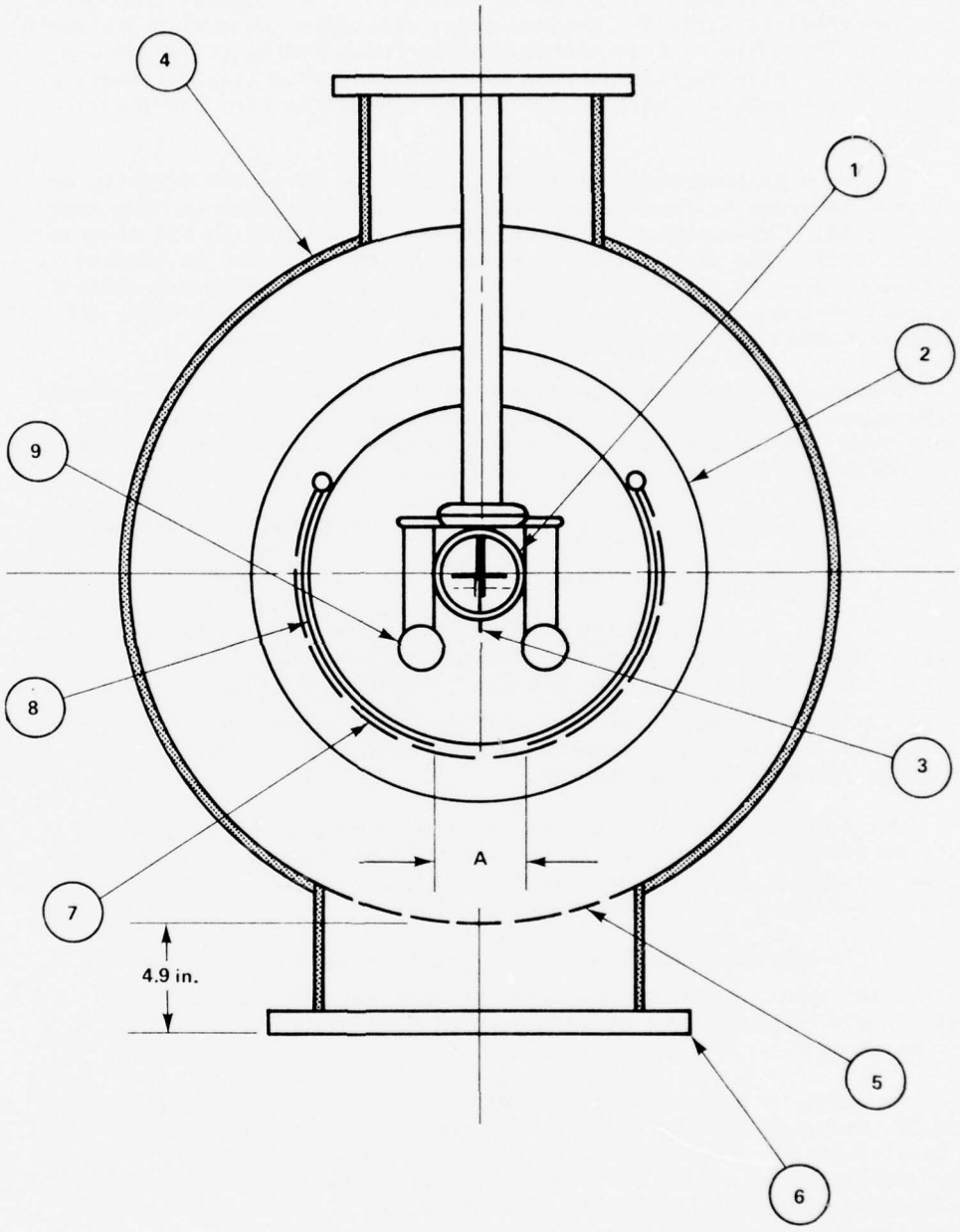


Figure 27. Schematic drawing of triode cold cathode electron gun with focussing electrodes (Table 3 identifies the numbered components).

TABLE 3. KEY TO COMPONENTS OF ELECTRON GUN SHOWN IN FIGURE 27

Component No.	
1	Cathode holder and electric field shaping electrode. 3-in. diameter.
2	Grid support ring. One ring at each end of grid. 15-in. outside diameter (OD), 11.25-in. inside diameter (ID).
3	Cathode. Tantalum, 0.0003-in. thick × 0.5-in. wide (typical (typical) × 18-in. long.
4	Vacuum chamber. 23.5-in. ID.
5	Anode screen. 2 mesh × 0.050-in. diameter wire. Transparency 81%.
6	Water cooled electron beam window. Support rib transparency 69%. Foil is 0.001-in. aluminum.
7	Grid. 8 mesh × 0.029-in. diameter wire. Transparency 60%. Grid diameter 12 in.
8	Grid aperture sheets. Aluminum. Aperture width "A."
9	Focus electrodes (representative). Figure 28 gives focus electrode dimensions.

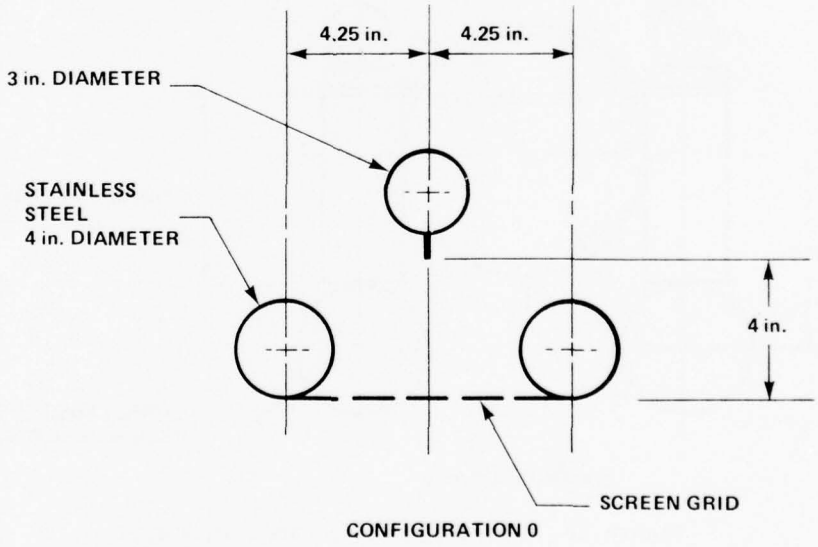
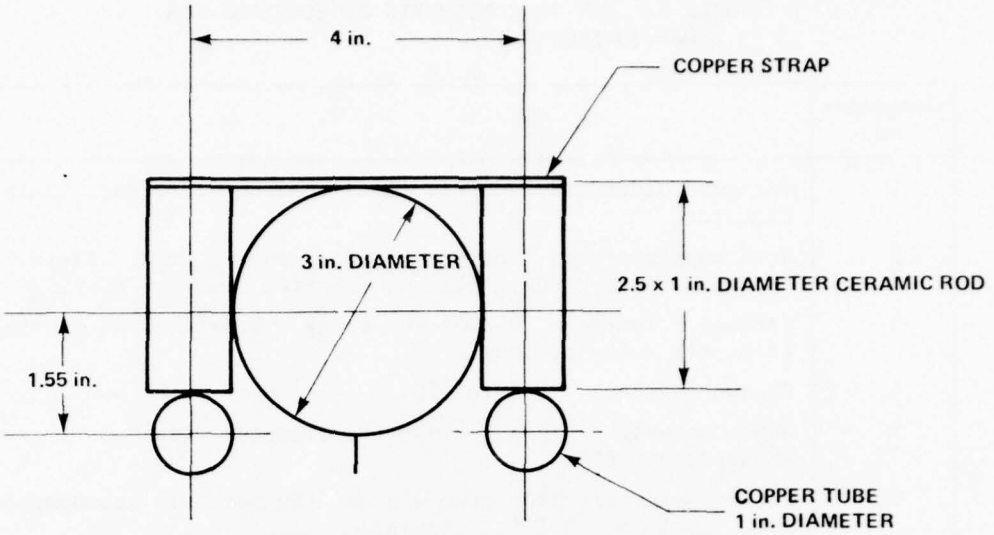
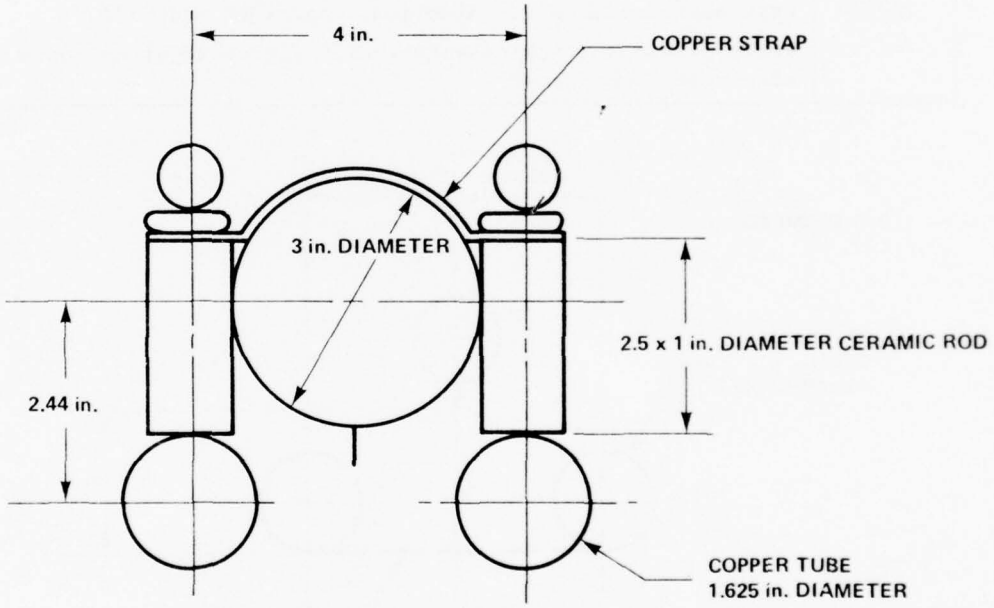


Figure 28. Focus electrode dimensions (a).



CONFIGURATION 1



CONFIGURATION 2

Figure 28. Focus electrode dimensions (b).

TABLE 4. ELECTRODE CONFIGURATIONS OF FOCUS ELECTRODE SHAPES SHOWN IN FIGURE 28 (a) AND (b)

Description	Cathode-Grid Spacing (cm)	Focus Electrode Configuration	Grid Aperture (cm)
10-0-21.6	10	0	21.6
5-N-11.4	5	None	11.4
5-1-11.4	5	1	11.4
10-N-11.4	10	None	11.4
10-N-0	10	None	Opaque Grid
10-N-2	10	None	2
10-N-2A	10	None	2 (Azimuthal slot)
10-N-0.5	10	None	0.5
10-N-3.8	10	None	3.8
10-2-3.8	10	2	3.8

The gun power supply had adequate average power capability so that, with one exception, problems with repetitive pulse, high average power operation were not encountered. The one exception was the grid resistor. These were liquid resistors made from 0.5-in. ID Tygon tubing filled with an aqueous solution of $CuSO_4$ or NH_4Cl, depending on the required resistance. On several occasions, grid resistors were destroyed by running at high repetition rates with too frequent bursts. The failure mode was heating of the solution, leading to vaporization and expansion which finally caused the Tygon tubing to rupture.

This problem can easily be avoided in future systems by designing grid resistors with sufficient power handling capacity.

The grid resistor would also change resistance values slightly during a burst, but the change was generally negligible.

The SF_6 filled series spark gap used as a voltage peaking switch between the pulse transformer and the gun performed satisfactorily over the entire range up to 125 sec^{-1}. It was generally set at a pressure of 20 psig corresponding to a measured self-firing voltage of 250 kV. It had been hoped that it would be possible to operate without the voltage peaking switch, but this was not found to be feasible. As explained in Section 3B of the Appendix, a fast rising voltage pulse is necessary to produce uniform multiple initial emission sites along the length of the cathode. When the SF_6 pressure was lowered so that

the gap self-fired below 100 kV, emission was erratic and non-uniform. Visual observation of the cathode showed that instead of several emission sites per centimeter (the case for the 250 kV self-breaking setting), only one or two sites were formed along the entire 46-cm cathode. Thus, it appears that a peaking switch will be required on future systems, because it seems unlikely that pulse transformers or other types of power supplies will be able to supply a sufficiently fast rising pulse without a peaking device in the circuit.

Other than the previously described effects, repetition rate had little observable effect on the gun operation or pulse characteristics.

2. Pulse Length and Impedance Collapse

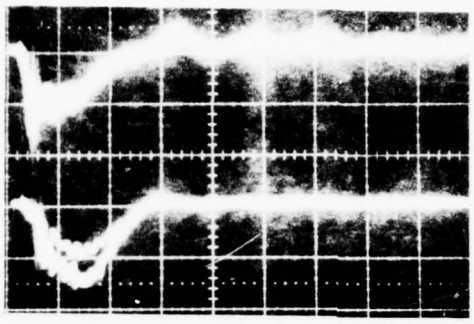
An important issue in cold cathode gun technology is whether the maximum pulse length that can be obtained is satisfactory for the specific laser application. The pulse length limitation is caused by "impedance collapse," the decrease in the gun's space-charge impedance, as plasma created at the cold cathode surface moves toward the anode.

This phenomenon has been described by many investigators. It is found that the speed of impedance collapse varies slightly depending upon the materials used for constructing the gun; the collapse "speed" range is from approximately 0.8 to 8 cm/μsec. For example, a minimum anode-cathode spacing of approximately 20 cm would be required for 10-μsec pulses from a cold cathode diode, if the diode collapse speed were 2 cm/μsec. After impedance collapse, the voltage across the diode is very small and the diode current large. However, because of the low voltage, electrons will not have sufficient kinetic energy to penetrate the window foil and no external beam current will be observed.

The measurements taken here with triode guns during this phase of the program have produced some gun behavior not previously observed, but consistent with impedance collapse speeds in the preceding range.

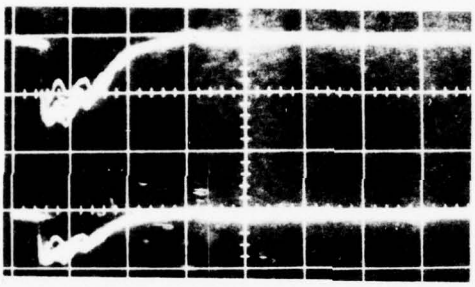
As Table 4 and Figure 28 indicate, the grids used were a 10-cm cathode-grid spacing and an unapertured grid with focus electrodes which were an integral part of the grid assembly.

Figure 29 shows a typical set of waveforms for this configuration (10-0-21.6). The cathode voltage monitor at the time of these measurements was on the pulse transformer side of the peaking switch; therefore, the trace labelled V_K actually shows the voltage pulse at the transformer output prior to the time the peaking switch fires and then the voltage on the cathode. The trace shows that the voltage rose to approximately 235 kV and then dropped to approximately 165 kV when the switch fired.



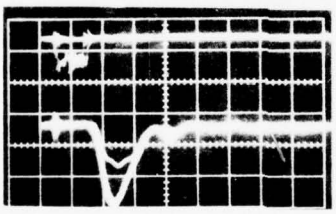
V_K: 136 kV/DIVISION

I_K: 100 A/DIVISION



V_G: 120 kV/DIVISION

I_G: 40 A/DIVISION



I_{coll}: 2 A/DIVISION

$I_{clipper}$: UNCALIBRATED

Figure 29. Gun waveforms, configuration 10-0-21.6, V_{dc} - 14 kV, R_G = 5 kΩ, 50 pps, 7 pulses, 10 μsec/division.

All the waveforms in Figure 29 have pulse lengths (full width half mixiumum [FWHM]) of 11 to 12 μsec. At the time of the measurements, it was thought that this was a good indication that the impedances were not collapsing in less than this time, which corresponds approximately to the PFN pulse length.

The beam collector trace in particular was taken as evidence that the impedance was maintained. This collector is an aluminum plate which is mounted 1 cm from the window foil to collect the entire beam current after it passes through the foil. Collector voltage is read across a resistor (typically 1 to 10 ohms) connected between the collector and ground. Even though the indicated beam current was small (≈2 A), if the impedance had collapsed during the voltage pulse, the beam electrons would not have continued to pass through the foil for the full 10 to 11 μsec.

Previous experience with diode guns influenced the investigations done here. It is now suspected, based on observations described in the following paragraphs, that the impedance in the cathode-grid region may not have been maintained as well as the investigators thought at the time.

The difference in voltage between the grid and cathode at the beginning of the pulse is very small, approximately 10 kV, and may be the same after approximately 5 μsec, although it is difficult to resolve the traces with sufficient accuracy to be certain of the voltage difference.

These early triode measurements also introduced the phenomenon now called the "lost current problem." The current waveforms of Figure 29 show that at the beginning of the pulse (for example) the cathode is I_K = 80 A, I_G = 34 A, and $I_{coll} \simeq$ 2 A. Even accounting for window rib and anode screen transparency (≈0.69 net) and foil absorption, there is still roughly 40 A, or 50% of the cathode current which has been "lost." The assumption then was that this current was hitting the anode plane outside of the window area, or that there was current flowing directly from the plasma in the grid-cathode region to the chamber walls. The latter current is denoted "I_3" in the analyses of Section IV.

It was also suspected that emission was occurring from portions of the cathode holder, and was not confined to the tantalum cathode blade. However, this was eliminated as a possibility by removing the Ta cathode foil and pulsing the gun. All of the diagnostics indicated that no current was flowing in the gun; it appeared to be a fully open circuit and it held the pulse voltage (≈160 kV for the test) for the full pulse length.

Configuration 5-N-11.4 was installed to get a better definition of where current was flowing. The grid/focus electrode configuration 10-0-21.6 was replaced with a cylindrical grid structure without focus electrodes. Most of the grid was made opaque by installing aluminum sheets directly on the grid, leaving a longitudinal aperture 11.4-cm wide directly in line with the cathode (Figure 27).

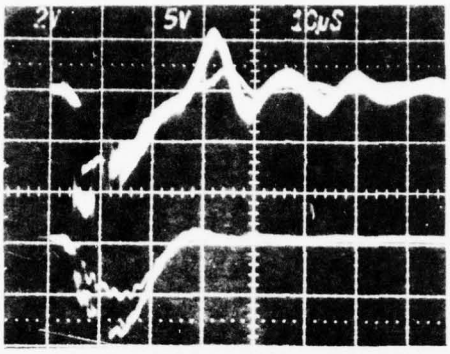
The relatively small spacing of 5 cm was used for two reasons: First, previous work with large beam area diode guns and triode configurations showed impedance collapse speeds less than 0.9 cm/μsec, and in the interest of gun compactness, the smallest cathode-grid spacing was required which could produce 10 μsec or longer beam pulses. Secondly, the cathode-grid geometry with small spacing was more approximately planar than with larger spacings, and it was expected that the space-charge limited current could be checked against results from other guns.

Figure 30 shows waveforms representative of this configuration. The cathode voltage monitor has now been moved to the gun side of the peaking switch; therefore, the voltage waveform now shows only the voltage applied to the cathode.

Instead of increasing the ratio I_G/I_K, the new configuration decreased it; however, it also gave indications that the overall efficiency I_{coll}/I_K has improved, although the transmitted current pulse was very peaked due largely to the drop in electron kinetic energy during the pulse. At $t \simeq 4$ μsec, (just before the abrupt change in cathode voltage), $I_K \simeq 140$ A and $I_G \simeq 34$ A. The beam current peak $I_{coll} \simeq 4.4$ A, which after correction gives $I_2 \simeq 13$ A. Therefore, $I_G/I_K \simeq 0.24$ and $(I_G + I_2)/I_K \simeq 0.34$.

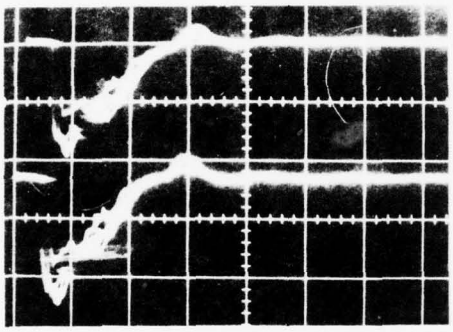
Comparison of Figures 29 and 30 shows little change in the gun pulse lengths. There is, however, an abrupt decrease in the waveforms of Figure 30 at $t \simeq 4$ μsec not seen in Figure 29. At $t \simeq 8$ μsec, $I_G/I_K \simeq 24$ 180 $\simeq 0.13$, and $(I_G + I_2)$ $I_K \simeq 0.17$. This was interpreted as indicating expansion of the grid-cathode plasma, and increassd current flow (I_3) directly from the cathode to ground in the upward direction between the grid and cathode support (Figure 27).

To eliminate this path for lost current and to focus the beam in the forward direction, the focus electrodes were installed as shown in Table 4 and Figure 28 as configuration 5-1-11.4. Waveforms from this configuration displayed the high frequency oscillations, beginning at $t \simeq 4$ μsec, seen in Figure 26. The oscillations start at a slightly later time than when the abrupt decrease in cathode voltage occurred for configuration 5-N-11.4 as shown in Figure 30.



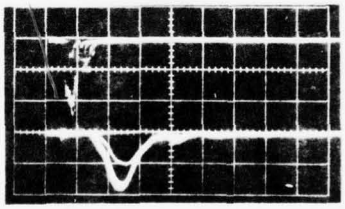
V_K: 54 kV/DIVISION

I_K: 100 A/DIVISION



V_G: 60 kV/DIVISION

I_G: 20 A/DIVISION



I_{coll}: 2 A/DIVISION

$I_{clipper}$: UNCALIBRATED

Figure 30. Gun waveforms, configuration 5-N-11.4. V_{dc} = 14 kV, R_G = 3 kΩ, 50 pps, 7 pulses, 10-μsec/division.

Figure 31 shows waveforms similar to Figure 26 except the 20-MHz filters have been used to reduce the oscillation on the cathode voltage and current waveforms. By displaying the oscillations with a faster oscilloscope sweep speed, it was found that the period was approximately 8 nsec, or at a principle frequency of approximately 125 MHz. The oscilloscope used for the grid waveforms could not respond to this frequency and the grid waveforms during the oscillations are not meaningful.

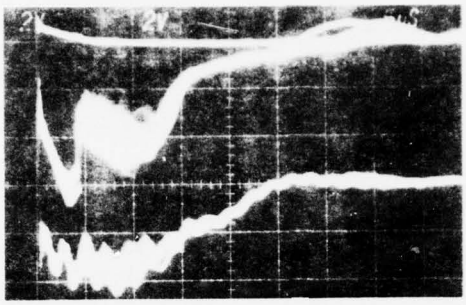
It is now believed that the oscillations began when the impedance in the cathode-grid region collapsed, thus bringing the grid and cathode to approximately the same voltage. The oscillations were probably present in the previous configuration 5-N-11.4 but without the focus electrodes in place, the coupling between cathode and grid was not as strong.

These parasitic oscillations appear to be related to stray capacitances and inductances of the circuit because the known lumped-element values of circuit inductance and capacitance do not provide a circuit loop with the correct high frequency response. For example, for an assumed loop inductance (grid and cathode feeds, etc.) of 1 μH, a series capacitance of 1.6 pF is required.

Another possible explanation is that the oscillations are related to oscillations of the plasma electrons; 125 MHz corresponds to a plasma electron density of approximately $1.9 \cdot 10^{8}$ cm^{-3}.

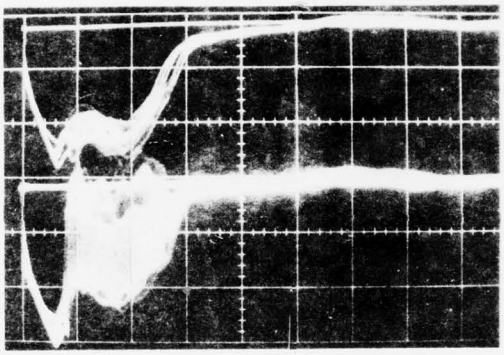
The magnitudes of the changes which occur in the various voltages and currents at the time of grid-cathode impedance collapse depend on the circuit conditions prior to the collapse. For example, the cathode voltage before impedance collapse depends on the PFN pulse charge and the ratio of gun input impedance to line PFN impdeance, $(V_K/V_{PFN}) = (1 + Z_{PFN}/Z_K)^{-1}$. ($Z_{PFN}$ is referred to the transformer secondary). If Z_K changes little, or if $Z_{PFN}/Z_K \ll 1$ before and after impedance collapse, the change in V_k will be small. Figures 31 through 33 show traces for the same configuration and PFN charge voltage, but different R_G.

Table 5 lists some of the parameters calculated from the data in these figures. It can be seen that Z_K changes very little for the case of Figure 33; V_K has a correspondingly small change. None of these three cases corresponds to $Z_{PFN}/Z_K \ll 1$; in general, an attempt is made to match $Z_{PFN} \simeq Z_K$ for efficient operation of the system.



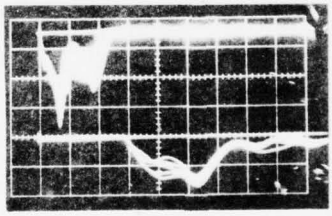
V_K: 54 kV/DIVISION

I_K: 40 A/DIVISION



V_G: 60 kV/DIVISION

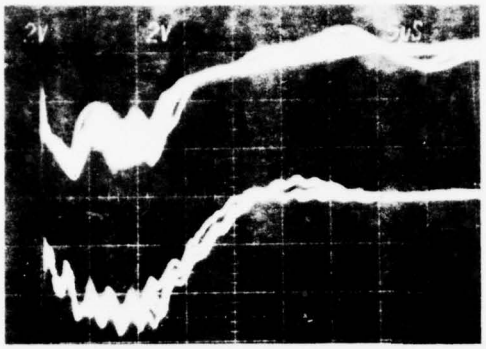
I_G: 2 A/DIVISION



I_{coll}: 5 A/DIVISION

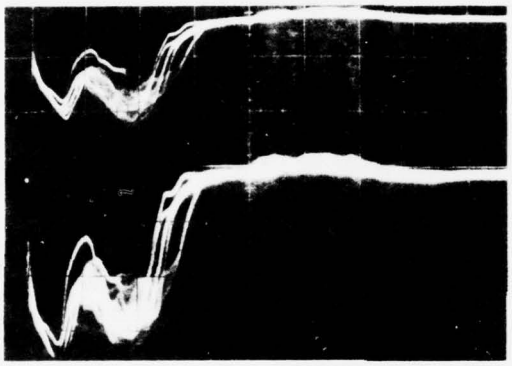
$I_{clipper}$: UNCALIBRATED

Figure 31. Gun waveforms, configuration 5-1-11.4, V_{dc} = 10 kV, R_G = 26.7 kΩ, 50 pps, 7 pulses, 5 μsec/division.



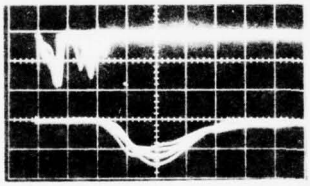
V_K: 54 kV/DIVISION

I_K: 40 A/DIVISION



V_G: 60 kV/DIVISION

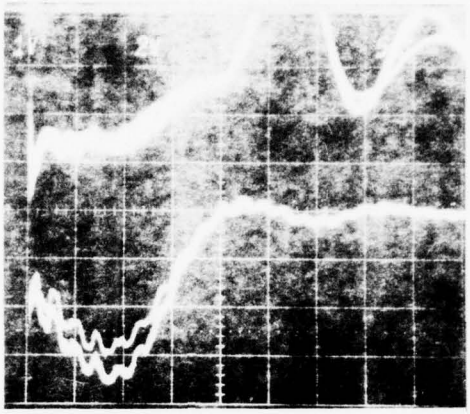
I_G: 4 A/DIVISION



I_{coll}: 5 A/DIVISION

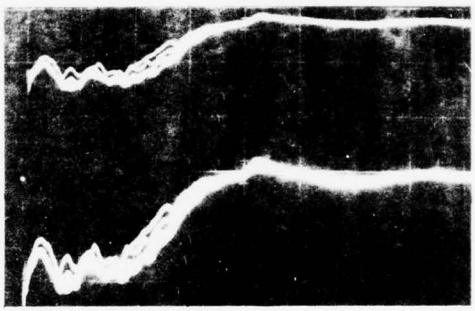
$I_{clipper}$: UNCALIBRATED

Figure 32. Gun waveforms, configuration 5-1-11.4, V_{dc} = 10 kV, R_G = 9.6 kΩ, 50 pps, 7 pulses, 5 μsec/division.



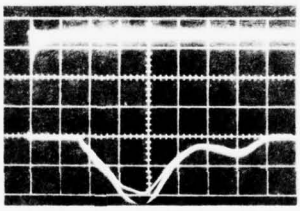
V_K: 27 kV/DIVISION

I_K: 40 A/DIVISION



V_G: 30 kV/DIVISION

I_G: 20 A/DIVISION



I_{coll}: 1 A/DIVISION

$I_{clipper}$: UNCALIBRATED

Figure 33. Gun waveforms, configuration 5-1-11.4, V_{dc} = 10 kV, R_G = 1.2 kΩ, 50 pps, 7 pulses, 5 μsec/division.

TABLE 5. VOLTAGE, CURRENT AND IMPEDANCE FROM WAVEFORMS OF FIGURES 31 THROUGH 33

	Figure 31		Figure 32		Figure 33	
	Before	After	Before	After	Before	After
Cathode Voltage, V_K (kV)	179	92	125	65	46	41
Cathode Current, I_K (A)	72	56	85	92	108	116
Gun Input Impedance, Z (kΩ)	2.48	1.64	1.49	0.710	0.430	0.350
Grid Voltage, V_G(kV)	144	108	96	66	45	30
Grid Current, I_T (A)	5.4	3.2	10	7.2	38	31
Grid Impedance, R_G (kΩ)	26.7	33.8	99.6	9.2	1.2	0.97
Anode Current in Gun, I_2 (A) (from corrected collected beam current)	32	32	---	---	---	---

Note: V_{dc} = 10 kV, 50 pps, 7 pulses, configuration 5-1-11.4.

A very interesting aspect of grid-cathode impedance collapse, and an effect that is very different from impedance collapse in a diode gun, is the transmitted beam current behavior. When the impedance of a diode gun collapses, the beam is terminated because there is no longer an electron accelerating voltage in the gun. In a triode gun, however, when the grid-cathode impedance collapses, there is still the possibility, depending on gun and circuit parameters, for the grid and cathode to remain at a high voltage for the entire duration of the pulse. Electrons from the grid-cathode plasma which pass through the grid are still accelerated toward the anode and if the voltage is high enough (above approximately 100 kV for 1-mil aluminum windows), the beam will penetrate the window. This effect is clearly seen in the I_{coll} traces of Figures 31 through 33. In Figure 31, the beam current continues to increase with cathode voltage and current until the impedance collapse at $t \simeq 4$ μsec. It then takes a sharp dip but increases again as the plasma continues to expand and the cathode voltage rises. In contrast, in Figure 33 the cathode voltage is too low before and after impedance collapse and a beam is not collected at any time.

The sharp dip in the beam current seen in Figure 31 is apparently due entirely to attenuation by the foil and collector backscatter, which vary dramatically as a function of beam kinetic energy. As Table 5 shows, after the collected current is corrected for window transmission and collector backscatter, it appears that the current I_2 incident on the inside of the anode has the same value, $I_2 \simeq 32$ A, immediately before and after the grid-cathode impedance collapse.

Even more interesting is the increase in the ratio I_2/I_K. For Figure 23, just before impedance collapse is complete, $I_G \simeq 5.4$ A, $I_2 \simeq 32$ A, and $I_K \simeq 80$ A. Thus, the focus electrodes have greatly reduced the "sidewise" current to the grid, and redirected it toward the anode, as they were intended to do. After impedance collapse, the grid no longer controls the beam. The grid resistor is then effectively connected between the cathode and ground and loading down the line pulser.

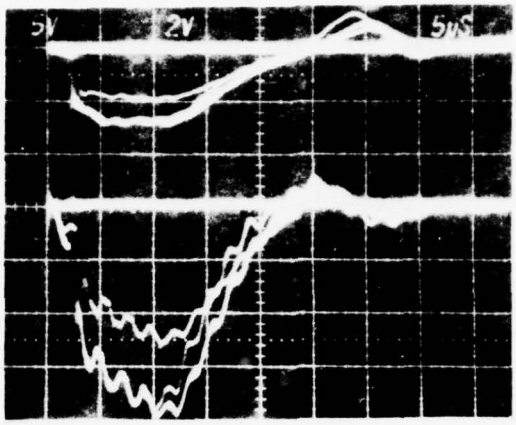
The next electrode configuration studied, 10-N-11.4, had doubled grid-cathode spacing (10 cm), no focus electrodes, and the same 11.4-cm grid aperture. This configuration was only studied briefly before a plate was installed to close the aperture completely. The reason for doing this was an attempt to define as closely as possible where the current was flowing in the gun. With the grid opaque, there were only two possibilities: either it flowed to the grid or from cathode to chamber wall as "lost" current. With a grid aperture, there were two additional paths: through the window and to the anode but outside the window area. The former could be measured, but not the latter.

As the waveforms of Figure 34 show, the impedance collapse no longer occurred at $t \simeq 4$ μsec with the 10-cm spacing. It appeared that the full required pulse length was now greater than 10 μsec, so the subsequent measurements were all taken with a 10-cm grid-cathode spacing. The emphasis in these experiments was on current measurements; they are described in the following sections.

C. Beam Control

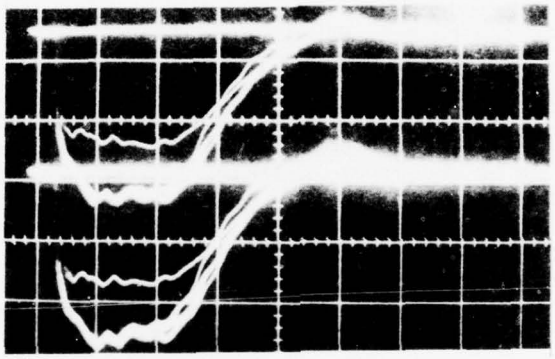
1. Beam Shape

The beam shape is important for two reasons. First, there is the need for the beam to create uniform ionization throughout the volume of the laser discharge cavity. Secondly, a beam which just fills the window is essential to build a high efficiency gun. Many of the smaller (10×100 cm^2) diode guns have been very inefficient, in part due to a beam area which is much larger than the window. Some of the larger guns (35×200 cm^2) in which the beam area better matches the



V_K: 136 kV/DIVISION

I_K: 40 A/DIVISION



V_G: 60 kV/DIVISION

I_G: 40 A/DIVISION

Figure 34. Gun waveforms, configuration 10-N-0, V_{dc} = 16 kV, R_G - 1.5 kΩ, 50 pps, 7 pulses, 5 μsec division.

window area, have been remarkably efficient, with a ratio of transmitted current to cathode current greater than 90%.

In addition to the preceding reasons for wanting a well-defined beam shape, there is also a need to know the total beam area in order to correlate measurements and calculations. For example, in trying to understand the "lost current" problem, it is necessary to know whether the beam area was greater than the window area. In order to correlate the beam current with the cathode-grid voltage, the current density at the grid must be known.

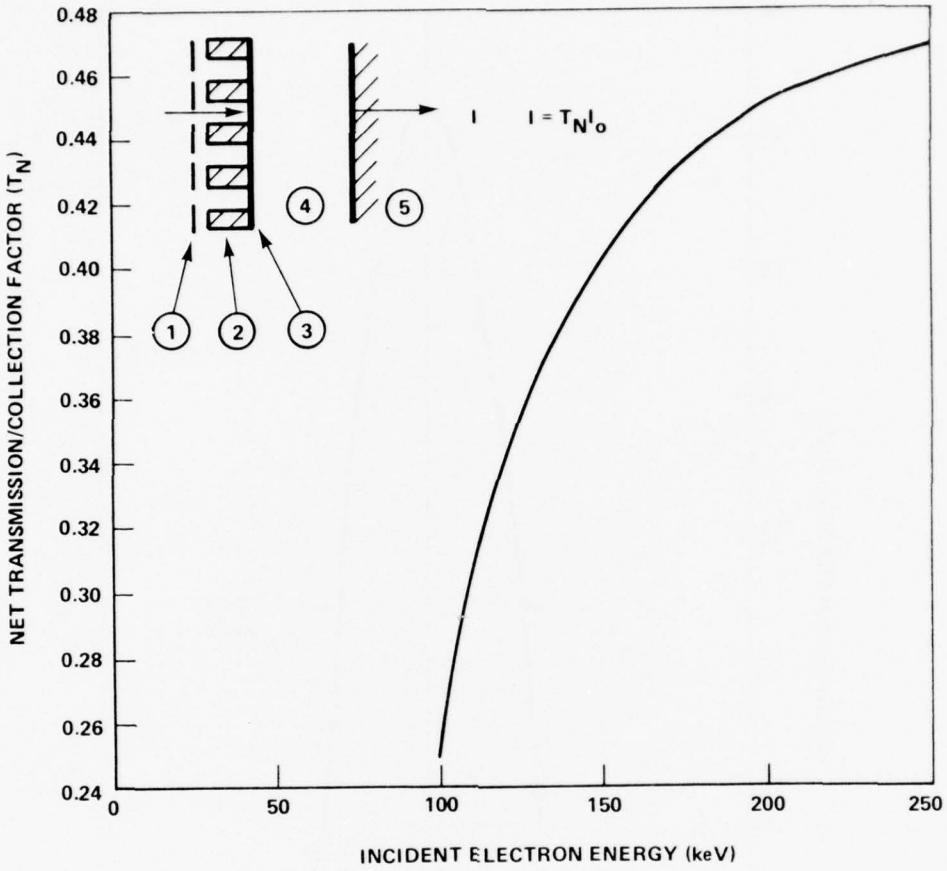
The diagnostic tool for time integrated measurements of the beam current density was a blue cellophane foil which was purchased from Simulation Physics, Inc. The foil was placed against the outside of the gun's 1-mil aluminum foil window. The blue color was bleached from the cellophane in proportion to the energy deposited by the electron beam. Scanning the cellophane with a densitometer then gave a profile of relative beam current density. The cellophane was not calibrated for response as a function of electron energy; hence, only relative measurements were made.

The apertures used at the grid have already been described. They allowed definition of the effective area to the grid, and determination of the degree of beam spreading between the grid and the window.

In order to calculate the current density inside the gun from the measured current density outside the window, it is necessary to account for absorptinn by the anode screen, foil support ribs, window foil, and air between the window and the detector. A correction must be made for backscatter from the foil and from the collector. The anode screen and rib transmission factor can be adequately calculated from their shapes and sizes; their net transmission for these experiments was (0.60) (0.81) = 0.49. The other factors depend on the kinetic energy of the incident beam electrons. The net correction factor was obtained for the foil, 1 cm of air, and an aluminum collector plate by using a Monte Carlo code. The calculation was made at 25-keV increments between 100 and 250 keV. The resulting net correction curve, which includes anode screen and ribs, and backscatter, is shown in Figure 35.

To use Figure 35, it is necessary to know the accelerating voltage. Correction factors have already been used from the curve in discussing data in previous sections.

The first measurement with the cellophane dosimeter was with the gun in configuration 10-N-2A, in which the grid aperture was an azimuthal slot 2-cm wide in the direction parallel to the cathode. Figure 36 shows the resulting profile parallel to the cathode. It is seen that the beam spreads in the longitudinal as well as the transverse direction, the 2-cm wide slot having produced a beam of 3.6-cm FWHM. The causes for longitudinal spreading are presumably scattering by the grid and anode



1. ANODE SCREEN (81% TRANSPARENT)
2. RIBS (60% TRANSPARENT)
3. 1–mil ALUMINUM
4. 1–cm AIR
5. THICK ALUMINUM

Figure 35. Net correction factor for beam transmission and collection.

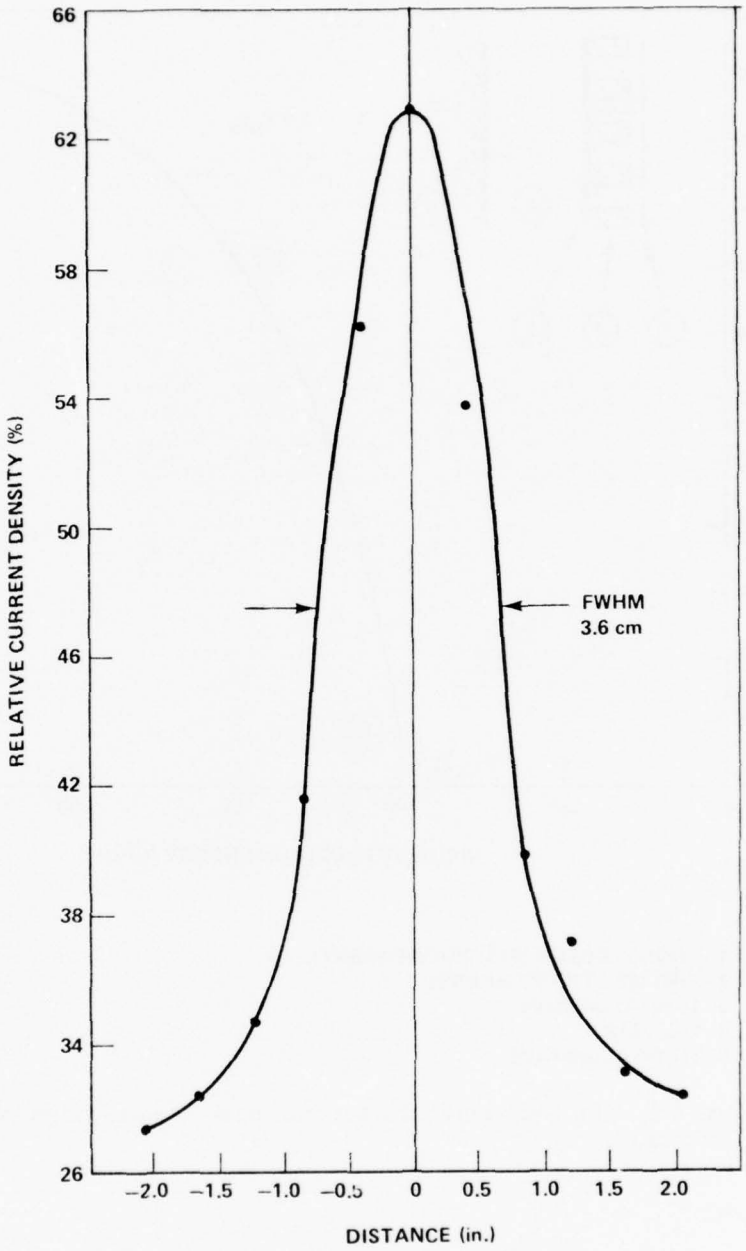


Figure 36. Time integrated current censity profile. Configuration 10-N-2A. V_{DC} = 12 kV, R_G = 5.8 kΩ, 50 pps.

screen wires and foil, and perhaps a lens effect caused by distortion of the electron field near the screen wires and penetration of the field through the screen.

As expected because of the cylindrical geometry, beam spreading is far more pronounced in the dimension transverse to the cathode. Figure 37 shows transverse profiles for configuration 10-N-2 with two different cathode voltages. Figure 37 shows that the FWHM did not change significantly when V_{dc} was doubled from 7 kV to 14 kV, and that the ratio of beam FWHM (transverse) to grid aperture width is in the range of 3.5 to 4 for this geometry. Similar results were obtained for all of the configurations studied.

On the basis of the results shown in Figure 37 a 3.8-cm wide aperture was installed for configuration 10-N-3.8, because it was estimated that the beam should just fill (transversely) the 7-in. (18-cm) wide window. Figure 38 shows that, approximately, the beam did fill the window. The FWHM is 14.6 cm.

Finally, the entire window was covered with a piece of cellophane and scanned along the paths indicated in Figure 39. The resulting profiles are shown in Figures 40 through 42.

All of these profiles show that the beam is very uniform over most of the window area. It should be recalled that the cathode is 17-in. (43-cm) long and the window is 60-cm long. Figure 40 shows that there is very little variation of density for the full cathode length, but that the beam does spread in the longitudinal direction to fill completely the 60-cm long window.

The transverse profiles of Figures 41 and 42 show that the transverse width of the beam fills the window to longitudinal positions corresponding to the cathode ends and that the uniformity is good over the same range.

It was concluded from these measurements that with the 3.8-cm aperture, almost all of the beam current was hitting the window area, and that for purposes of calculating the current density from the collector plate data, an effective beam area corresponding to the full window dimension, $\approx$1000 cm^2 could be used.

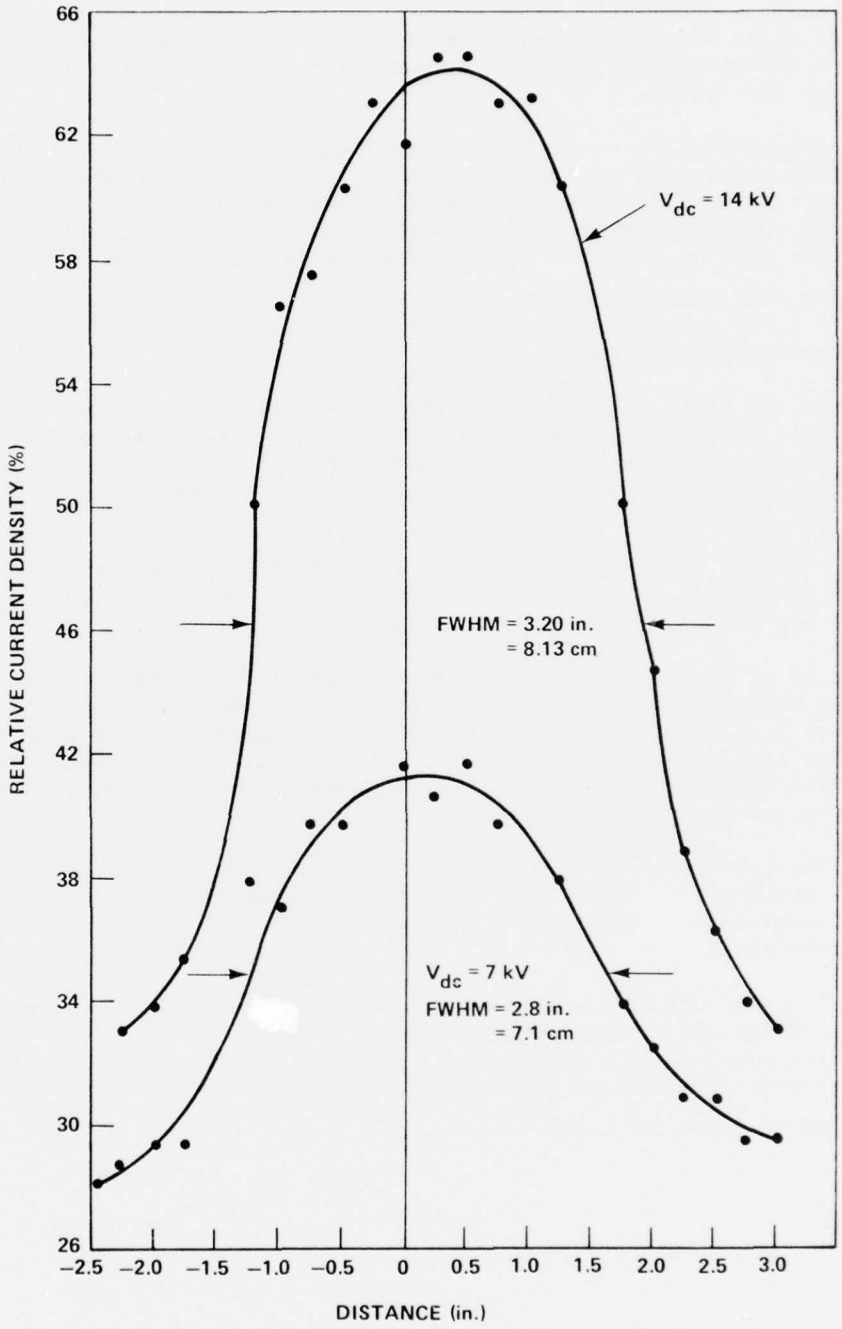


Figure 37. Time integrated current density profiles, configuration 10-N-2, V_{dc} = 7 kV and 14 kV, R_G = 3 kΩ, 50 pps.

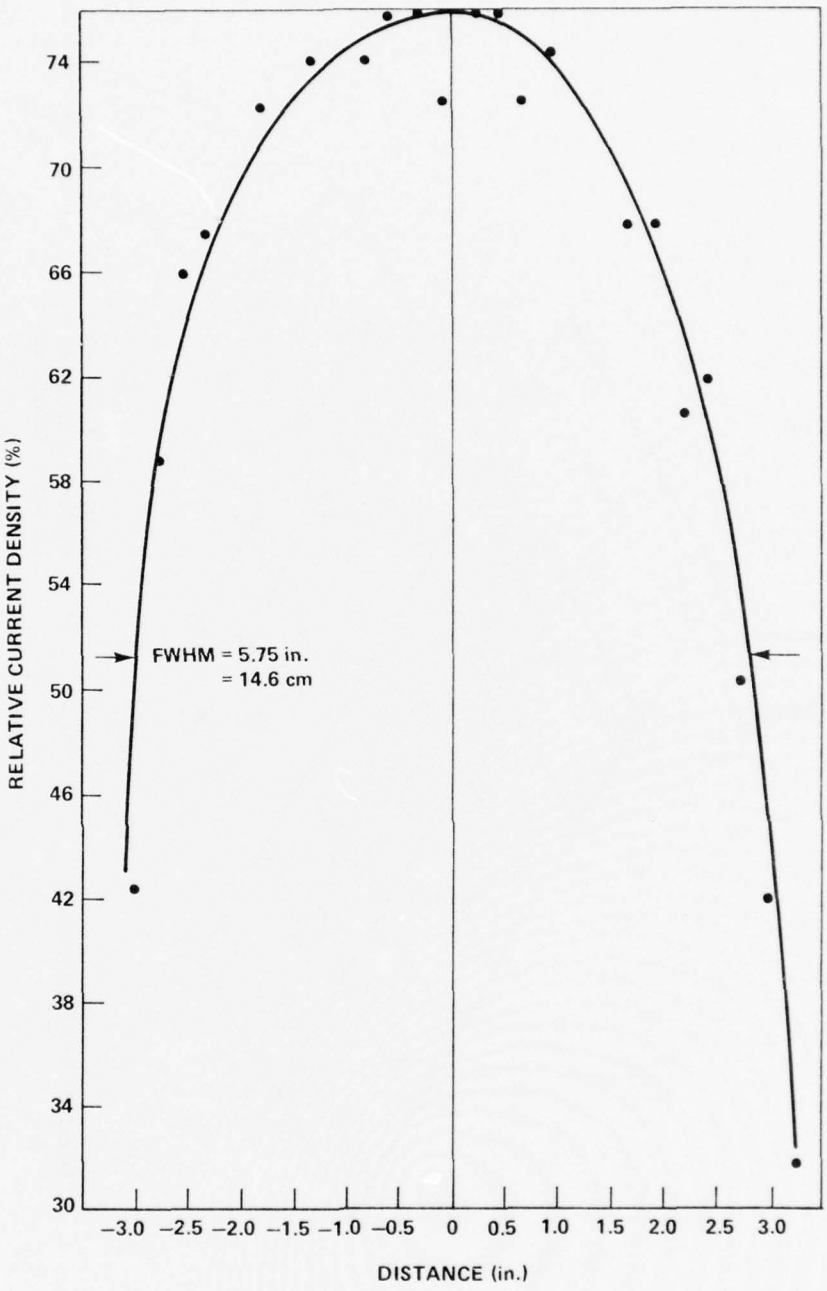


Figure 38. Time integrated current density profile, configuration 10-N-3.8, V_{dc} = 14 kV, R_{Ω} = 3 kΩ, 50 pps.

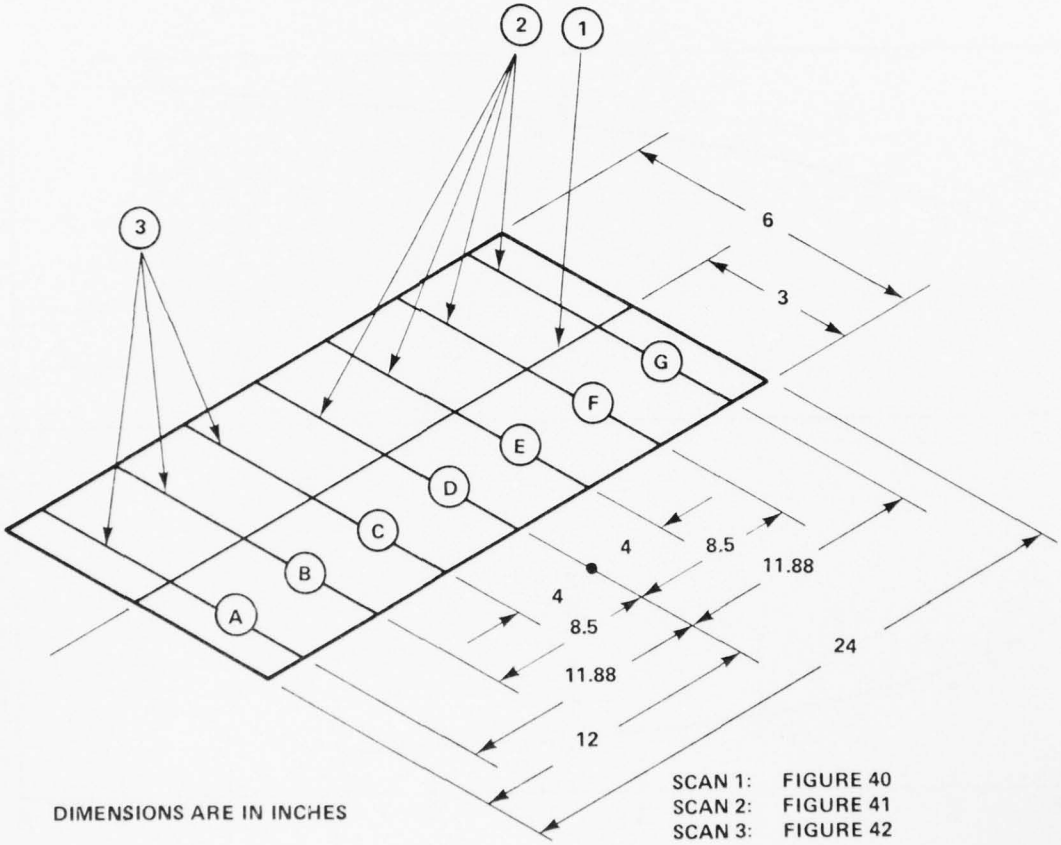


Figure 39. Key to current density profiles of Figures 40 through 42.

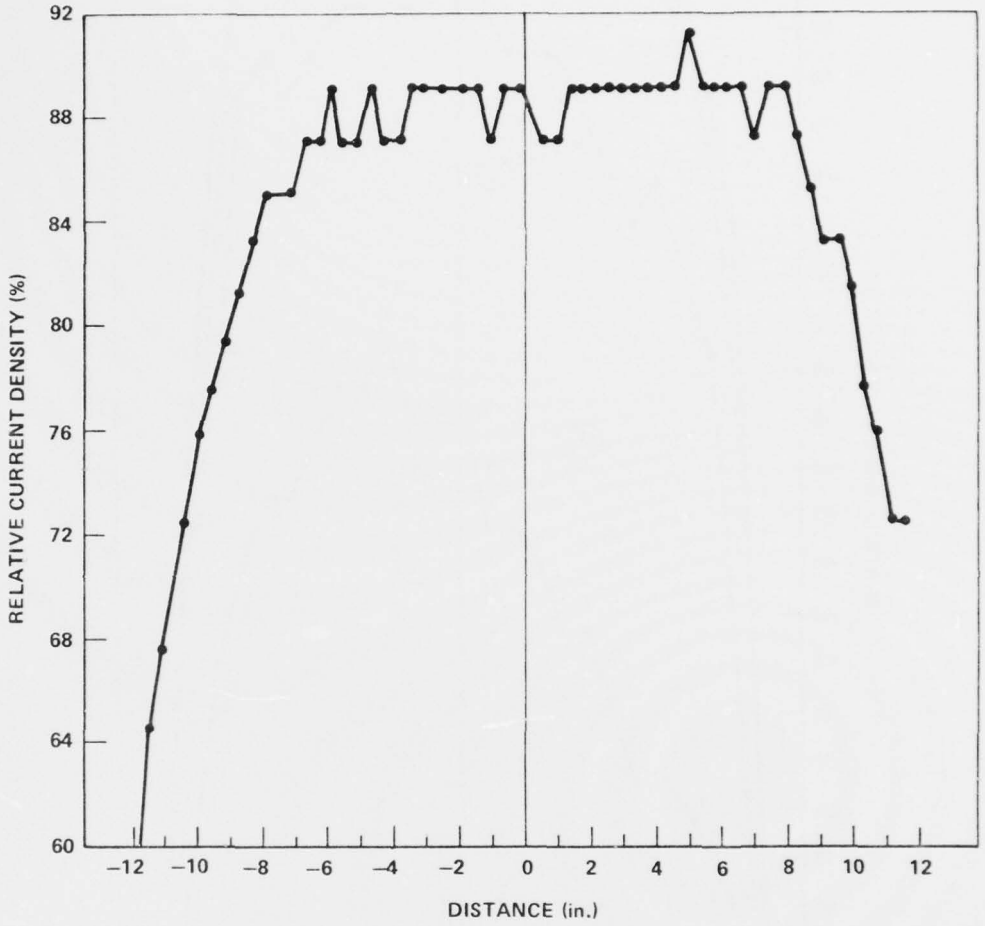


Figure 40. Time integrated current density profile (longitudinal), configuration 10-N-3.8 (key to profile shown in Figure 39).

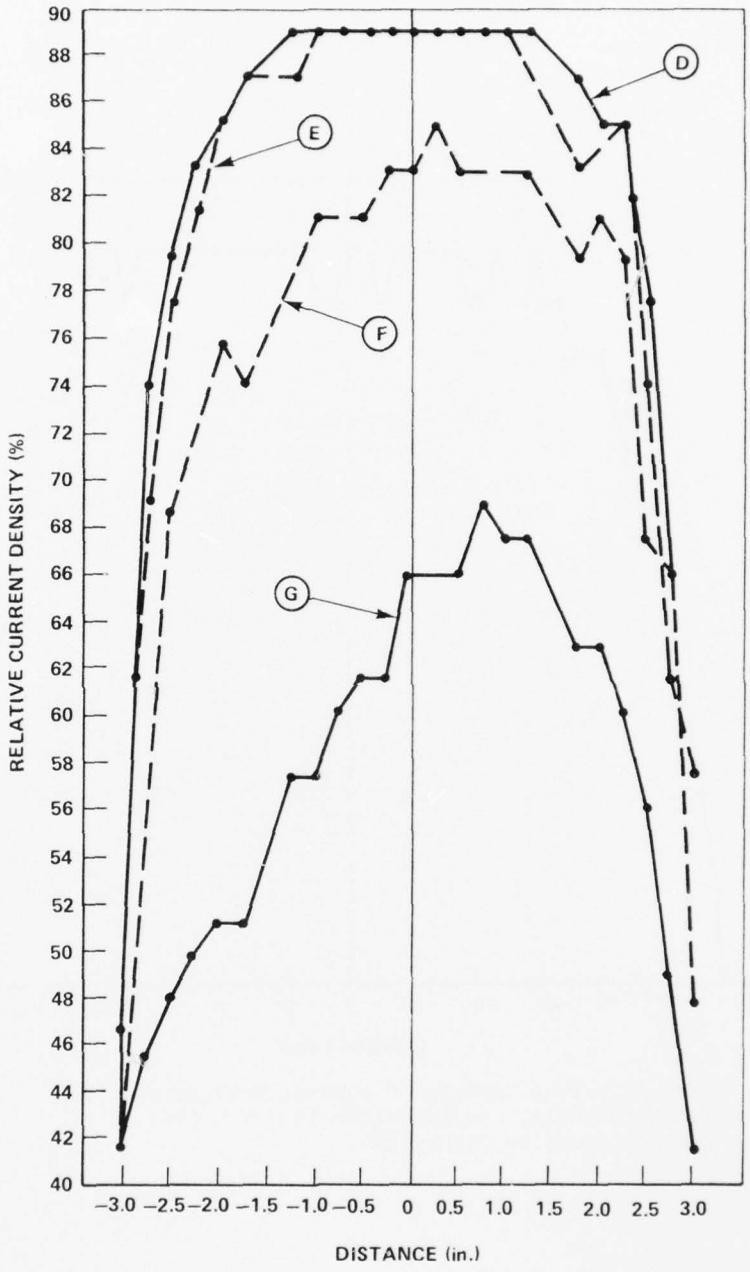


Figure 31. Time integrated current density profiles (transverse), configuration 10-N-3.8, (key to profiles shown in Figure 39).

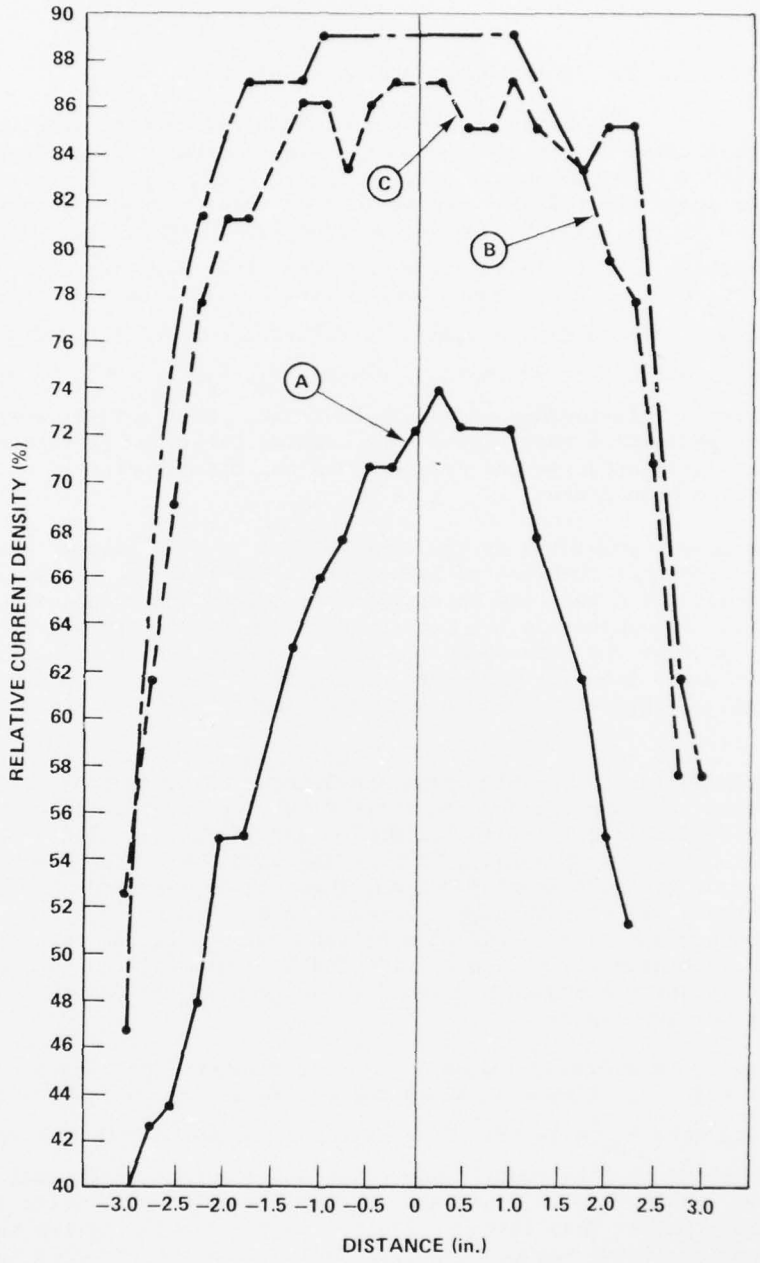


Figure 42. Time integrated current density profiles (transverse), configuration 10-N-3.8, (key to profiles shown in Figure 39).

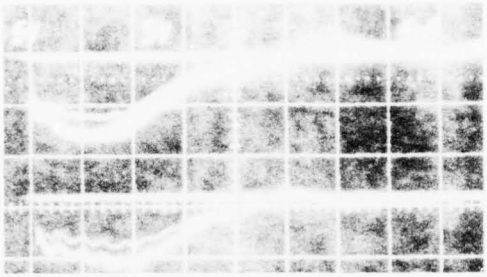
2. Pulse Shape and Beam Current

Study of the pulse shape and current density has been complicated by the problem of the "lost current" first discussed in Section V B2. When configuration 10-N-0 (opaque grid) was installed to investigate the relationship between cathode current and current collected by the grid, V_K was varied from 140 kV to 260 kV and R_G from approximately 1 kΩ to 10 kΩ. For each case the "lost current" was calculated $I_3 \equiv I_K - I_G$ and was found to vary widely from 4 A to 18 A. An attempt was made to find a simple correlation between I_3 and any of the other gun voltages or currents, including V_G, V_K, $V_K - V_G$, I_K and I_G, but a simple relationship could not be found. From this it was inferred that the phenomenon must depend on a complex relationship between the electric field strength and gradient and the distribution of plasma in the grid-cathode space.

Because suppression of the lost current was of interest here rather than developing a complicated means for calculating it, the foil dosimeter measurements were made and focus electrodes were installed with the objective of suppressing the lost current component. It was thought that by placing the focus electrodes in positions which blocked line-of-sight paths from the grid-cathode region to the upper half of the gun chamber, currents would be prevented from flowing in those directions.

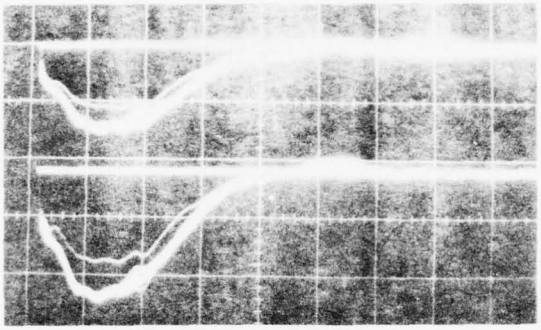
Considering the problem from the standpoint of equipotential distributions, it is preferable to enclose the cathode totally within the grid to eliminate all possibilities for any current to flow directly from the cathode to ground. This was impossible with the feedthrough geometry of the experimental system; the cathode feedthrough and grid feedthroughs all came through the top of the chamber. A system with the feedthroughs at the ends of a cylindrical gun is far more easily adapted to a geometry with the grid totally enclosing the cathode. The conceptual gun design presented in Section VI follows the end-fed cylindrical gun approach.

Figure 18 showed the waveforms obtained with configuration 10-2-3.8 and V_{dc} = 10 kV. Figure 43 shows the waveforms for the same electrode structure when V_{dc} = 14 kV. Each of these waveforms (Figures 44 through 48) and others in this report show consecutive pulses which fall within a narrow amplitude-time band, and usually one pulse of similar shape but lower amplitude. This latter pulse is the first pulse in the burst; it has lower amplitude because the first pulse from the PFN does not have the full ring-up voltage if the PFN has been in a fully charged condition for some time prior to firing the burst.



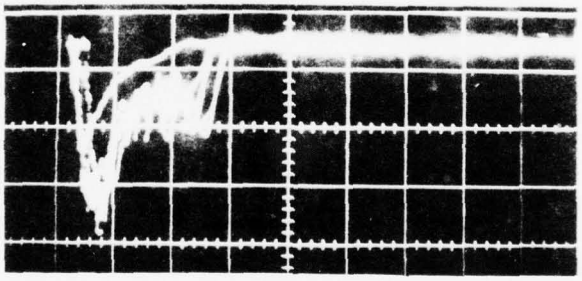
V_k: 136 kV/DIVISION

I_k: 100 A/DIVISION



V_G: 120 kV/DIVISION

I_G: 40 A/DIVISION



I_{coll}: 2.4 A/DIVISION

Figure 43. Gun waveforms, configuration 10-2-3.8, V_{dc} = 14 kV, R_G = 1940 ohms, 50 pps, 7 pulses, 5 μsec/division.

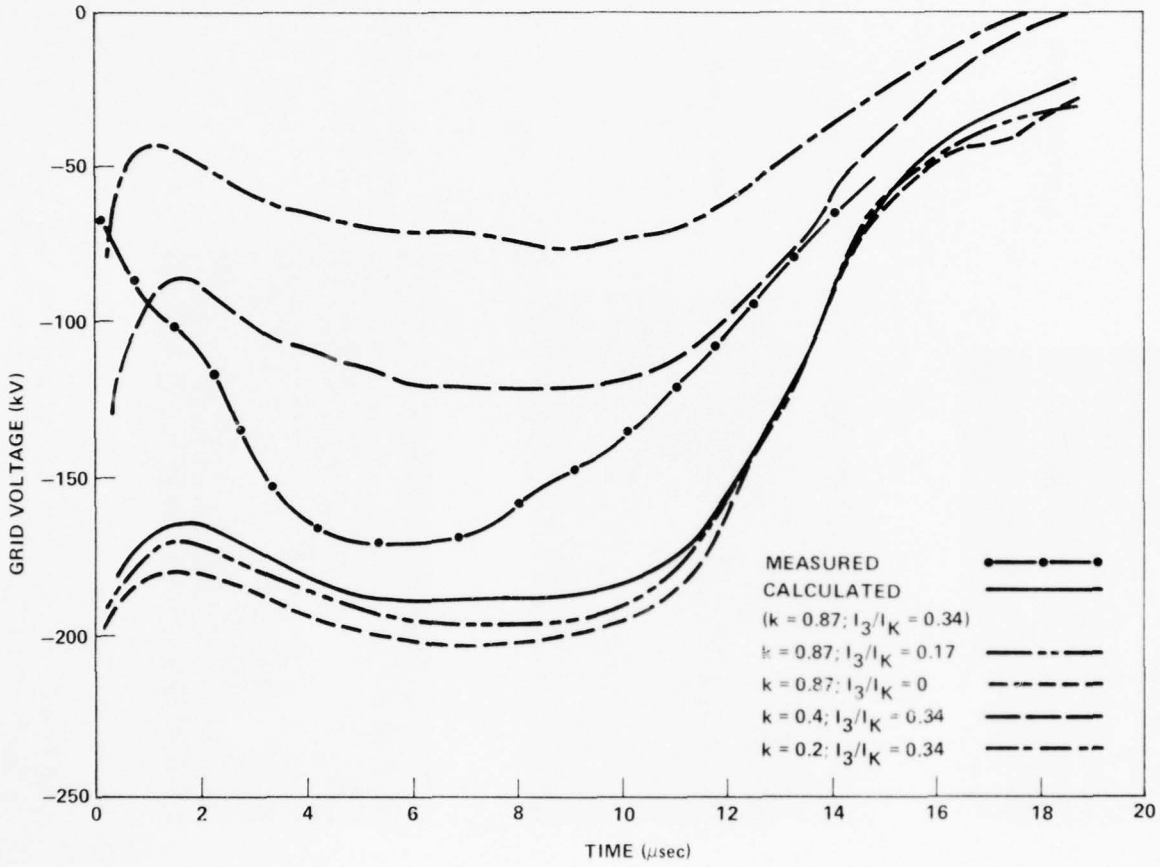


Figure 44. Measured, calculated, and extrapolated grid voltage from waveforms of Figure 43.

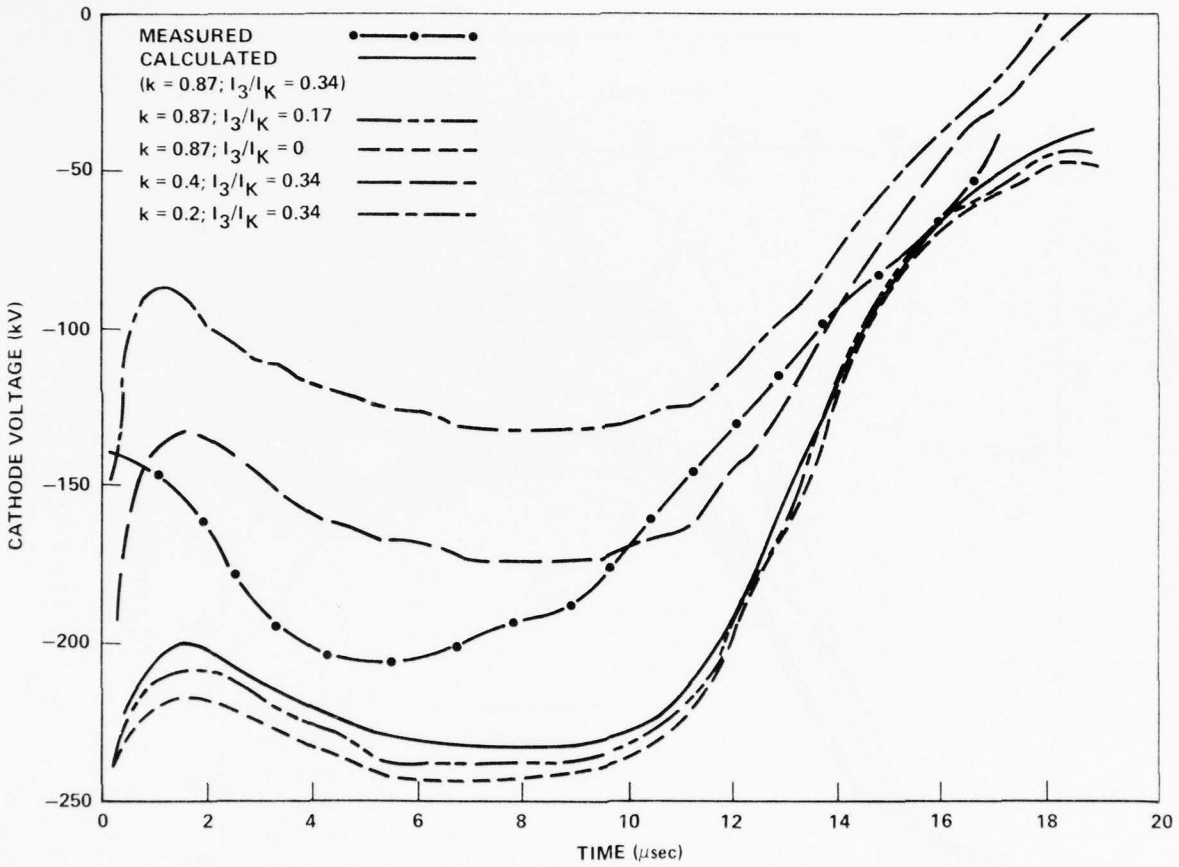


Figure 45. Measured, calculated, and extrapolated cathode voltage from waveforms of Figure 43.

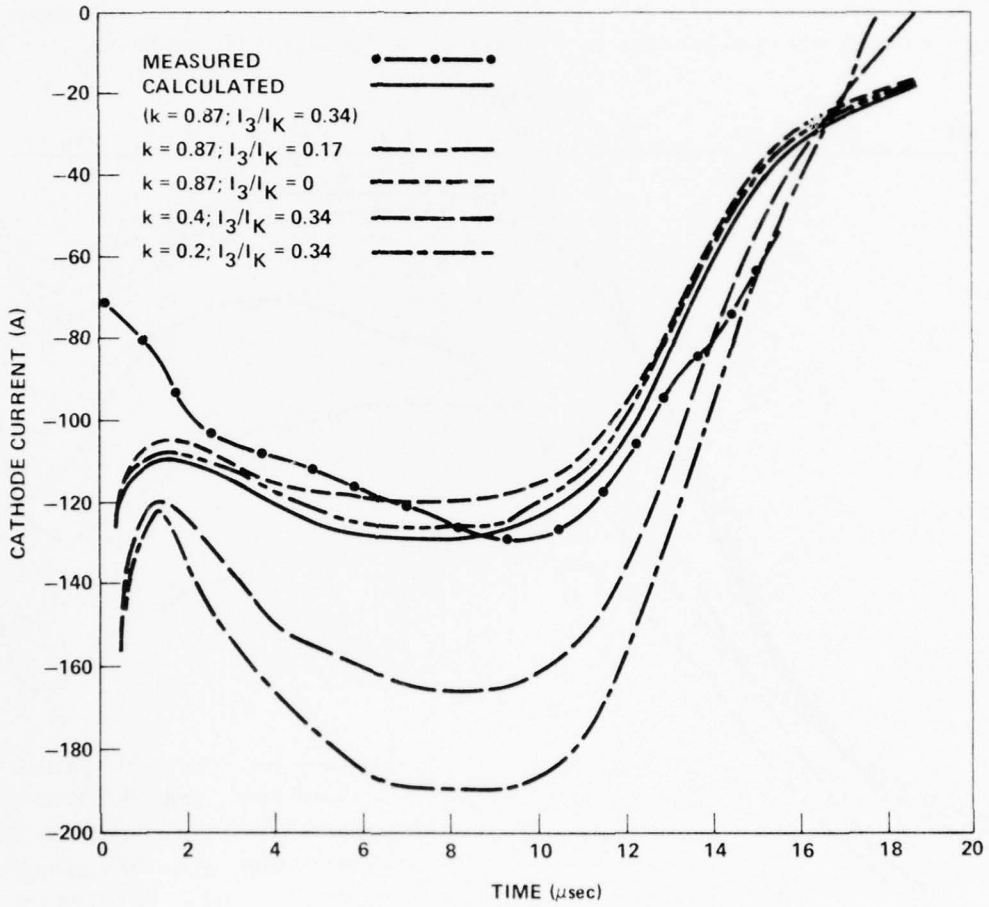


Figure 46. Measured, calculated, and extrapolated cathode current from waveforms of Figure 43.

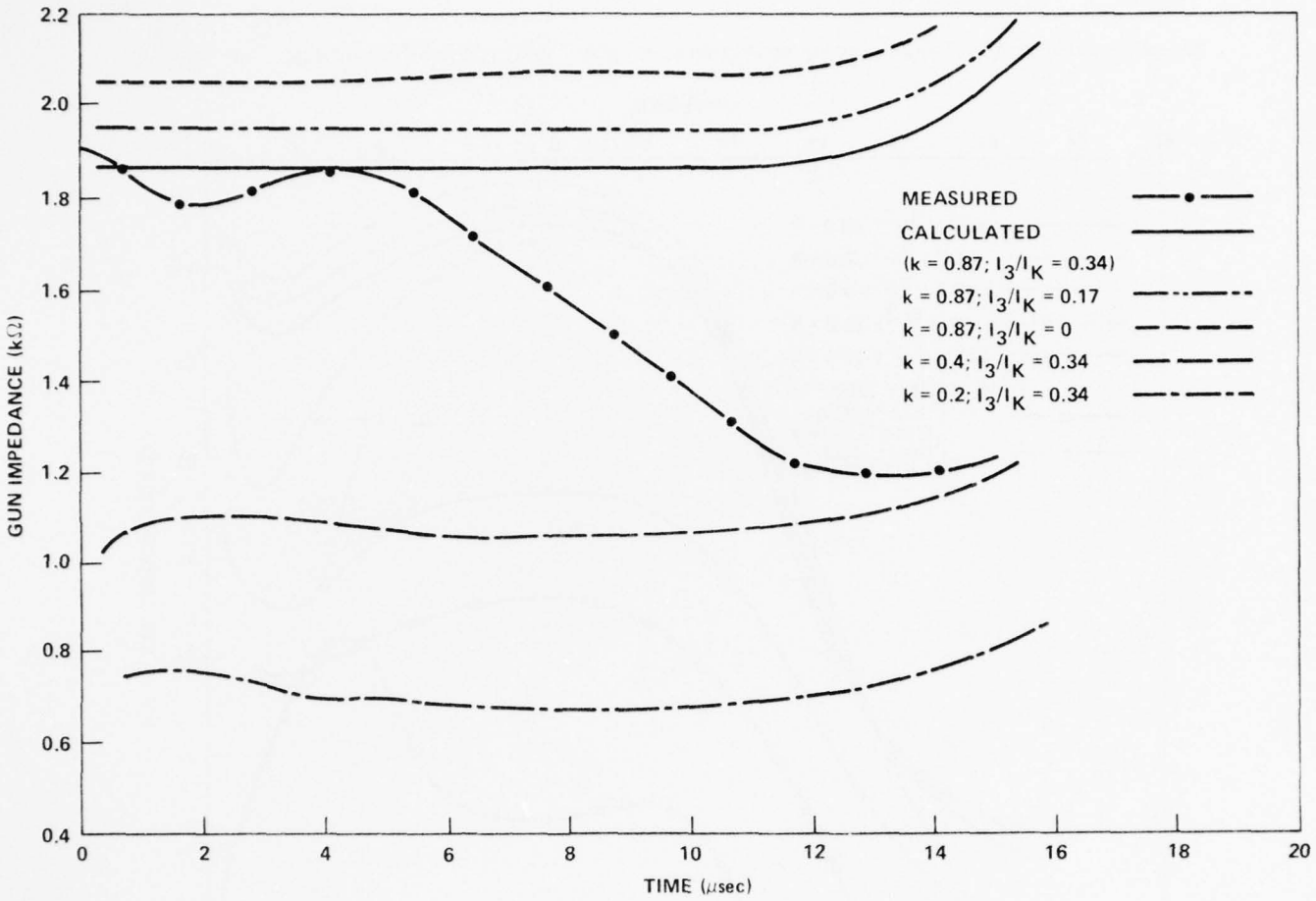


Figure 47. Measured, calculated, and extrapolated gun impedance from waveforms of Figure 43.

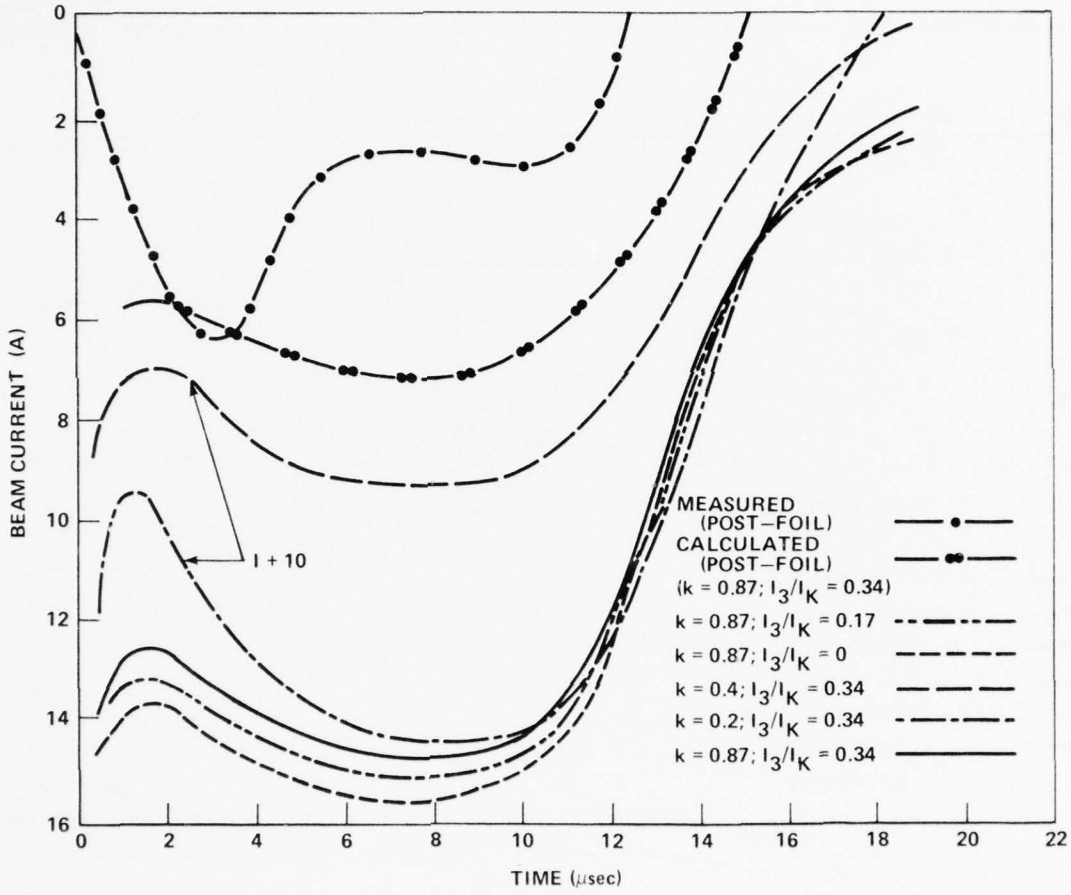
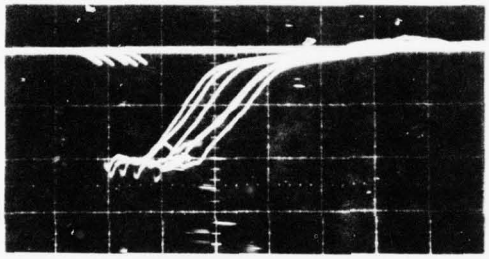


Figure 48. Measured, calculated, and extrapolated beam current from waveforms of Figure 43.

Pulse shape reproducibility of the gun waveforms is generally very good; however, large variations appear in the transmitted current pulse. Most waveforms shown in the report were obtained by internally triggering the oscilloscope from either the V_K or I_K signal, and using a gate output from the V_K, I_K oscilloscope to trigger the other oscilloscopes. This method provided time synchronization of the waveforms within each set, referenced to the pulse zero, but it gives no information regarding jitter.

To measure pulse jitter, the oscilloscopes are triggered by a pulse coincident with the output pulse from the low-level pulse generator used to generate the pulse train. Figure 49 shows a V_K waveform for a six-pulse burst referenced to the signal generator output. It shows that the typical total jitter for this system was approximately ±2.5 μsec. This jitter can undoubtedly be greatly reduced by better triggering of the PFN ignitrons, or by replacing them with thyratrons. However, jitter was not of concern in the present program.



V_k: 54 kV/DIVISION

5 μsec/DIVISION

Figure 49. Cathode voltage waveforms, pulse jitter measurement, V_{dc} 7 kV, R_G = 2 kΩ, 50 pps, 6 pulses.

The waveforms of Figure 18 are compared to the calculated values in Figures 19 through 23. The calculated and measured waveforms of V_K, V_G, and I_K agree reasonably well in amplitude and shape, except for $t \lesssim 2$ μsec, although V_K and V_G are as much as ≈20% lower than the calculated value at times during the first 10 μsec. The generally rounded (as opposed to square) shape results from the particular combination of PFN, pulse transformer, stray impedances, and gun impedance.

There is not an optimum match between the line pulser and gun impedance because both the pulser and gun were constructed by modifying existing components of the S-Cubed Repetitive Pulse Facility. In Section VI an identical equivalent circuit approach is used to calculate the response of a system which has been designed with a better impedance match, it will be seen that the waveforms are much closer to the ideal square pulse.

The calculated waveforms for V_K, I_K, and V_G all indicate initial peaks which are not seen on the measured waveforms; the largest discrepancy between calculated and measured waveforms occurs for $t \lesssim 2$ μsec and is due to this peak. It is believed that the voltage and current monitors correctly measure the waveforms. All of the monitors demonstrated risetimes of 100 nsec or less during repeated in-situ calibrations. The likely explanation for the differences in the initial portion of calculated andmeasured waveforms is that the equivalent circuit model does not include the stray capacitances and inductances which are important for the early-time response of the gun.

There is stray capacitance from grid to cathode, grid to ground, and cathode to ground, as well as inductance due to circuit connections and feedthroughs. When the voltage pulse appears at the cathode, the grid-cathode capacitance must be charged in order for the grid-cathode voltage to rise to the calculated value. Likewise, the grid-ground capacitance must be charged. It is the charging of the stray capacitances which prevents the appearance of the initial peaks.

The large initial peak of the measured post foil current is also partially due to the stray capacitance effects. The grid to cathode voltage is momentarily larger while the grid capacitances are charging, thus a much larger space-charge current can be drawn from the cathode. As the stray capacitances are charged, the grid-cathode voltage decreases and the beam current also decreases.

The interpretation of the collected current vaveform is more difficult than that of the grid and cathode waveforms. The necessity for applying a factor to account for transmission loss and collector backscatter has already been discussed. An additional factor to be considered is the divergent beam geometry of the cylindrical gun.

Reference to Figure 27 and Table 3 shows the ratio of grid-to-anode screen radii to be 1:2 and the ratio of grid radius to radial position of the window foil to be ≈1:2.8. The time-integrated foil dosimeter measurements showed the ratio of grid aperture width to post foil beam FWHM to be approximately 1:3.8. In Figure 23 the measured post foil current is compared to the current calculated by applying the window and anode screen correction factor to the calculated beam current in the gun.

The measured post foil beam current in Figures 18 and 23 varies from a peak of approximately 7 A at $t \approx 1$ μsec to a plateau value of 2.5 to 3 A for $4 \lesssim t \lesssim 10$ μsec. Taking the beam area to be 1000 cm^2 gives average current densities during the pulse ranging from 7 to 2.5 mA/cm^2. These values are related to the total current being supplied by the cathode because there is a large component of "lost current"; in the case shown in Figure 18, the "lost" current is approximately 22 A at t = 5 μsec.

Figure 43 shows waveforms similar to those of Figure 18, but for V_{dc} = 14 kV instead of 10 kV. Comparison of the waveforms in Figures 43 and 18 shows that the general features described previously apply equally well for both cases.

Figures 44 through 48 show the measured waveforms of Figure 43 and the corresponding calculated waveforms. Agreement between the measured and calculated waveforms is not as good for the V_{dc} = 14 kV case shown in Figures 44 through 48 as it is for the V_{dc} = 10 kV case of Figures 19 through 23. It seemed that in general the agreement was less satisfactory between calculated and measured cases as the voltage was increased. This might be explained by differences in the details of the cathode plasma formation and subsequent expansion. The calculated gun input impedances are almost constant for both cases; however, the measured value for Figure 18 only varies from the calculated values by approximately ±8%, whereas for Figure 43, the variation ranges from approximately 0 to -22% (at t = 10 μsec). Even the latter rather large variation is acceptable for the PFN load impedance.

In addition to the measured and calculated waveforms, Figures 44 through 48 each have four additional calculated waveforms representing different extrapolations of the measured case. Figures 50 through 54 are further calculated extrapolations.

With the extrapolations, insight was gained into how the system would have responded had suppression of the "lost current" been accomplished and how it would then respond with different values of grid transparency or grid resistance.

The solid curve labelled k = 0.87, I_3/I_K = 0.34 is the calculation corresponding to the measured data. The factor k was calculated per the discussion of Section IV B 2 by finding the ratio of grid current to cathode current less lost current, at t = 5 μsec; $k = I_G/(I_K - I_3)$. The ratio I_3/I_K indicates the fraction of total current not accounted for as grid or beam current. The curves k = 0.87, I_3/I_K = 0.7 and 0 therefore show the expected effect if the lost current, I_3, is reduced by 50% and completely eliminated.

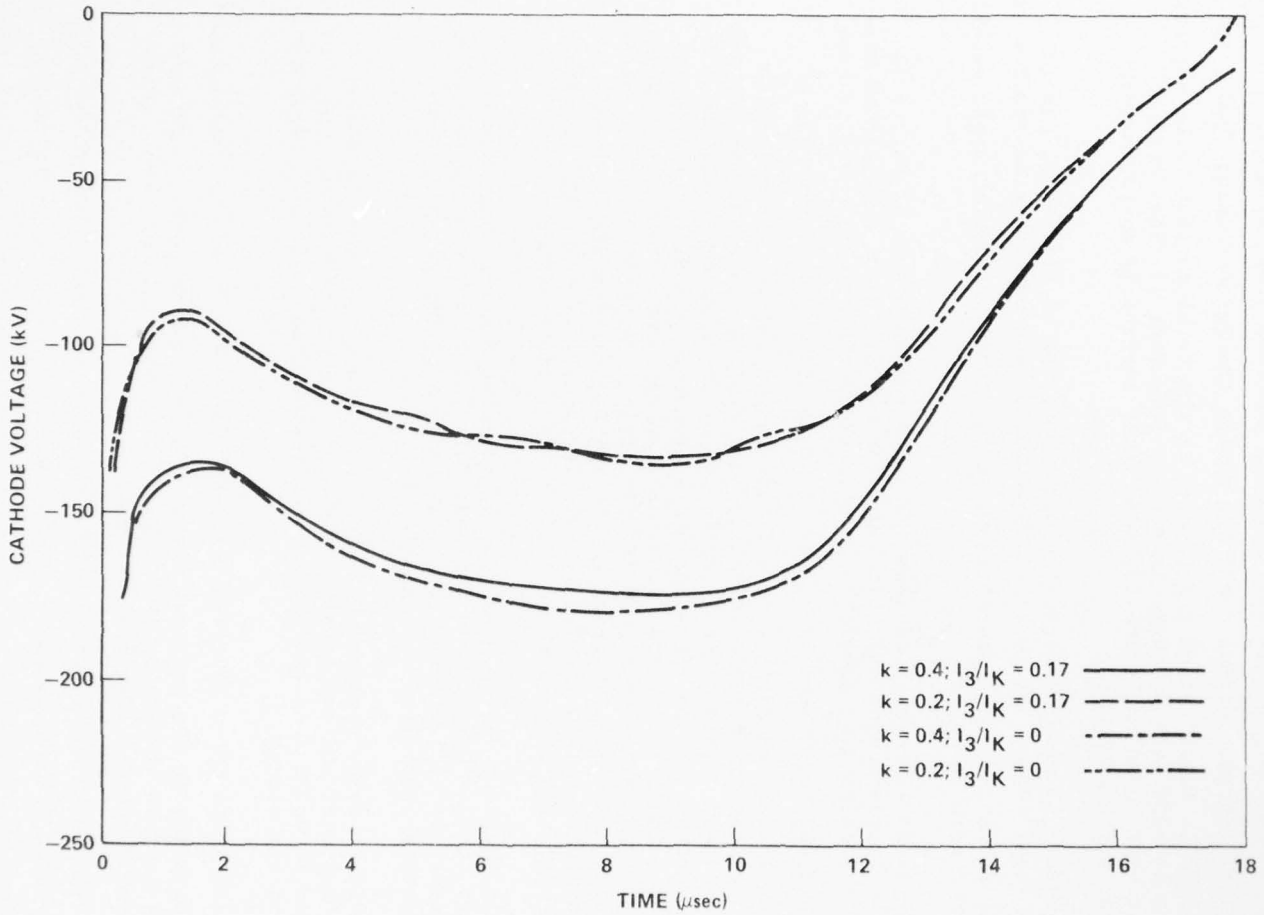


Figure 50. Extrapolated cathode voltage from waveforms of Figure 43.

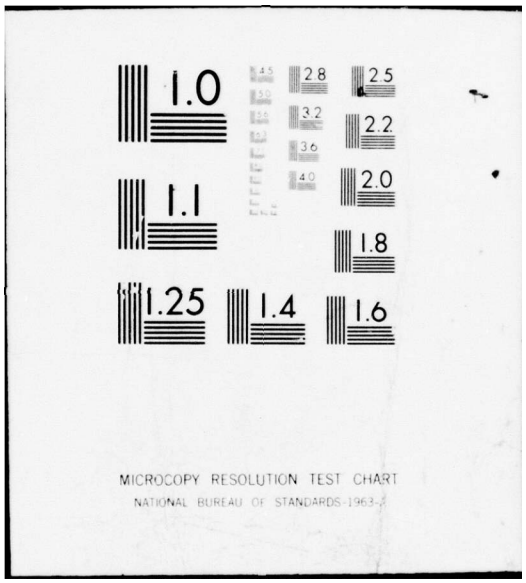
AD-A037 734 SYSTEMS SCIENCE AND SOFTWARE HAYWARD CALIF F/G 9/1
INVESTIGATION OF COUPLING OF FIELD EMISSION COLD CATHODE GUNS F--ETC(U)
FEB 77 G LODA, D A MESKAN DAAH01-74-C-0624
UNCLASSIFIED DRDMI-H-77-1 NL

2 OF 2
AD
A037 734



END

DATE
FILMED
4-77


1.0
1.1
1.25
1.4
1.6
1.8
2.0
2.2
2.5
2.8
3.2
3.6
4.0
4.5
MICROCOPY RESOLUTION TEST CHART
NATIONAL BUREAU OF STANDARDS-1963-A

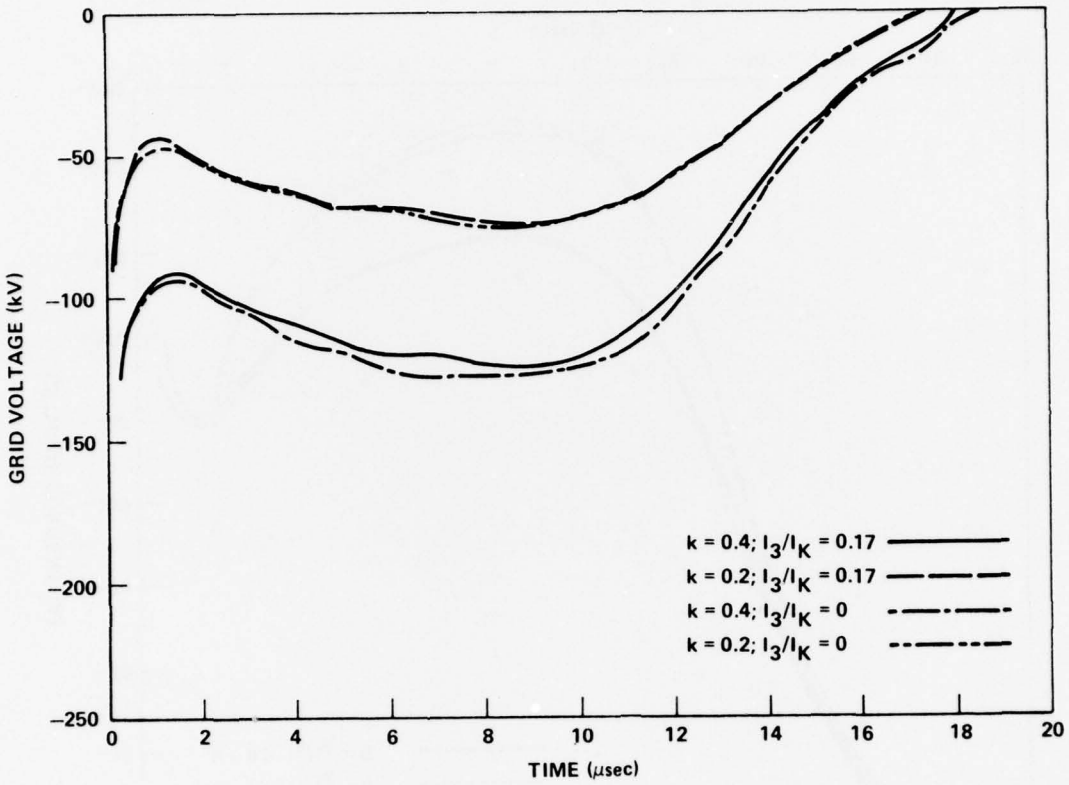


Figure 51. Extrapolated grid voltage from waveforms of Figure 43.

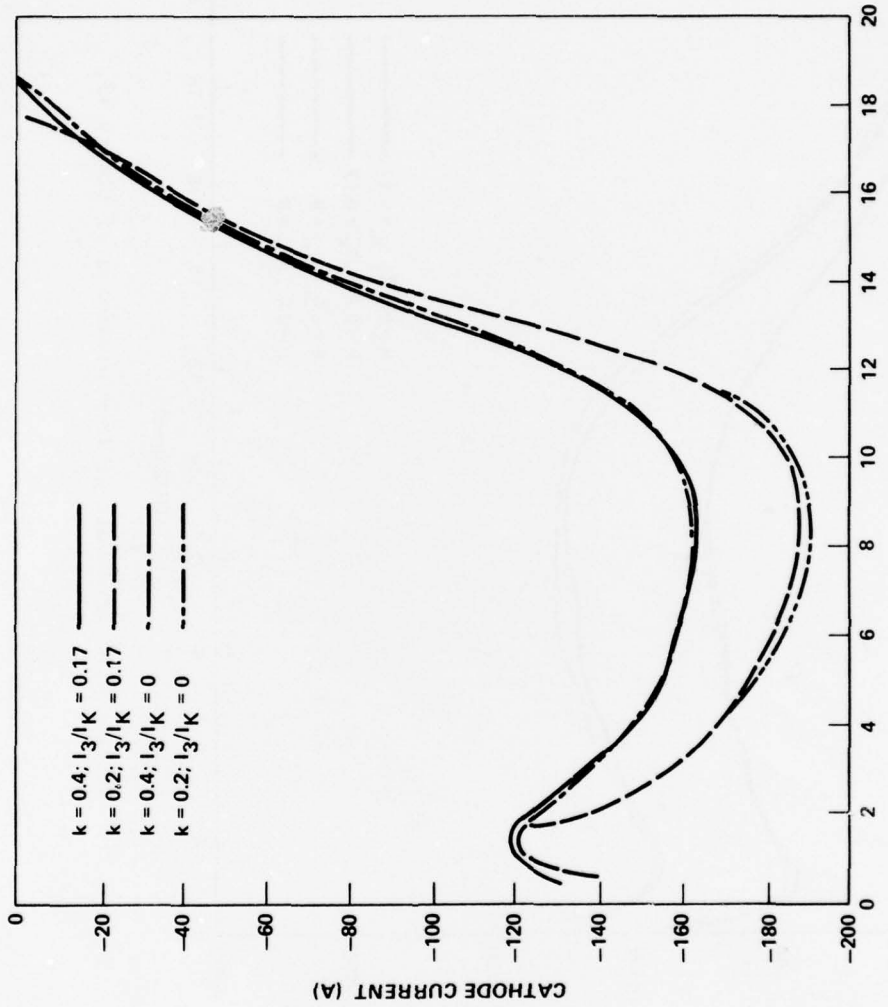


Figure 52. Extrapolated cathode current from waveforms of Figure 43.

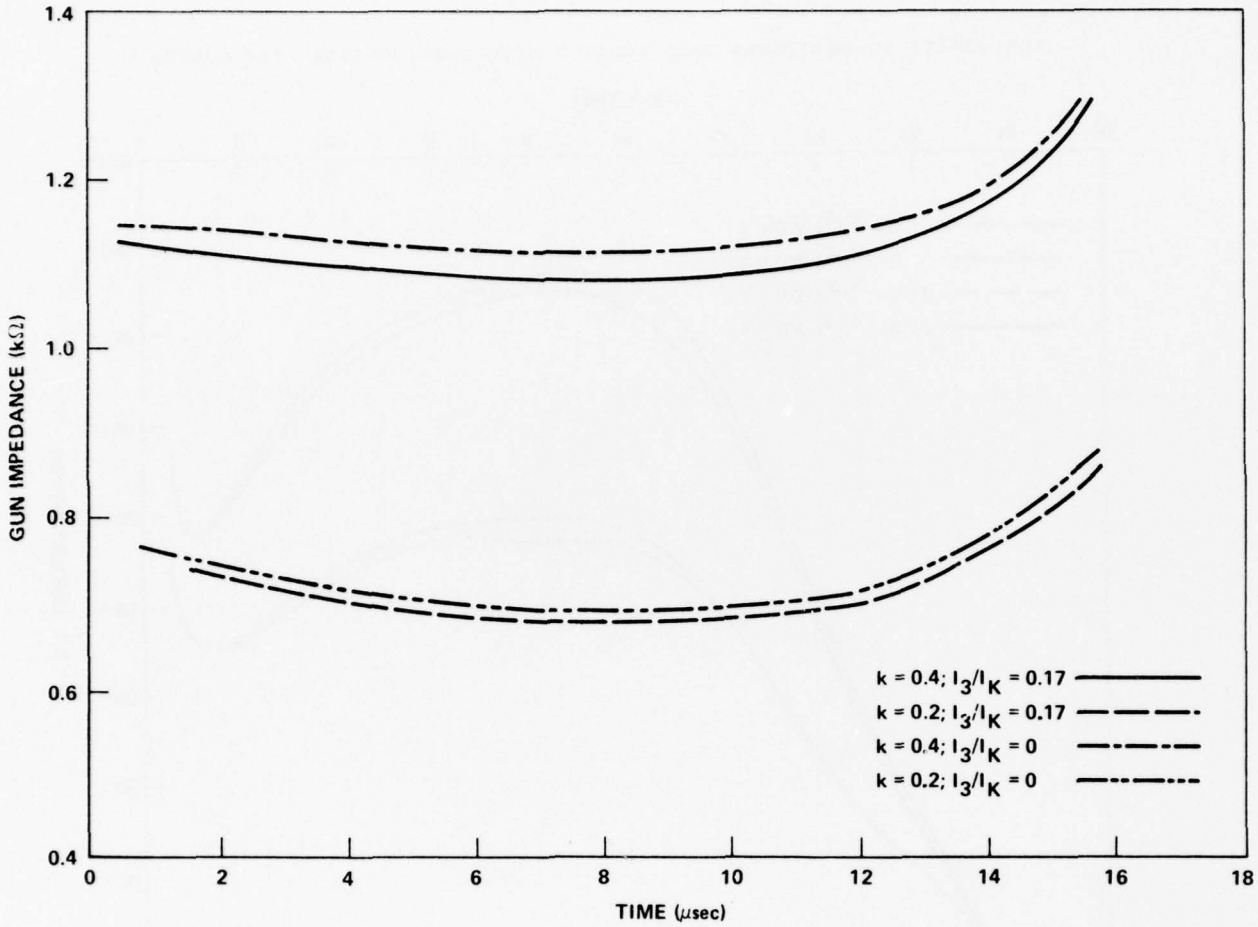


Figure 53. Extrapolated gun impedance from waveforms of Figure 43.

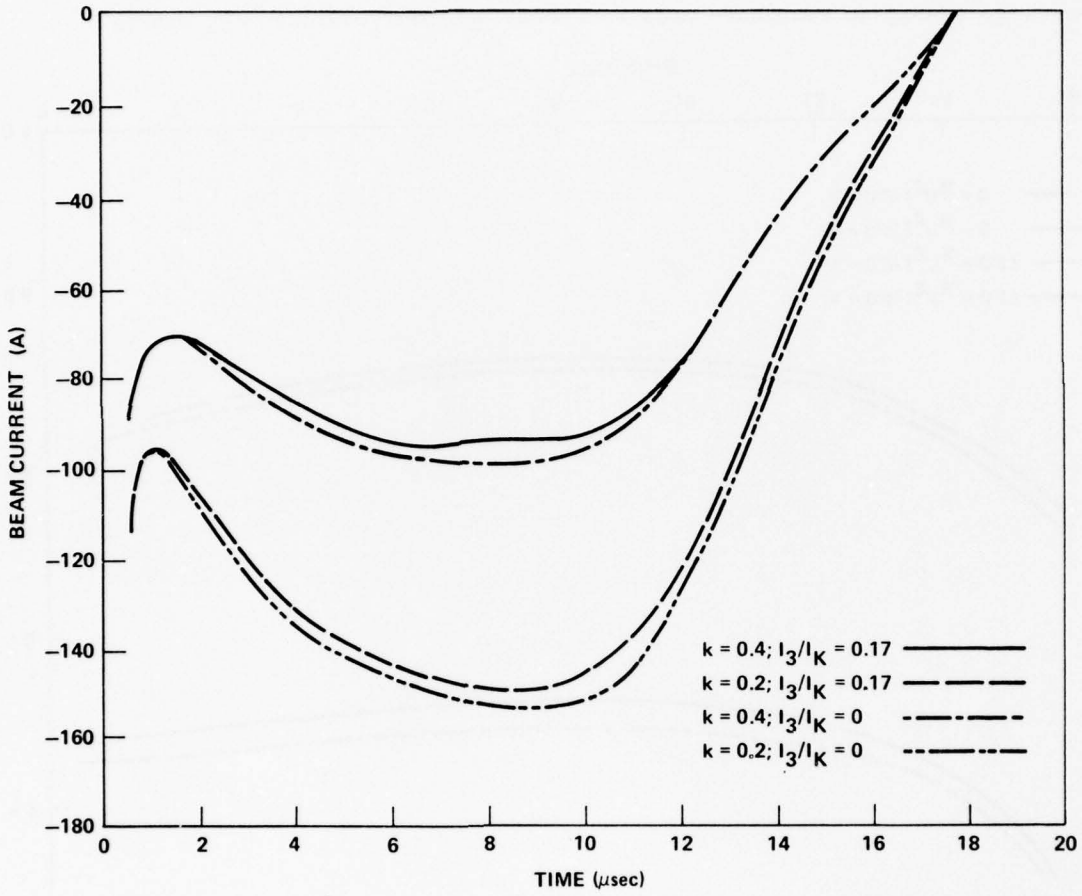


Figure 54. Extrapolated beam current from waveforms of Figure 43.

As the curves show, reduction of I_3 increases the gun's impedance, slightly increasing V_K and decreasing I_K. The increase in beam current however is less than expected, because the grid, being self-biased, also has increased voltage which limits the cathode current. The beam current remains the same fraction of the grid current.

Changing the grid resistance or changing k has far more effect on the gun response as shown by the curves for k = 0.4 and 0.2. The gun impedance decreases substantially, producing a lower cathode voltage but a much higher cathode current and beam current. The current transmitted through the window would not increase proportionally because of the lower kinetic energy of the electrons, resulting from the lower cathode voltage.

The general shape of these calculated waveforms is not significantly affected by changes in lost current or grid coupling. As the comparison of measured data with calculated waveforms showed, these calculations do not completely model the dynamics of the gun, particularly regarding the initial portions of the pulses and effects due to plasma motion.

The extrapolated waveforms of Figures 50 through 54 show the same behavior; a much stronger dependency on grid coupling than on the amount of lost current I_3. The curves for k = 0.4, $I_3/I_K = 0$ are interesting because they correspond to the circuit values which would be used for the gun in this configuration if there were no lost current and if the effective grid opacity, k, were equal to the optical opacity of the grid screen, k = 0.4. The beam current in this case is an order of magnitude greater than the beam current calculated using the measured parameters (k = 0.87, $I_3/I_K = 0.34$). The corresponding peak cathode voltage as approximately 130 kV, so the net effect on post-foil beam current would be an increase by a factor of 8. If this gun geometry were physically realized, it would be operated at a higher PFN charge voltage and probably higher R_G in order to increase the cathode voltage and improve foil transmission, and to provide a better impedance match between line pulser and gun.

VI. CONCEPTUAL DESIGN FOR A 7.5-kW BEAM POWER COLD CATHODE GUN

In this section, the design parameters are set forth for a multiple pulsed cold cathode triode system having the following parameters:

Cathode Voltage	350 kV
Current density (post-foil)	25 mA/cm^2
Pulse duration	10 μsec
Pulse repetition frequency	100 sec^{-1}
Duty	One 10-sec burst every 10 min
Beam Size	15×200 cm^2

For this conceptual design the triode geometry, grid resistor values, and the power supply design will be indicated. In addition, scaling parameters and limiting features will be described to allow design of guns operating at various other current densities, pulse lengths and voltages.

A. Conceptual Design - Triode

For a given accelerating voltage, the anode current density in a resistively biased triode gun can be adjusted by variation of any or all of the following parameters

1) Cathode-grid separation
2) Grid resistance
3) Grid opacity
4) Grid-anode separation

The dependencies of these parameters have been shown in the previous sections.

The first parameter to be considered in the design of a gun is the cathode-grid separation. There are two conditions that will determine the separation to be used. First the separation must be small enough so that with the grid at ground potential (the diode case), sufficient space-charge limited current can be drawn to satisfy the maximum current density conditions. This means

$$X_1 \leq \left[\frac{2.335 \cdot 10^{-6}(1 - k_1)(1 - k_2)V_o^{3/2}}{J} \right]^{1/2} \qquad (14)$$

where

X_1 = cathode-grid separation

V_o = cathode-grid voltage, grid voltage = 0

k_1 = grid opacity

k_2 = window structure opacity

J = output beam current density.

The second condition that must be satisfied deals with the time to spark down problem inherent in all self-ignited cold cathode guns. A description of this sparking phenomenon can be found in the Appendix. The time to spark down can be given by some characteristic velocity times time. The limits on the cathode-grid separation are defined to be

$$Vt_p < X_1 \leq \left[\frac{2.335 \cdot 10^{-6}(1 - k_1)(1 - k_2)V^{3/2}}{J} \right]^{1/2} \qquad (15)$$

where t_p is the pulse length.

As shown in Section V B of this report, the velocity v is 1.0 cm/μsec. A small safety factor of 1.2 is normally used if it is allowed by the space-charge condition in Equation (14).

For the 10-μsec, 25-mA/cm^2 pulse of the design system 12 cm was chosen as the cathode grid separation. Checking to see if it satisfied Equation (15), the following is obtained:

$$8.3 \text{ cm} < 10 \text{ cm} \leq 83.53 \text{ cm} \quad .$$

$(1 - k_1)$ and $(1 - k_2)$ were chosen as 0.83 and 0.72, respectively. The grid resistance will now be determined. The grid transparency has already been defined as $(1 - k_1)$. The grid current will be determined by this grid transparency plus any lost current to the opaque portions of the grid. Thus

$$I_G = (k_1)[I_k - k_3 I_k] + k_3 I_k$$

or

$$I_G = [(k_1)(1 - k_3) + k_3] I_k$$

where k_3 is the fraction of the cathode current striking the opaque portion of the grid. For $k_3 = 0.2$, this gives an effective k of 0.34 where k is defined as

$$I_G = kI_k \quad .$$

A graph indicating the grid resistor required for various current densities is shown in Figure 55. The output current density may now be changed by altering this resistor value without changing the gun geometry.

The grid-anode separation, X_2, must be large enough so that it does not space-charge limit the beam exiting from the grid structure. The condition is usually very easily satisfied and only requires

$$X_2 \leq \left[\frac{2.335 \cdot 10^{-6} k_2 V_{GA}^{3/2}}{J} \right]^{1/2}$$

or

$$X_2 \leq \left\{ \frac{2.335 \cdot 10^{-6} (1 - k_2) \left[V_K - \left(\frac{k}{1 - k} \right) \frac{JA}{(1 - k_2)} R_G \right]^{3/2}}{J} \right\}^{1/2}$$

where A = output beam area, and J = output beam current density. For the design condition, this gives

$$X_2 \leq 149 \text{ cm} \quad .$$

The gun has been designed in an almost reverse fashion, starting by choosing the grid cathode separation and then picking values for k_k, k_2, and k_3. The grid resistance requires a simple calculation after these parameters are chosen. Gun designs for two specific values of k_1, k_2, and k_3 will be discussed in the following paragraphs.

Considerable discussion in the previous sections was directed to the unexpected problem of abnormally high grid and anode ("lost") currents in the existing test device. These currents lead to large inefficiencies that must be controlled if an overall electron efficiency of 50% is to be achieved in the design system. The major losses in the test device occurred as a result of leakage of the cathode-anode electric field into the cathode grid space. This led not only to electrons streaming directly from the cathode to ground (and not the window aperture) but also to a distortion of the focussing field controlling the electron trajectory between the cathode and grid.

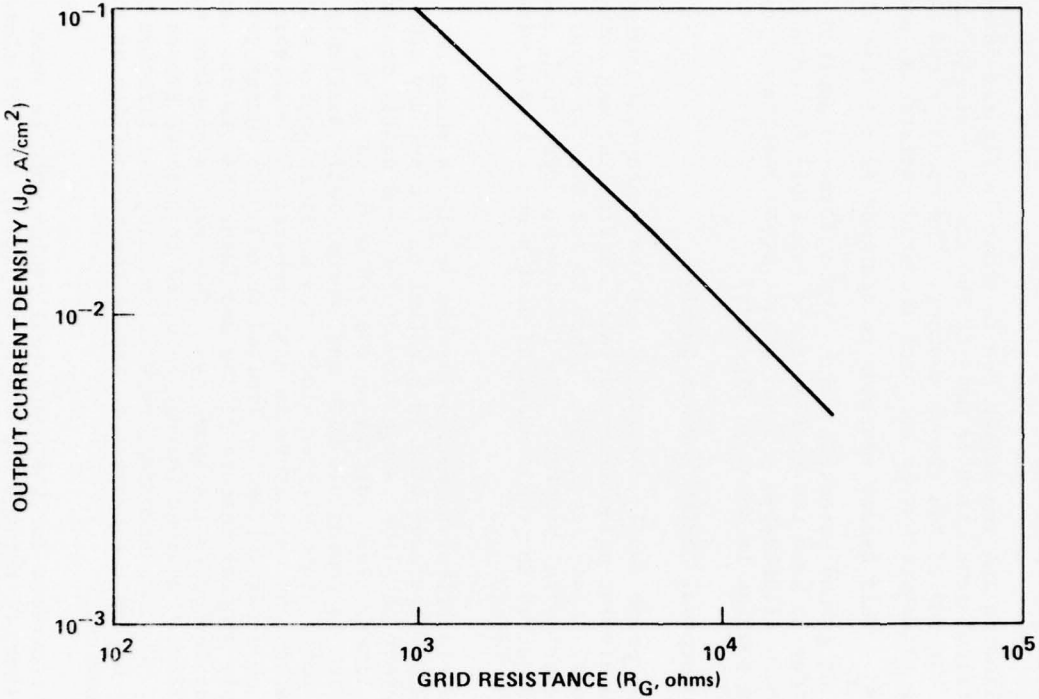


Figure 55. Output current density of the conceptual design gun as a function of grid resistance.

The solution of this problem is complete enclosure of the cathode by the grid structure. This modification to the existing gun could not be made beaause of the vacuum chamber and bushing design.

With a completely enclosed cathode design, the problem is reduced merely to a diode (cathode-grid) followed by an acceleration field. Focussing can then be achieved in the grid region in a similar fashion as that described in the Appendix.

A drawing illustrating the design gun is shown in Figures 56 and 57. The cathode electrical connection is made to the gun on a single high voltage cable at one end of the vacuum chamber. The opposite end has a similar bushing structure but it contains the grid resistor R_G and a second resistor R_F. This second resistor is designed to maintain the focus electrodes at ground potential before high voltage is applied to the cathode in order to have the maximum field available for cathode ignition. Figure 56 illustrates a longitudinal cross section of the gun; a transverse section is shown in Figure 57.

B. Conceptual Design - Power Supply

The power supply considered for the conceptual design study is a lumped element pulse line modulator driving the gun cathode through an iron core pulse transformer. This is the type of supply used throughout the experimental program. The impedance, power load, and repetition rate required for the conceptual design are all well within the limits of this technology.

A simplified electrical schematic for the supply is shown in Figure 58. Two PFNs have been used in parallel on the primary side of the pulse transformer to allow fabrication of the more easily constructed higher impedance lines. Peak voltage on the PFN would be on the order of 35 to 38 kV which is compatible with many commercially available thyratrons. The solid state clipper diode used to limit source voltage on both the thyratron and capacitors is also commercially available because its peak hold-off voltage is limited to only the charge voltage ($\approx$40 kV). The only special feature of the modulator that is not usually found in this type device is the spark gap. This gap is required to produce the very fast transient voltage required to produce proper cathode ignition. Coulomb transfer, repetition rate, and lifetime have been demonstrated during the program to insure the reliability of this pressurized gas switch.

An equivalent circuit for the conceptual design unit is shown in Figure 59. Capacitors C_1' through C_{10}' and L_1' through L_9' are PFN elements. Inductance L_{10}' is a combination of the inductance of the last PFN element and the stray inductance associated with the thyratron connection. C_{11}' and L_{11}' are the stray capacitances and inductances associated with

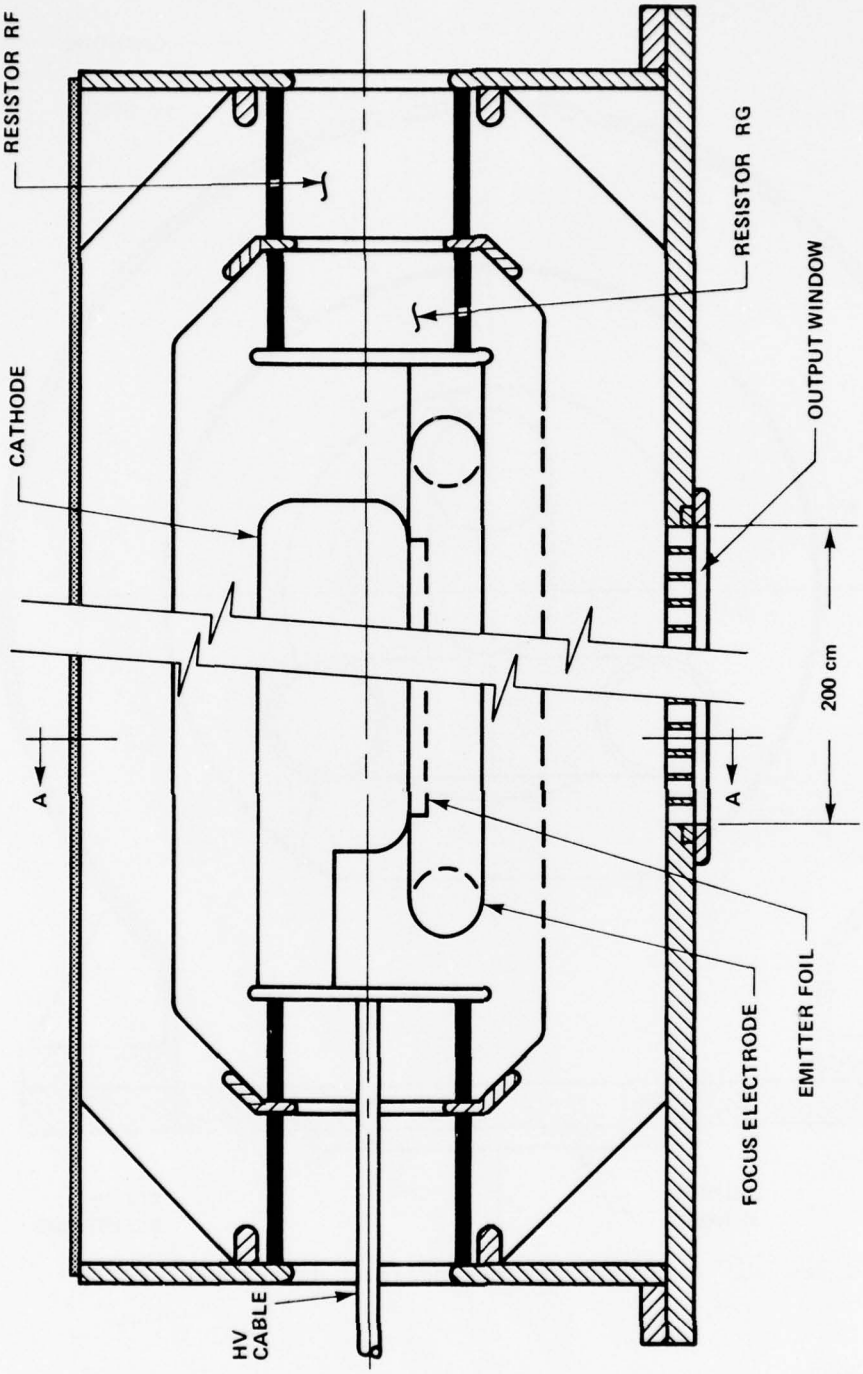


Figure 56. Triode conceptual design, cut-away view.

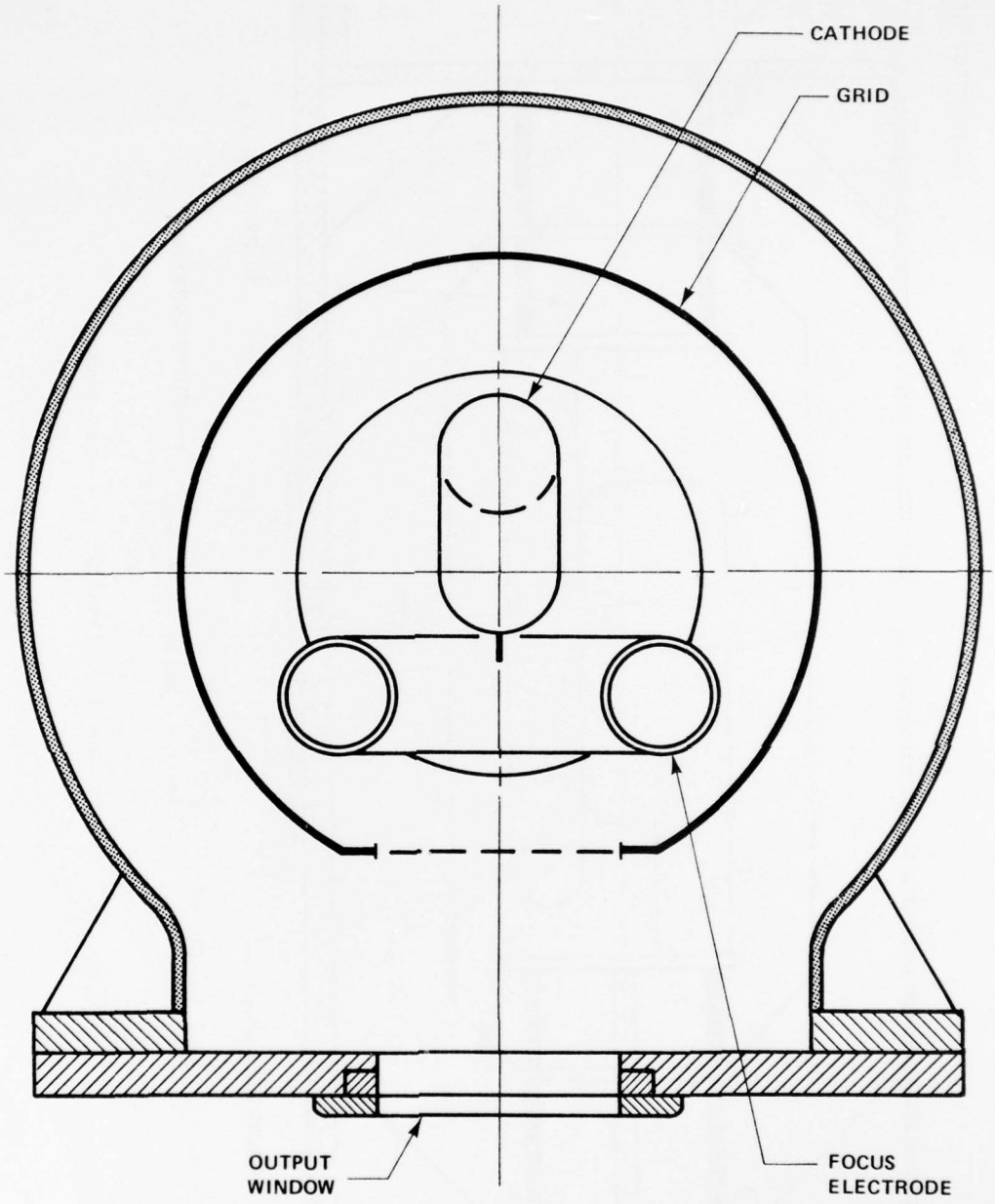


Figure 57. Cross section of conceptual design gun.

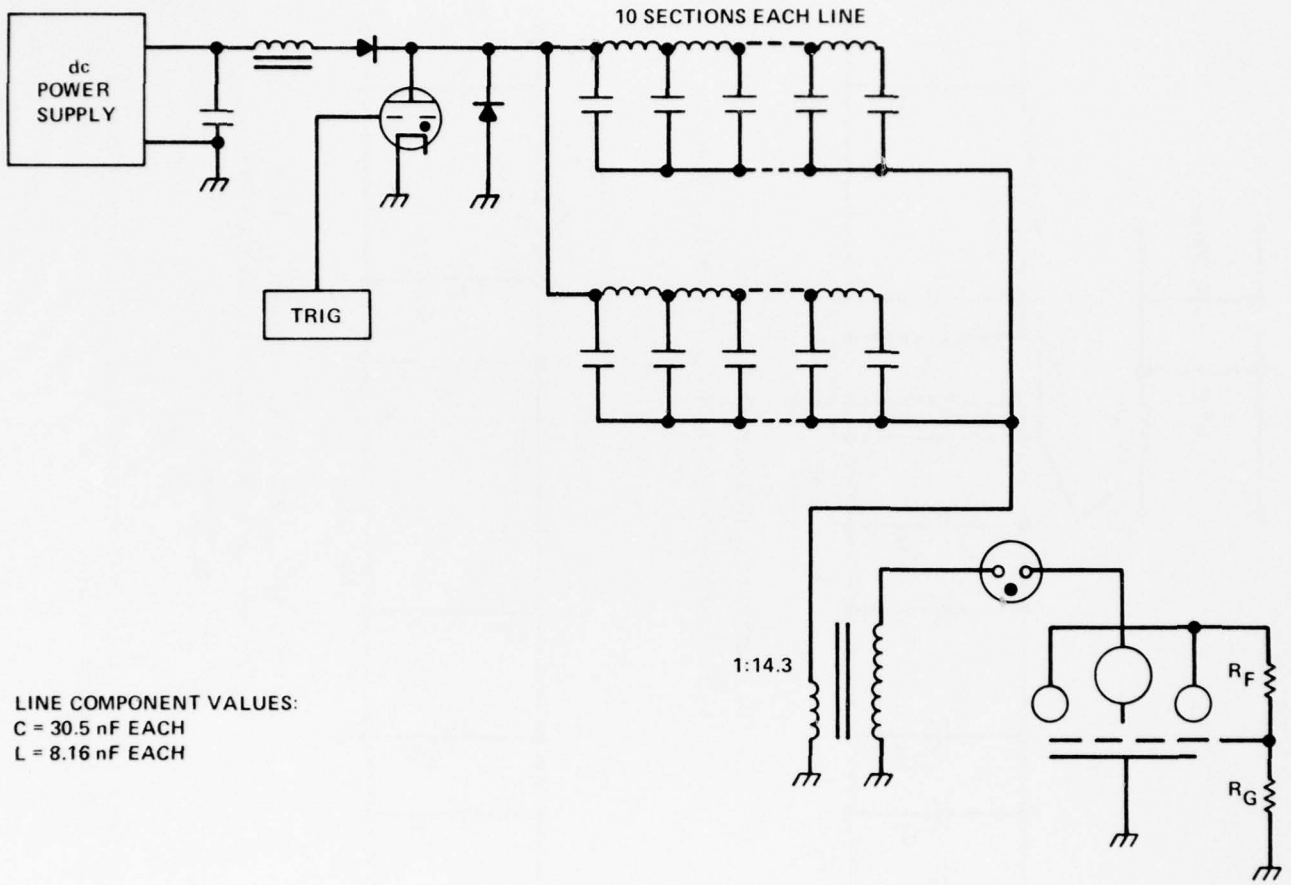
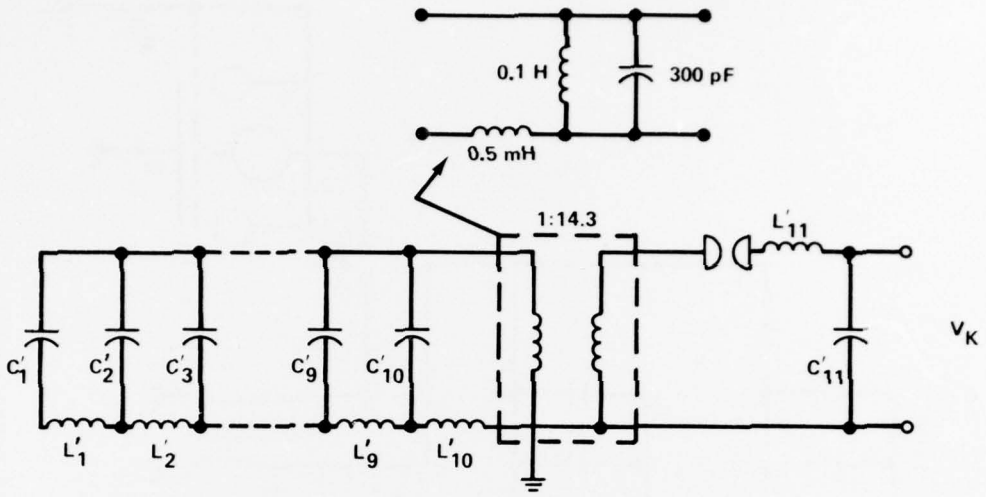


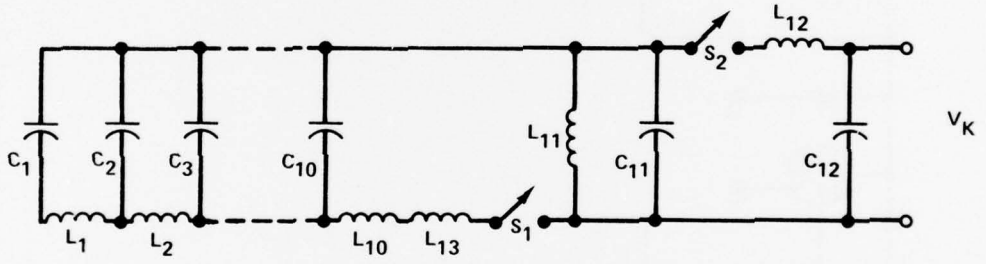
Figure 58. Conceptual design: PFN pulsed power supply.



C'_1 THROUGH C'_{10}; 61.2 nF EACH; C'_{11} = 50 pF

L'_1 THROUGH L'_9; 4.08 μH EACH; L'_{10} = 2.1 μH; L'_{11} = 5 μH

(a)



C_1 THROUGH C_{10}: 299.3 pF; C_{11} = 300 pF; C_{12} = 50 pF

L_1 THROUGH L_9: 0.834 mH; L_{10} = 0.429 mH; L_{11} = 0.1 H;

L_{12} = 5 μH; L_{13} = 0.5 mH

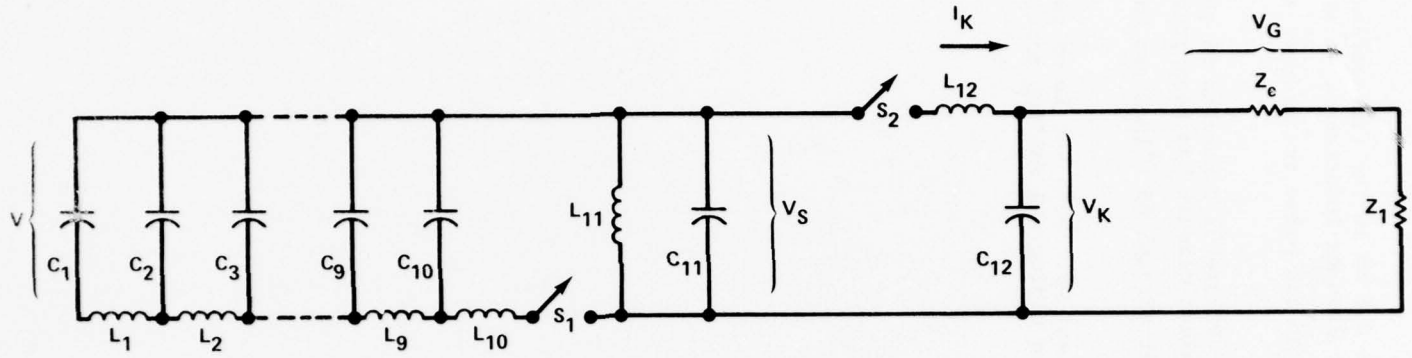
(b)

Figure 59. Conceptual design: equivalent circuit for PFN pulsed power supply.

the cabling to the electron gun. The 0.5 mH in the transformer equivalent circuit (L_{13}) is the transformer leadage inductance. A shunt capacity of 300 pF would be expected on the pulse transformer and is indicated by C_{11}.

Figure 60 illustrates the PFN of Figure 59 connected to the space-charge limited diode Z_1. This equivalent circuit has been previously explained in Section IV B. Figures 61 through 65 illustrate the waveshapes predicted by ECAP.

The pulse waveshapes are consistent with both the laser requirements and window heating caused by the rising and falling portions of the voltage.



C_1 THROUGH C_{10}, 299.3 pF; C_{11} = 300 pF; C_{12} = 50 pF

L_1 THROUGH L_9, 0.834 mH

L_{10} = 0.929 mH; L_{11} = 0.1 H; L_{12} = 5 μH

$$Z_1 = \frac{1}{K_1 V_K^{1/2}} = \frac{1}{K_1^{2/3} I_K^{1/3}} = 1072/I_K^{1/3}$$

Z_e = (0.34) (4309) = 1465 ohms

Figure 60. Conceptual design: complete equivalent circuit for pulsed power supply and triode electron gun used for ECAP calculations. All impedances referred to secondary of 1:14.3 pulse transformer.

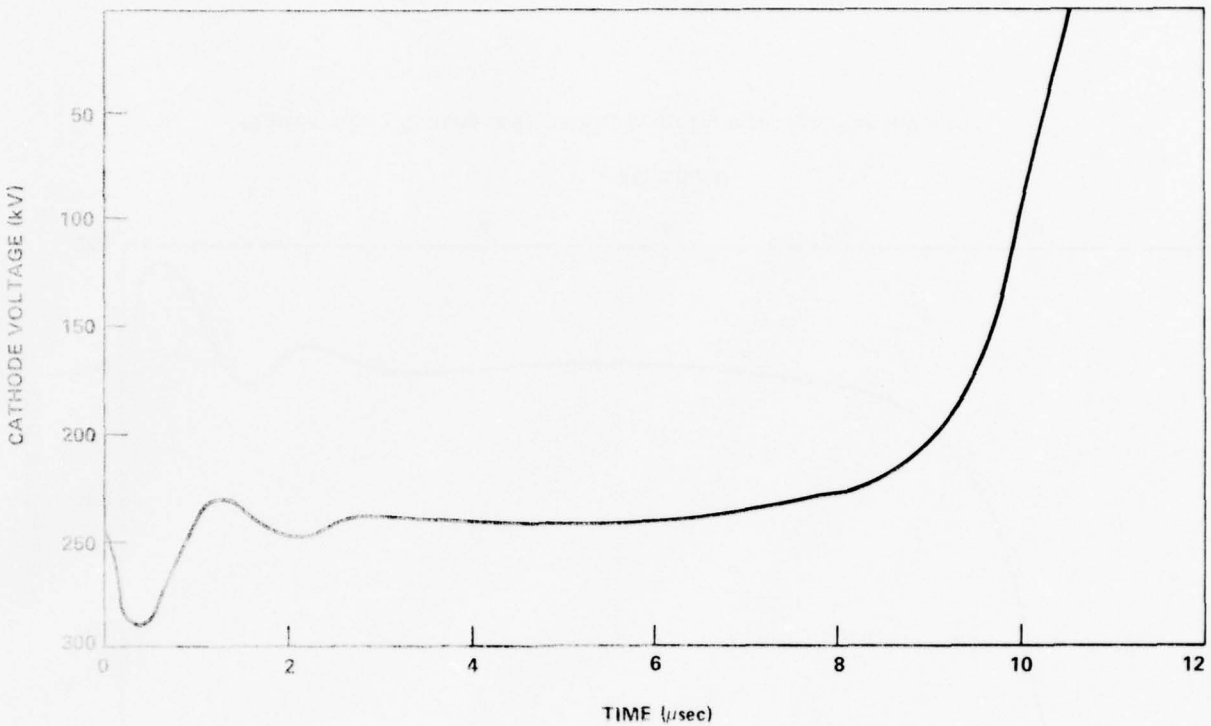


Figure 61. Conceptual design; cathode voltage versus time.

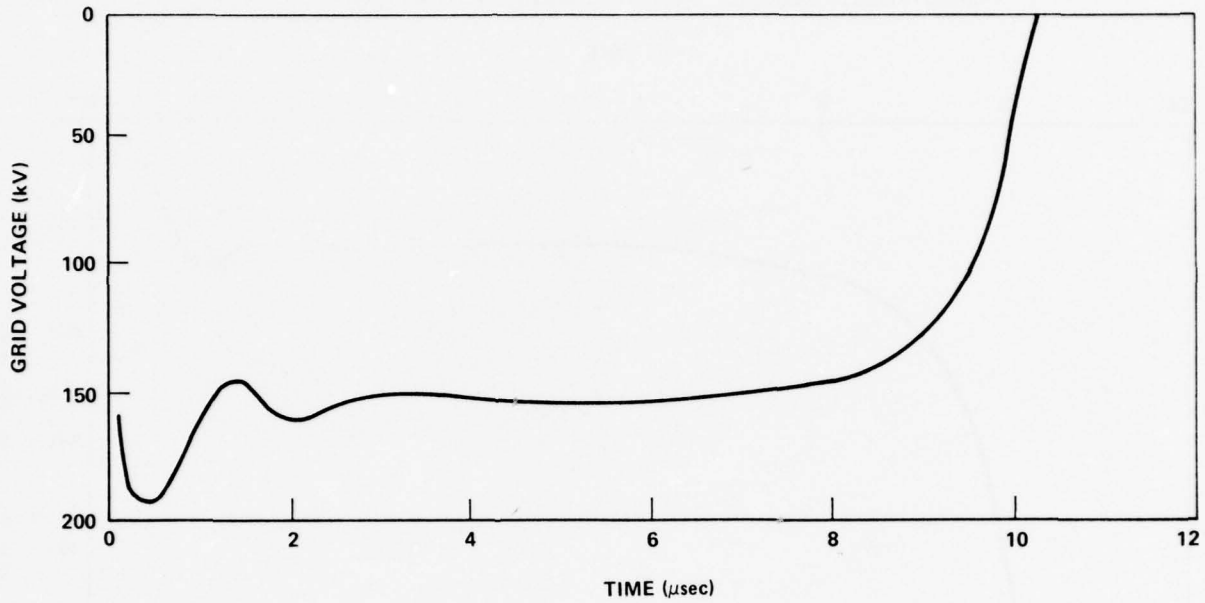


Figure 62. Conceptual design; grid voltage versus time.

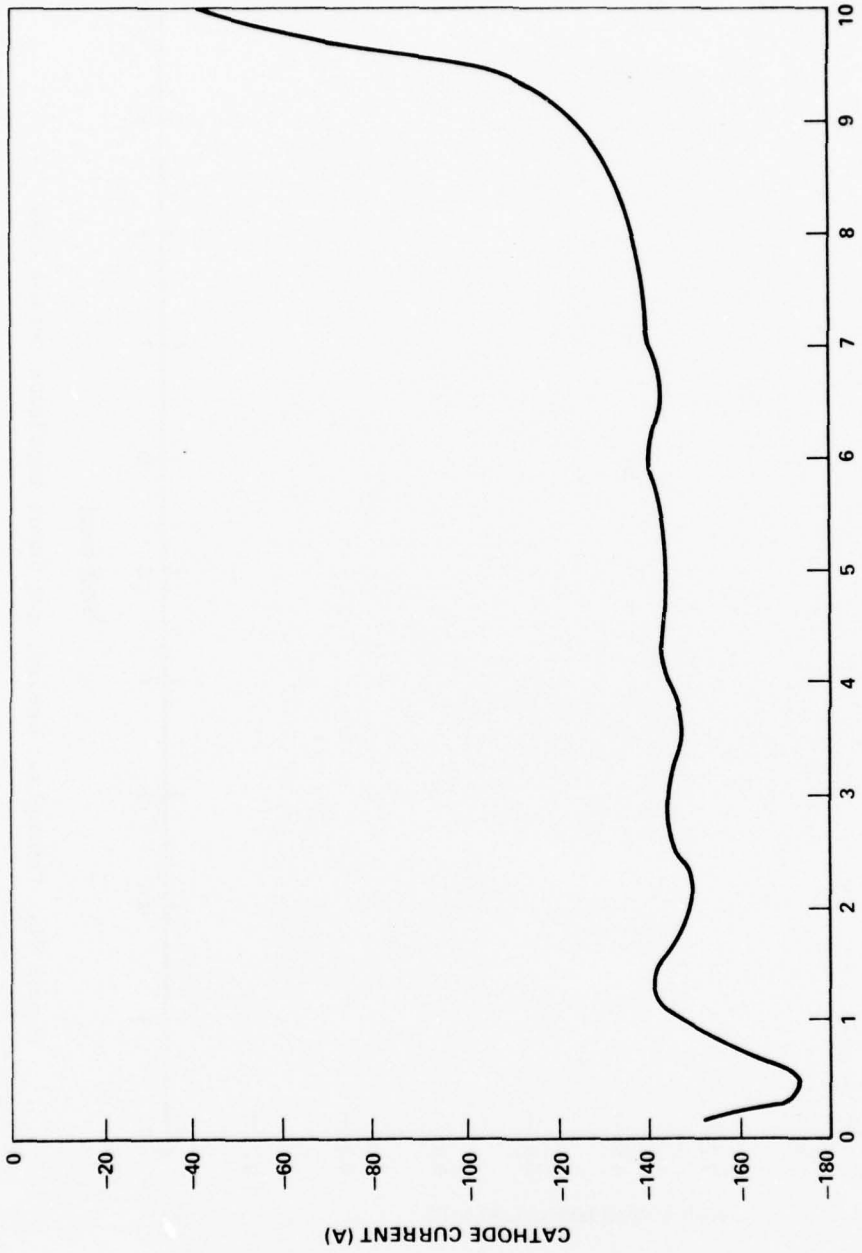


Figure 63. Conceptual design; cathode current versus time.

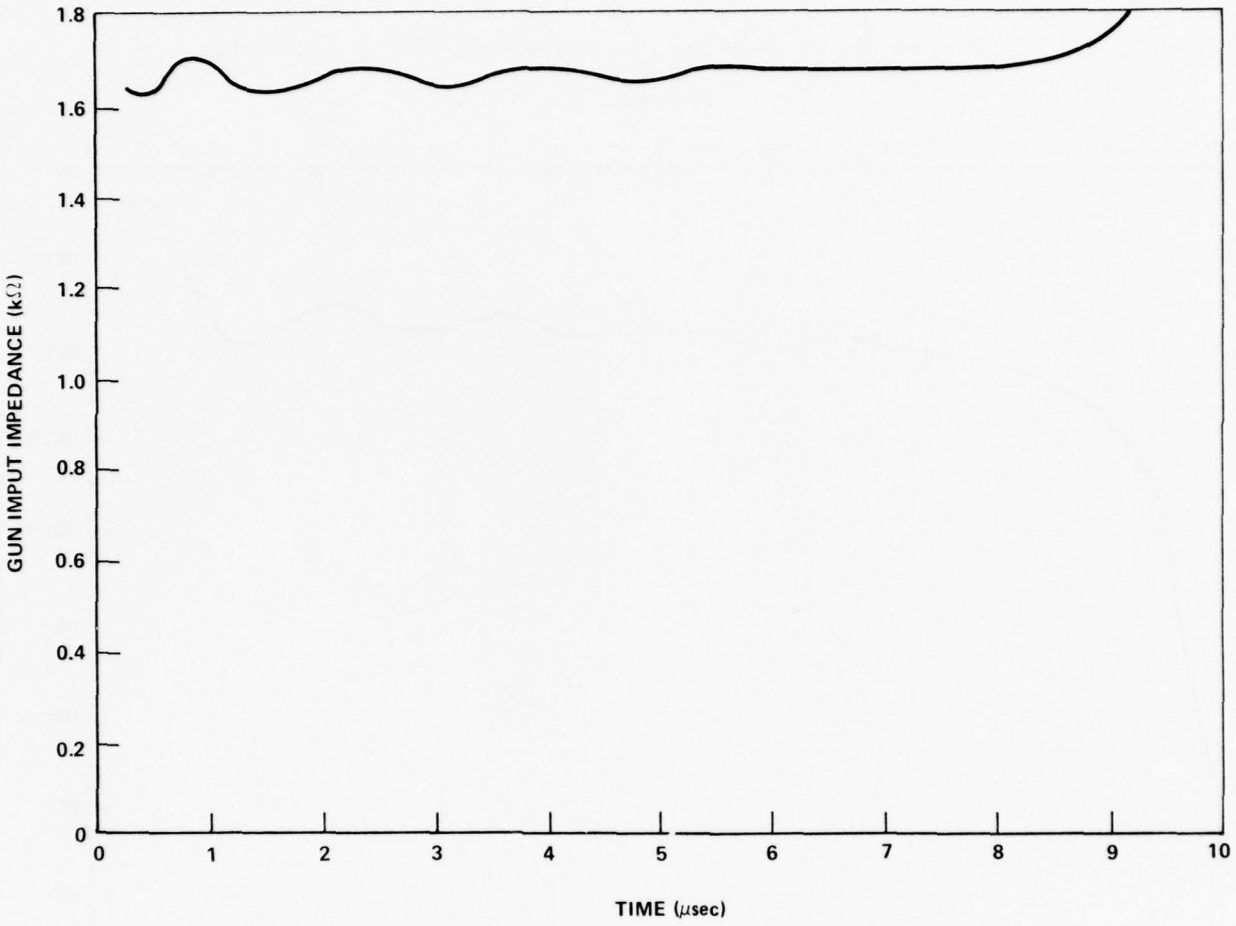


Figure 64. Conceptual design; gun input impedance versus time.

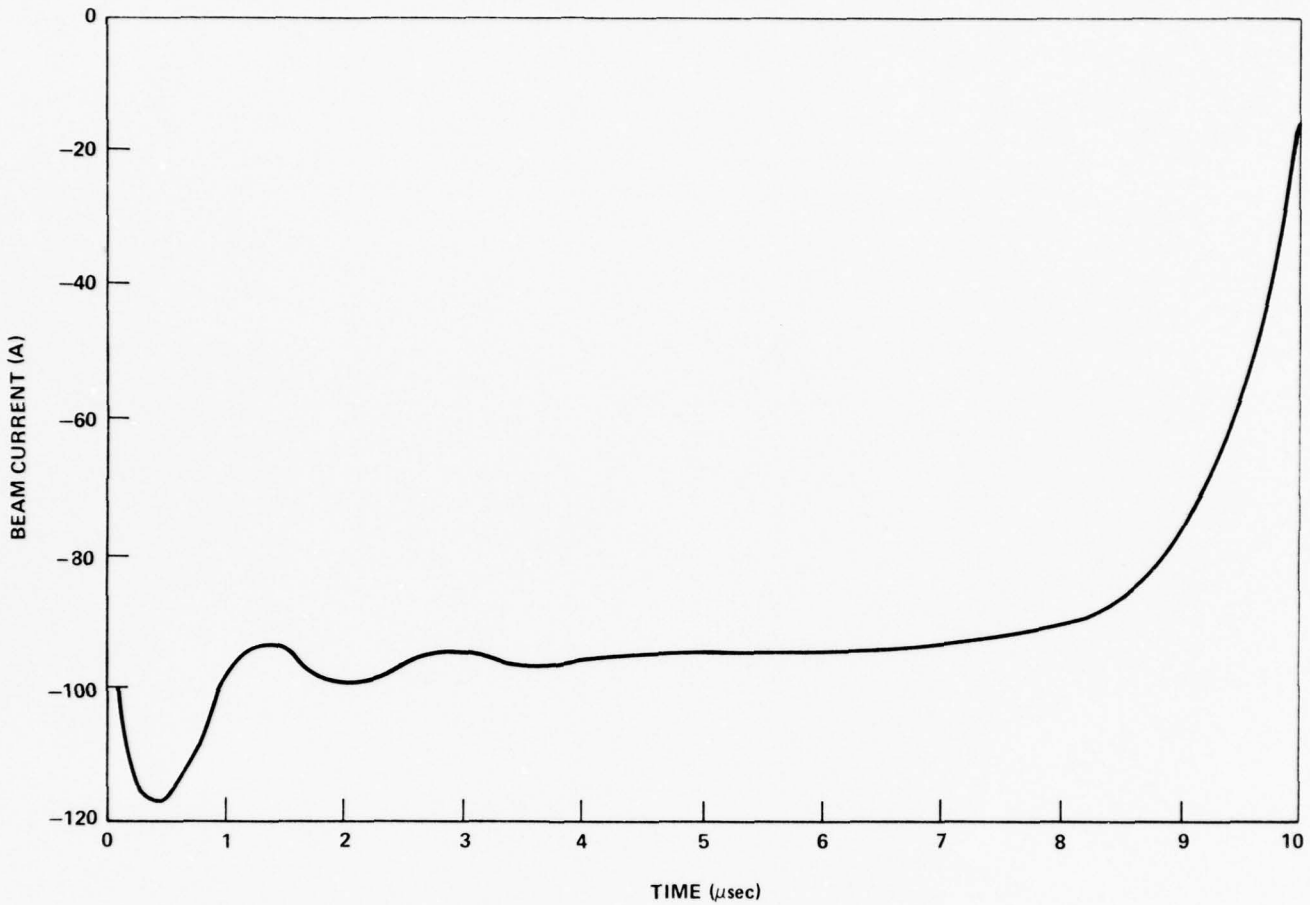


Figure 65. Conceptual design; beam current (pre-foil) versus time.

PRECEDING PAGE BLANK-NOT FILMED

Appendix. INTERIM REPORT

1. Introduction

This interim technical report documents the results obtained during the contract period from April 8, 1974 to March 30, 1975 for MIRADCOM contract No. DAAH01-74-C-0624. The objectives of this research effort, to determine the operational characteristics of high repetitive rate cold cathode electron guns and use the data in the conceptual design of an example system, have been achieved.

All performance characteristics required for the conceptual device have been demonstrated with an experimental electron gun. This laboratory device is full scale in all of its important dimensions. The data are therefore directly applicable to the conceptual design of an example system.

All of the performance requirements have been equalled or exceeded. Many design goals have also been exceeded.

The first study of multi-pulse cold cathode guns was a small independent research and development (IR&D) effort at Systems, Science and Software (S-Cubed). Operation (25 pps) of a 200-cm^2, 50-nsec pulse duration gun was demonstrated. Research programs subsequently funded by MIRADCOM, other agencies, and S-Cubed have advanced this new technology.

Significant technology advancements include the following:

a) Demonstration of 50-pps, 3- sec, 0.5-A/cm^2 operation. (MIRADCOM DAAH01-74-C-0624).

b) Demonstration of gun current extraction efficiency much greater than 50% (MIRADCOM DAAH01-74-C-0624).

c) Demonstration of 1000-pps, 10- sec, 0.03-A/cm^2 operation (S-Cubed IR&D).

d) Demonstration of a high efficiency large area (35 × 200 cm) double-sided cold cathode) (S-Cubed IR&D, LASL KH-5-78091).

The data from these programs significantly contributed to understanding large area multiple pulse cold cathode electron guns and enhanced the effectiveness of the present program.

The experimental facility, subsystems, and components are described in the following section. Section 3 contains the results of the measurements performed on the facility during this program. Section 4 contains the conceptual design study. The report is summarized in Section 5.

Table A-1 correlates the experimental work and results with the program objectives and requirements.

TABLE A-1. INDEX TO PROGRAM TASKS

Section 3 Requirements	Report Section
3.1 The research program shall cover the following area of investigation on cold cathode electron beam guns to derive data and engineering design criteria for the conceptual design described berein.	3.1 Introduction
3.1.1 Pulse repetiton rate of cold cathode guns shall be investigated.	
3.1.1.1 The pulse repetition rate up to 50 pps for the post foil beam current densities up to 0.5 A/cm^2 at 3 μsec width will be investigated. Life expectancy of foils and cathodes will be determined. The goal is for a life of 50,000 pulses. Factors affecting pulse rate such as vacuum pump size, cooling requirements, and foil holder will be examined and their requirements determined. Damage mechanisms of foils and cathodes will be identified and methods for increasing the life beyond 50,000 pulses will be considered.	3.1.1.1 a) Operation (50 pps) - Section 3 B b) Life expectancy of windows/damage mechanisms - Section 3 E c) Life expectancy of cathodes/damage mechanisms - Section 3 B d) Vacuum pump requirements - Section 3 D e) Foil holder - Section 3 E
3.1.1.2 Drive circuits for the e-beam gun will be studied in terms of requirements for large systems. A limited effort in the design of specific circuits will be directed toward determining methods to fulfill the gun drive requirements.	3.1.1.2 Section 4 D

TABLE A-1. (Continued)

Section 3 Requirements	Report Section
3.1.2 The contractor shall conduct an investigation to determine possible methods of extending the electron beam pulse time approximately 2 to 10 μsec. The electron beam current density will be collected at one or more centimeters from the high pressure or laser side of the foil window.	3.1.2 Section 3 B
3.1.3 The contractor shall conduct an investigation to determine possible methods of operating the gun at a voltage up to 300 kV covering post foil e-beam current pulse widths from 2 to up to 10 μsec.	3.1.3 Section 3 B
3.1.4 The contractor shall conduct an investigation to determine possible methods which affect the post foil beam current density efficiency and uniformity. A gun current efficiency (defined as the total post foil current/input current) of 50% is the goal. The electron beam current density uniformity should be within ±10% across the central region at peak efficiency.	3.1.5 Section 3 B
3.1.5 The possible use of a control grid in the gun shall be considered to determine if it shows promise in simplifying the gun drive circuits.	3.1.5 Section 3 B
3.1.6 The possible optimization of the gun voltage shall be considered in terms of its impact on the foil and cathode life, pulse width, repetition rate, and gun drive circuit complexity.	3.1.6 Section 3 F
3.1.7 Impedance matching characteristics of the gun design to power supply requirements will be considered in general. These characteristics will include methods to vary the cathode emitted currents, impact on the power supply requirements, and gun beam current efficiency.	3.1.7 Section 3 B
3.1.8 Scalability rules obtained from research laboratory test devices must be examined. Probable risk areas in the design of large gun systems shall be identified.	3.1.8 Section 4 A

TABLE A-1. (Concluded)

Section 3 Requirements	Report Section
3.1.9 The contractor shall generate a conceptual design of a cold cathode electron beam gun supported by the results obtained from the research conducted during this program. It is to have a post foil electron beam emitting area of 15 × 200 cm. It must operate at 50 pulses/sec in 10-sec burst with sufficient time between operation to allow the components to cool. It must have a uniform post-foil electron beam current density of a minimum of 0.5 A/cm^2 and with a goal of 8.0 μsec. The design must allow operation into 1.0 and 2.0 atm of laser gas. The design post-foil gun current efficiency goal is 50%.	3.1.9 Section 4
3.1.10 An experimental analysis of the electron beam energy spectrum effects on the foil will be made based on measurements of temperature rise of window foils of varying thickness and of gun operation of varying pulse widths and voltage. These data will be used by the contractor to make estimates of the time dependent electron beam energy distribution. Foil heating effects and resulting cooling requirements will be developed and related to gun operating parameters such as voltage, pulse current density, and pulse width and average current density.	3.1.10 Section 3 F

2. Experimental Facility

A. Rapid Pulse Facility

The experimental equipment used for this program comprises the S-Cubed Rapid Pulse Facility (RPF) shown in Figure A-1. This unique facility was developed to conduct research on cold cathode electron guns for laser simulation and radiation processing applications. The high voltage modulator, which includes a pulse transformer in an oil tank, is located in the metal house. The electron gun is mounted below the pulse transformer oil tank. The electron beam emerges vertically downward from the gun. All controls and diagnostic equipment are located in a ground level control rack.

The dc power supply for the RPF develops 32 kW at its 20-kV output voltage. It may be used to drive various PFN subsystems which use thyratrons, ignitrons or spark gaps as the switching elements. A low impedance PFN with ignitron switching is used in the present program.

A 60-cm ID by 320-cm long cylindrical stainless steel vacuum chamber contains the electron gun. Its size allows the production and extraction of electron beams with cross sections up to 25 × 165 cm. All dimensions and electrical feedthrough hardware are designed for 250-kV pulsed operation. The control console contains the circuits for controlling the high voltage level and all triggering circuits required for operation of the device. The trigger circuits control the pulsed operation from 1 pps to greater than 1000 pps. Other manual control functions located on the control console are the adjustments for the spark gap pressures, pulse transformer core bias, thyratron reservoir heater power, filament power, etc. All adjustments necessary to operate the device are in the control console.

B. Line Pulser

The power supply used in this program uses a lumped element line-driver pulsed-transformer combination (Figure A-2). Nominal specifications for this unit are as follows:

Output voltage	250 kV
Output current	750 A
Pulse duration	3 μsec
Maximum pulse repetiton rate	50 pps
	100 pps optional
Duty	10-sec burst every 15 min.

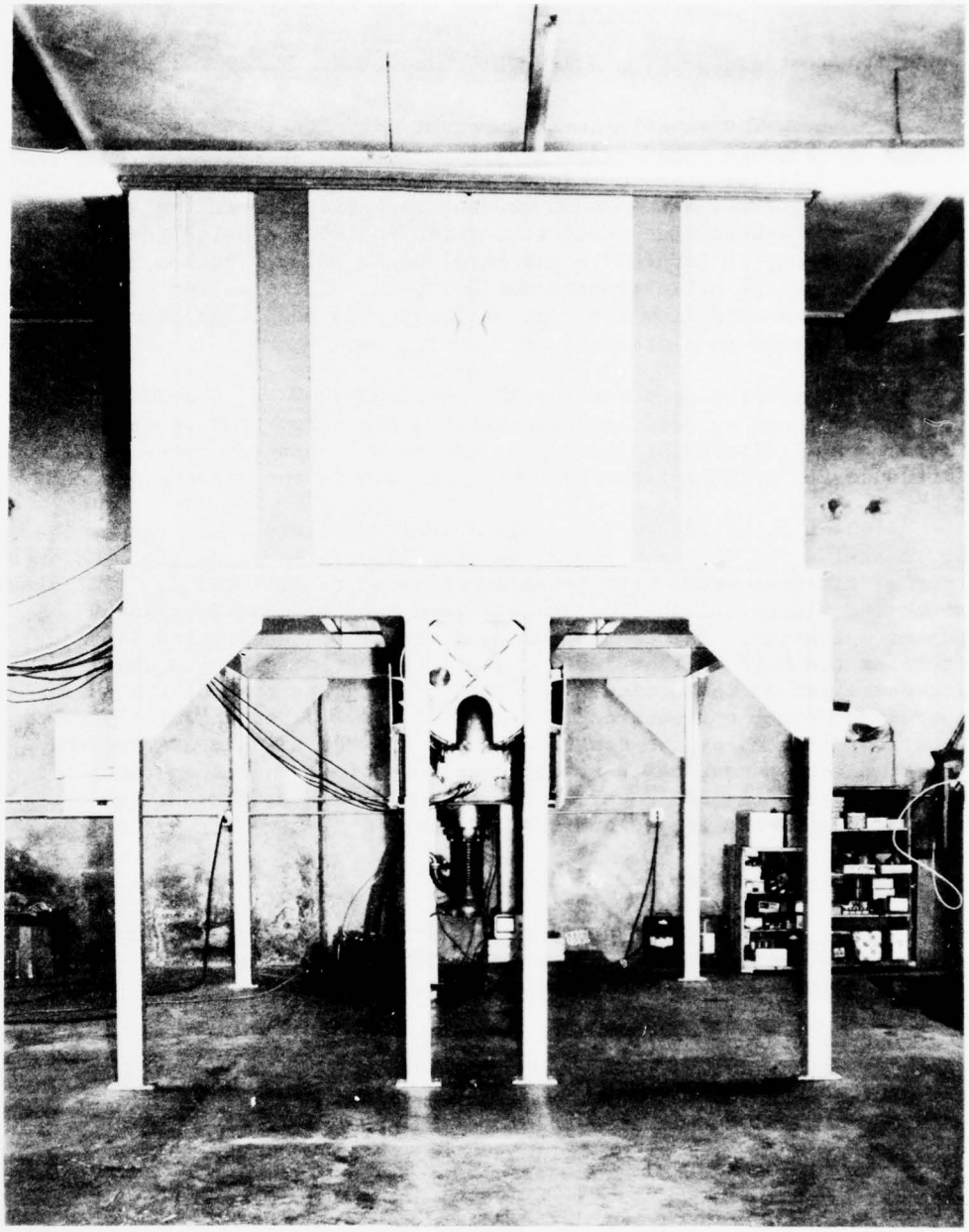


Figure A-1. High power cold cathode facility.

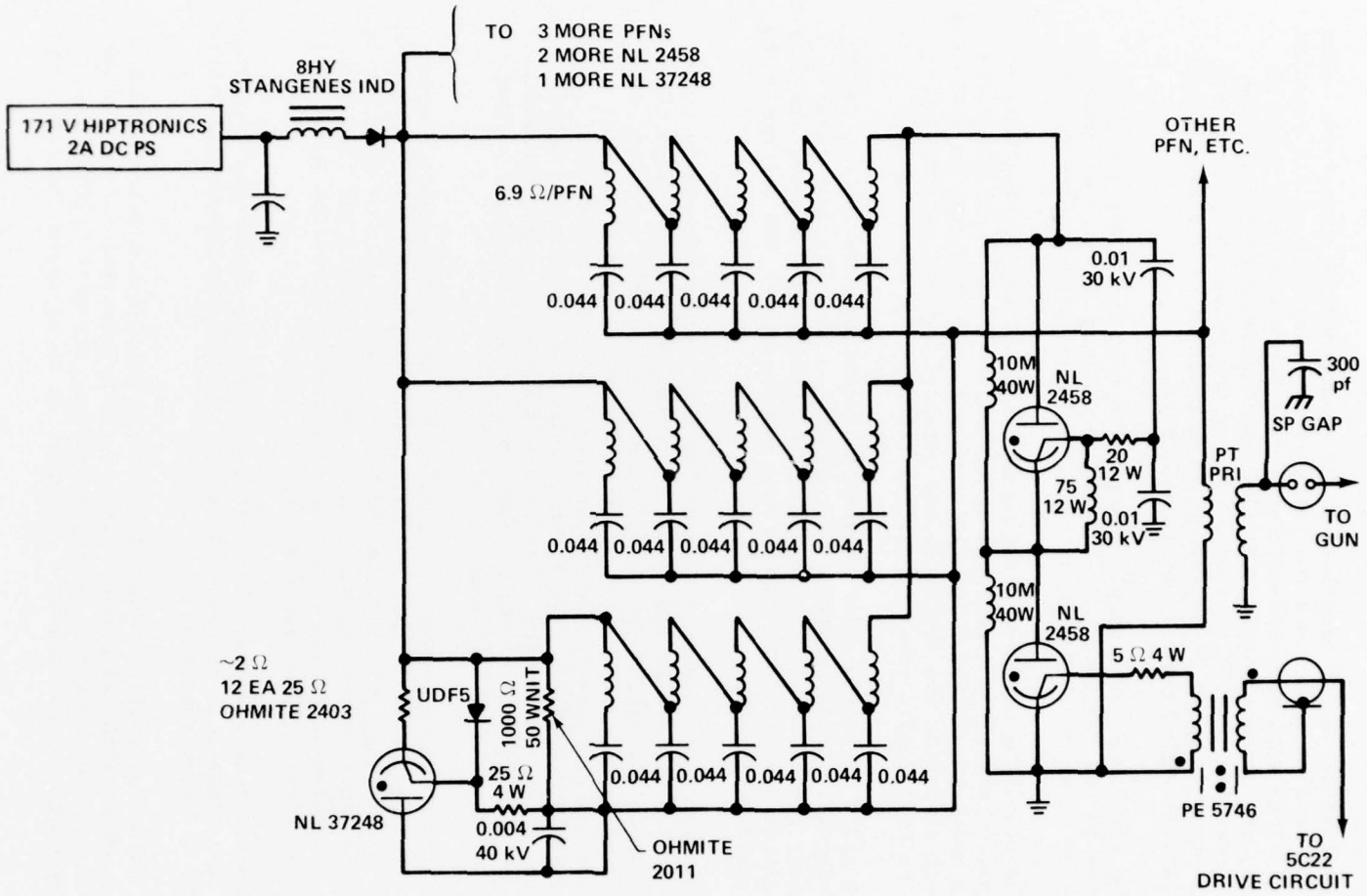


Figure A-2. Schematic drawing of lumped element line-driver pulsed-transformer combination.

The line driver is comprised of 30 capacitors and inductors. Five identical sets of capacitors and inductors make up each of six parallel PFNs. In this way, each PFN maintains a moderate impedance level of six ohms, producing a total paralleled PFN impedance of 1 ohm. The leads connecting the PFN to the primary of the pulse transformer are kept as short as possible so that the L/R risetime of the system will be compatible with 3-μsec pulse durations.

The RPF 32-kW power supply charges the PFN; the power supply is connected to the PFN through a charging choke and diode combination to produce 34 kV on the PFN with 17 kV on the high voltage power supply.

The resulting resonant charging waveform allows clearing time for the ignitron switches. The large ignitrons are D size National Electronics model No. NL2458. Two ignitrons are used in series to withstand the 34-kV charge on the PFN; a second parallel set of ignitrons provides the high duty current capability required for the program.

Standard thyratron pulse generating technology was used to switch the ignitrons. These ignitrons have proven to be quite dependable throughout the course of the study. At no time have there been clearing difficulties due either to rapid reapplication of the PFN voltage or to peak current limitations.

The open core pulse transformer has a primary to secondary turn ratio of 17.5:1. A thin laminated iron core provides the large time-voltage product required for this program. Thus, when operating with matched impedance, a charge of 34 kV on the PFN (or 15 kV for the dc power supply) produces 250-kV output from the pulse transformer. This voltage is then applied directly to the cathode of the gun. Alternatively, it can be applied first to a small peaking capacitor which, by use of a small self breaking spark gap, is then connected to the cathode of the gun (Figure A-3).

The spark gap steepens the risetime of the voltage pulse applied to the cathode. Without this capacitor/spark gap combination, the risetime of the voltage pulse is limited by the L/R risetime of the circuit. Stray inductances in the primary and secondary circuits and flux leakage in the pulse transfomer limit the risetime (without the spark gap) to approximately 1 μsec (Section 3 b).

The electron beam gun also used two focussing electrodes (Figure A-3 A-3). The electrical potential attained by these electrodes was determined by the electron beam.

A capacitor/resistor assembly connects the focus electrodes and ground. These focus electrodes assume ground potential before a pulse is applied to the cathode. During the pulse, the grid holding capacitor charges up to the cathode's voltage. It takes approximately 100 nsec

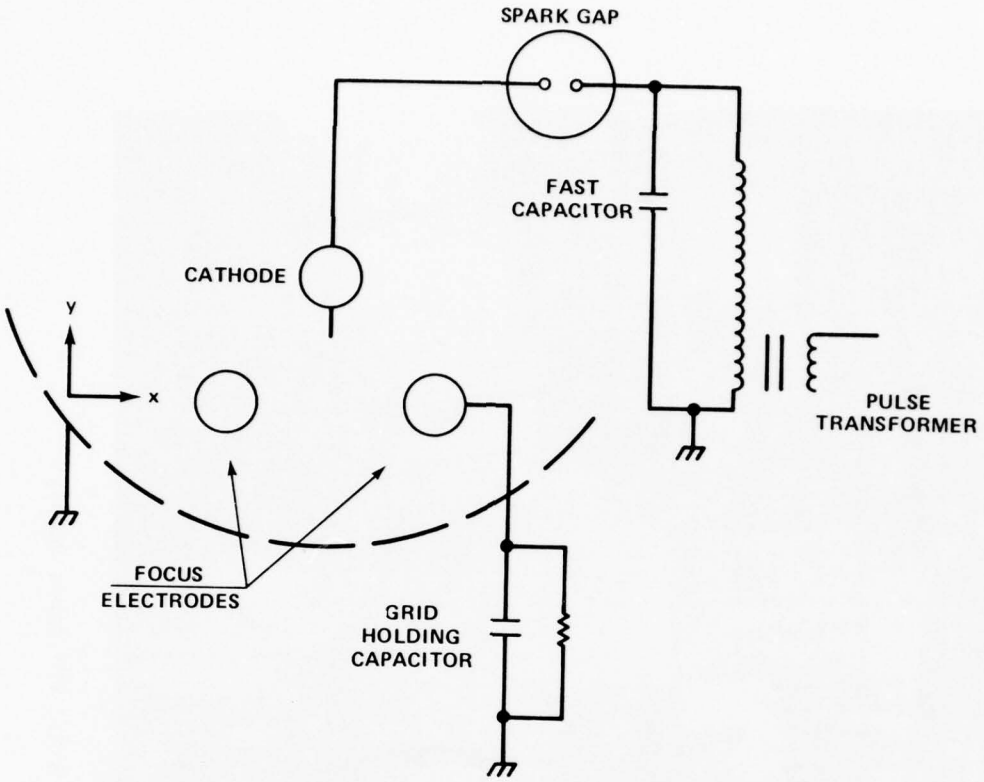


Figure A-3. Cold cathode gun structure schematic.

to charge this holding capacitor. The capacitor and the external resistor determine the electrodes' e-folding discharge time, which is approximately 20 μsec.

A photograph of the entire PFN/pulse transformer combination (Figure A-4) has been included. No attempt was made to minimize the size of this power supply; however, a relatively small volume device was constructed. This compactness is an inherent advantage of the line driver technology (Section 4).

C. High Voltage Feedthrough Insulators

Three high voltage ports leading directly from the pulse transformer oil tank were used to access the stainless steel vacuum chamber of the RPF electron gun. The electron beam window is mounted horizontally on a 25-× 165-cm rectangular port at the base of the vacuum chamber. The water-cooled window (built for this program)

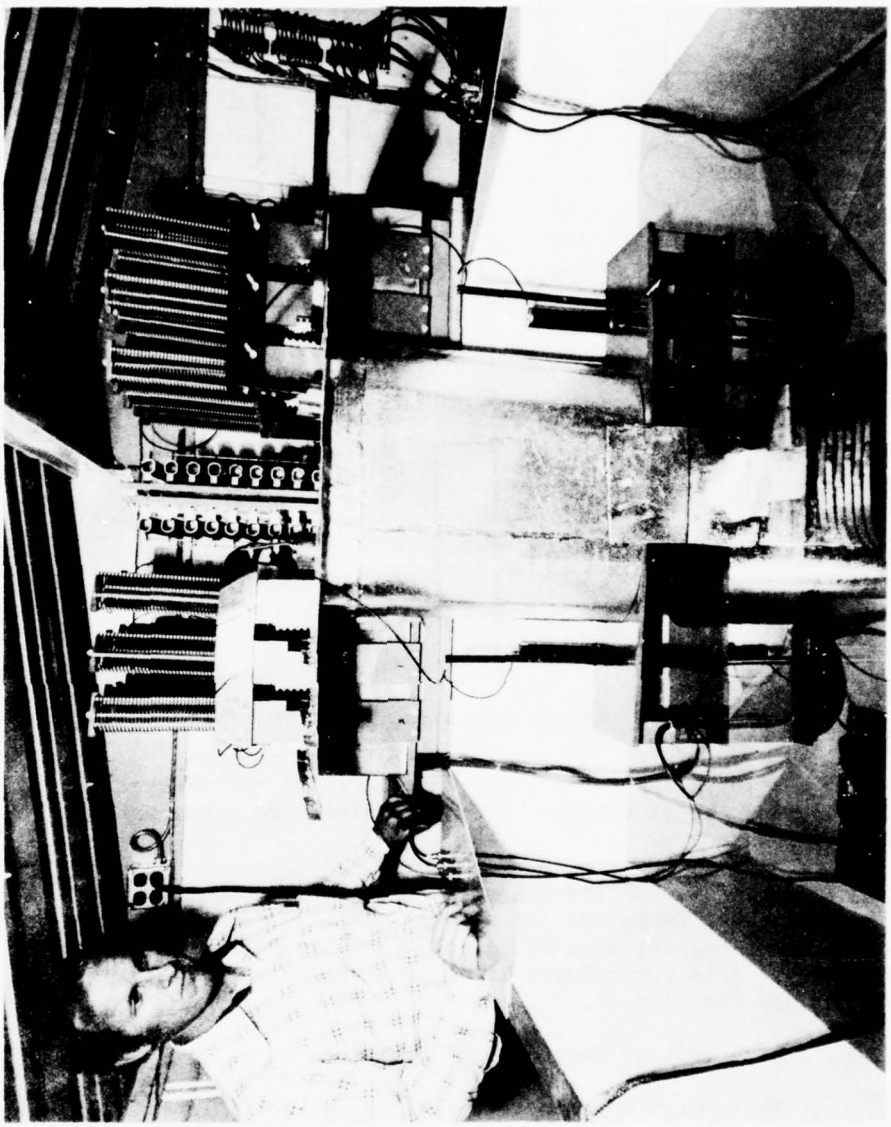


Figure A-4. PFN power supply.

measures 15 × 50 cm; it is mounted on the port with an adapter plate. Construction and design of the water-cooled window will be further discussed in Section 3 E.

Figure A-5 shows the interior structure of the cold cathode electron beam gun. The gun's open structures permitted the anode-cathode separation and the beam focussing elements to be changed rapidly. The extreme simplicity of the cold cathode gun is evident in this paragraph.

Bonded metal ceramic bushings transmit high voltage from the pulse transformer tank into the vacuum chamber. In all previous programs performed on the RPF, the bushing performed well up to 250 kV. During this program, however, 300 kV and more was attempted. The bushings failed at these higher voltage levels because of sparking between the grading rings and the central metal feedthrough rod (Figure A-6). Repeated sparking made the bushings completely useless. New bushings were then designed, constructed, and installed (Figure A-7). Design of the new bushings was limited by the existing structure of the RPF. The new bushings withstood voltages in excess of 300 kV without failure; they have performed satisfactorily to date.

D. Vacuum System

The vacuum system used in these tests included a Consolidated Vacuum Corporation 6-in. (1400-ℓ/sec) oil diffusion pump, a 190-cfm mechanical rotary pump and appropriate ion gauges, controllers, and readout devices. Strip chart recorders were used on the ion gauge readouts to obtain gassing rates during operation of the cold cathode electron gun. *Pumping speed* for the vacuum system will be analyzed in Section 3 D.

A gate valve between the diffusion pump and the vacuum chamber facilitated changes in the gun structure. Liquid nitrogen baffles and cold traps were not used. This has been the usual practice on single pulse cold cathode electron guns. A schematic diagram of the vacuum system is shown in Figure A-8.

E. Total System Operation

All of the previously described components have been operated together successfully. A photograph of the electron beam was taken as it emerges through the foil. The sharp cutoff for the electron range in the air is clearly evident in the photograph. The glowing zone is from N_2^+ radiation as the air is excited by the multiple pulsed electron beam.

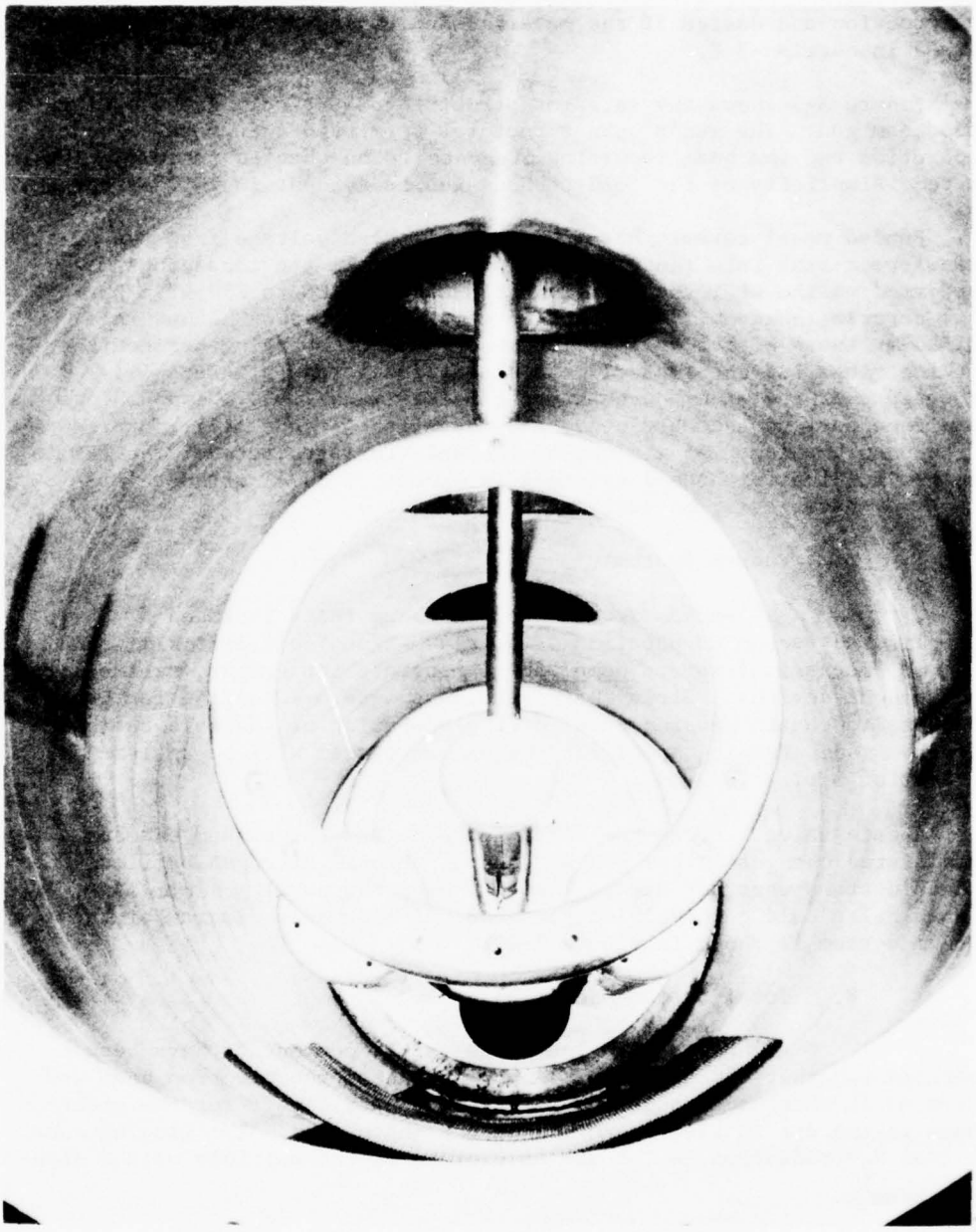


Figure A-5. Cold cathode gun structure.

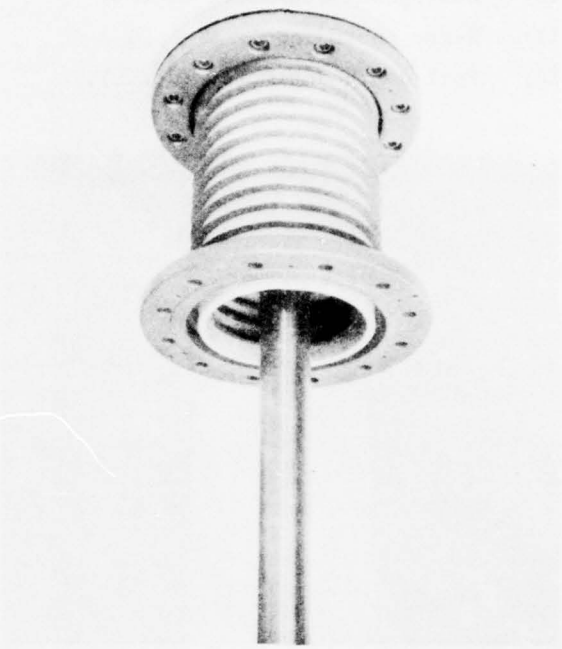


Figure A-6. Original RPF high voltage bushing.

3. Experimental Program

A. Experimental Procedures-Diagnostics

The complete RPF diagnostics complement was available for this program. Parameters measured and instrumentation included the following:

1) Power supply charge voltage (dc).
2) Power supply current (dc).
3) PFN pulse current.
4) Pulse transformer secondary current.
5) Cathode voltage.
6) Focus electrode pulse current.
7) Focus electrode voltage.

8) Output beam current density monitor.

9) Beam current density uniformity array.

10) Cellophane dosimeter sheets.

11) X-ray photodiode.

12) Foil depth dosimeter (dq/dx).

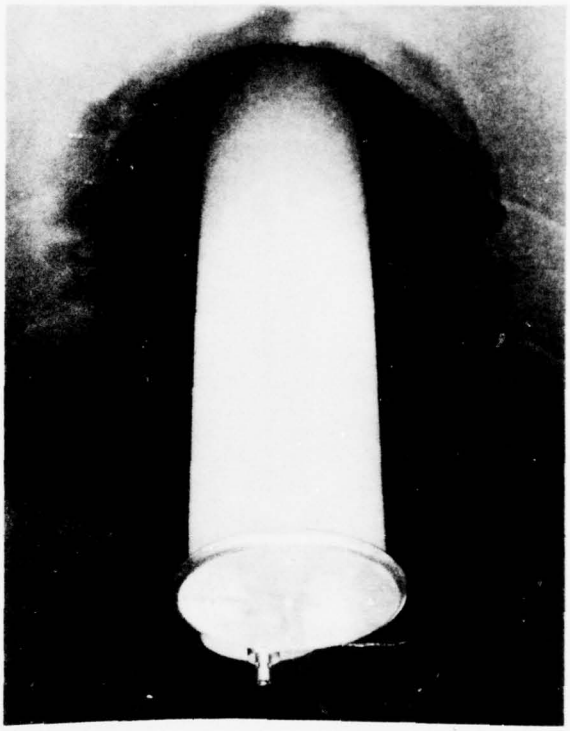


Figure A-7. New RPF high voltage bushing.

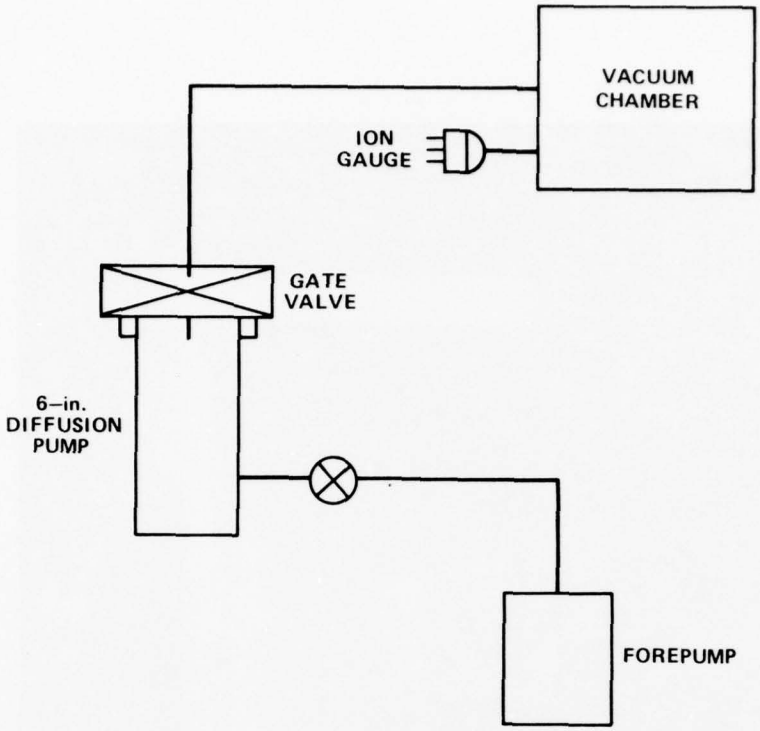


Figure A-8. Vacuum system schematic.

Standard metering strings and voltage drop techniques were used to determine the dc power supply charge voltage and current. PFN pulse current and the pulse transformer secondary current (which is also the electron gun cathode current) were measured with Pearson wide band current transformers with risetimes under 10 nsec. The transformer's frequency response was adequate to provide accurate data for the entire pulse length.

The cathode voltage was measured with a Power Designs Model 1603, 350-kV capacitive divider.

The focus electrode pulse current and voltage were measured with diagnostics similar to those used for the cathode voltage and current.

Output beam current density was measured by two methods. The first method used a Pearson toroidal current transformer that was shielded from the electron beam by an electrically grounded metal plate. The electron beam passed through a hole in the shield and through the toroid; thus the beam acted as the transformer's primary current. With this method, the resulting signal is free of interpretive complications from secondary electron production.

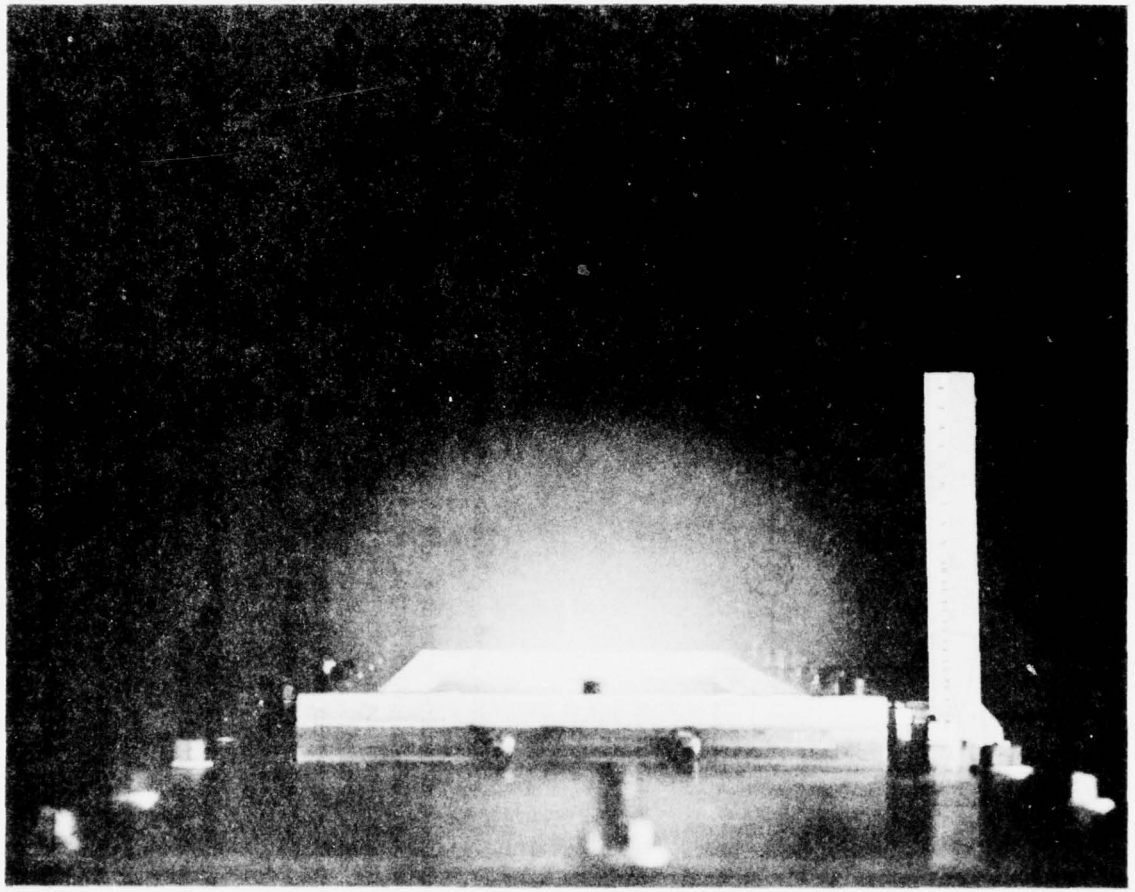
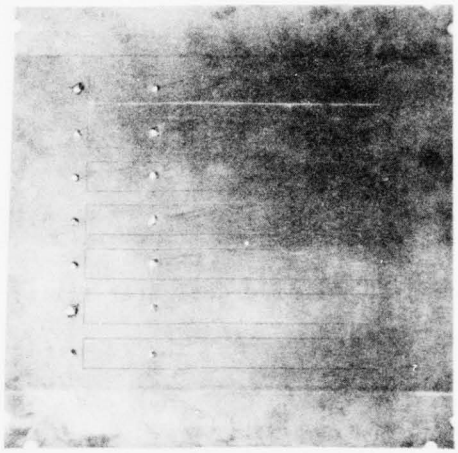


Figure A-9. N_2 + radiation from air excited by the electron beam of the multiple pulsed cold cathode electron gun.

The second method used copper current collectors on a printed circuit board. An array of these collectors mapped the beam current density outside the transmitting window. A photograph of one of the arrays is shown in Figure A-10. These arrays can be used with full beam power and low duty cycles or with reduced beam power for longer times.

The cellophane dosimeter foils were used only for a qualitative comparison with the current density uniformity arrays.



1 x 7 Array
Elements 2 x 20 cm^2

Figure A-10. Current collector array.

X-ray photodiodes proved useful in the initial operation of the device; they insured that the signals observed were in fact due to high energy electrons.

The dq/dx foil dosimeter shown in Figures A-11 and A-12 was used to determine the electron energy spectrum of the beam (Section 3 C). Because the dosimeter foils were insufficiently cooled, low duty operation of the gun was necessary when the detector was being used.

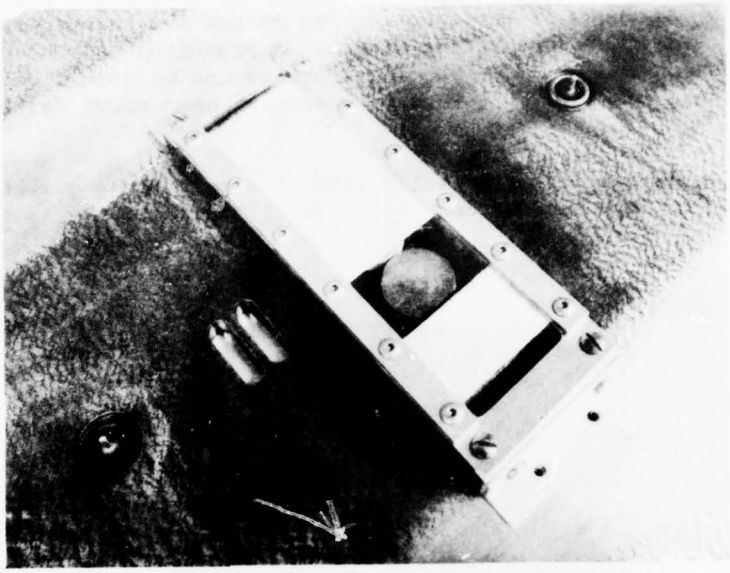


Figure A-11. Charge dosimeter foils.

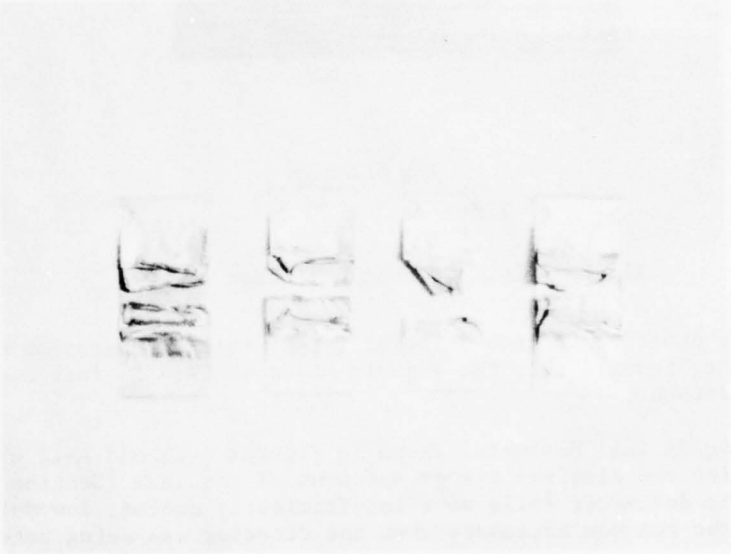


Figure A-12. Charge dosimeter foils; excess beam power.

Each time the gun chamber was opened, the following routine procedures were followed before testing was resumed:

1) Cleaning - All portions of the gun were cleaned either with Freom TF or, if small enough, in a hot vapor degreaser. The interior surfaces were inspected to see whether excess sparking or insulator flashover had occurred during the previous run. With each inspection the condition of the device was determined and it was compared to conditions during previous inspections.

2) Vacuum System - Oil levels in roughing and diffusion pumps were routinely checked. Prior to each experiment, a complete vacuum check of the system was performed with a helium (mass spectrometer) leak detector. This last procedure was crucial to the experiments success.

Cold cathode guns can operate at pressures of 10^{-4} torr or lower. In the past, misinterpretation of this modest vacuum requirement has caused carelessness in maintaining the vacuum integrity of similar systems. A cold cathode gun will not operate at 10^{-4} torr if this pressure is caused by a leak in the vacuum system. A vacuum tight system is required. Small leaks, even those permitting indicated pressures of 10^{-6} torr in the vacuum chamber, have caused significant problems, particularly sparking. Sparking, either from cathode to anode or along the surface of the insulator can occur when a small leak in a high vacuum system increases the local pressure above the average indicated pressure. Local pressuees can be above 10^{-4} or 10^{-3} torr even when 10^{-6} torr is indicated by an ion gauge. Local pressures above 10^{-4} torr will almost certainly lead to breakdown.

3) Complete calibrations of the system's scope channels and high voltage monitors were performed before each data run.

Normal laboratory techniques were followed during this program. Other than the particular care in making sure that the system was vacuum tight, no special precautions or procedures were needed to operate the electron gun.

B. Emission and Current Density Control

1. Emission Process

The cathodes used for this program were tantalum foil strips 0.0003 in. thick. Tantalum strips have performed excellently in all S-Cubed single pulse cold cathode electron guns built during the last few years. A single emitting foil was used to obtain the necessary well-defined emitting surface (Section 3 C).

The cold cathode emission process is not yet completely understood. It is known, however, that initially the cathode is a metal surface in a high vacuum. When the high voltage pulse is applied, a plasma forms along the edge of the emitter foil and expands with a velocity characteristic of the cathode material.

The impedance characteristics of this plasma emission process are well understood; the details of plasma formation, however, remain obscure.

To obtain good plasma formation and emission from a cold cathode, the electric field applied to the emitter surface must be of the order of 10^7 V/cm. Surface microstructure then produces localized fields several orders of magnitude higher. In typical single pulse cold cathode electron guns, there is sufficient emitter microstructure to "turn on" the cathode with a few tens of kilovolts applied between the cathode and anode. The surface microstructure is gradually eroded by tens of thousands of shots until the voltage required to turn on the cathode increases to many hundreds of kilovolts. A hypothetical probability curve demonstrating this phenomenon is shown in Figure A-13. The dashed curve in the figure corresponds to the probability that for a given electric field, emission sites will be formed on a new emitter. The solid curve illustrates the same probability for an emitter that has had tens of thousands of shots.

To obtain a uniform electron beam, many emission sites must be formed per unit length of the cathode. As the emitter is aged by use, the probability approaches zero for forming emission sites at the maximum electric field obtainable with a specific device. Few emission sites are then formed; the actual number depends upon the electric field. When operating the gun with a net cathode voltage limited to 250 kV, there is a low probability that emission sites will form. However, because the cold cathode gun is initially an open circuit, a fast rising 250-kV pulse will ring up to almost 500 kV and produce good emission.

The initial high impedance changes dramatically once the emission threshold is reached and an emission site forms. Because the voltage exceeds the threshold only during the formation of the first site, additional sites cannot be formed for the particular pulse. The time required for the abrupt drop of voltage on the cathode surface depends on the gun geometry and the power supply. The normal time requirement is 100 to 200 nsec. Thus, to obtain uniform generation of emission sites (and uniform emission) an extremely high field must be applied in less than 100 nsec. This is accomplished by the following methods:

1) The tantalum foil is approximately 8 μ thick; this allows achievement of the highest practicable fields.

2) Because the characteristic risetime of the pulse transformer is approximately 1 μsec, a small peaking capacitor and spark gap were

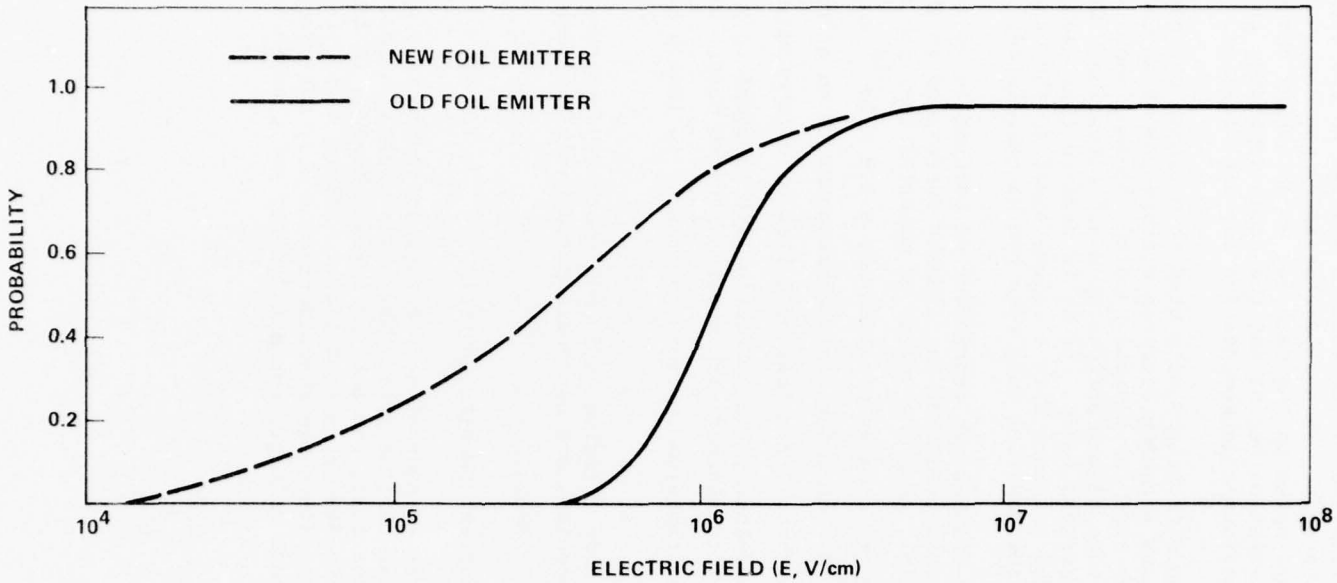


Figure A-13. Hypothetical probability curve.

used to decrease the risetime of the voltage applied to the cathode to a few tens of nanoseconds. This capacitor/spark gap combination applies a sharp voltage spike to the cathode, establishing the emission sites. Once current emission begins and the diode impedance is established, the pulse transformer determines the current risetime.

Scanning electron micrographs were used to estimate cathode lifetime. Figure A-14 shows scanning electron micrographs of an unused emitter and an emitter used for several hundred thousand shots. The photographs show the edge of each emitter at a 45° elevation. Scale size of the pits and craters is 1 μ. If it is assumed that each slot ejects from the surface a sphere with a volume equal to the crater volume, then the emitter material loss rate can be calculated.

A maximum of ten flashes per centimeter of cathode length were observed, and if it is assumed that the flashes correspond to the ejection of cathode material, then the volume of material lost per centimeter is given by $V = \pi r^3$ (number of sites/cm) = 3.9×10^{-12} cm^3/shot. For an emitter 7.6×10^{-4} cm thick, this corresponds to an average loss rate of 5.2×10^{-9} cm shot. If a loss of 0.1 cm of emitter material ends the cathode's usefulness, the emitter's life is equal to 2×10^7 shots. This number is consistent with observations to date. After more than 10^5 shots on tantalum emitters, no change in length has been observed.

The required cathode lifetime of 50,000 shots is therefore easily achieved. Lifetime problems are not anticipated until the requirements exceed 10^6 to 10^7 shots.

2. Current Density Control

The cathode of a cold cathode device is a plasma near the surface of the emitter foil. When this plasma is in contact with the surface of the foil, the emitted current density is limited only by the macroscopic discharge conditions. Figure A-15 (from work in 1972) shows that the discharge characteristics obey the space charge law that relates cathode voltage, current density and cathode-anode spacing (Child's Law)

$$J = 2.335 \times 10^{-6} \frac{V^{3/2}}{D^2}$$

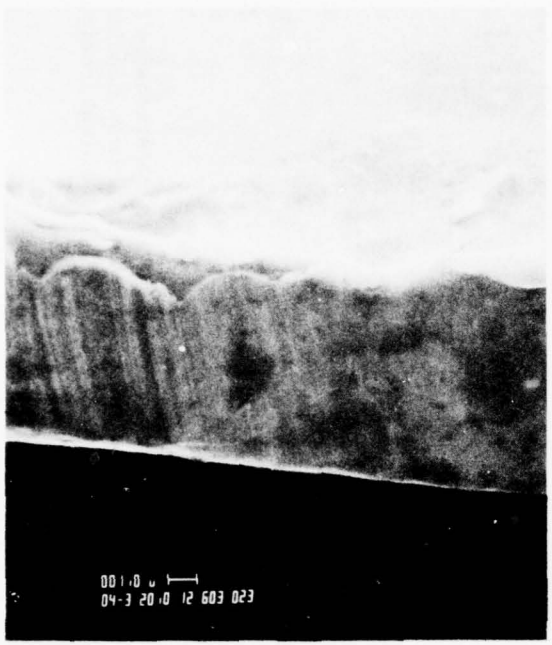




Figure A-14. Scanning electron micrograph.

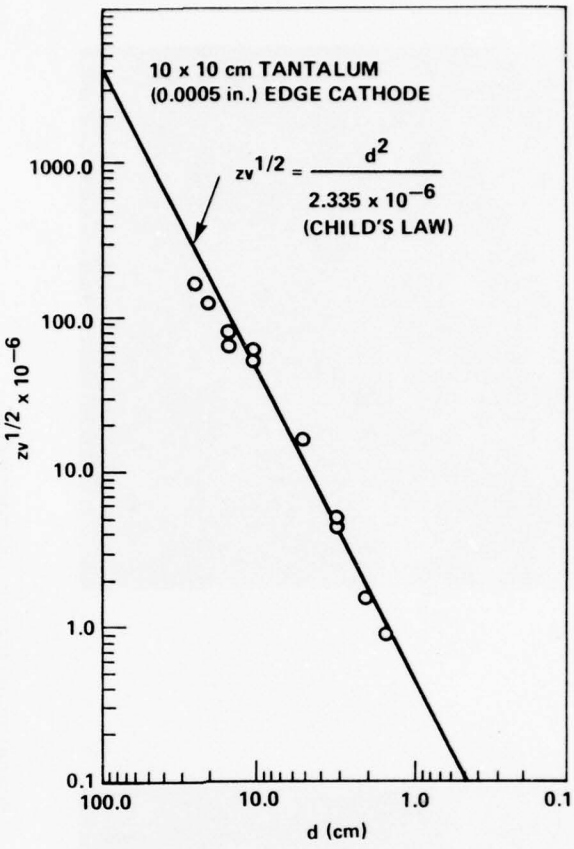


Figure A-15. Impedance characteristics for tantalum cathode.

where

V = the cathode voltage (V)

D = the anode-cathode separation (cm)

J = the current density (A/cm^2).

The present measurements again agree with this relationship (Figure A-16). In addition, it is now observed that these conditions are satisfied at any repetition rate as long as the ambient residual gas pressure remains low.

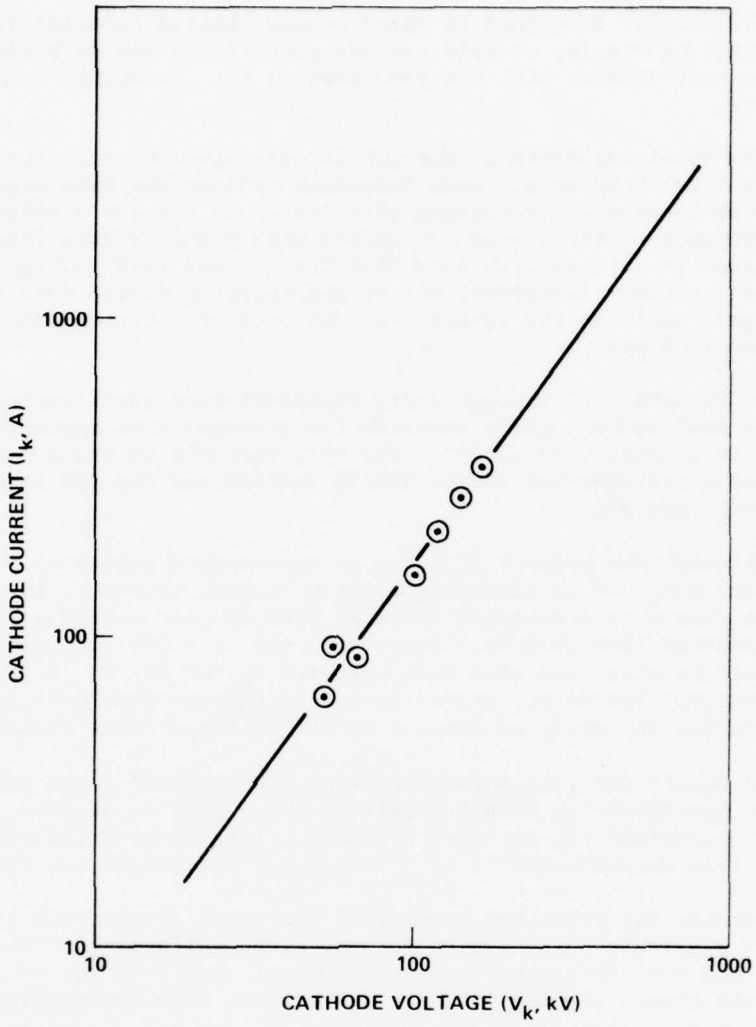


Figure A-16. Cathode current as a function of cathode voltage (10 pps).

This strict adherence to space charge limited behavior simplifies the design and scaling of cold cathode guns; it is now possible to predict current density with the same ease as for thermionic cathode devices.

The total impedance of the gun is determined by the current density and the total beam area. Beam focussing reduces the beam area and maximizes impedance. Focussing also increases the gun's efficiency. The impedance of the 50-pps gun agreed with previous data from single pulse guns as well as with data from the S-Cubed IR&D 1000-pps cold cathode program. Therefore, all of the existing design data for single pulse guns apply to the 50-pps case and other repetition rates up to at least 1000 pps.

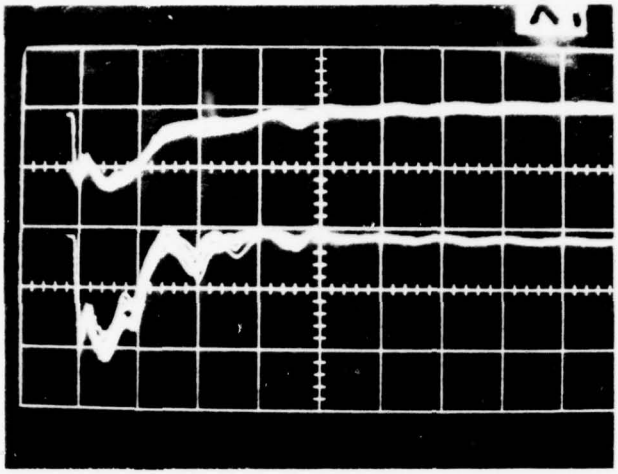
In Figures A-17 through A-21, representative oscilloscope traces show the cold cathode gun's behavior for voltages from approximately 170 kV to greater than 300 kV. The only variable in these data was the PFN charge voltage; the anode-cathode spacing and the PFN impedance were kept constant.

Although the primary goal was to investigate pulses of 3 μsec, a secondary goal was to investigate pulse lengths from 2 to 10 μsec. Cold cathode guns were previously operated with 10-μsec pulses at 1000 pps in an S-Cubed IR&D program. Large area (20 cm $\times$ 200 cm) single pulse cold cathode guns have also been operated in the 10- to 12-μsec pulse width range. Therefore, significant difficulties were not expected to arise during the study of 10-μsec pulses on the present facility.

To obtain the long pulse durations, the PFN had to be required so that it contained two parallel sets of three PFNs in series; originally, the PFN contained six parallel networks. This changed the PFN pulse length from approximately 3 to 9 μsec and also changed the PFN impedance.

Because the volt-time product of the pulse transformer limits the maximum available pulse length for any given voltage, approximately 100 kV was the operating voltage instead of the usual 200 kV. Because the space charge limited behavior had already been demonstrated for the repetitively pulsed cold cathode diode, the results obtained at 100 kV can be directly scaled to higher voltages. Representative traces showing the long pulse behavior of the cold cathode gun are shown in Figures A-22 and A-23.

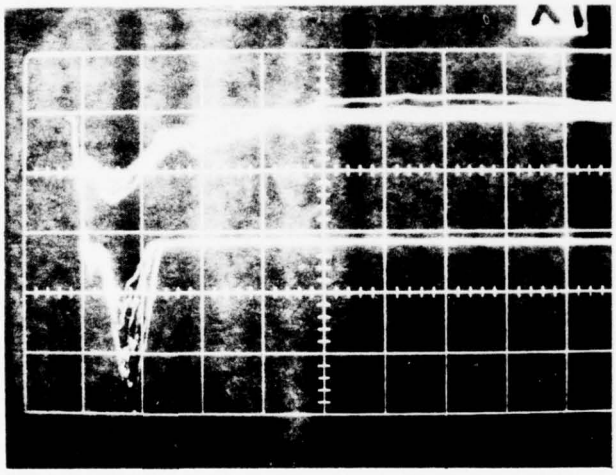
Long duration pulses make it easier to determine accurately the dynamic impedance characteristics of the gun. Figure A-24 shows a plot of the normalized diode impedance versus time.



V_k = 212 kV/DIVISION

I_k = 100 A/DIVISION

T = 5 μsec/DIVISION



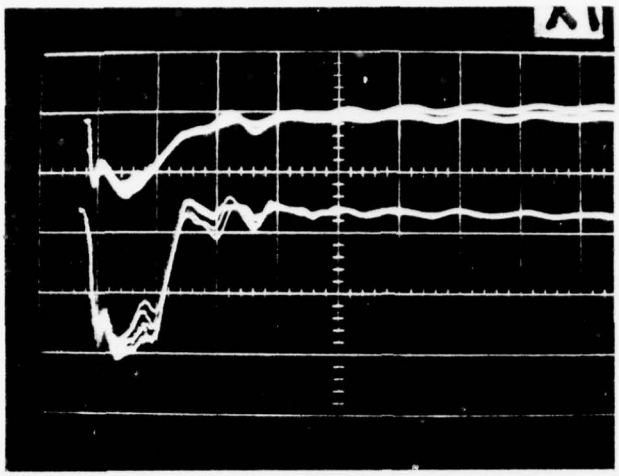
V_k = 212 kV/DIVISION

J = 0.05 A/cm^2/DIVISION

T = 5 μsec/DIVISION

CATHODE VOLTAGE AND CURRENT AND BEAM CURRENT DENSITY VERSUS TIME. 10 pps

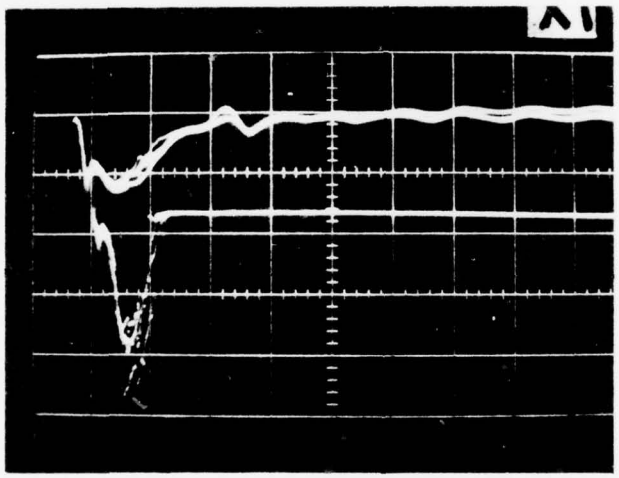
Figure A-17. PFN charge voltage (20 kV).



V_k = 212 kV/DIVISION

I_k = 100 A/DIVISION

T = 5 μsec/DIVISION



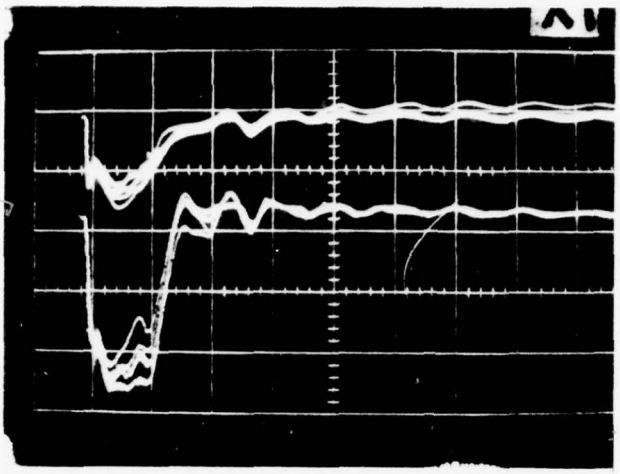
V_k = 212 kV/DIVISION

J = 0.05 A/cm^2/DIVISION

T = 5 μsec/DIVISION

CATHODE VOLTAGE AND CURRENT AND BEAM CURRENT DENSITY VERSUS TIME. 10 pps

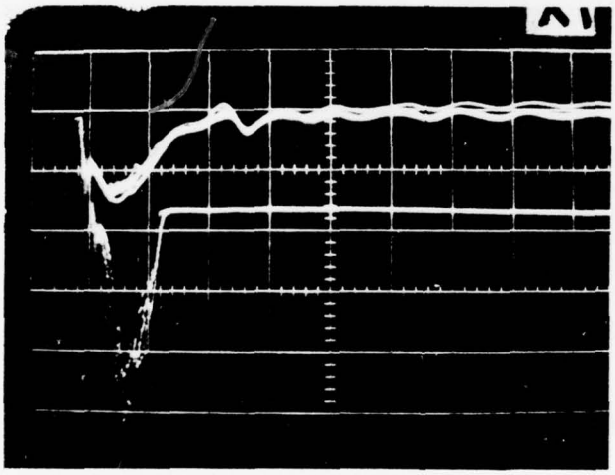
Figure A-18. PFN charge voltage (24 kV).



V_k = 212 kV/DIVISION

I_k = 100 amp/DIVISION

T = 5 μsec/DIVISION



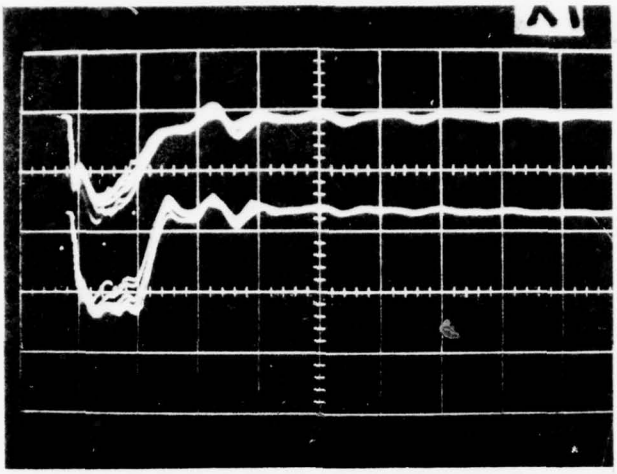
V_k = 212 kV/DIVISION

J = 0.05 amp/cm^2/DIVISION

T = 5 μsec/DIVISION

CATHODE VOLTAGE AND CURRENT AND BEAM CURRENT DENSITY VERSUS TIME. 10 pps

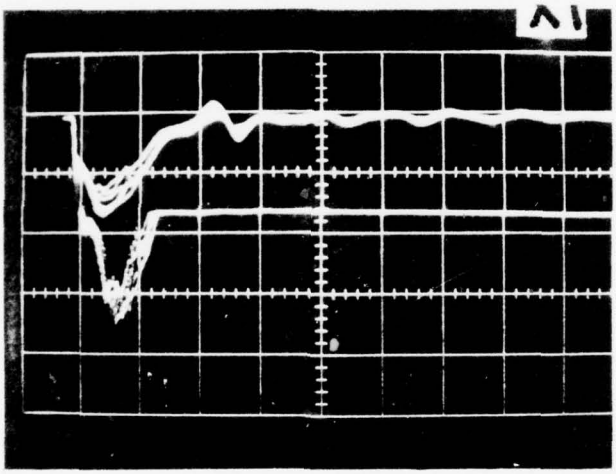
Figure A-19. PFN charge voltage (28 kV).



V_k = 212 kV/DIVISION

I_k = 200 amp/DIVISION

T = 5 μsec/DIVISION



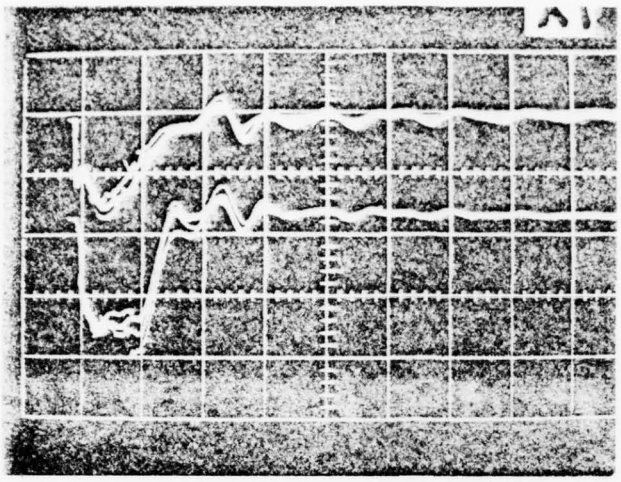
V_k = 212 kV/DIVISION

J = 0.125 amp/cm^2/DIVISION

T = 5 μsec/DIVISION

CATHODE VOLTAGE AND CURRENT AND BEAM CURRENT DENSITY VERSUS TIME. 10 pps

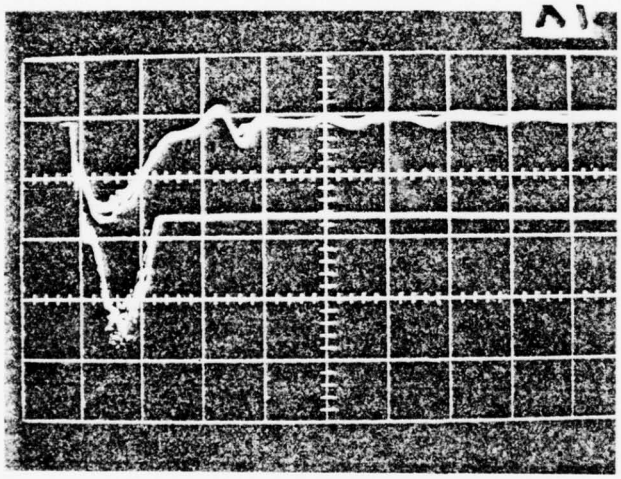
Figure A-20. PFN charge voltage (32 kV).



V_k = 212 kV/DIVISION

I_k = 200 amp/DIVISION

T = 5 μs/DIVISION



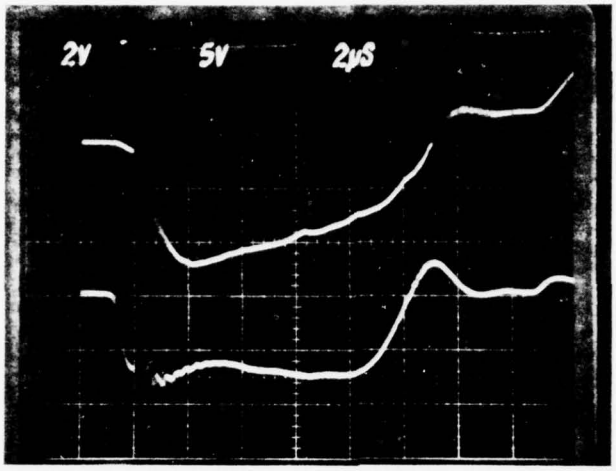
V_k = 212 kV/DIVISION

J = 0.125 A/cm^2/DIVISION

T = 5 μsec/DIVISION

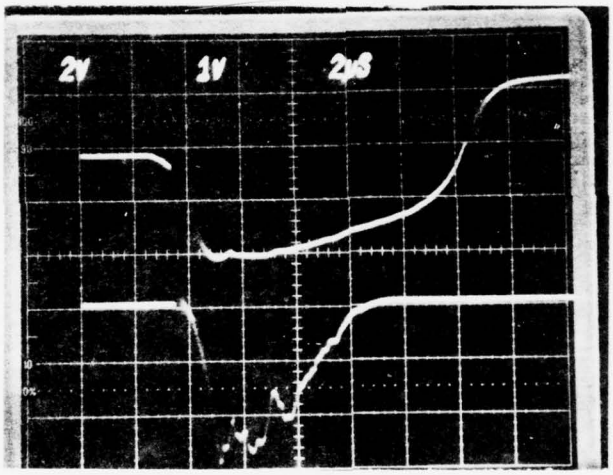
CATHODE VOLTAGE AND CURRENT AND BEAM CURRENT DENSITY VERSUS TIME. 10 pps

Figure A-21. PFN charge voltage (36 kV).



V_k = 40 kV/DIVISION

I_k = 100 amp/DIVISION



V_k = 40 kV/DIVISION

J = 0.025 amp/cm^2/DIVISION

CURRENT VOLTAGE AND CURRENT AND BEAM CURRENT DENSITY VERSUS TIME. 10 pps

Figure A-22. 10-μsec duration pulse.

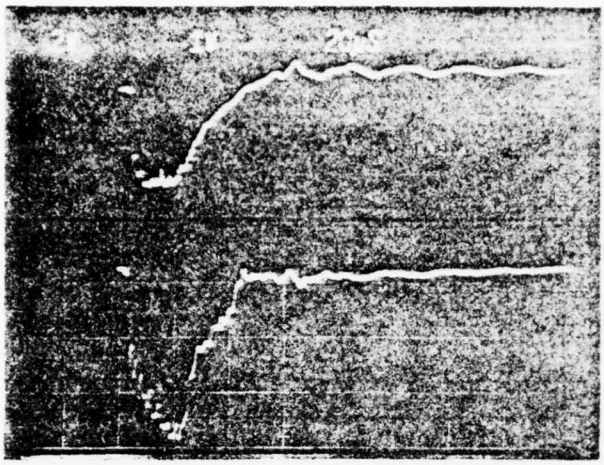


Figure A-23. 20 μsec duration pulse (1 pps).

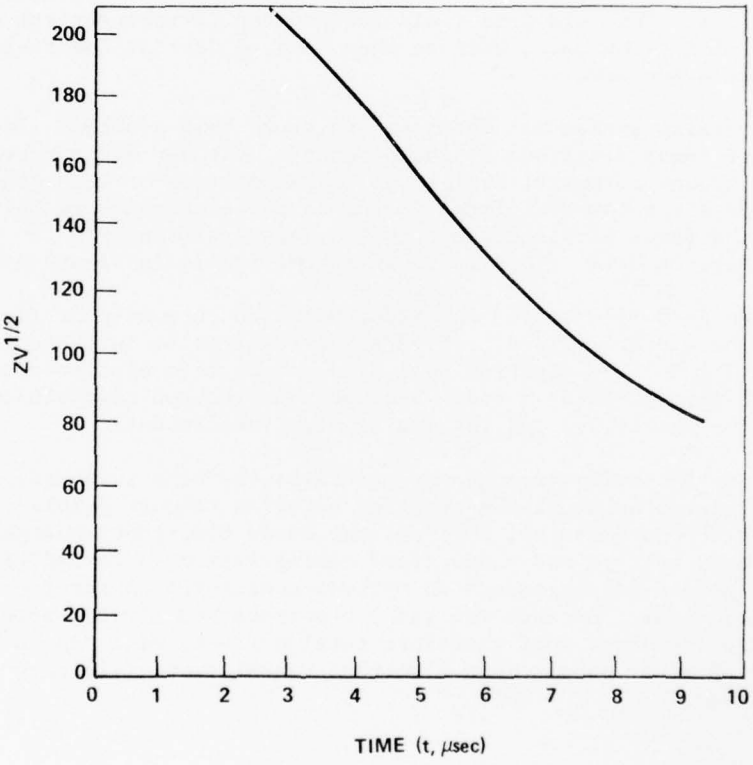


Figure A-24. Diode impedance as a function of time (data from Figures A-22 and A-23).

C. Beam Focussing - Uniformity

The MIRADCOM program produced two significant technological advancements: (1) the design and development of an efficient beam focussing system, and (2) the attainment of a highly uniform electron beam. A uniform cathode emitting surface (produced by applying fast risetime pulses to the cathode) was one of the two key factors in achieving a highly uniform electron beam.

The second factor is the focussing of the electron beam after the emitting plasma cathode has been formed. Previous cold cathode electron guns produced highly uniform electron beams only with a loss of efficiency. Cathode-anode configurations, in which only a small portion of the electron beam was extracted through the electron beam window, have been used; efficiencies of the order of 5% to 10% were quite common. For the high power/high repetition rate system required here, efficiencies of 5% to 10% are clearly unacceptable. Beam focussing seems to be an obvious solution. As was stated in Section 3 B, an intense electric field is required on the emitter foil in order for emission sites to form. This electric field requirement is inconsistent with most focussing techniques, because they tend to depress the field near the cathode's surface.

A focussing system was developed to avoid this problem. In this system, the focus electrode is independent of the cathode structure and maintains ground potential during the formation time of the cathode plasma. Once the cathode plasma is formed and electrons are being emitted, the focus electrodes assume the potential required for focussing the electron beam. This is shown schematically in Figure A-2.

Figure A-25 illustrates the electrode structure without focus electrodes. The electric field configuration required to initiate the cathode plasma is shown. The electron beam produced by this electrode structure is emitted into at least π rad. Because the electron beam window subtends approximately 0.1 rad the gun is very inefficient.

The new focussing arrangement maintains the high intensity electric field configuration until the onset of emission (Figure A-26). At the start of electron emission, however, the focus electrodes charge to the electron beam voltage and a new field configuration is formed (Figure A-27). Figure A-27 represents an optimum configuration for focussing the electron beam. Because the cathode surface has already been formed, the impedance (and therefore total current) will depend on the new field geometry only. High electron transmission efficiency is therefore achieved.

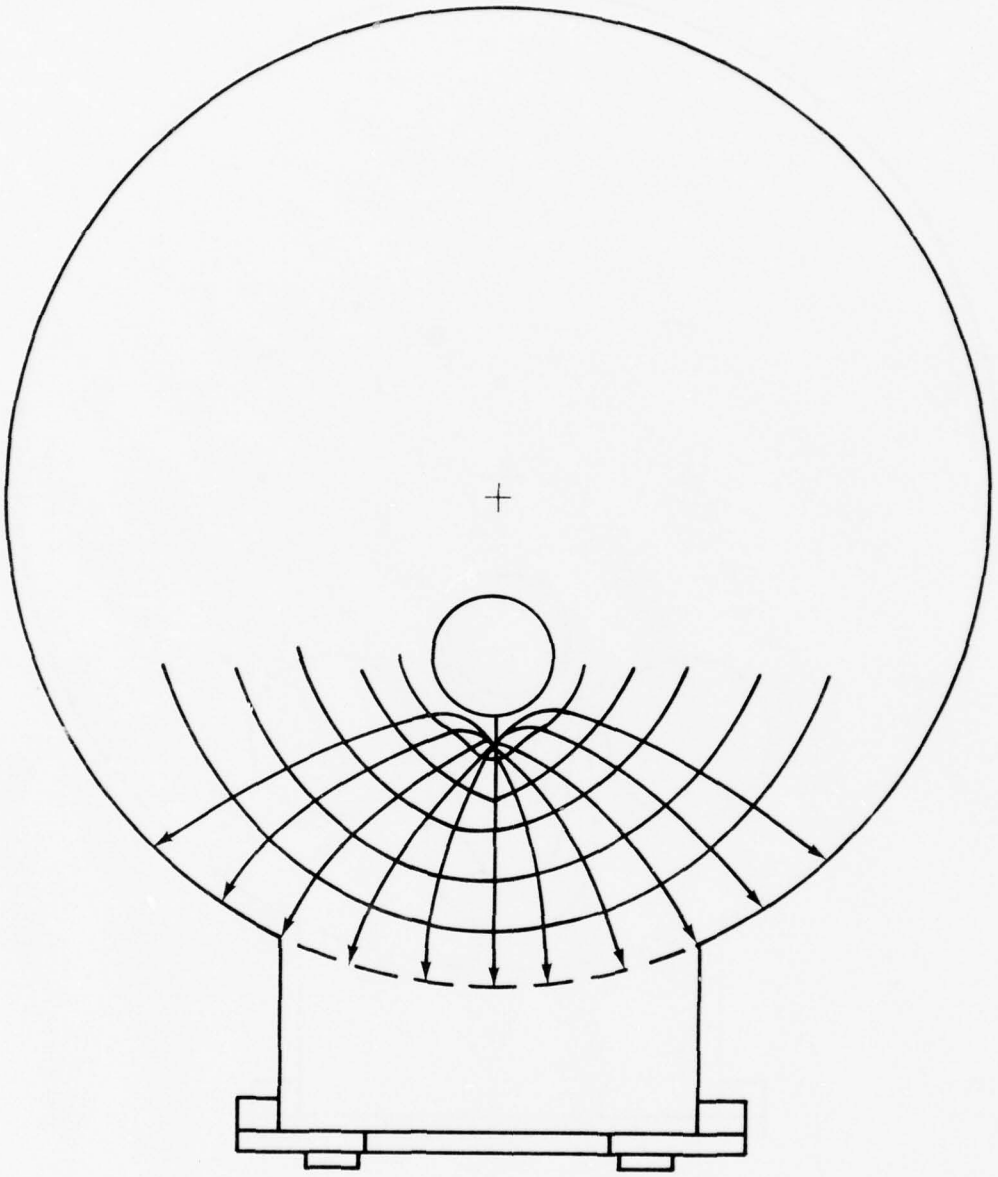


Figure A-25. Schematic of system with no focussing.

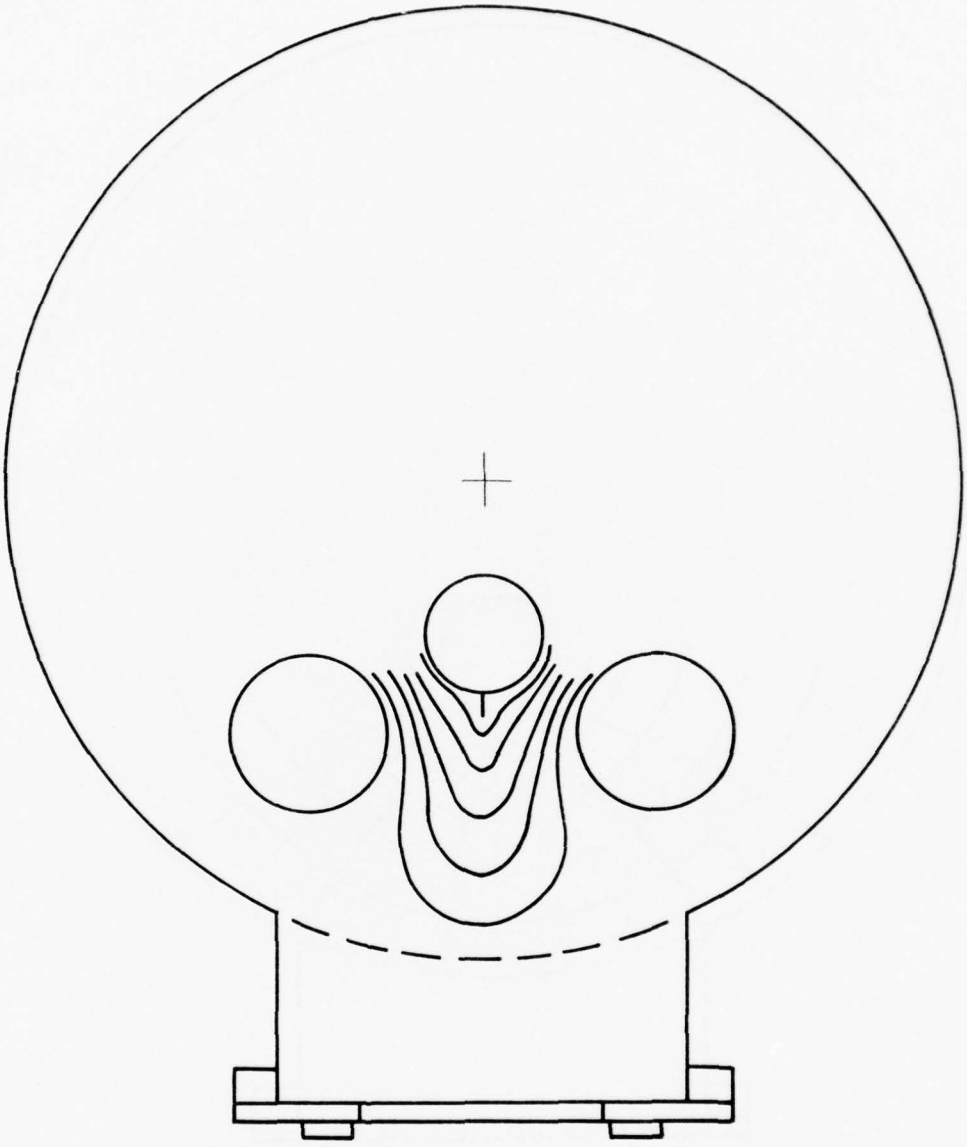


Figure A-26. Schematic, focus electrode added, ground potential.

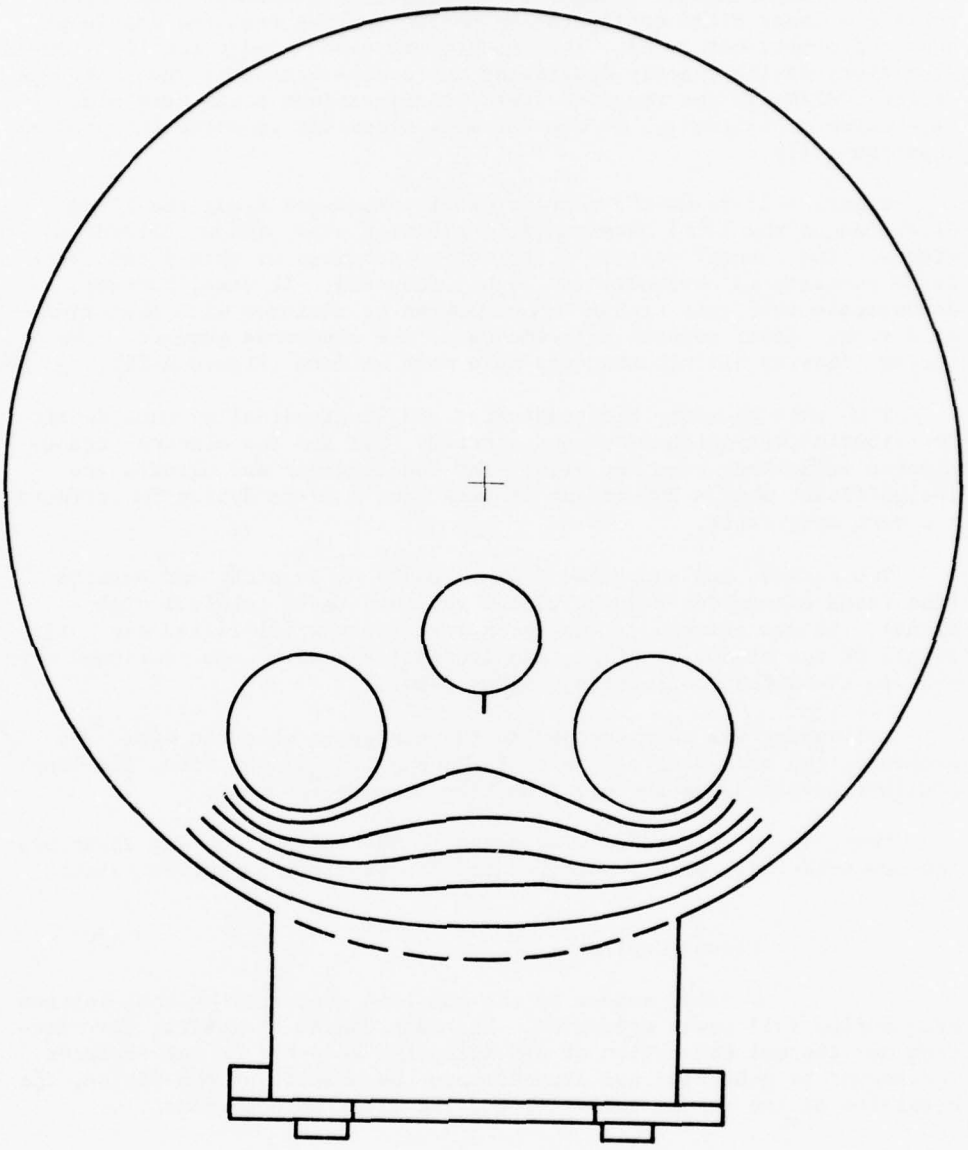


Figure A-27. Schematic, focus electrodes added, cathode potential.

Small experimental changes in spacings and geometries were made until the exact field configuration needed for the required degree of beam uniformity was found. This method was used because the 15- × 50-cm laboratory device exactly duplicates the cross-section of the prototype device. Although the required field configurations could have been calculated analytically, it was far more expedient to solve the problem experimentally.

Figure A-28 shows the current density measured along the 15-cm dimension of the 1-mil aluminum foil electron beam window, outside the window. The current density distribution produced by this first electrode geometry is obviously too highly focussed. It does, however, demonstrate that very high efficiencies can be achieved with this type of device. After several adjustments of the electrode geometry, the current density distribution was made more uniform (Figure A-29).

With this geometry the transverse and longitudinal current density distribution was uniform to approximately 10% and the electron transmission efficiency remained high. The longitudinal end effects are insignificant when a 200-cm gun is used; for a 50-cm device the effects are more noticeable.

The cathode was shortened from 50 to 20 cm to study end effects (the focus electrodes and the window retained their original dimensions). It was observed visually that the beam still filled the entire length of the window opening. Longitudinal spreading was confirmed with the use of current collectors (Figure A-30).

Cellophane was then exposed to the energetic electron beam. By examining the shadowing of the cellophane by the window ribs, the longitudinal spreading of the electron beam becomes apparent.

Next, focus electrodes were added to the ends of the gun structure; the new uniformity data showed reduced longitudinal spreading (Figure A-31).

D. Vacuum Gassing

Gassing refers to the gas load generated by the electron beam during full power operation. The main causes of gassing are electron and thermal desorption of gas molecules absorbed on the surfaces. The amount of generated gas depends upon the history of the device, the condition of the vacuum surfaces, and the electron beam power.

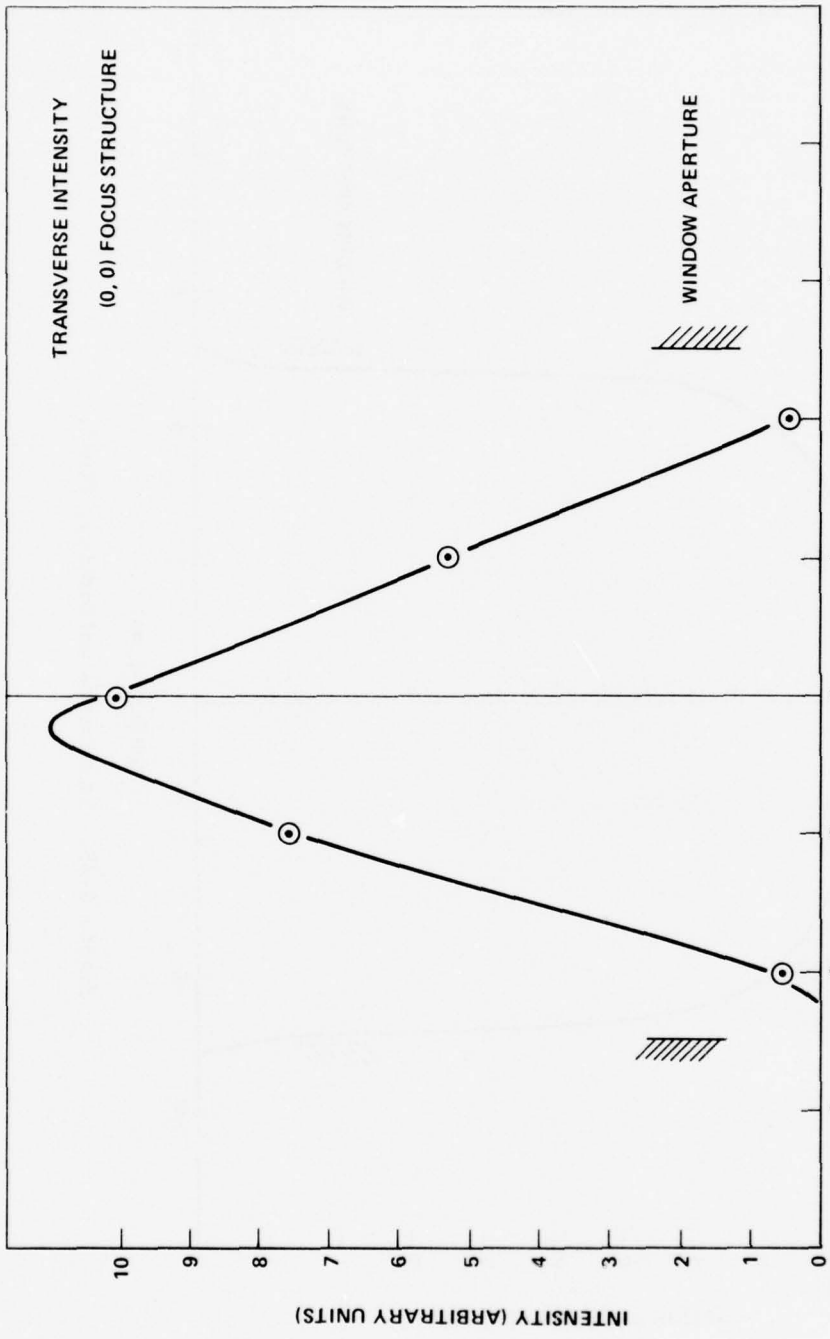


Figure A-28. Transverse uniformity, initial.

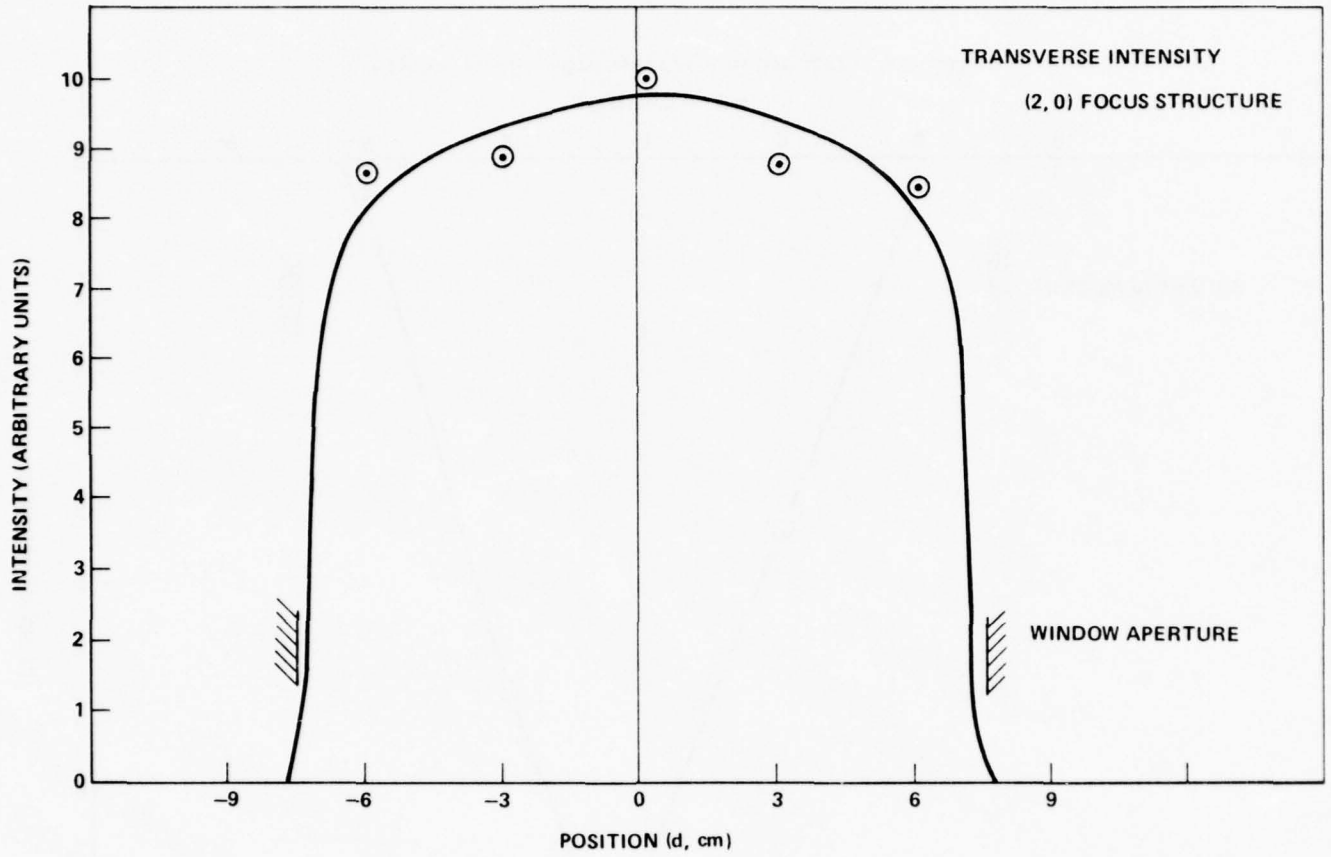


Figure A-29. Transverse uniformity, final.

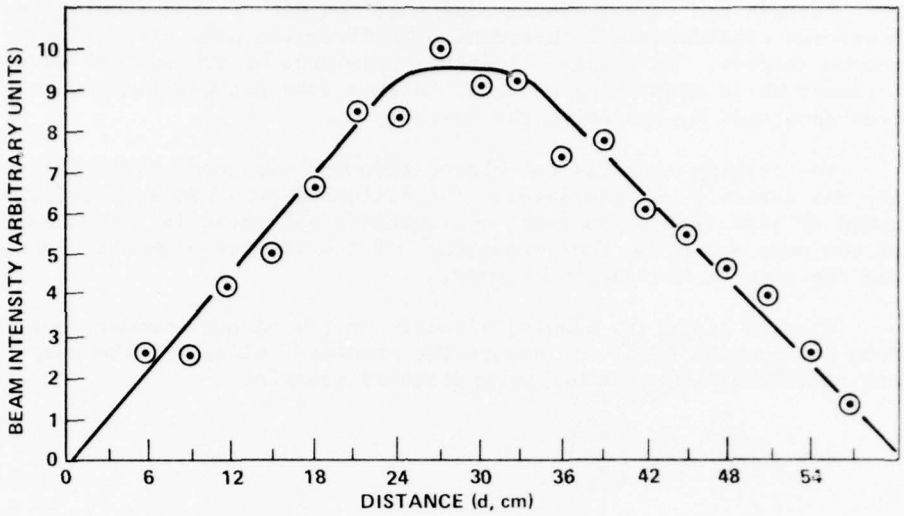


Figure A-30. Longitudinal intensity profile, unfocussed.

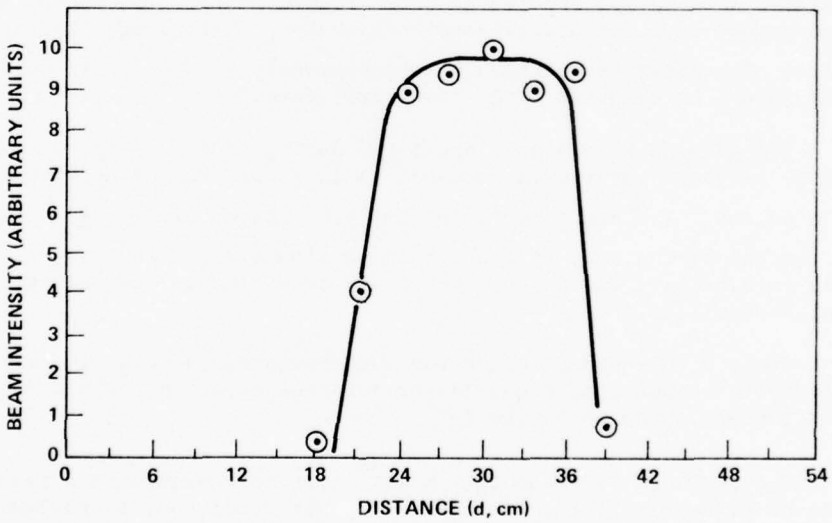


Figure A-30. Longitudinal intensity profile, unfocussed.

Because the vacuum system used here did not utilize a cold trap, there was considerable backstreaming of diffusion pump oil into the vacuum chamber. No special cleaning procedures or precautions were followed while assembling the gun. System bake-out was limited to the heat generated by operating the device.

The gassing rate was calculated from the measured pressure rise and the system's pumping speed. The diffusion pump has a specification speed of 1400 ℓ/sec. However, the system's net speed is a combination of the pump speed and the conductance of the various elements connecting the pump to the vacuum chamber.

The ion gauge was mounted directly on the vacuum chamber (away from the pumping port) to measure the pressure reliably. The pump speed was calculated using the following standard equation:

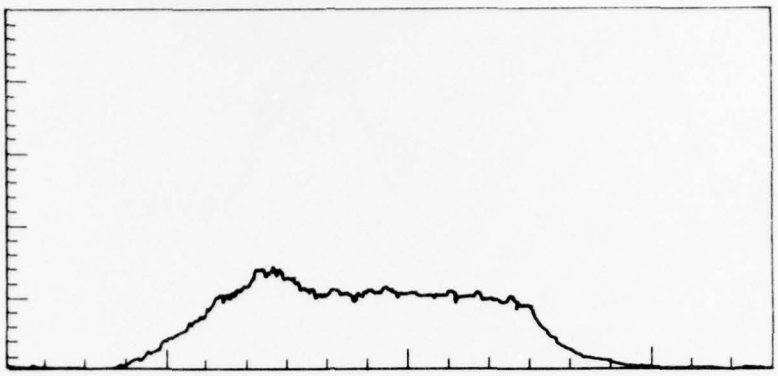
$$S = -\left(\frac{V}{t}\right) \log_e \left(\frac{P_2}{P_1}\right)$$

The pump speed of 1400 ℓ/sec is constant below approximately 10^{-3} torr; it can be expected to decrease at higher pressures. For steady state conditions, the gassing factor, Q, is equal to the pumping speed times the pressure. Gassing coefficients corresponding to electron and thermal desorption of gas were measured. Electron desorption was responsible for the pressure rise observed when the electron beam was operated at a 10-pps repetition rate (Figure A-32). The system had been pumped down for approximately three hours before measurements were taken. The pressure increase by approximately 1×10^{-4} torr during the measurement corresponds to $Q \simeq 45$ mtorr ℓ/sec.

The gassing rate slowly decreased during continued operation. In Figure A-33 the gassing is shown for a long term run of approximately 2000 pulses. The pressure is initially approximately 1×10^{-4} torr. By the end of the run, it drops to approximately 5×10^{-5} torr. After this point, there was no evidence of further cleanup and reduction of the gassing rate.

Next, a full power 10-sec run was attempted to determine the gassing rate at the conditions required for the prototype gun. The results of this run are shown in Figure A-34.

The pressure increase to 5×10^{-4} torr corresponds to a gassing rate of 0.22 torr ℓ/sec. At the full power condition, approximately 20 kW is supplied to the gun chamber. At least 12 kW of this power is transmitted through the thin aluminum foil to the atmosphere. The remaining 8 kW is deposited in the chamber walls, the foil, and the foil supporting ribs. The gassing rate of 0.22 torr ℓ/sec corresponds to a release of 7×10^{19} nitrogen molecules/sec.



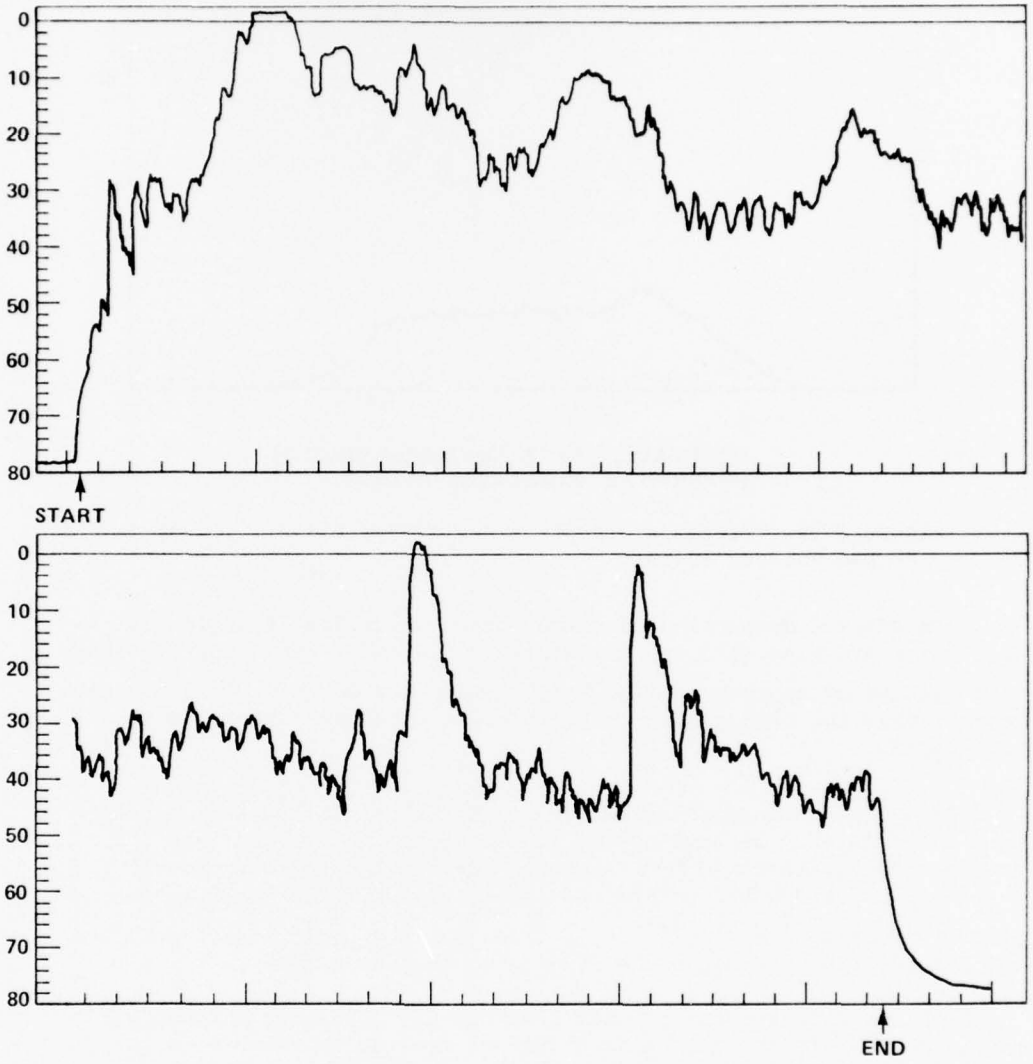
VERTICAL: 1×10^{-4} torr/LARGE DIVISION
HORIZONTAL: 20 sec/LARGE DIVISION

Figure A-32. Pressure history - new system 250 kV, 600 A, 3-μsec pulses, 10 pps.

For thermal desportion of chemabsorbed molecules, energies of desorption are generally approximately 100 kC/mole. This corresponds to a release of approximately 4×10^{20} molecules/sec (for 8 kW of beam power); thus the high gassing rate is consistent with thermal desorption rates.

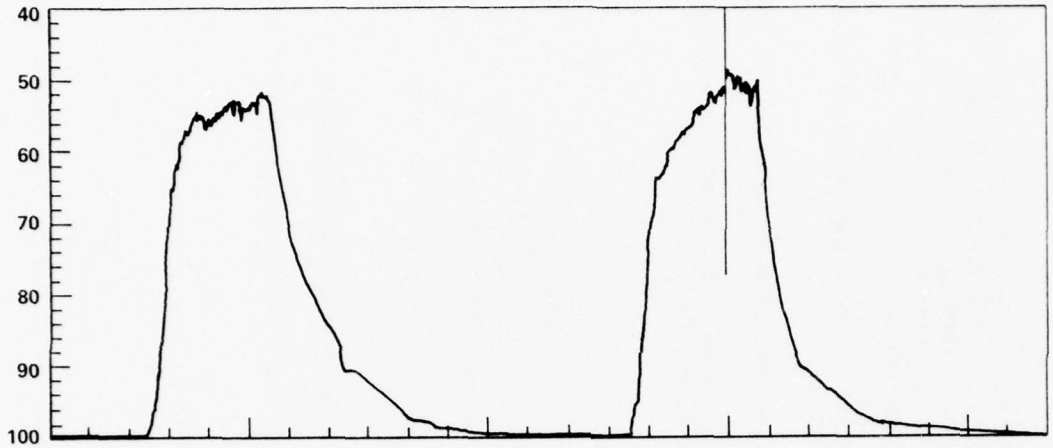
With the residual pressure at 5×10^{-4} torr, it takes 1 μsec to form a monolayer. Because of the fast repopulation of the absorbed gas, a clean surface is never achieved despite the sufficient heat available to desorb the monolayers completely. If the residual gas pressure were 10^{-7} or 10^{-8} torr, a clean surface could be produced and maintained; the tremendous gas loading would then cease.

In long duration runs, other portions of the vacuum chamber will become heated via thermal conductivity of the vacuum chamber walls, preventing the system from maintaining its pressure. To obtain a completely clean system, average temperatures of the vacuum chamber walls' inside surfaces must reach 400°C.



VERTICAL: 1×10^{-5} torr/LARGE DIVISION
HORIZONTAL: 20 sec/LARGE DIVISION
BASELINE: 2×10^{-5} torr

Figure A-33. Pressure history — long duration run 250 kV, 600 A, 3-μsec pulses, 10 pps.



VERTICAL: 1×10^{-4} torr/LARGE DIVISION
HORIZONTAL: 20 sec/LARGE DIVISION

Figure A-34. Pressure history — full power run 250 kV, 600 A, 3 μsec pulses, 10 pps.

E. Window Technology

A window that can transmit the full 0.5 A/cm^2 beam is well within the present technological capability. The average current is 75 $\mu A/cm^2$ -- much less than the present maximum of approximately 300 $\mu A/cm^2$.

In designing the window, the thermal problem was separated into two distinct one-dimensional problems; the first dealt with transport of heat from the foil into the ribbed foil support structure; the second treated heat transport from the ribs into the window's surrounding heat sink and the water cooling tubes.

The window material used in all of the experiments and calculations was 1-mil aluminum alloy No. 5051T6.

1. Problem 1. Thermal Transport from Foil to Rib

The following thermal calculation was used to determin the maximum temperature in the foil:

$$\frac{\text{Power absorbed in foil}}{\text{Unit area}} \approx q_2''$$

$$\frac{\text{Power absorbed in foil}}{\text{Unit volume}} \approx q_2'''$$

then the temperature difference in the foil is given by

$$\theta_o = \frac{q_2'''}{2k} L^2$$

where K = thermal conductivity and 2L = width of window foil.

If it is assumed that 20% of the beam power is deposited in the foil, then

$$q_2'' = 4 \text{ W cm}^2 = 12760 \text{ BTU hr}\cdot\text{ft}^2$$

$$q_2''' = 1.5 \times 10^8 \text{ BTU hr}\cdot\text{ft}^3 \quad .$$

If separation between ribs is chosen as 2L = 0.281 in. the the temperature drop is

$$\theta_o = \frac{(1.5 \times 10^8)}{2(130)} \left(\frac{.14}{12}\right) = 79°F$$

from the center of the foil to the rib.

The rib must then conduct the heat from the foil; and the energy deposited directly into the rib, to the heat sinks.

2. Problem 2. Thermal Transport from Rib to Heat Sinks

For mechanical reasons, a rib width of 0.125 in. and a height of 0.5 in. has been chosen as follows:

$2L$ = 2 lengths between heat sinks

q_1'' = (heat transfer from foil) + (energy deposited in rib)

$q_1'' = 160 \text{ BTU/hr}\cdot\text{ft}^2$

$q_1''' = 3.8 \times 10^3 \text{ BTU/hr}\cdot\text{ft}^3$

$$\theta_1 = \frac{q_1'''}{2k} L^2$$

$\theta_1 = 8.30°\text{F}$.

Thus, the maximum foil temperature is as follows:

$$T = T_{\text{ambient}} + \theta_{\text{rib}} + \theta_{\text{foil}}$$

$T = 72°\text{F} + 8.3°\text{F} + 79°\text{F}$

$T = 160°\text{F}$

This temperature is well below material temperature limits. The window was constructed according to the given dimensions (Figure A-35).

These calculations indicated that thermal loading of the window foil should not be a problem. None were encountered during the experiments. Window foils were damaged, however, either as a result of sparking within the gun or because of stress concentration caused by wrinkles in the foil. It is important that all edges where the window foil contacts the support structure have adequate radii. Sharp edges at the contact point will cause stress fatigue in any repetitive pulse application. These problems are not likely to appear in a full size fieldable device.

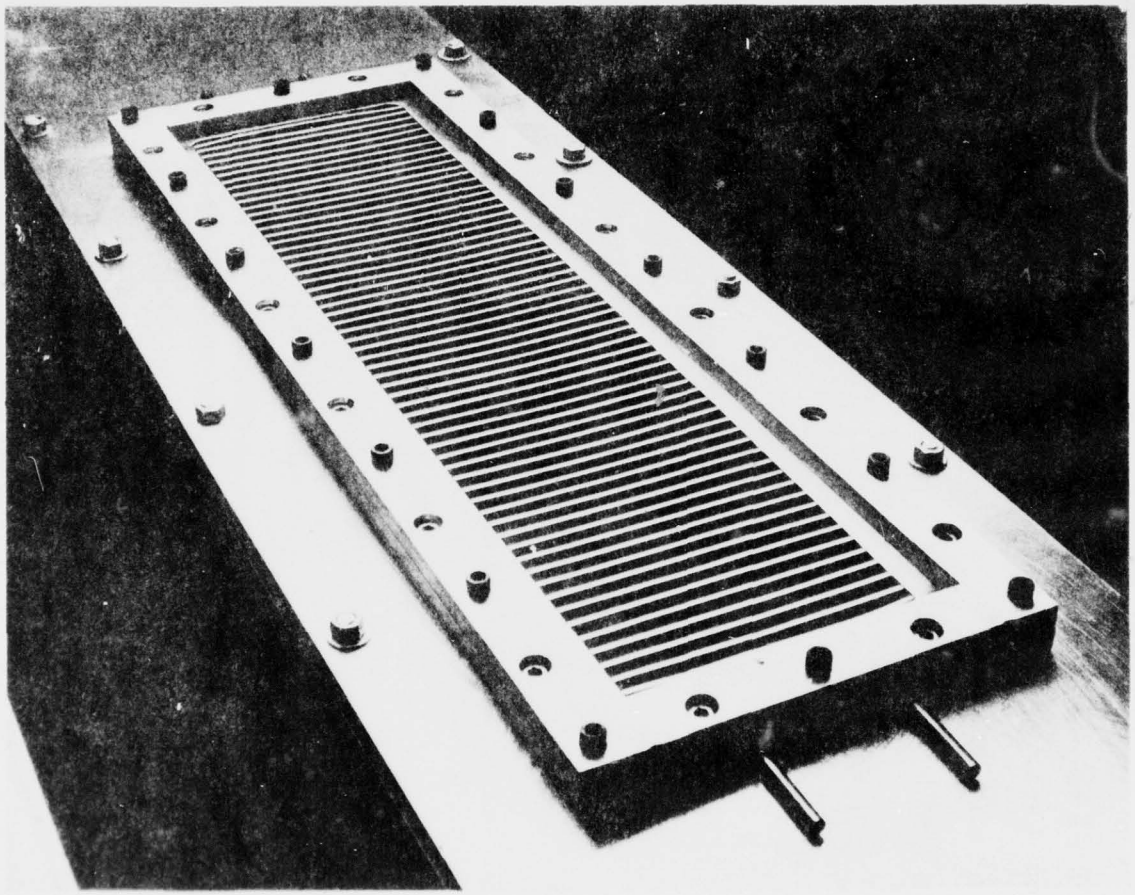


Figure A-35. Water-cooled window structure.

F. Beam Spectrum Analysis

An experimental analysis of the electron beam energy spectrum was made with charge dosimeter foils (Figure A-11). This apparatus was mounted inside the vacuum chamber of the electron beam gun. Five current collectors and four foils were positioned so that there was no foil over the first collector, a 1-mil foil over the second, a 2-mil foil over the third, a 3-mil foil over the fourth, and a 4-mil foil over the fifth collector. All foils connected directly to ground; all collectors were isolated from ground.

The signal measured by each collector was in proportion to the total incident electron current less any current trapped within the foil. The reflections of incident electrons were ignored, because both the foil and collectors were made of aluminum. This techiique was used in favor of the originally proposed foil heating measurement.

A dn/de probability distribution was established for the S-Cubed Eltran Monte Carlo code using the time varying cathode voltage and current as normalizing factors. The Monte Carlo electron code selected individual particles depending on the probability distribution. The code was set up to solve a five-slap problem, with 1-mil aluminum specified for the first four slabs and 50-mil aluminum for the fifth slab. The calculated charge deposition in each of the slabs was then compared to the measurements made with the foil/collector array (Figure A-36). The calculated and measured values agree. From this, it is concluded that there are no unknown low energy components in an electron beam generated by a cold cathode. Therefore, standard Monte Carlo techniques, the gun voltage, and current pulse shapes can be used to calculate the heating factor.

Window loading is minimized when the beam electrons have high kinetic energy and when the pulse rise and fall times are short compared to the pulse duration.

4. Design Study

The data from this program were used to develop a conceptual design for a cold cathode electron beam gun with a 15- × 200-cm emitting area; the gun can operate at 50 pps for 10-sec bursts. (Sufficient time must be provided between bursts to let the components cool.)

The design point for electron beam current density was 0.5 A/cm^2 at voltage up to 300 kV.

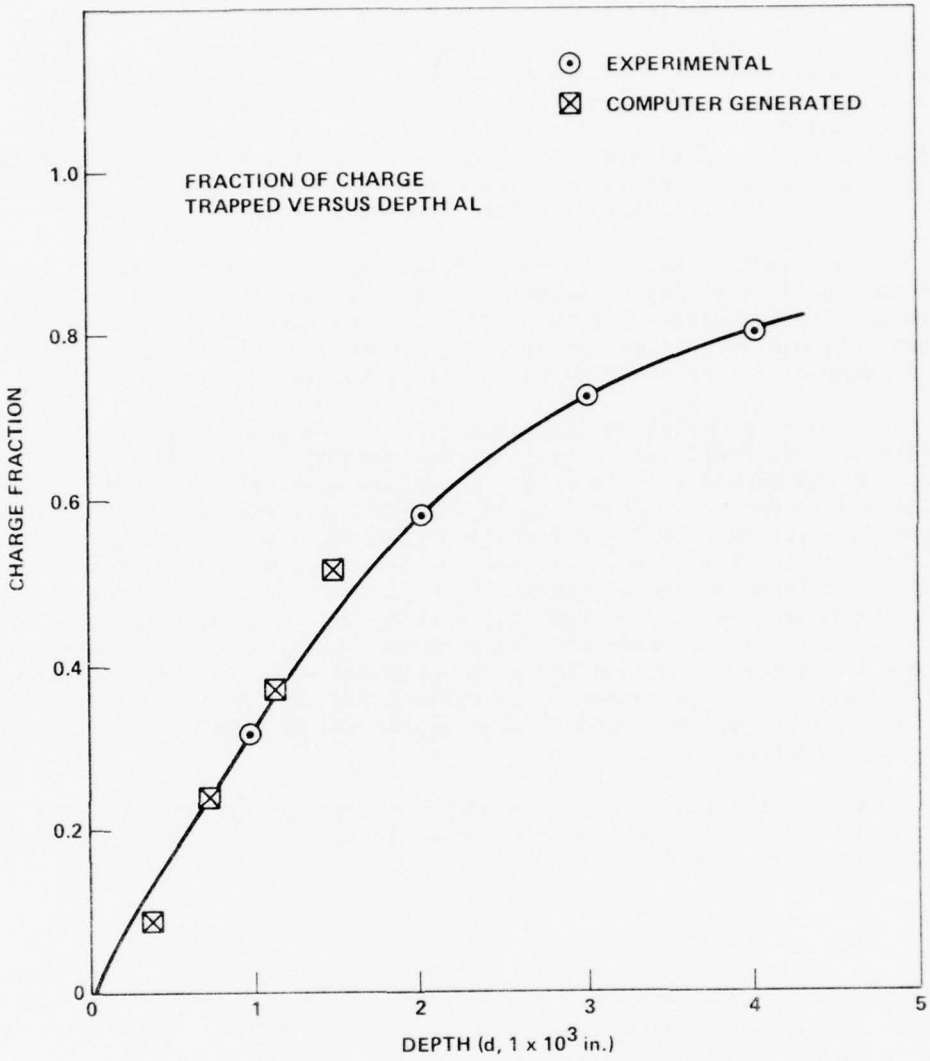


Figure A-36. Curve (dq/dx).

This section will discuss the following:

1) The exact design required for the electrode structure.

2) An output window capable of meeting the design specifications.

3) Vacuum systems sized to handle the gassing load developed by the high power beam.

4) A prototype design for the power equipment.

A. Electrode Structure

As foreseen, use of a full scale cross-section gun in the laboratory experiments enabled design of the prototype gun with minimal scaling of data. The only significant difference between the laboratory and prototype gun is the increase in length from 50 to 200 cm. Previous S-Cubed programs have established that single pulse guns scale linearly with length from 50 to at least 200 cm; no additional complications are introduced by multipulse operation.

A detail of the cathode cross section is shown in Figure A-37. Further details are given in Section E.

B. Output Window

The window structure developed for the test device satisfies all of the prototype device requirements.

A second window design, however, has been considered. The second design is intended to minimize the angular deflection of the foil at the edges of the cooled ribs. This area of the foil will most easily suffer damage in repetitive pulse operation. One solution to this problem is further subdivision if the supporting ribs. For example, rather than using ribs 0.125 in. wide as in the test device, ribs 0.03 in. wide can be spaced to obtain the same optical transmission. The angular deflection of the foil is considerably lessened. It should be noted that construction costs increase rapidly with the number of ribs.

An alternative technique is to use a thin, perforated high-conductivity metal sheet behind the foil with support ribs spaced 1 to 2 in. apart (Figure A-38). (The metal sheet can be perforated either by chemical etching or by punching.) This reduces the angular deflection by approximately one order of magnitude, greatly increasing the foil's lifetime. It should be noted, however, that the test device should have foil lifetimes well in excess of the 50,000-shot goal for the prototype system.

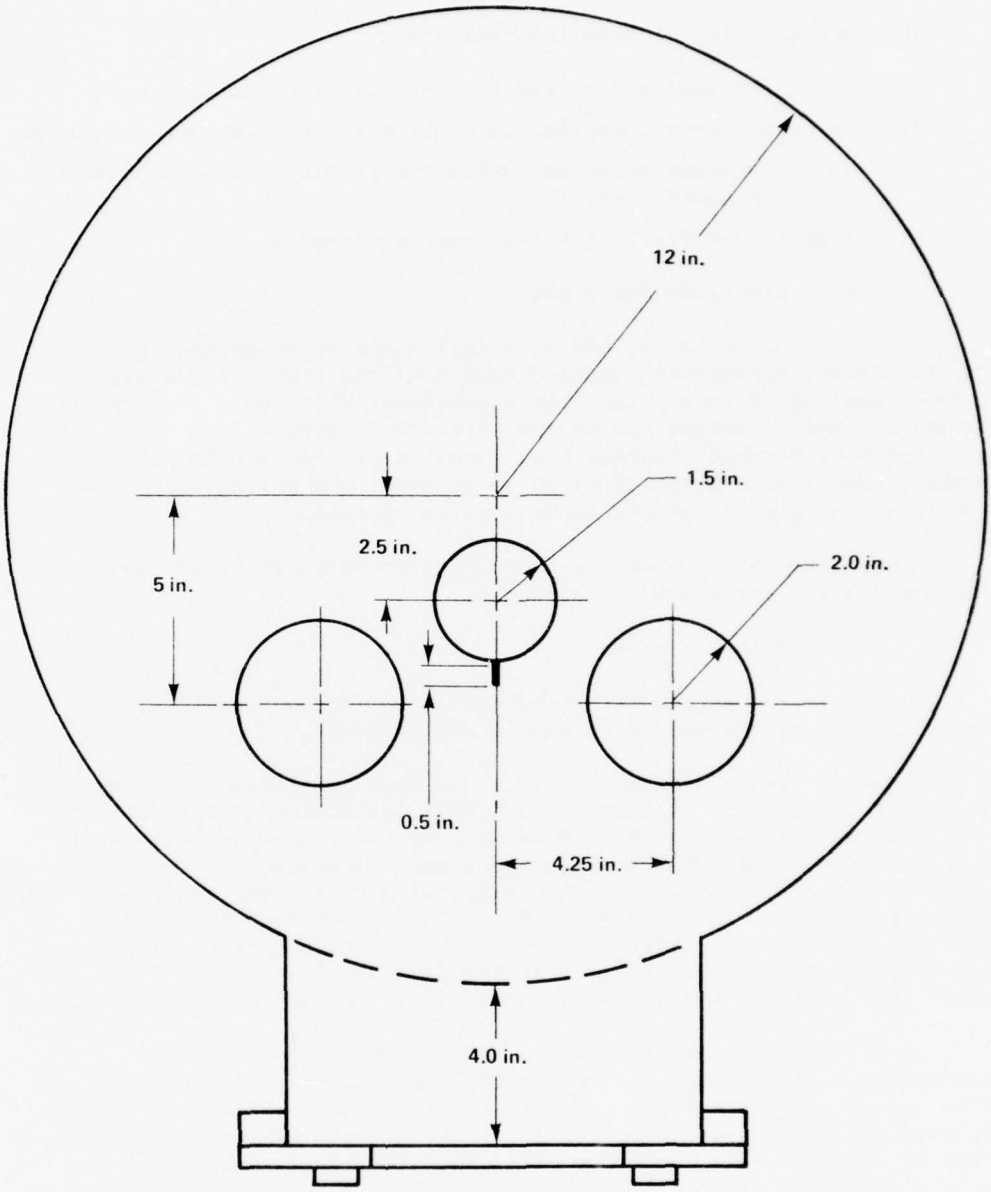


Figure A-37. Electrode geometry prototype device.

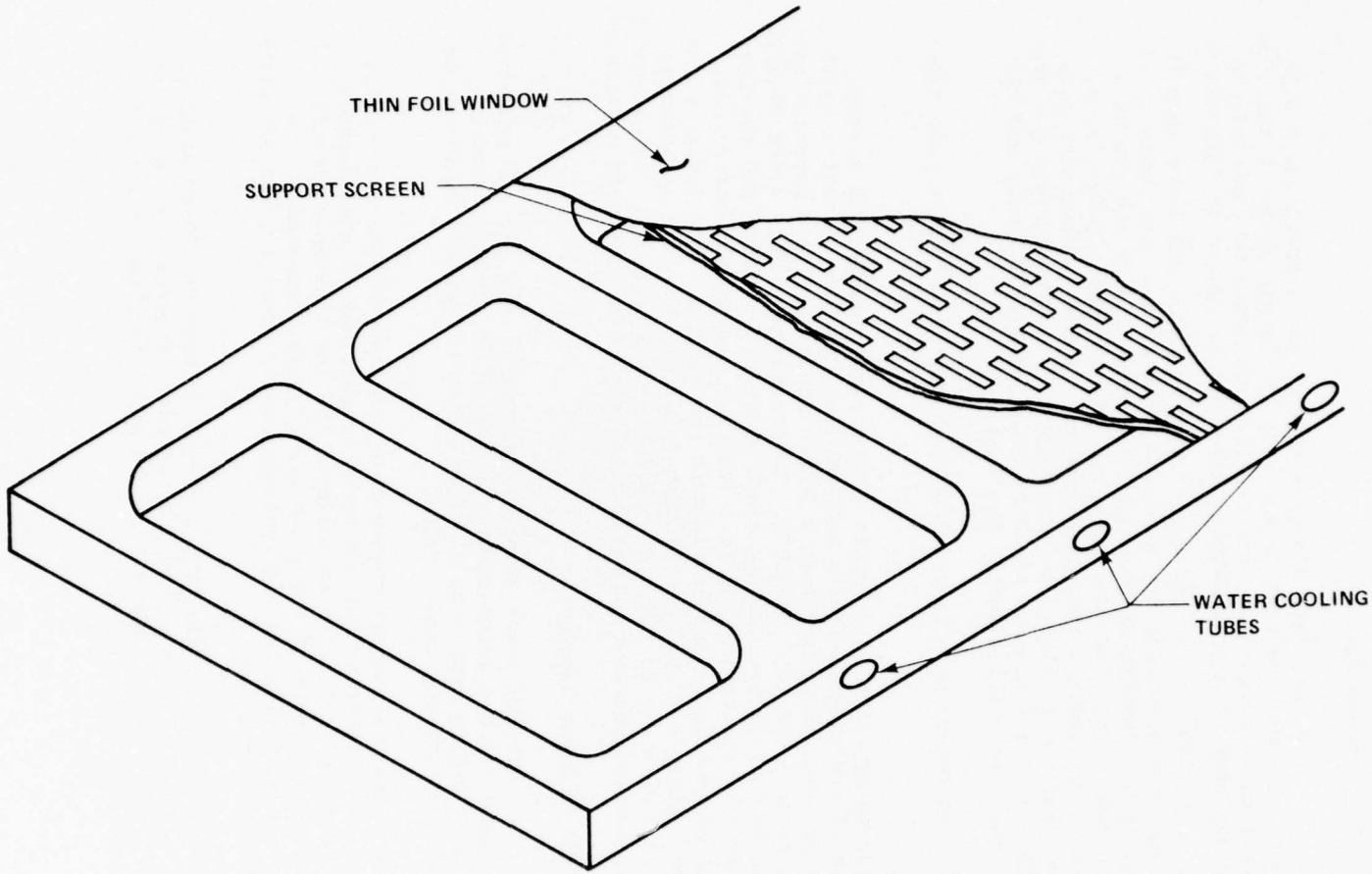


Figure A-38. Perforated window support scheme.

DISTRIBUTION

C. Vacuum System

The test device's gassing rate was approximately 0.22 torr ℓ/sec. Because the test device is a 1/4 length scale of the prototype device, an outgassing rate of 0.88 torr ℓ/sec is expected. A net pumping speed of approximately 4400 ℓ/sec is needed to maintain a pressure of 2×10^{-4} torr. (2×10^{-4} torr is two times lower than the maximum suitable operating pressure, as shown in the test device.) A conservative net pumping speed has been chosen because the use of a diffusion pump with a low backstreaming rate was anticipated; also, mild bake-out procedures can be instituted. A 10-in. diffusion pump with a Mexican hat to limit backstreaming can adequately pump the prototype device. This assumes close coupling between the pump and the vacuum chamber (overall assembly drawing).

A 24-cfm rotary pump is required to back the diffusion pump system.

A second approach is to begin with a clean, well-baked system. This type of system generates a much smaller gas load so that a smaller pump can be used. However, such a system would require a bake-out temperature of at least 400° to 450°C. Temperatures of this order require all-metal seals (rather than the usual elastomer o-rings) and require several days of processing before a stable vacuum can be maintained. The required techniques are standard in the electron tube industry. At the present time, cost of construction (plus the downtime experienced in the event of a window failure) precludes this approach. For advanced fieldable devices, however, this approach should be seriously considered.

D. Power Supply

Several power supply types can be used for the prototype device. These include pulse forming lines, pulse forming networks, series pulse forming networks, Blumlein networks, and all combinations with or without step-up transformers.

A PFN pulse transformer combination was used for the test device power supply. Whether or not a step-up transformer is used depends upon the relative difficulty of building the low impedance circuit required in the primary of the pulse transformer, compared to the difficulty in achieving the high voltage requirements for the PFN without the transformer.

In the case of a single PFN, a charge voltage of 500 kV would be required to obtain 250 kV on the gun cathode. Figures A-39 through A-42 illustrate several of the basic types of power supplies suitable for the cold cathode electron gun.

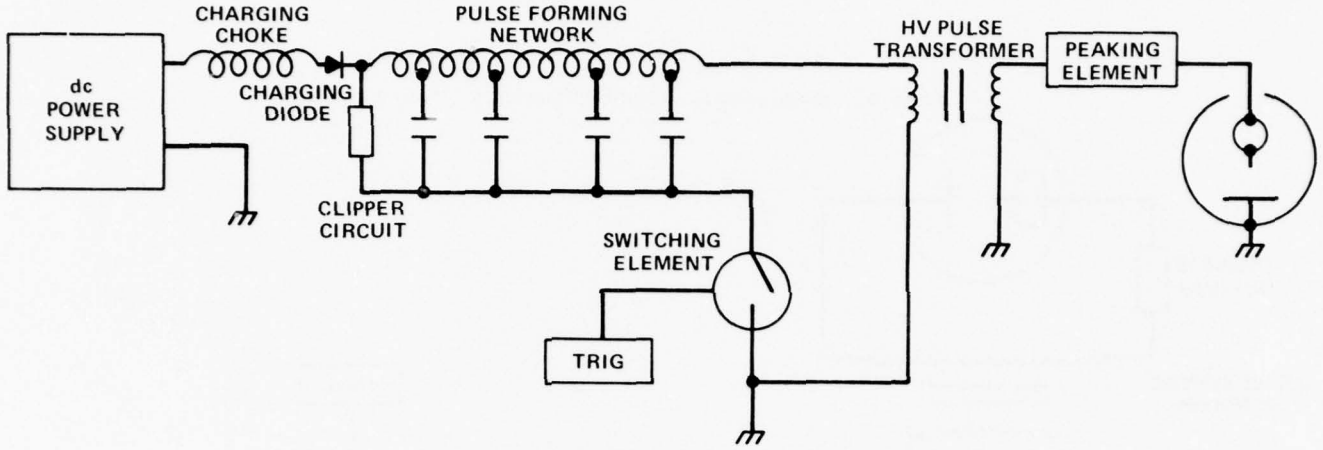


Figure A-39. PFN, pulse transformer pulser.

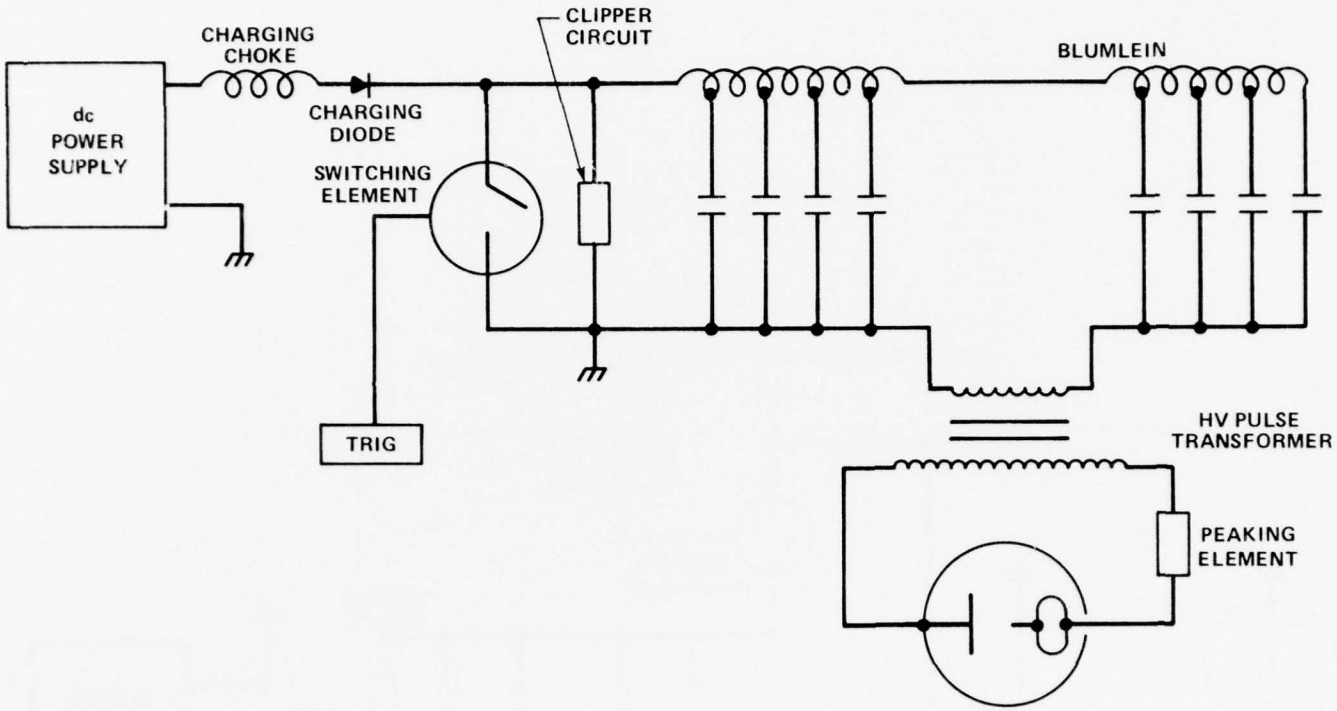


Figure A-40. Blumlein, pulse transformer pulser.

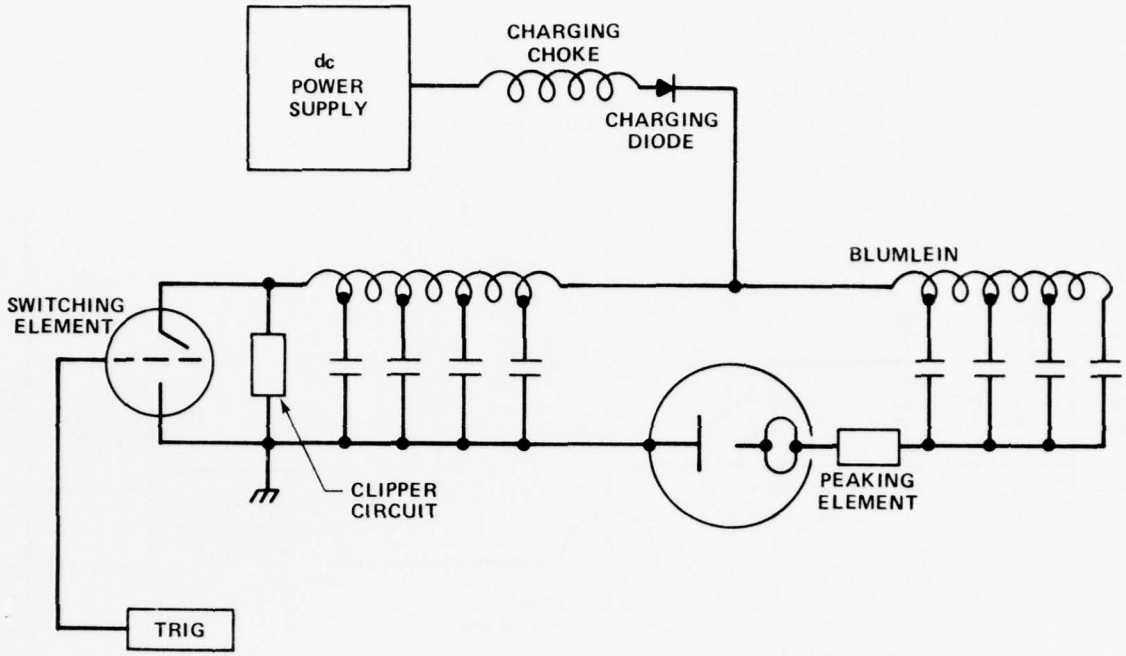


Figure A-41. High voltage Blumlein pulser.

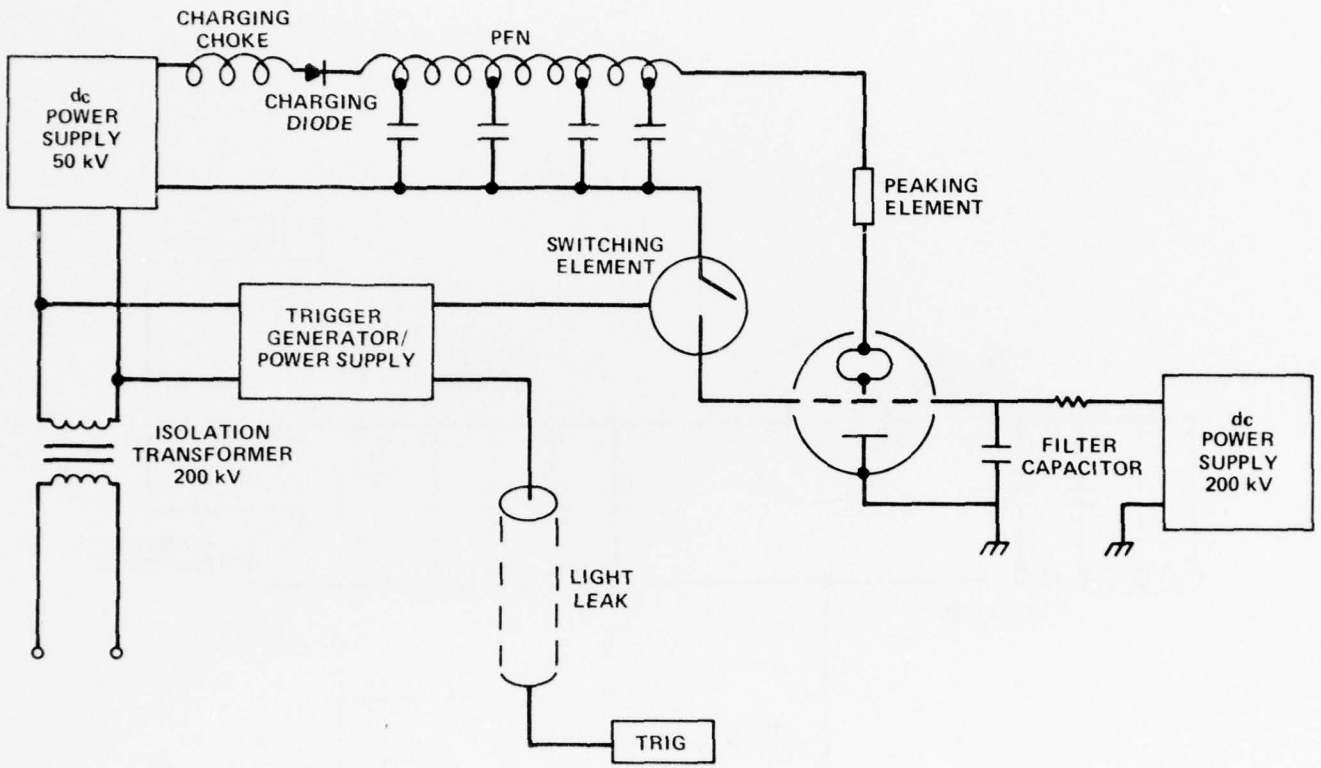


Figure A-42. Grid modulated cold cathode gun.

Parameter values for several combinations are given in Table A-2. PFN parameters listed are nominal; adjustment of the PFN impedance would compensate for the variable impedance of the cold cathode diode.

Assuming that the ECOM-MAPS-70 thyratron is available, the Blumlein-transformer combination (listed in the second column of Table A-3) is the optimum choice. The Blumlein offers the advantage of a low turns ratio pulse transformer while maintaining a moderate primary circuit impedance and reliable thyratron switching. The entire supply (not including the 70-kV charging supply) can fit in a $4 \times 6 \times 5$ ft enclosure.

Depending on the situation, i.e. laboratory test bed, mobile unit, etc., other supplies may have a greater applicability than the one chosen. For example, spark gaps can offer significant volume and weight savings over the other types of devices listed.

In hopes of simplifying the modulator required for the diode type of gun, a grid-modulated cold cathode (triode) gun (Figure A-42) was investigated. With this grid-modulator, nearly all of the power comes from the dc supply; only a fraction is contributed by the modulator. This type of supply is used extensively on thermionic electron guns.

An important difference between cold cathode and thermionic cathode guns is the formation of a cathode plasma that can short circuit the cold cathode gun's grid to its anode. Grid-cathode shorts are not problems if they occur after the transmitted electron pulse.

The distances between the cathode, focus electrode, and anode in this experimental device are similar to the distances between cathode, control grid, and anode of a grid modulated cold cathode gun. These measurements show that the focus electrode maintained the bias voltage determined by the RC time constant of the biasing circuit (Figure A-43). The data show that (1) the plasma did not short circuit any electrodes and (2) a voltage applied to an electrode (grid) by a self-biasing circuit or dc supply will be maintained.

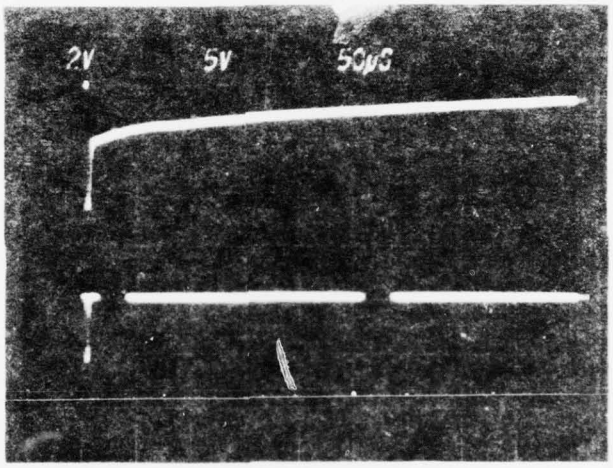
Therefore, a grid-modulated power supply (Figure A-42) could, in principle, be adapted to a cold cathode gun. High field strengths are needed to obtain uniform emission (Section 3. B. 1.). This implies a lower limit to the modulator voltage of at least 50 kV. The necessity for high voltage nullifies any advantage this type of scheme may have offered. Therefore, this type of power supply was not investigated further.

TABLE A-2. ALTERNATE POWER SUPPLY PARAMETERS

	PFN - Transformer	Blumlein - Transformer No. 1	Blumlein - Transformer No. 2	Blumlein
$Z_{Secondary}$	83 Ω	83 Ω	83 Ω	83 Ω
V_{Charge}	70 kV	70 kV	70 kV	70 kV
Turns Ratio	1:7.2	1:3.6	1:1	1:6.25
$Z_{Primary}$	1.6 Ω	6.4 Ω	2.1 Ω	83 Ω
$I_{Primary}$	22 kA	11 kA	19 kA	3 kA
Switching Element	1. 3 each EEV-CX1175 -Thyratron 2. 1 each ECOM-MAPS -70- 3. (Spark Gap)	1. 2 each EEV-CX1175 -Thyratron 2. 1 each ECOM-MAPS -70-Thyratron 3. (Spark Gap)	1. 2 each NE-NL -Ign 2. 3 each EEV-CX1174 -Thyratron 3. 1 each ECOM-MAPS 4. (Spark Gap)	1. 1 each ECOM 250 kV Tube 2. (Spark Gap)

TABLE A-3. DESIGN FEATURES OF OPTIMUM SYSTEM

Subsystem	Design Features
Gun	Single tantalum strip emitter Self biasing focus electrodes Stainless steel construction Water-cooled window
Vacuum System	10-in. close couple low backstreaming Diffusion pump 24-cfm mechanical rotary pump
Power Supply	Blumlein driver pulse transformer Thyratron switching Spark gap peaking switch



TOP: VOLTAGE FOCUS ELECTRODE
50 μs/DIVISION, 100 kV/DIVISION
BOTTOM: OUTPUT CURRENT DENSITY
50 μs/DIVISION, ~0.2 A/cm^2/DIVISION

Figure A-43. Focus electrode voltage trace.

E. Prototype Design Summary

The prototype design embodies all of the design features developed during the experimental program. Table A-3 summarizes the design features of the system.

A cutaway isometric view of the electron gun is shown in Figure A-44. A complete system view is shown in Figure A-45. The latter view includes the electron gun, vacuum pump, and power supply.

5. Summary

The S-Cubed Rapid Pulse Facility has been used to study repetitive pulse operation of cold cathode electron beam guns with accelerating voltages to 300kV, pulse lengths from 2 to 10 μsec and repetition rates to 50 pps. Data obtained from this study were used to design conceptually a 15 × 200 cm repetitively pulsed cold cathode electron beam gun system.

Some of the highlights of the data obtained in this program are contained in the following paragraphs.

A. Emitter Foil Lifetime

Correlation of the number of emission sites and the mass removed per emission site indicates that foil lifetimes in excess of 50,000 shots are easily achieved. Lifetimes up to 10^7 shots are probable, provided that a fast rising voltage pulse is applied to the cathode.

B. Gun Impedance

Measurement of gun impedance at 50 pps for pulse widths from 3 to 9 μsec shows that both repetitively and single pulsed guns operate in a space charge limited mode. It follows that existing data from single pulse guns can be used in the design of multiple pulse guns by using the voltage and area scaling rules for space-charge limited operation.

C. Beam Focussing and Efficiency

It was demonstrated that self-biasing focussing electrodes can shape the beam profile in both transverse and longitudinal dimensions. Measurements of the beam current density outside the foil window (using a collector array and cellophane dosimeters) revealed that the beam edge profile can be dramatically altered with focussing electrodes. This will increase gun efficiency substantially above 50%.

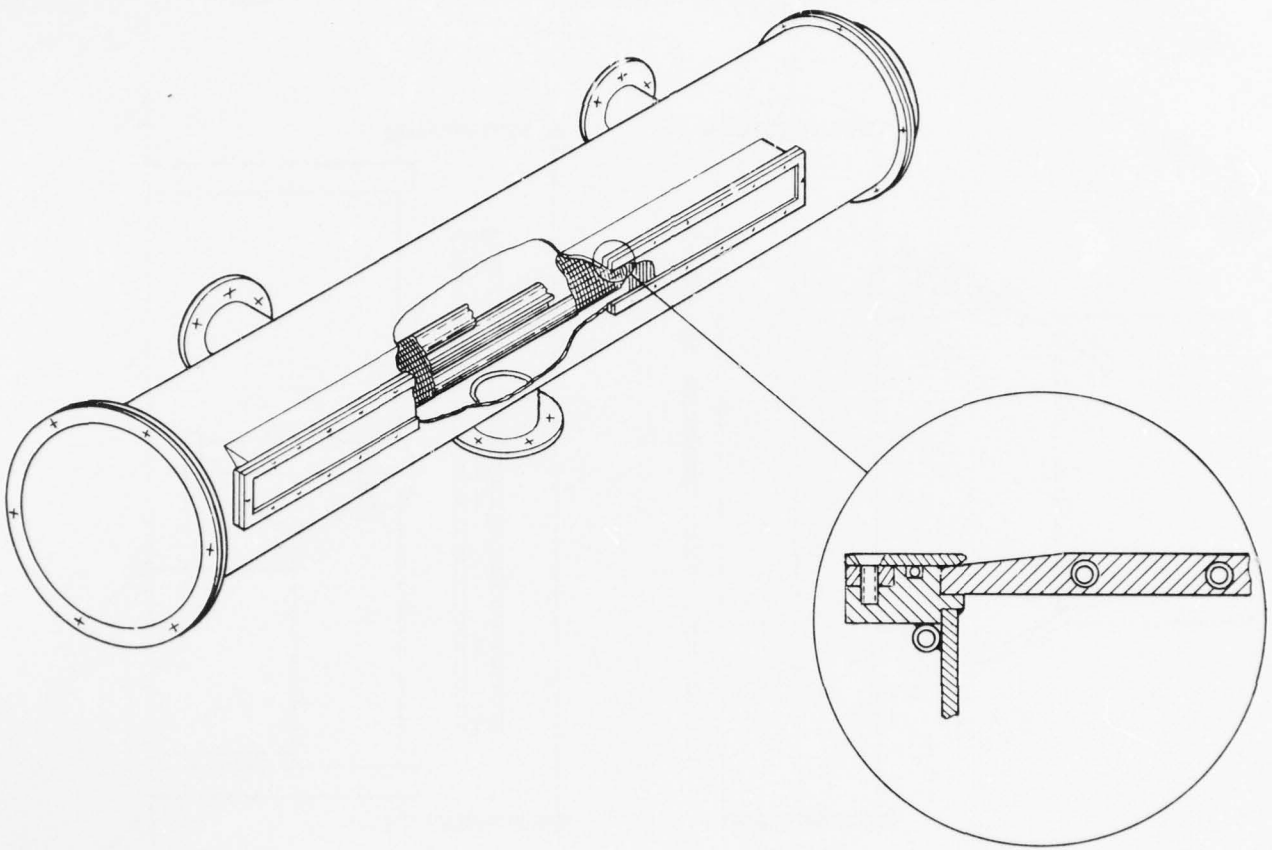


Figure A-44. Full scale prototype gun.

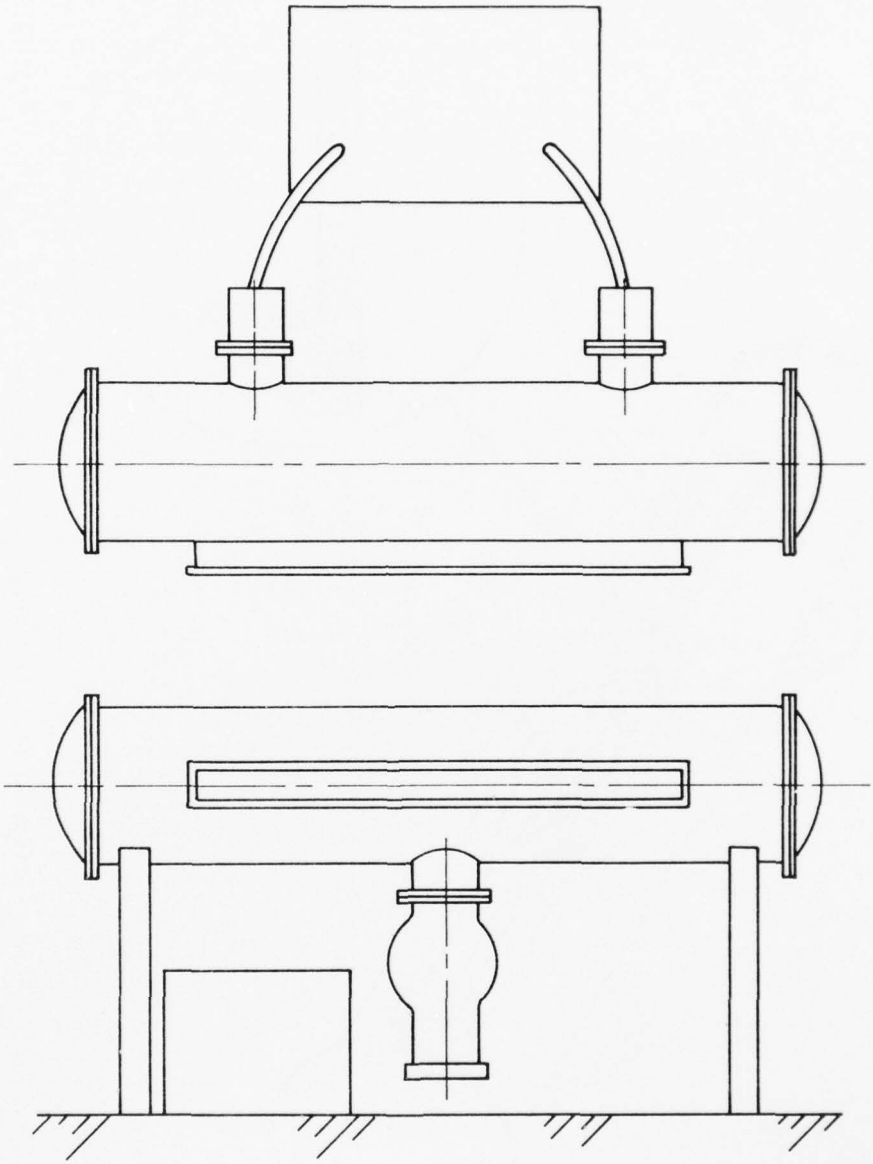


Figure A-45. Full scale prototype system less 20 kV charging supply.

D. Vacuum Requirements

The measured gassing rate under high-average power conditions is consistent with thermal desorption of gas from the gun chamber walls. Operation of the gun at pressures of 10^{-4} torr causes rapid reabsorption and precludes gun clean up. This suggests two approaches to gun/vacuum system design:

1) Moderate vacuum technology should be used and operated with large vacuum pumps.

2) Very high vacuum technology should be developed for the large guns and smaller pumps should be used.

In either case, the extreme importance of a leak free system is emphasized.

E. Thermal Loading of the Electron Beam Window

Thermal loading of the window by 75 $\mu A/cm^2$ as required for a full scale system does not limit the life of the window foils. (Failure mechanisms such as gun arcs or repeated extreme flexing of the foil must be avoided.)

F. Beam Energy Spectrum

Measurements made by placing current collectors behind absorbers of various thickness correlated with calculations of electron energy spectra made with the Eltran Monte Carlo code. An input spectrum based on the voltage and current waveforms was used. This demonstrated that anomalous low energy electrons, if present, are insignificant. Window loading can be calculated when the gun voltage and current waveform are known.

The design study focussed on a 15- × 200-cm electron beam gun system. The gun can operate at 50 pps for 10-sec bursts and provide 0.5 A/cm^2 at voltages up to 300 kV. The laboratory gun was purposely designed with full scale transverse dimensions, thereby simplifying the design of the full-scale gun. The electron beam window designed and built for the laboratory gun was also suitable for the full scale gun, although alternative methods for reducing foil flexing under multiple pulse conditions were suggested.

A vacuum system based on a conventional 10-in. oil diffusion pump and 24-cfm mechanical roughing pump best serves the present needs. Very clean, highly baked guns should be considered for future systems.

Assuming that the ECOM-MAPS-70 thyratron is available, a Blumlein-transformer with thyratron switching is the optimum choice for the power supply. The entire power supply should fit inside a $4 \times 6 \times 5$ ft enclosure.

Summaries of the conceptual design parameters and drawings of the gun and system are provided. Alternatives to the chosen power supply, vacuum system, and window are also provided.

DISTRIBUTION

	No. of Copies
Defense Advanced Research Projects Agency 1400 Wilson Boulevard	
Attn: Director, Laser Division	1
MAJ G. Canavan	1
Arlington, Virginia 22209	
OODR&E	
Attn: Assistant Director (Space and Advanced Systema)	1
The Pentagon Washington, D.C. 20301	
US Atomic Energy Commission Division of Military Application	
Attn: Dr. Lawrence E. Killion	
Washington, D.C. 20545	
National Aeronautics and Space Administration Lewis Research Center	
Attn: Dr. John W. Dunning, Jr.	1
21000 Brookpark Road Clevelend, Ohio 44135	
Defense Documentation Center Cameron Station	
Alexandria, Virginia 22314	12
Department of the Army DCSRDA	
Attn: DAMA-WSM-A (LTC Holmes)	1
DAMA-WS (Dr. McCorkle)	1
DAMA-AR (Dr. Garber)	1
Washington, D.C. 20310	
Department of the Army Deputy Chief of Staff for Plans and Operations	
Attn: DAMA-RQD (LTC Mayhew)	1
DAMA-RQD (LTC Fox)	1
Washington, D.C. 20310	
Department of the Army Assistant Chief of Staff Intelligence	
Attn: LTC Martin	1
Washington, D.C. 20310	
Commander US Army Mobility Equipment R&D Center	
Attn: SMEFB-MW	1
Fort Belvoir, Virginia 22060	
Commander Rock Island Arsenal	
Attn: SARRI-LR, Mr. J. W. McGarvey	1
Rock Island, Illinois 61201	
Director Ballistic Missile Defense Advanced Technical Center	
Attn: ATC-O, Mr. Davis	1
Mr. Hagefstration	1
Dr. G. Sanmann	1
ATC-T, Mr. L. Webster	1
ATC-R, Mr. Don Schenk	1
P.O. Box 1500 Huntsville, Alabama 35807	
Commander US Army Materiel Command	
Attn: DRCRD-T (Mr. Paul Chernoff)	1
DRCPM (CPT Phillips)	1
5001 Eisenhower Avenue Alexandria, Virginia 22333	

	No. of Copies
Director US Army Ballistic Research Lab	
Attn: Dr. Robert Eichelberger	1
Mr. Frank Allen	1
Dr. E. C. Alcaraz	1
Aberdeen Proving Ground, Maryland 21005	
Commander US Army Electronics Command	
Attn: DRSEL-CT-L (Dr. R. G. Buser)	1
Ft. Monmouth, New Jersey 07703	
Commander Letterman Army Institute of Research	
Attn: Division of Non-Ionizing Radiation	1
Presidio of San Francisco, California 94129	
Department of the Navy Deputy Chief of Naval Materiel (Dev)	
Attn: Mr. R. Gaylord (MAT 0328)	1
Washington, D.C. 20360	
Naval Missile Center	
Attn: Gary Gibbs (Code 5352)	1
Point Mugu, California 93042	
Naval Sea Systems Command Project Manager, High Energy Laser Project	
Attn: CPT Alfred Skolnick	1
PM 22 Washington, D.C. 20362	
Superintendent Naval Postgraduate School	
Attn: Library (Code 2124)	1
Monterey, California 93940	
US Naval Weapons Center	
Attn: Mr. E. B. Niccum (Code 4085)	1
China Lake, California 93555	
Naval Research Laboratory	
Attn: Dr. J. M. MacCallum (Code 5503) EOTPO	1
Washington, D.C. 20375	
Naval Ordnance Laboratory White Oak	
Attn: Mr. K. Enkenhus (Code 034)	1
Mr. J. Wise (Code 047)	1
Mr. Jack Alpers (Code 422)	1
Silver Spring, Maryland 20910	
Air Force Weapons Laboratory	
Attn: COL Donald L. Lamberson (AR)	1
MAJ J. Hines	1
MAJ Burkel	1
Kirkland Air Force Base, New Mexico 87117	
HQ, SAMBO	
P.O. Box 92960, Worldway Postal Center	
Attn: LTC J. R. Doughty (DYU)	1
Los Angeles, California 90009	
Air Force Materiels Laboratory (LPL)	
Attn: MAJ Paul Elder (LPC)	1
Wright Patterson Air Force Base, Ohio 45433	
Air Force Aero Propulsion Laboratory	
Attn: LTC Bobbie L. Jones	1
Wright Patterson Air Force Base, Ohio 45356	

	No. of Copies
Rome Air Development Center Attn: OCSE (Mr. R. Urtz) Griffiss Air Force Base, New York 13441	1
HQ, Electronics Systemd Div (ESD) Attn: CPT Allen R. Tobin (XRE) Hanscom Air Force Base, Maryland 01731	1
HQ, Air Force Special Communications Center (USAFSS) Attn: LTC Wade E. Firmin, USAF Director of Technical Development San Antonio, Texas 78243	1
Defense Intelligence Agency Attn: Mr. Seymour Berler (DT4A) Washington, D.C. 20301	1
Central Intelligence Agency Attn: Mr. Julian C. Nall (OSI/PSTD) Washington, D.C. 20505	1
Aerospace Corporation P.O. Box 92957 Attn: Dr. Walter Warren Los Angeles, California 90009	1
The Garrett Corporation P.O. Box 92248 Attn: Mr. A. Colin Stancliffe Mr. Jim Tyler Los Angeles, California 90009	1 1
Atlantic Research Corporation 5390 Cherokee Avenue Attn: Mr. Robert Naismith Alexandria, Virginia 22314	1
AVCO - Everett Research Laboratory 2385 Revere Beach Parkway Attn: Dr. George Sutton R. M. Feinberg Everett, Maryland 02149	1 1
Battelle Columbus Laboratory 505 King Avenue Attn: Mr. Fred Tietzel (STOLAC) Columbus, Ohio 43201	1
Bell Aerospace Company Division of Textron Inc. P.O. Box 1 Attn: Dr. Wayne C. Solomon Buffalo, New York 14240	1
Boeing Company Aerospace Division P.O. Box 3999 Attn: Mr. M. I. Gamble ORGN 2-5006, MS8C-88 Seattle, Washington 98214	1
ESL Incorporation 495 Java Drive Attn: Arthur Einhorn Sunnyvale, California 94086	1
General Dynamics Pomona Division P.O. Box 2507 Attn: Mr. F. B. Kuffer Pomona, California 91766	1
General Electric Company P.O. Box 8555 Attn: Mr. W. J. East Dr. R. R. Sigismonti Philadelphia, Peansylvania 19101	1 1
General Electric Company 100 Plastics Avenue Attn: Mr. D. G. Harrington, Rm 1044 Pittsfield, Maryland 01201	1
General Research Corporation Westgate Research Park, Suite 700 7655 Old Springhouse Road Attn: Gary F. Gurshe McLean, Virginia 22101	1
Hughes Research Laboratories 3011 Malibu Canyon Road Attn: Dr. Arthur N. Chester Malibu, California 90265	1
Hughes Aircraft Company Centinela & Teale Street Attn: Dr. Eugene Peressini Bldg 6, MS/E-125 Culver City, California 90230	1
Institute for Defense Analyses 400 Army Navy Drive Attn: Dr. Alvin Schnitzler Arlington, Virginia 22202	1
Johns Hopkins University Applied Physics Laboartory John Hopkins Road Attn: Dr. R. E. Gorozdos Laurel, Maryland 20810	1
Lawrence Livermore Laboratory P.O. Box 808 Attn: Dr. Joe Fleck Dr. John Emmett Livermore, California 94550	1 1
Los Alamos Scientific Laboratories P.O. Box 1663 Attn: Dr. Keith Boyer (MS 530) Los Alamos, New Mexico 87544	1
Lulejian & Associates, Inc. Del Amo Financial Center, Suite 500 21515 Hawthorne Boulevard Torrance, California 90503	1
Lockheed Missiles & Space Comaany P.O. Box 504 Attn: Mr. Ben Dunn Sunnyvale, California 94088	1
Mathematical Sciences NW, Inc. P.O. Box 1887 Attn: Mr. Peter H. Rose Bellevue, Washington 98009	1
Massachusetts Institute of Technology Lincoln Laboartory P.O. Box 73 Attn: Dr. Marquet Dr. Rediker Lexington, Maryland 02173	1 1
MITRE Corporation P.O. Box 208 Attn: Mr. A. C. Cron Bedford, Maryland 07130	1

	No. of Copies
Physical Sciences Inc. 607 North Avenue, Door 18 Lakeside Office Park Attn: Dr. Anthony N. Pirri Wakefield, Maryland 01880	1
Northrop Corporation Research and Technical Center 3401 W. Broadway Attn: Dr. Gerard Hasserjian Hawthorne, California 90250	1
Rand Corporation 1700 Main Street Attn: Dr. Claude R. Culp Santa Monica, California 90406	1
Raytheon Company Research Division 28 Seyon Street Attn: Dr. Hermann Statz Waltham, Maryland 02164	1
Raytheon Company Bedford Laboratories Missile Systems Division Attn: Dr. H. A. Mehlhorn Optical Systems Department M/S S4-55 Bedford, Maryland 01730	1
Radio Corporation of America Missile and Surface Radar Division Attn: Mr. J. J. Mayman, Sys Proj Morrestown, New York 08057	1
Riverside Research Institute 80 West End Street Attn: Dr. L. H. O'Neill HP/EGL Library New York, New York 10023	1 1
R&D Associates, Inc. P.O. Box 9695 Attn: Dr. R. Hundley Marina Del Rey, California 90291	1
Rockwell International Corporation Rocketdyne Division 6633 Canoga Avenue, P.O. Box 552 Attn: Marc T. Constantine Canoga Park, California 91304	1
W. J. Schafer Associates, Inc. Lakeside Office Park 607 North Avenue, Door 14 Attn: Francis W. French Wakefield, Maryland 01880	1
Stanford Research Institute 333 Ravenswood Attn: Dr. R. A. Armistead Menlo Park, California 94025	1
Science Applications, Inc. P.O. Box 2351 Attn: Dr. John Asmus La Jolla, California 92037	1
Science Applications, Inc. 1651 Old Meadow Road Attn: Mr. Lawrence PecKam McLean, Virginia 22101	1
Science Applications, Inc. P.O. Box 328 Attn: Dr. R. E. Meredich Ann Arbor, Michigan 48103	1
Science Applications, Inc. 6666 Powers Ferry Road, Suite 202 Attn: Mr. Harvey Ford Atlanta, Georgia 30339	1
Systems, Science and Software, Inc. P.O. Box 1620 Attn: Mr. Alan F. Klein La Jolla, California 92037	10
TRW Systems Group One Space Park Attn: Mr. Norman F. Campbell Bldg 01, Room 1050 Redondo Beach, California 90278	1
United Aircraft Research Center 400 Main Street Attn: Mr. G. H. McLafferty Mr. Albert Angelback East Hartford, Connecticut 06108	1 1
United Technologies Corporation Pratt and Whitney Aircraft Division Florida R&D Center Attn: Mr. Ed Pinsley W. Palm Beach, Florida 33402	1
Westinghouse Electric Corporation Defense and Space Center Friendship International Airport Box 746 Attn: Mr. W. F. List Baltimore, Maryland 21203	1
Westinghouse Research Laboratory 1310 Beulah Road (Churchill Boro) Attn: Dr. E. P. Riedel Dr. L. Denes Pittsburgh, Pennsylvania 15235	1 1
C. S. Draper Laboratory, Inc. 68 Albany Street Attn: Gerald A. Quellette, MS 70 Cambridge, Maryland 02139	1
Product Manager Aircraft Survivability Equipment, AMC P.O. Box 209 Attn: COL Jack L. Keaton, DRCPM-ASE-TM St. Louis, Missouri 63166	
General Research Corporation Southern Operations 307 Wynn Drive Attn: Dr. Carl Warmbrod Huntsville, Alabama 35807	1
General Research Corporation P.O. Box 3587 5383 Hollister Avenue Attn: Dr. Ned Dotson Santa Barbara, California 93105	1
BDM, Inc. 3322 S. Memorial Parkway, Suite 32 Attn: John D. Aitken, Manager Huntsville, Alabama 35801	1

	No. of Copies
TRW Systems, Inc. 7702 Governors Drive, W. Attn: Mr. Dan DeHaven Huntsville, Alabama 35805	1
Stanford Research Institute 306 Wynn Drive, N.W. Attn: Mr. Harold Carey Huntsville, Alabama 35807	1
DRCPM-HEL	3
DRSMI-FR, Mr. Strickland	1
-LP, Mr. Voigt	1
DRDMI-X, Dr. McDaniel	1
-T, Dr. Kobler	1
-H, Mr. Cason	10
-TB	3
-TI (Record Set)	1
(Reference Copy)	1